An Integrated Performance Model for High Temperature Gas Cooled Reactor Coated Particle Fuel
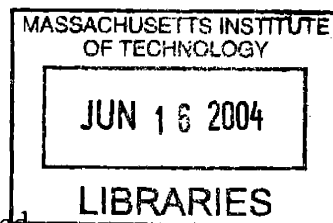
by

Jing Wang

B.S., Technical Physics
Peking University, 1998

SUBMITTED TO THE DEPARTMENT OF NUCLEAR ENGINEERING
IN PARTIAL FULFILLMENT OF THE REQUIREMENTS FOR THE DEGREE OF

DOCTOR OF PHILOSOPHY IN NUCLEAR ENGINEERING
AT THE
MASSACHUSETTS INSTITUTE OF TECHNOLOGY
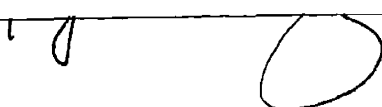
January 2004 [Feb 2004]

Signature of Author _____
Department of Nuclear Engineering
January 28, 2004

Certified by _____
Ronald G. Ballinger
Associate Professor of Nuclear Engineering
Associate Professor of Materials Science and Engineering
Thesis Supervisor

Accepted by _____
Sidney Yip
Professor of Nuclear Engineering
Thesis Co-advisor

Accepted by _____
Mujid S. Kazimi
Professor of Nuclear Engineering
Thesis Reader

Accepted by _____
Jeffrey A. Coderre
Chairman, Departmental Committee on Graduate Students

An Integrated Performance Model for High Temperature Gas Cooled Reactor Coated Particle Fuel

by

Jing Wang

ABSTRACT

The performance of coated fuel particles is essential for the development and deployment of High Temperature Gas Reactor (HTGR) systems for future power generation. Fuel performance modeling is indispensable for understanding the physical behavior of fuel particles and achieving their high reliability during operations and accidents through a guided design process.

This thesis develops an integrated fuel performance model of coated particle fuel to comprehensively study its mechanical behavior and define an optimum fuel design strategy with the aid of the model. Key contributions of the thesis include a pyrocarbon layer crack induced particle failure model with a fracture mechanics approach, mechanical analysis of particles with better representation of irradiation induced creep, a proposed fuel optimization procedure, the capability to simulate arbitrary irradiation histories, and the incorporation of Monte Carlo sampling to account for the statistical variation of particle properties.

Stress calculations in this model were benchmarked with the FUEL code and finite element calculations of Idaho National Engineering and Environmental Laboratory (INEEL) and with model predictions for High Temperature Test Reactor (HTTR) first-loading fuel. Fuel failure predictions were made for New Production-Modular HTGR irradiated fuel capsules, which show good agreements with experiments. Based on the simulations, it is suggested that in most cases the pyrocarbon crack induced fuel failure mechanism plays a much more important role in fuel performance than the more widely accepted pressure vessel fuel failure mechanism. After the establishment of the model, parametric study was conducted to find out the effects of various input variables on fuel performance, and fuel design and optimization procedure was proposed accordingly. Simulations with optimized fuel configurations demonstrate that superior fuel performance can be achieved with model analysis. The model also prepares interfaces for further improvements on various modules upon arrival of new information.

Thesis Supervisor: Ronald G. Ballinger
Title: Associate Professor of Nuclear Engineering and Materials Science and Engineering

Acknowledgements

Table of Contents

List of Figures

14

List of Tables

Chapter 1.

Introduction

1.1. Overview of High Temperature Gas-cooled Reactors

With nuclear energy being a significant contributor in the light of increasing energy demands of the future, the High Temperature Gas-cooled Reactor (HTGR) has been drawing attention with the expectation of achieving the goal of a safe, efficient, environmentally acceptable and economic high temperature energy source for the generation of electricity and for industrial process heat applications such as the production of hydrogen. All HTGR systems feature graphite moderated, helium cooled cores which utilize ceramic coated fuel particles dispersed in a graphite matrix. The use of a ceramic core and helium as the coolant permits an increase in the operating temperature, which benefits the efficiency of the power generating system. HTGRs also exhibit exellent safety characteristics due to: the high heat capacity of the graphite core, the chemical stability and inertness of the fuel, coolant, and moderator, the encapsulation and high retention of fission products by coated fuel particle configurations, the single phase characteristic of helium coolant, and the inherent negative temperature coefficient of reactivity of the core [1].

Development of HTGRs began in the 1950s, and both prismatic type fuel elements (block type reactor) and spherical fuel elements (pebble bed type reactor) have been employed. Figure 1-1 and Figure 1-2 show schematics of the fuel system for each type of reactors. The Pebble Bed Reactor (PBR) design uses coated fuel particles that are approximately 900 μm in diameter embedded in spherical graphite fuel "pebbles". A pebble, of approximately 6 cm diameter, contains approximately 15,000 coated particles within the graphite matrix, as shown in Figure 1-1. For a typical 120MWe reactor core design, there are approximately 360,000 pebbles. The pebbles, unlike the fuel rods in a

conventional Light Water Reactor (LWR) which are stationary, move through the core on a continuous basis during operation.
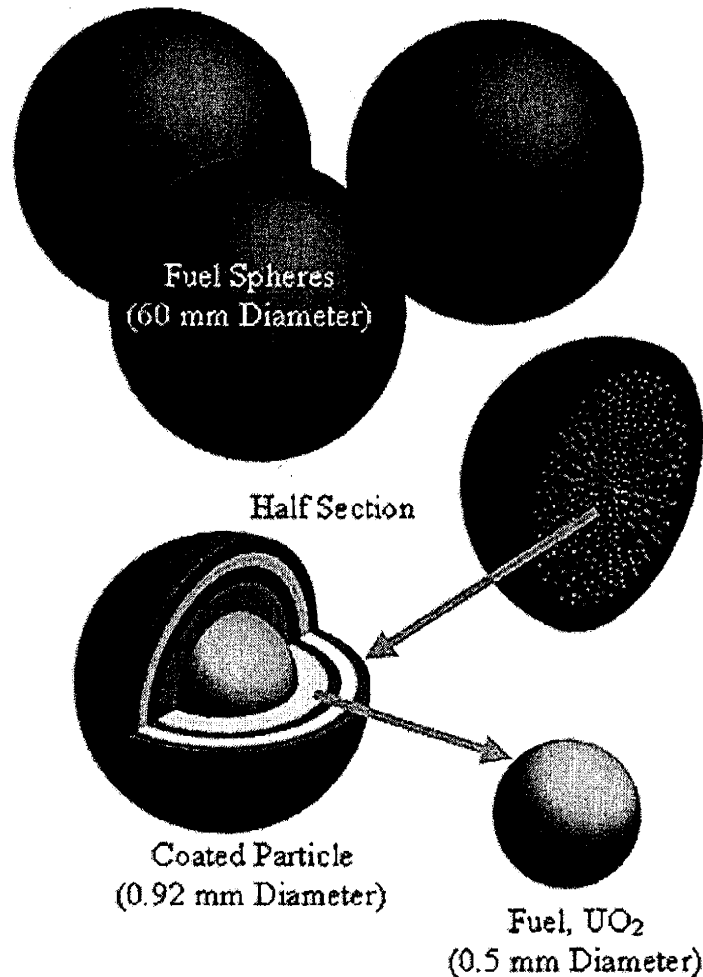
Figure 1-1. Schematic of the pebble bed fuel system (courtesy ESKOM, South Africa)

Partially burned and fresh fuel, when necessary, is added to the top of the core which has a geometry similar to that of a fluidized packed bed. Fuel pebbles then flow down through the core region. Upon exiting the core after a particular pass the pebbles are checked for accumulated burnup and integrity. Based on the results of this analysis a pebble is either removed from the stream and a new one added or it is recycled to the top (entrance) of the core for another cycle. Heat is transferred from the fuel to, in most cases, helium flowing through the core.

Pyrolytic Carbon
Silicon Carbide
Porous Carbon Buffer
Uranium Oxycarbide

Particles   **Compacts**   **Fuel Assembly**
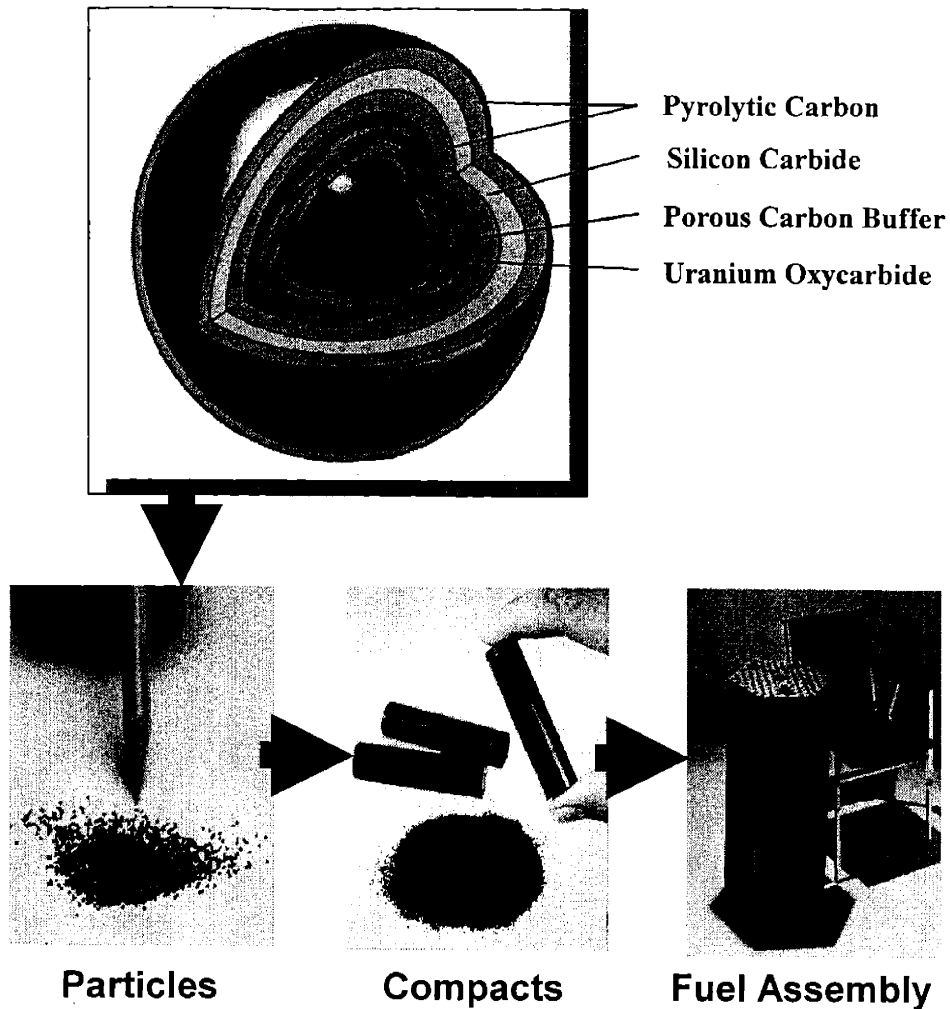
Figure 1-2. Schematic of the prismatic fuel system (courtesy General Atomics)

The block type reactor uses a conventional stationary system in which the fuel particles are embedded in cylindrical fuel "compacts" which are then embedded in graphite fuel blocks to form fuel assemblies, as shown in Figure 1-2. In addition to fuel, the fuel blocks also contain cooling passages and locations for absorber and control material. This type of reactor is refueled by periodic removal of depleted fuel blocks and the addition of fresh fuel.

A detailed description of the history, joint efforts, and projected developments of HTGRs is given in an IAEA publication [1]. Here we highlight a few historical events which are representative or pertinent to the contents of this thesis.

Early developments of HTGRs were conducted in the UK, Germany, and US. The Dragon Reactor Experiment in the UK that first operated at power in July 1965 incorporated graphite fuel elements with high enriched uranium-carbide coated fuel particles. The plant demonstrated successful performance of many components [2], and served as a productive research tool for the development of helium gas cooled reactors and advanced fuel particle coatings [1]. In Germany, the 15 MWe Arbeitsgemeinshaft Versuchsreaktor (AVR), a pebble bed type HTGR, began operation in 1967 and continued until December 1988. The AVR was the main fuel development tool for the pebble bed concept. In the US, the helium cooled 40 MWe Peach Bottom (No. 1) HTGR, operated from 1967 to 1974, provided the majority of experience for the continue commercialization of HTGR technology.

In the 1980s, the modular HTGR concept was proposed and soon led to substantial developments in various countries over the past two decades. This concept was attractive due to its passive safety in addition to the general characteristics of HTGRs [3]. These features are embodied in the following design concepts.

- The incorporation of spherical coated fuel particles which are able to retain all radiologically relevant fission products up to about 1600°C.

- The assurance that a maximum fuel temperature of 1600°C is not exceeded during any accident is achieved by a low power density of 3 MW/m^3 – 4 MW/m^3. Decay heat during accidents is removed by means of passive heat transport mechanisms, including conduction, natural convection, and radiation, to simple surface coolers.

- Small reactor core diameter of about 3m comes from the requirement for reactor shutdown using only free falling control rods into boreholes in the reflector.

- Graphite, whose failure temperature is far above 1600°C, is used for core structures and fuel matrix.

- The single phase noble gas, helium, which is neutral from viewpoints of chemistry and neutron physics, is used as coolant.

Currently, both experimental and commercial HTGRs are either under development or being operated. These include the Pebble Bed Modular Reactor (PBMR) being developed by ESKOM of South Africa, British Nuclear Fuels plc. (BNFL) of United

Kingdom, the Gas Turbine-Modular Helium Reactor (GT-MHR) being developed by a consortium of General Atomics of United States, MINATOM of Russia, Framatome of France, and Fuji Electric of Japan, and test reactors including the High Temperature Test Reactor (HTTR) developed by the Japan Atomic Energy Research Institute (JAERI) and the High Temperature Reactor (HTR-10) developed by the Institute of Nuclear Energy Technology (INET) in Beijing, China. In addition to these reactor development efforts, R&D programs are being conducted by institutions, national laboratories, etc., within United States, United Kingdom, Germany, China, France, Japan, South Africa, Netherlands, Russia, and Indonesia, to address HTGR safety and performance issues.

1.2. Coated Fuel Particles

Various countries have been using the same generic coated fuel particles in the designs for their HTGRs, though with some differences in fuel materials and coating structures. As stated above, excellent coated particle fuel quality and performance will be essential for the development and deployment of HTGRs for future power generation. Two micrographs of actual coated fuel particles are shown in Figure 1-3.
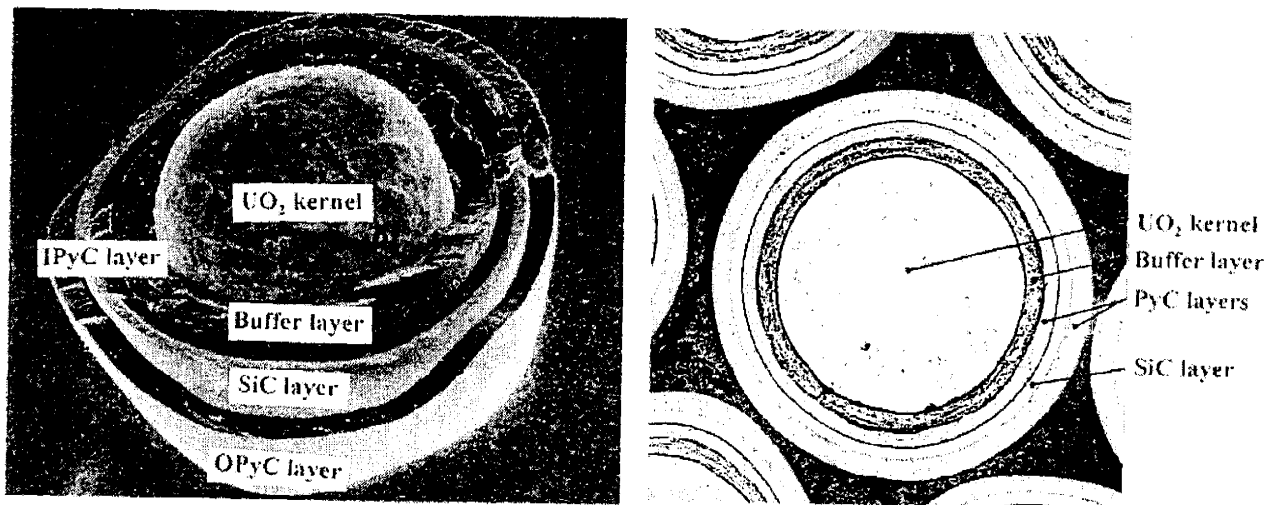
Figure 1-3. Micrographs of coated fuel particles (from K. Sawa and K. Minato [4])

The function of the coated fuel particle is to generate energy while containing the produced fission products. The fuel particle, commonly about 1mm in diameter, consists

of a fuel kernel, typically UO_2 or Uranium Oxy-carbide (UCO), surrounded by a low density pyrolytic carbon (PyC) buffer layer, and followed by structural coatings of a triple-layered composite material consisting of a silicon carbide layer (SiC) sandwiched between dense PyC layers, termed inner PyC layer (IPyC) and outer PyC layer (OPyC). The resulting particle is called a TRISO fuel particle (tri-isotropic PyC/SiC/PyC structural layers). Before discussing the manufacturing of coated particles and functions of the various layers, we talk about the fluidized bad technique briefly.
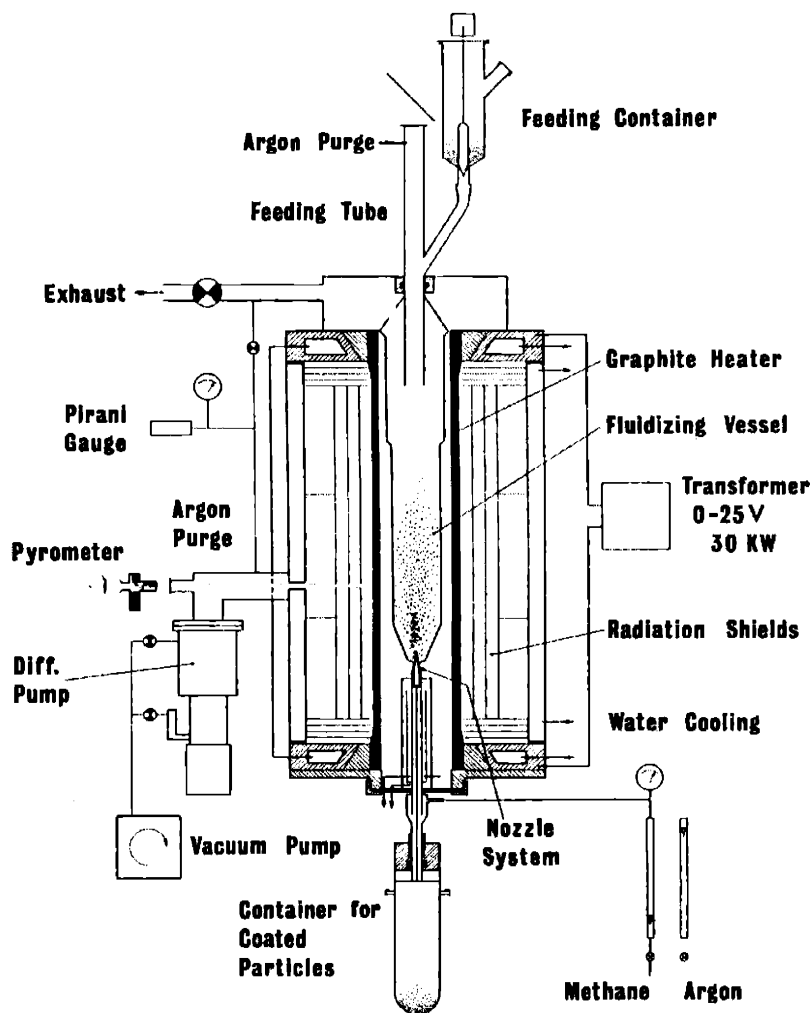
Figure 1-4. Schematic diagram of laboratory scale fluidizing furnace (from Huddle et al. [5])

The use of high temperature fluidized beds to coat fuel microspheres emerged from several processes which were in vogue in the early 1960s [6] as the standard manufacturing method. A schematic of a fluidizing furnace is shown in Figure 1-4. The

23

particles are introduced into the fluidizing vessel via the feeding tube on top of the furnace and are fluidized normally in a spouted mode throughout the coating operation by injecting gas containing gaseous hydrocarbons (in the case of coating pyrolytic carbon) at the base of the system. The particles in the vicinity of the axis of the coating vessel are brought into the gas stream. The gas mixture is heated by the surrounding walls of the coating vessel, and the coating agent decomposes to form a cloud of nuclei which then grow in size, collide together, and coalesce before being captured by the particle surface.

We now take a closer look at each part of a coated fuel particle.

(1) Fuel Kernel. The kernel is typically $300 - 600$ μm in diameter, and contains UO_2 or UCO. During the nuclear fission process, the kernel produces a mixture of radioactive fission products. Among the fission products there are gaseous species which cause stresses in the coatings, as well as solid metallic species which chemically interact with the coatings. The fuel kernel swells with increasing burn-up of the fuel, and tends to migrate off-center under a sufficient thermal gradient, which is called the amoeba effect. Because the kernel is the substrate on which the coating layers are deposited, it is desirable that the fuel kernel should be as spherical as possible.

(2) PyC Buffer Layer. This is the layer that is directly in contact with the kernel. Conditions in the fluidized bed are arranged to keep the density of this layer in the range of $0.9 - 1.1$ g/cm^3, compared with theoretical density of $2.26 g/cm^3$ for pyrocarbon. The porous buffer layer is an absorber of fission recoils and provides free volume to accommodate fission products and kernel swelling. It also serves as a mechanical separation between the kernel and the structural coating layers.

(3) Inner PyC Layer. This layer is generally referred to as the IPyC layer, and is the first of three structural layers. It is usually deposited from a mixture of C_2H_2 and C_3H_6 at a temperature of 1300°C in a fluidized bed and has a density of $1.8 - 2.0 g/cm^3$. The layer forms the first barrier against the fission gas pressure from the fuel kernel, and resists migration of actinides and fission products. The IPyC layer is a practically impenetrable barrier for fission gases like Krypton and Xenon and fission product Iodine, but it becomes increasingly pervious for Cesium and Strontium at higher (higher than normal operational) temperatures. It performs poorly at stopping Silver.

24

(4) Silicon Carbide Layer. The SiC layer is deposited from trichlormethylsilane (CH_3SiCl_3) at approximately 1500°C under appropriate conditions, and has a density of about 3.20g/cm^3, which is very close to its theoretical density. This layer provides better retention of basically all fission products, therefore assuring that it will remain intact under all normal reactor core conditions is a key to the success of HTGRs. Additional attractive features of SiC are its higher mechanical strength than that of dense PyC layers, and its stability under fast neutron irradiation [7]. However, SiC has some problems as well that need to be taken into account. At temperatures above 1600°C, SiC will be attacked by Palladium (Pd) and rare earth elements if exposed for long hours. Also, Cesium and Strontium begin to migrate through intact SiC layer under such conditions. The fission product Ag^{110m} sometimes transports through intact SiC layer at elevated temperature, and it is believed this process is driven by diffusion. Recent experimental results suggest that the diffusion assumption is highly questionable, and Ag^{110m} penetrates SiC through a network of micro-cracks induced by thermal cycling and/or radiation damage in the material. In addition to the above, at temperatures in the region of 2000 - 2200°C, thermal decomposition of SiC takes place, which will be discussed further later on.

(5) Outer PyC Layer. This layer is generally referred to as the OPyC layer. It is deposited the same way as the IPyC layer. This layer protects the SiC layer from being damaged during the fuel manufacturing processes following the coating process. It also applies compression onto the SiC layer because of its shrinkage during fast neutron irradiation, so that the SiC layer is not easily fractured by over-pressurization.

Before fuel particles are mixed with the graphite matrix material and pressed into fuel elements, an overcoat of graphite matrix material is applied to each coated fuel particle to prevent them from contacting wit each other (as can be seen from Figure 1-3), and thereby damaging their coatings during pressing of the fuel elements.

The overall coated fuel particle design has evolved over the years and there have been several variations in terms of overall structure and fuel and coating materials. Historically the original coated particle fuel design contained a binary layer system. This "BISO" particle did not contain a SiC layer and had only one dense PyC layer which was

deposited on top of the buffer layer [8]. The fuel kernel has been fabricated using a number of fissile or fertile combinations including UO_2, UC_2, UCO, ThO_2, (U, Th)O_2, (U, Pu)O_2, depending upon the applications of the fuel and considerations of fuel performance. The performance of these types of fuel except for (U, Pu)O_2 has been discussed at length by Bullock et al. [9][10]. With respect to the SiC barrier layer, there has been considerable interest in the properties of Zirconium Carbide (ZrC) in place of SiC, because ZrC appears to show better retention of fission products and better stability at very high temperatures [11][12].

1.3. Coated Fuel Particle Failure Mechanisms

Experience accumulated from extensive irradiation and heating tests and material properties studies has provided a fundamental understanding of the performance of TRISO fuel particles and has propelled advances in the modeling of fuel performance. A considerable body of information on fuel behavior and failure mechanisms has been compiled [1], [13]-[16], and are summarized below together with newly proposed fuel failure mechanisms which this thesis and its corresponding model have been studying. The following is a brief discussion of failure mechanisms. The details of mechanical failure mechanisms and modes will be discussed later in the fuel failure model Section 2.5 of Chapter 2. Chemical failure mechanisms, which are not the concentration of this thesis, are discussed in a limited way in this section.

(1) Over-Pressurization Failure. As stated in Section 1.2, fission gases generated from the fuel kernel will impose pressure on the structural layers and induce tensile stresses in them. If sufficient tensile stress is created in a particular layer and exceeds the strength of that layer, it will fail. The internal pressure in a coated particle builds up as burnup increases, so at high burnup, this type of fuel particle failure may take place. Most fuel performance models treat this failure mechanism.

(2) PyC Crack Induced Failure. . This is the fuel failure mechanism that will serve as the model in this thesis and represents a new approach to the fuel failure process. The modeling of this mechanism is based on a fracture mechanics approach. Its focus is on the stress concentration in the SiC layer created by a through-thickness crack in

the IPyC or OPyC layer. The SiC layer can be failed by high stress concentration even if the far field stress in it is compressive. This failure mechanism is very different from over-pressurization failure failure and the modeling of this mechanism represents a new and more realistic approach to the failure process.

(3) Peel-off of Particle Outer Coating. The fuel particles are embedded in the graphite matrix, which is a type of lower density graphite material compared with the dense particle PyC coatings. Irradiation leads to relatively high shrinkage of matrix material, which imposes severe tearing stress on the particle outer coating. If the binding between the matrix and the PyC coating is strong, the coating may be damaged. Such coating failures can be avoided by designing the fuel element so that the coupling between the outer coating of the fuel particle and the surrounding matrix material is weak [1].

200 μm
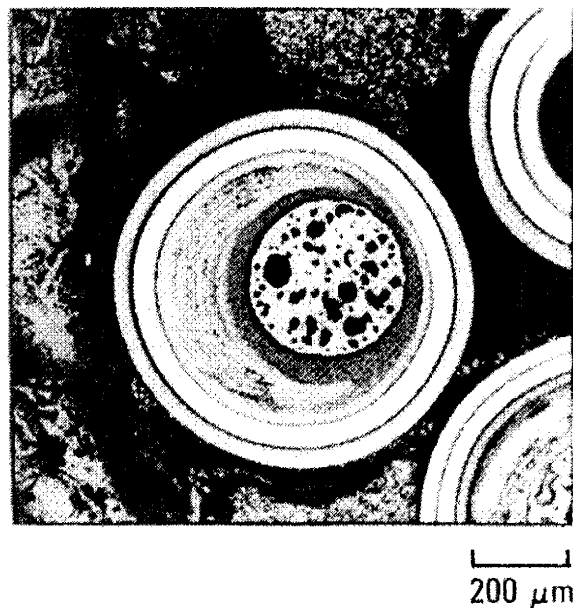
Figure 1-5. A metallographic photo of a TRISO UO2 particle with kernel migration after irradiation (from Ketterer and Myers [19])

(4) Kernel-Coating Interaction. This is a specific type of corrosion failure of the SiC layer due to fuel kernel migration. The mechanism for kernel migration is essentially a carbon transport cycle on an extremely small scale [17][18]. The process basically involves carbon oxidation to CO on the hot side of the kernel and transport to the cooler side. The oxygen released due to carbon deposition on the cooler side finds it

27

way back to the hot side either by diffusion through the kernel or by gas transport as CO_2. The net effect is the movement of the kernel relative to the coating layers in the direction of increasing temperature, as shown in Figure 1-5. Three factors considered as increasing kernel migration rate are the magnitude of the temperature gradient, the temperature level, and the oxygen pressure within the IPyC layer. Thermodynamic calculations and experimental results indicate that the effects of kernel migration and fission product diffusion are minimized by using a mixed oxide/carbide fuel kernel [20]. Additionally the maximum fuel temperature and temperature gradient in HTGRs can be carefully designed to be within limits. For careful designs, kernel migration and hence kernel-coating interaction is currently not considered to be a significant contributor to fuel failure.

20 μm   100 μm
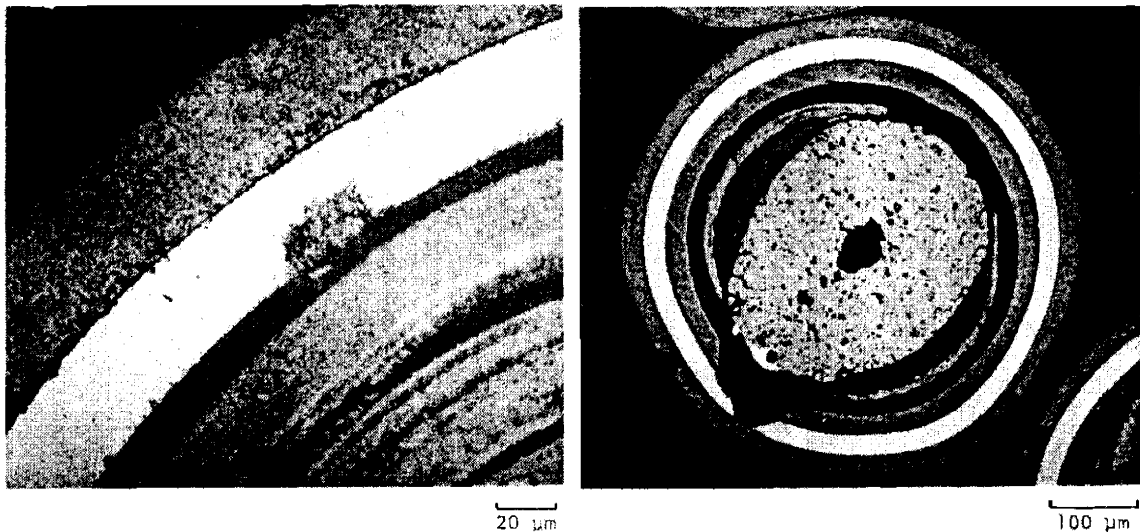
Figure 1-6. Metallographic cross sections of representative TRISO fuel after irradiation. Degradation of SiC resulted in excessive metallic fission product release (from Gulden et al. [23])

(5) SiC Degradation by Fission Products and Impurities. As stated in previous sections, fission products like Palladium and rare earth elements may reach the SiC layer and interact chemically with it, resulting in its degradation and even failure. Additionally, SiC may be chemically attacked by HCl formed from the coating gas during SiC deposition [21]. Scheffel and Tang [22] also state that excessive impurity levels of Fe, Ni, and Cr, incorporated with the kernel during manufacturing, may also corrosively

28

damage the SiC layer. Figure 1-6 shows SiC degraded fuel particles, which result in excessive metallic fission product release (the white ring in the figure is the SiC layer). To mitigate these effects, proper choice of fuel composition is needed and excessive introduction of impurities can be excluded by careful fuel fabrication.

(6) SiC Decomposition at High Temperatures. Thermal decomposition of the SiC layer becomes significant at 2000°C - 2200°C, leading to increasing porosity of the SiC and ultimate failure. Again this effect can be eliminated by reactor design.

(7) Fabrication defects.

The first three of the above mechanisms link to the mechanical behavior of the fuel particles, and mechanisms (4) - (6) appear to concern the chemical aspects of them. Quantitative fuel performance models considering the above chemical fuel failure mechanisms and the over-pressurization mechanical failure have been developed on the basis of data from irradiation tests, heating tests, and material properties studies, and these models are utilized in the design of reactor cores for the purpose of achieving a high degree of reactor safety. However, mechanism (2) is the least understood one, and little modeling work has been done with regard to it. In this research, a PyC crack induced fuel failure model has been developed using a fracture mechanics approach, and improved step by step as we gain insights on the corresponding physical process and build knowledge on how to effectively integrate such a model into an overall fuel performance model.

1.4. Problems and Challenges in Fuel Performance Modeling

The most important goal in the improvement of the manufacturing process of the fuel element is to reduce the coated particle defect fraction and to minimize uranium contamination. The most important goal in the development of a coated particle fuel performance model is to configure the fuel particles so that a minimum number of them with intact coatings would experience failures during operation. However, before such a model can be deployed to optimize fuel particles for best possible fuel performance, the confidence in the results should be high. Ideally, the model must be constructed to reflect the correct physics of fuel particle behavior, must be tested and verified against a whole

spectrum of existing models and irradiation and heating experiments, and accepted by the HTGR community. Unfortunately, the nature of coated fuel particles results in some intrinsic challenges and difficulties on the way of establishing a robust and viable model. These challenges are listed below.

(1) Because the coated fuel particles are tiny and layer dimensions are typically in the range of 30 – 100 μm, many material properties, such as irradiation induced dimensional changes and creep coefficient of PyC, elastic constants of PyC and SiC, and strengths of PyC and SiC, are measured on experimental specimens rather than the particles themselves. Typically they are obtained from strip samples prepared from CVD coatings deposited on graphite or sapphire discs levitated in fluidized beds of particles. This leads to whether the material properties are affected by the geometry, size and spherical configuration of the particles, and if so, how big a difference they would make. One can imagine that the strengths of PyC and SiC will probably be modified by the size of the materials because defects are confined by that size. Additionally, the experimental data will often exhibit wide variations on many material properties. In this work we address this problem by sampling the data variations with statistical distributions so that ensemble behaviors can be revealed.

(2) The first step for a model to evaluate mechanical fuel particle failure is the evaluation of stresses in a particle based on material properties, the irradiation state, and the environment the particle is in. We can then determine whether the stresses exceed the strength of the particle. However, the stresses in a particle are not measurable. Consequently, we are left to compare our stress calculations with those from other parties. By doing so, we are able to make sure the mathematical derivations are right, but have to use experience and engineering judgment on the correctness of constitutive laws for materials.

(3) Since the ultimate goal of fuel performance modeling is to provide specifications to fuel manufacturers to make optimized coated fuel particles for certain type of HTGRs, the correlations between manufacture controlling parameters, such as fluidized bed temperature, feeding gas composition, gas flow rate, and bed surface area, and material properties and morphology of pyrocarbon and silicon carbide have been studied thoroughly in the past forty years. Such work will be summarized in

Chapter 5. Although material properties like density and Bacon Anisotropy Factor (BAF) are considered in all of the fuel performance models nowadays, little information regarding the microstructure and morphology of materials was incorporated in those models. If we take a look at pyrocarbons, it is known that depending on the depositing conditions, pyrocarbons can be columnar, granular, laminar or isotropic, as will be shown in Chapter 5. A block of granular pyrocarbon and a block of laminar one may exhibit very similar density and BAF and therefore modeled the same way in current models, but their different microstructures may suggest different strengths and dimensional responses under irradiation, which dictates the actual failure processes. Unfortunately, past experiments were not designed to reveal such linkages, so fuel performance models in the near term will not be able to tell fuel failure mechanisms governed by the material microstructure and morphology.

Nevertheless, what we can do with modeling is to take a physical approach intrinsically and simulate realistic environments extrinsically based on the current knowledge of particle fuel behavior and the best set of data available, and benchmark our model predictions on various levels wherever possible with existing modeling results and experimental data, which will be detailed in Chapter 3. Meanwhile, we should consider in advance what improvements could be made in the future and develop the model such that it can be stretched and enhanced easily later on when more data are available and better understanding is gained of the fuel performance under normal operating and accident conditions.

1.5. Thesis Objective

The thesis objective is to: (1) develop an integrated fuel performance model for coated particle fuel in High Temperature Gas-cooled Reactors to study the mechanical and chemical aspects of fuel behavior under normal operating conditions, with the emphasis on mechanical behavior, (2) to use this model to predict fuel failures in irradiation tests and reactor operations, (3) to use this model to suggest ways to optimize

the fuel particle to achieve best possible fuel performance in terms of minimizing fuel failure probability.

Chapter 2.

Development of the MIT Fuel Performance Model

2.1. The Required Components in a Fuel Performance Model for HTGRs

Modeling of fuel performance requires that the details of the behavior of an individual particle be treated. However, in addition to this, it is critical that the environment in which the particle operates also be properly modeled. This is necessary in order that proper boundary conditions be established. This model development process can thus be broken into two major tasks: (1) modeling of the mechanical and chemical behaviors of the fuel and, (2) modeling the environment the fuel is operating in. Figure 2-1 shows a schematic to explain the components needed for completing the tasks.

Firstly we need to consider factors that contribute to the deformation of a coated particle. Based on the experience of the industry, these generally include irradiation-induced dimensional change, irradiation-induced creep, thermal expansion, and particle internal pressure buildup from fission gases produced from fuel kernels. These phenomena are functions of temperature, neutron fluence, burnup, and some material properties, as shown in Figure 2-1, so such dependencies have to be modeled first before a mechanical model is applied to convert the resulting deformation into stress and strain distributions in a particle. Meanwhile, a chemical model focuses on the chemical interactions and interfaces with the mechanical model, because some chemical reactions produce gaseous species which contribute to the internal particle pressure, and corrosions may cause thinning and weakening of coating layers. The information obtained above feeds into a fuel failure model. Mechanically, coating layer strengths and failure processes should be modeled. Chemically, the resistance of coating layers to chemical attacks should be modeled. Beside these core components, the variations of particle

33

dimensions and material properties are sampled by Monte Carlo technique due to the statistical nature of the fuel manufacturing process.
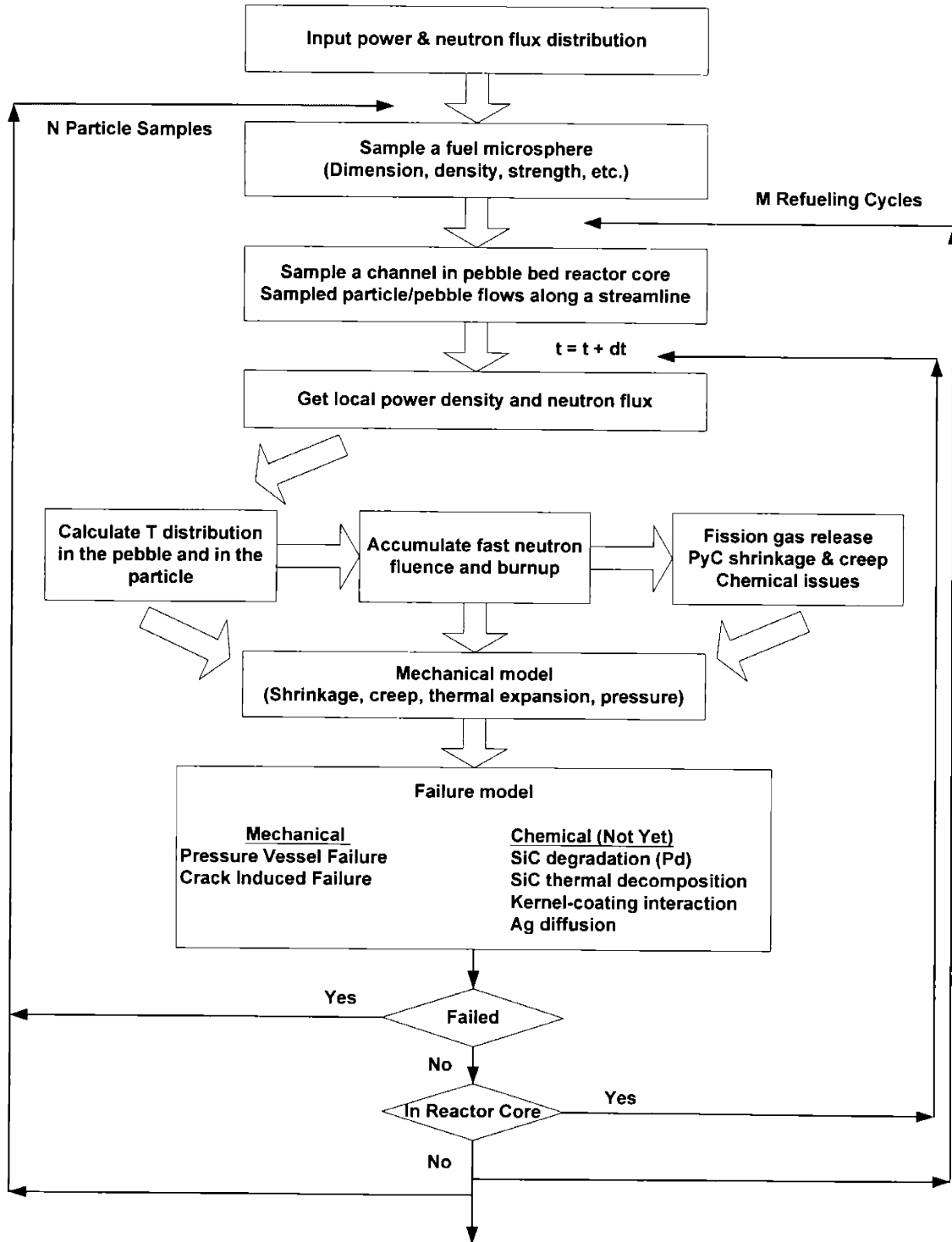
Figure 2-1. The flowchart of a fuel performance model

Secondly, the model should be able to simulate the virtual environment for the particles. In the case of a prismatic reactor core, the time dependent irradiation history of a fuel particle can be provided as inputs. However, the pebble bed reactor uses a multipass fueling system, as has been discussed in Section 1.1, in which fuel is cycled through the bed several times prior to ultimate discharge. Fuel pebbles are extracted from the bottom of the core and then returned to the top of the bed, but the location of the fuel pebble within a single pass is determined in a random manner based on the location of initial entry into the top of the bed. Thus, the modeling of the pebble-bed system requires that the flow paths for individual particles (associated with a particular pebble) be sampled through these cycles, and the local power density and neutron flux a particle encounters constitute a unique irradiation history for that specific particle. This refueling scenario is illustrated in Figure 2-1. We notice that the irradiation history for a particle is unknown beforehand for simulations in pebble bed reactor systems, and the other way around in stationary prismatic reactor systems, in which the refueling loops in Figure 2-1 need not be executed.

Each component is to be discussed in great detail in the following sections.

2.2. Fission Gas Release Model

The fission gas release model is based on a model developed by the University of Tennessee (UT) and the Institute for Safety Research and Reactor Technology at the Research Center in Germany (KFA) [24], which has been used in the code PANAMA to predict the outcome of German fuel irradiation tests [25]. The procedure is to calculate the amount of long-lived fission gases like Kr and Xe that are released from the fuel kernel into the porous buffer layer, as shown in Figure 1-3. The release is described by diffusion driven transport from a sphere, written mathematically as

$$\frac{\partial C}{\partial t} = \frac{D}{r^2}\left[\frac{\partial}{\partial r}\left(r^2 \frac{\partial C}{\partial r}\right)\right] + S,$$

$$(2.1)$$

where:

C is the fission product concentration (atoms.m^{-3}),

D is the diffusion coefficient (m^2/s), which is independent of r and depends functionally only on temperature T,

S is the uniform source of fission product C within the sphere (atoms.m^{-3}·s^{-1}), independent of radial dimension r and time t.

If initially there is no fission gas in the kernel and buffer layer, and assuming the value of C on the outer surface of the spherical fuel kernel ($r = r_1$) is zero at all times, then the analytical solution of eq. (2.1) is given by [26] as

$$C(r,t) = \frac{S}{6D}(r_1^2 - r^2) + \frac{2Sr_1^3}{\pi^3 Dr} \sum_{n=1}^{\infty} \frac{(-1)^n}{n^3} \sin\left(\frac{n\pi r}{r_1}\right) \exp\left(\frac{-n^2\pi^2 Dt}{r_1^2}\right). \qquad (2.2)$$

The fission product transfer rate at the sphere surface is

$$fission\ product\ transfer\ rate\ (r = r_1) = -D4\pi r_1^2 \left(\frac{\partial C}{\partial r}\right)_{r=r_1}. \qquad (2.3)$$

We then can calculate the fraction of fission gases that diffuses out of the fuel kernel during an irradiation time t, by integrating the fission product transfer rate out of the kernel, and dividing by the total generation of fission products in the sphere over the same time period, which is

$$f(t) = \frac{\int_0^t \left[-D4\pi r_1^2 \left(\frac{\partial C}{\partial r}\right)_{r=r_1} \right] dt'}{\int_0^t \left(S\frac{4}{3}\pi r_1^3 \right) dt'}. \qquad (2.4)$$

Substituting eq. (2.2) into eq. (2.4) and defining $\tau = Dt/r_1^2$, eq. (2.4) can be expressed in a simpler form of

$$f(\tau) = 1 - \frac{6}{\tau} \sum_{n=1}^{\infty} \frac{\left[1 - \exp\left(-n^2\pi^2\tau\right)\right]}{n^4\pi^4}. \qquad (2.5)$$

Eq. (2.5) gives the fractional fission gas release during irradiation and it is plotted in Figure 2-2. If the fuel is irradiated for a time ti (s) at temperature Ti (K) and after irradiation is heated for time t_a (s) at temperature T_a (K), it can be shown that the total fractional release F_d is calculated by [27]

$$F_d = f_i + f_a = \frac{(\tau_i + \tau_a)f(\tau_i + \tau_a) - \tau_a f(\tau_a)}{\tau_i}, \qquad (2.6)$$

and

$$\tau_i = DS(T_i) \cdot t_i, \tag{2.7}$$

$$\tau_a = DS(T_a) \cdot t_a, \tag{2.8}$$

where DS is the reduced diffusion coefficient (s^{-1}) of the fission gases in the particle kernel given by

$DS = D/r_1^2$ with D being effective diffusion coefficient at certain temperature and r_1 being the kernel radius.
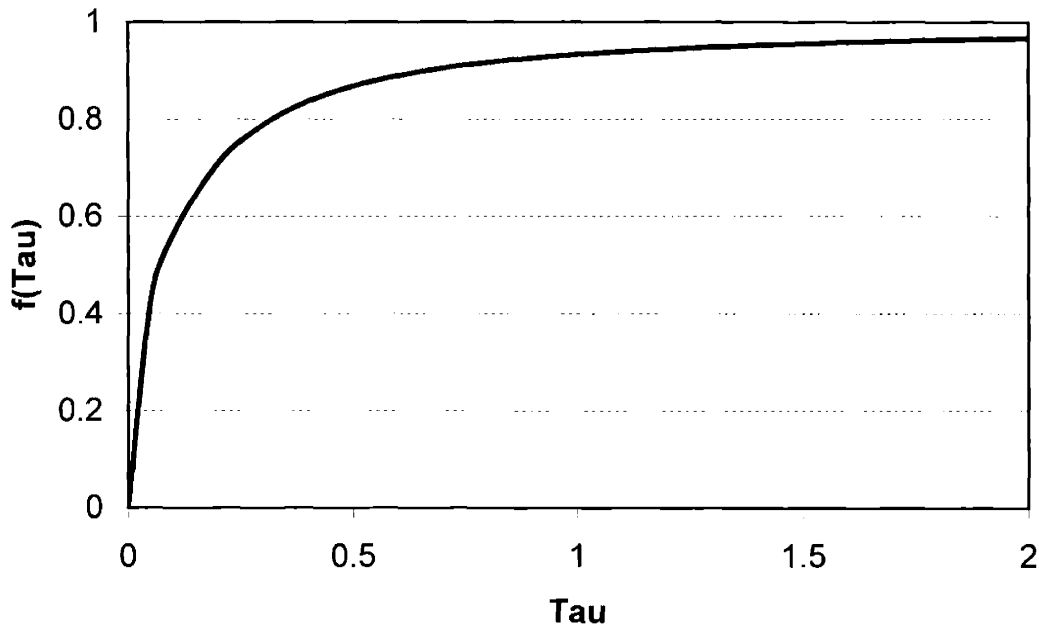
Figure 2-2. The fractional fission gas release

DS is a function of the type of particle fuel kernel. For UO_2 and UCO kernels, DS is given by [25]

$$\log DS = -2.30 - \frac{0.8116 \cdot 10^4}{T}, \tag{2.9}$$

and for $(Th, U)O_2$ fuel, it is [25]

$$\log DS = -5.94 + \frac{3.24}{1 + 0.11/F_b} - \frac{0.5460 \cdot 10^4}{T}, \tag{2.10}$$

where T is the temperature (K) and F_b is the heavy metal burnup (FIMA).

37

If there is no annealing involved, it can be seen from eq. (2.6) that F_d is simply $f(\tau_i)$.

In addition to fission gases, oxygen atoms are also released during the fission of U^{235} or Pu^{239}. The number of oxygen atoms released per fission (OPF) is calculated based on empirical relationships derived from mass-spectrometric measurements of CO in irradiated UO_2 fuel particles [25]. During irradiation, the equation is [25]

$$\log(OPF) = -10.08 - 8500/T_i + 2\log(t_i),$$ (2.11)

and during heating, it is [25]

$$\log(OPF) = -10.08 - 8500/T_i + 2\log(t_i) - 4.04\left[(1000/T_a) - 1000/(T_i + 75)\right].$$ (2.12)

For UCO kernel, no Oxygen production is assumed to happen, so

$$OPF = 0.$$ (2.13)

The following equation is valid for $(Th,U)O_2$ fuel [25]

$$\log(OPF) = 0.96 - 4420/T + 0.4\log N + 0.3\log F_b,$$ (2.14)

where N is the ratio of Th/U^{235}.

The internal gas pressure p (Pa) is determined by the ideal gas law in the following manner,

$$pV_f = \left[\left(F_d F_f + OPF\right)F_b\left(V_k/V_m\right)\right]RT,$$ (2.15)

where:

V_f is the void volume (m^3),

F_f is the fission product yield from stable fission gases, $F_f = 0.31$,

F_b is the heavy metal burnup (FIMA),

V_k is the kernel volume (m^3),

V_m is the molar volume of kernel (m^3/mol),

R is the ideal gas constant (8.31J/mol·K), and

T is the temperature (°K).

The molar volume of the heavy metal in a particle kernel is defined by the ratio of the mass of 1 mole of kernel material to its density.

For UO_2, we use

$$V_m = \frac{0.2672 kg/mole}{10960 kg/m^3} = 2.43796 \times 10^{-5} m^3/mole.$$ (2.16)

For UCO, we use

$$V_m = \frac{0.2682 kg / mole}{10700 kg / m^3} = 2.50654 \times 10^{-5} m^3 / mole .$$ (2.17)

For (Th,U)O₂, we use

$$V_m = \frac{0.2645 kg / mole}{10500 kg / m^3} = 2.51905 \times 10^{-5} m^3 / mole .$$ (2.18)

Equations (2.5), (2.11) and (2.12) are only valid for isothermal conditions either during irradiation or during post irradiation heating tests. Therefore for non-constant irradiation histories, the current version omits consideration of diffusion by assuming 100% gas release from kernels (F_d = 1). Diffusive release is only considered for isothermal irradiations. Future versions of the model will implement a more sophisticated fission gas release model that can be used with arbitrary temperature histories.

Based on the above derivation, we show a case study on TRISO coated particles with three types of fuel kernels: UO₂, UCO, and (Th,U)O₂. The input parameters including particle dimensions are listed in Table 2-1. The gas pressure that applies on the inner surface of IPyC layer was calculated at the end of irradiation. For simplicity, in this example the void volume V_f in eq. (2.15) is only given by the buffer porosity (porosity in the kernel also contributes to the void volume).

Table 2-1. Input parameters for internal pressure calculation

Parameter	Unit	Value
Kernel Diameter	μm	500
Buffer Thickness	μm	100
IPyC Thickness	μm	40
SiC Thickness	μm	35
OPyC Thickness	μm	40
Irradiation Time	year	1
Burnup	%FIMA	15
Irradiation Temperature	°C	600 - 1600
Yield of Stable Fission Gases	-	0.31
Buffer Density	g/cm³	1.125
Buffer Theoretical Density	g/cm³	2.250
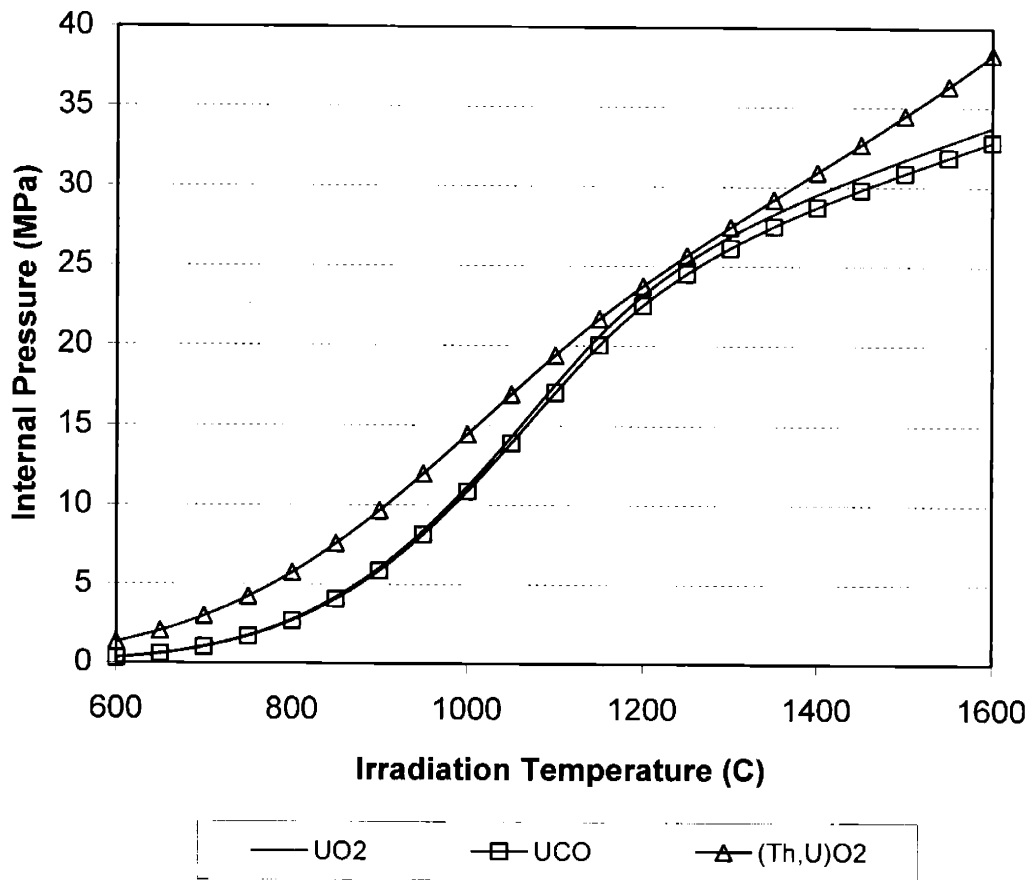
Figure 2-3. The fission gas pressure in TRISO coated particles (symbols for clarity)

Figure 2-3 shows the fission gas pressure as a function of irradiation temperature. We see that the pressure in UCO particle is a little lower than in UO_2 particle because the OPF is zero for UCO kernel. For $(Th,U)O_2$ fuel, the ratio Th/U^{235} of 10 is assumed. The gas pressure in this fuel is the highest because the reduced diffusion coefficient for $(Th,U)O_2$ under the setup conditions is higher than UO_2 and UCO. The particle internal pressure can be sufficient to burst the particle at elevated irradiation temperature and very high burnup, but at modest temperature and burnup, it helps to relieve the stresses induced by irradiation in structural layers, as will be seen later in Section 2.4.

2.3. Thermal Model for Pebbles and Particles

For any analyses of fuel particles, we always need the temperature information. This section details how the thermal model for pebbles and particles is formulated and tailored

to fit into the modeling of fuel performance in pebble bed reactor system, and how it can be easily applied to block type fuel (pellets) and particles in prismatic reactor systems, where the treatment is simpler.

The thermal calculation, while identical for each fuel system type once the particle surface temperature has been determined, is very different from the free stream gas temperature through either the prismatic block to a compact or to the pebble and individual particle. In a pebble red reactor system, the model needs to be able to calculate the temperature distribution in a fuel particle at any position in the reactor core and at any time. Our approach is shown schematically in Figure 2-4.
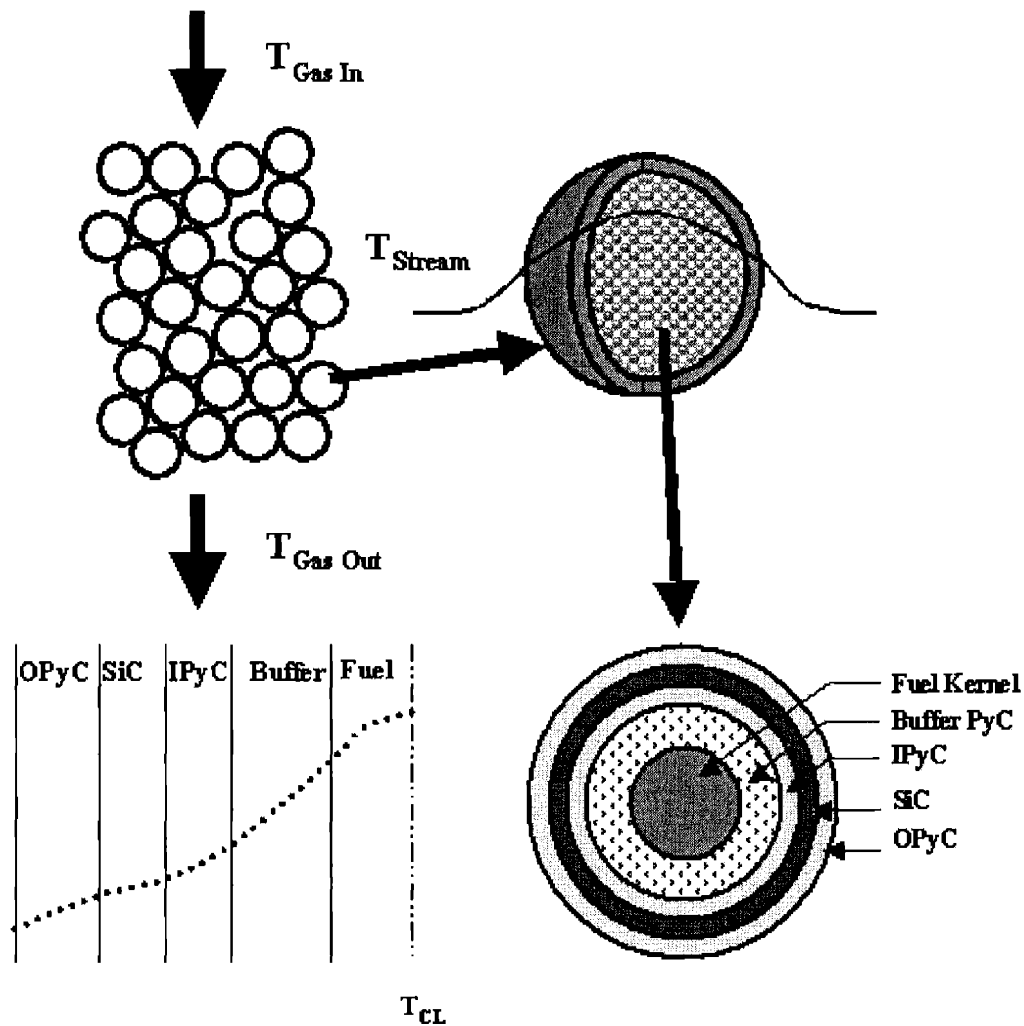
Figure 2-4. Schematic of thermal analysis in pebble bed reactor system

Suppose we know the power distribution and gas inlet and outlet temperatures of a system, then we can determine the free stream gas temperature at a pebble's location. Using this information and the pebble's local power, the temperature profile in the pebble can then be calculated. We then choose a particle we are interested in at a certain location in the pebble, and calculate the temperature profile in the particle based on the pebble temperatures we already have and the power of the particle. The mathematical framework below will follow this path. Power and neutron flux distributions are obtained from a neutronics code, which will be discussed in Section 2.6.

2.3.1. Gas Temperature Distribution and Pebble Surface Temperature

Given a known power distribution, both axially and radially, within the core, the helium mass flow rate, and the gas inlet temperature, the free stream gas temperature at any axial location in the core is calculated as follows:

$$T_{He,bulk}(z) = T_{in} + \frac{q(z)}{\dot{m}_{He} c_{pHe}},$$
(2.19)

where

T_{in} is the gas inlet temperature in °C,

$q(z)$ is the total heat added to the system to a height z per second, which can be calculated knowing the power distribution (volumetric heat generation rate),

$\dot{m}_{He}$ is the helium mass flow rate (kg/s), and

c_{pHe} is the helium specific heat (J/kg-°C).

To connect the Helium bulk temperature with the surface temperature of a pebble, we use heat convection boundary condition, which is

$$q''(r_{pbs}) = h_{He}(T_{pbs} - T_{He,bulk}(z)),$$
(2.20)

where

T_{pbs} is the pebble surface temperature (°C),

r_{pbs} is the radius of the pebble (m),

$q''(r_{pbs})$ is the heat flux at the surface of the pebble (W/m²), and

h_{He} is the heat transfer coefficient for Helium (W/m²-°C).

According to the conservation of energy, the energy generated in the pebble transfers out of the pebble surface, which implies

$$4\pi r_{pbs}^2 q''(r_{pbs}) = \frac{4}{3}\pi r_{fz}^3 q_{peb}''' ,$$ (2.21)

where

r_{fz} is the fueled zone radius in the pebble (m) (pebbles often have a fuel free region of about 5mm in thickness near the surface, as shown in Figure 2-4), and

q_{peb}''' is the average volumetric heat generation rate of the pebble (W/m^3).

From eqs. (2.20) and (2.21), we get

$$T_{pbs} = \frac{q_{peb}'''}{3}\frac{r_{fz}^3}{r_{pbs}^2}\frac{1}{h_{He}} + T_{He,bulk}(z) .$$ (2.22)

The heat transfer coefficient h_{He} is calculated using the Achenbach correlation for the Nusselt number, Nu, as suggested by Dobranich [28] as follows:

$$h_{He} = \frac{k_{He} Nu_{He}}{d_p} , \text{ and}$$ (2.23)

$$Nu_{He} = Pr_{He}^{1/3}\left[(1.18 Re_{He}^{0.58})^4 + (0.23 Re_{He}^{0.75})^4\right]^{0.25} ,$$ (2.24)

where

k_{He} is the thermal conductivity of the helium (W/m-°C),

d_p is the effective pebble diameter (m) calculated by

$$d_p = 6\frac{V_{peb}}{a_{peb}} ,$$ (2.25)

with V_{peb} (m^3) and a_{peb} (m^2) being the volume and surface area of a pebble, respectively, and the Reynold's number and Prandtl number for helium are given by

$$Re_{He} = \frac{\rho_{He} v_{He} d_p}{\mu_{He}} ,$$ (2.26)

$$Pr_{He} = \frac{\mu_{He} c_{pHe}}{k_{He}} ,$$ (2.27)

$$v_{He} = \frac{\dot{m}_{He}}{\rho_{He} \varepsilon_v A_c} , \text{ and}$$ (2.28)

$$A_c = \frac{\left(n_{peb} V_{peb}\right) h_{core}}{1 - \varepsilon_v},$$

(2.29)

where

ρ_{He} is the helium density (kg/m^3),

v_{He} is the helium characteristic velocity (m/s),

μ_{He} is the viscosity of the helium (kg/m-s),

c_{pHe} is the helium specific heat (J/kg-°C), as defined after eq. (2.19),

$\dot{m}_{He}$ is the helium mass flow rate (kg/s), as defined after eq. (2.19),

A_c is the core cross sectional area (m^2),

ε_v is the core void fraction (packing factor),

n_{peb} is the number of pebbles in the core, and

h_{core} is the height of the core (pebble bed height in m).

Some helium properties from Mills [29] are listed in Table 2-2.

Table 2-2. Helium properties as a function of temperature

Temperature (°C)	Thermal Conductivity (W/m-°C)	Density (kg/m^3)	Viscosity (10^{-6}kg/m-s)
-23.15	0.133	0.1950	17.9
26.85	0.149	0.1624	20.1
126.85	0.178	0.1218	24.4
226.85	0.205	0.0974	28.2
326.85	0.229	0.0812	31.7
526.85	0.273	0.0609	37.8
726.85	0.313	0.0487	43.3

(Note: the specific heat of helium is 5200 J/kg-°C.)

2.3.2. Pebble Temperature Distribution

A typical fuel pebble consists of a fueled region surrounded by a thin unfueled region at the surface. The fueled region has a radius of approximately 25mm and consists of a graphite matrix surrounding 11,000 – 15,000 fuel particles. This fueled sphere is surrounded by a 5 mm thick non-fueled layer of graphite matrix resulting in a fuel pebble

44

with a total diameter of 60 mm. If we assume a homogeneous volumetric heat generation rate in the pebble fueled region q_{peb}^{m}, then based on energy balance on spherical geometry, we have

$$\frac{d}{dr}\left(r^2 q_{fz}^{''}\right) = q_{peb}^{m} r^2 \text{ for the fueled region, and} \tag{2.30}$$

$$\frac{d}{dr}\left(r^2 q_{nfz}^{''}\right) = 0 \text{ for the non-fueled region,} \tag{2.31}$$

where $q_{fz}^{''}$ and $q_{nfz}^{''}$ are the heat fluxes in two regions.

We then apply Fourier's law to link temperature gradient to heat flux [30], which is

$$q_i^{''} = -k_i \frac{dT}{dr}, \tag{2.32}$$

where k_i is the thermal conductivity of fueled or non-fueled region, and i is a dummy symbol standing for various cases.

To solve for temperatures, we substitute eq. (2.32) into eqs. (2.30) and (2.31) and apply proper boundary conditions. At the material interface (between the pebble fueled zone and non-fueled zone) both continuity of heat flux and continuity of temperature must be satisfied. In addition, the heat flux at the center of the pebble (r=0) must be finite and the temperature at the pebble surface is T_{pbs}, given in eq. (2.22). The boundary conditions are summarized in Table 2-3.

Table 2-3. Boundary conditions for pebble temperature calculation

Radius	Continuity of heat flux	Continuity of Temperature
r = 0	$dq_{fz}^{''} / dr = 0$	
r = r_{fz}	$q_{fz}^{''}\left(r_{fz}\right) = q_{nfz}^{''}\left(r_{fz}\right)$	$T_{fz}\left(r_{fz}\right) = T_{nfz}\left(r_{fz}\right)$
r = r_{pbs}		$T\left(r_{pbs}\right) = T_{pbs}$

The temperature at any position in the fuel pebble can be calculated by the following relationship:

$$T_{peb}(r) = T_{pbs} + \frac{q_{peb}^{m} r_{fz}^3}{3}\left[\frac{1}{k_{nfz}}\left(\frac{1}{r_{fz}} - \frac{1}{r_{pbs}}\right) + \frac{1}{2k_{fz}}\left(\frac{1}{r_{fz}} - \frac{r^2}{r_{fz}^3}\right)\right], \tag{2.33}$$

for $0 \le r \le r_{fz}$, and

45

$$T_{peb}(r) = T_{pbs} + \frac{q'''_{peb} r_{fz}^3}{3} \left[\frac{1}{k_{nfz}} \left(\frac{1}{r} - \frac{1}{r_{pbs}} \right) \right], \tag{2.34}$$

for $r_{fz} \leq r \leq r_{pbs}$, where

T_{pbs} is given in eq. (2.22),

k_{nfz} is the volume average conductivity of the non-fueled region of the pebble (W/m-°C),

k_{fz} is the volume average conductivity of the fueled region of the pebble (W/m-°C).

Because the pebble fueled region contains coated fuel particles and graphite matrix material in between them, the volume average conductivity of the fueled region of the pebble is estimated as follows:

$$k_{fz} = \frac{1}{V_{fz}} \left(V_f k_f + V_b k_b + V_g k_g + V_I k_I + V_S k_S + V_O k_O + V_{fzm} k_{fzm} \right), \tag{2.35}$$

where

V_f, V_b, V_g, V_I, V_S, V_O, and V_{fzm} are the volumes (m³) of the fuel kernel, buffer, any gas gap that may form in the fuel particles during irradiation, IPyC layer, SiC layer, OPyC layer in the particles and graphite within the fuel zone of the pebble, respectively. Additionally, k_f, k_b, k_g, k_I, k_S, k_O, and k_{fzm} are the corresponding thermal conductivities (W/m-°C). V_{fzm} is calculated be subtracting the sum of the volumes of the particles from the total volume of the pebble fuel zone, namely,

$$V_{fzm} = V_{fz} - n_{par} V_{par}, \tag{2.36}$$

where

n_{par} is the number of particles per pebble, and

V_{par} is the volume of one coated fuel particle (m³).

2.3.3. Particle Temperature Distribution

For an individual fuel particle the temperatures within individual particle layers can be determined by knowing the particle surface temperature (from the pebble temperature at the location of the particle within the pebble), and the volumetric heat generation rate in the particle. We assume that the temperature is symmetric about the particle center

which is a simplification since, in fact, there will be a gradient due to the temperature distribution in a pebble and, indeed, this temperature distribution will also not be symmetric. However, the effect of this assumption will be minor since the actual temperature difference from one side of a particle surface to another is on the order of 1°C given the small size of the particle. Similar to the case of a pebble, the governing equations for a particle are

$$\frac{d}{dr}\left(r^2 q_f''\right) = q_{par}''' r^2 \text{ for the fuel kernel,} \tag{2.37}$$

$$\frac{d}{dr}\left(r^2 q_j''\right) = 0 \text{ for all layers in a particle, and} \tag{2.38}$$

$$q_j'' = -k_j \frac{dT}{dr} \text{ for the kernel and the layers,} \tag{2.39}$$

where q_f'' and q_j'' are the heat fluxes in the fuel kernel and in all layers of a particle, and k_j is the corresponding thermal conductivity of certain material if the equations are evaluated in that material.

In order to completely solve the system of equations in six layers, the boundary conditions satisfying continuity of heat flux and temperature are listed in Table 2-4.

Table 2-4. Boundary conditions for particle temperature calculation

Radius	Continuity of heat flux	Continuity of Temperature
$r = 0$	$dq_f'' / dr = 0$	
$r = r_f$	$q_f''(r_f) = q_b''(r_f)$	$T_f(r_f) = T_b(r_f)$
$r = r_b$	$q_b''(r_b) = q_g''(r_b)$	$T_b(r_b) = T_g(r_b)$
$r = r_g$	$q_g''(r_g) = q_I''(r_g)$	$T_g(r_g) = T_I(r_g)$
$r = r_I$	$q_I''(r_I) = q_S''(r_I)$	$T_I(r_I) = T_S(r_I)$
$r = r_S$	$q_S''(r_S) = q_O''(r_S)$	$T_S(r_S) = T_O(r_S)$
$r = r_O$		$T_O(r_O) = T_{pars}$

The temperature at any location in a particle is given by

47

$$T_{par}(r) = \frac{q_f''' r_f^3}{3}\left[\frac{1}{k_O}\left(\frac{1}{r_S} - \frac{1}{r_O}\right) + \frac{1}{k_S}\left(\frac{1}{r_I} - \frac{1}{r_S}\right) + \frac{1}{k_I}\left(\frac{1}{r_g} - \frac{1}{r_I}\right) + \frac{1}{k_g}\left(\frac{1}{r_b} - \frac{1}{r_g}\right) + \frac{1}{k_b}\left(\frac{1}{r_f} - \frac{1}{r_b}\right) + \frac{1}{2k_f}\left(\frac{1}{r_f} - \frac{r^2}{r_f^3}\right)\right] + T_{pars}$$

, (2.40)

for $0 \le r \le r_f$,

$$T_{par}(r) = \frac{q_f''' r_f^3}{3}\left[\frac{1}{k_O}\left(\frac{1}{r_S} - \frac{1}{r_O}\right) + \frac{1}{k_S}\left(\frac{1}{r_I} - \frac{1}{r_S}\right) + \frac{1}{k_I}\left(\frac{1}{r_g} - \frac{1}{r_I}\right) + \frac{1}{k_g}\left(\frac{1}{r_b} - \frac{1}{r_g}\right) + \frac{1}{k_b}\left(\frac{1}{r} - \frac{1}{r_b}\right)\right] + T_{pars}$$

, (2.41)

for $r_f \le r \le r_b$,

$$T_{par}(r) = \frac{q_f''' r_f^3}{3}\left[\frac{1}{k_O}\left(\frac{1}{r_S} - \frac{1}{r_O}\right) + \frac{1}{k_S}\left(\frac{1}{r_I} - \frac{1}{r_S}\right) + \frac{1}{k_I}\left(\frac{1}{r_g} - \frac{1}{r_I}\right) + \frac{1}{k_g}\left(\frac{1}{r} - \frac{1}{r_g}\right)\right] + T_{pars},$$

(2.42)

for $r_b \le r \le r_g$,

$$T_{par}(r) = \frac{q_f''' r_f^3}{3}\left[\frac{1}{k_O}\left(\frac{1}{r_S} - \frac{1}{r_O}\right) + \frac{1}{k_S}\left(\frac{1}{r_I} - \frac{1}{r_S}\right) + \frac{1}{k_I}\left(\frac{1}{r} - \frac{1}{r_I}\right)\right] + T_{pars},$$ (2.43)

for $r_g \le r \le r_I$,

$$T_{par}(r) = \frac{q_f''' r_f^3}{3}\left[\frac{1}{k_O}\left(\frac{1}{r_S} - \frac{1}{r_O}\right) + \frac{1}{k_S}\left(\frac{1}{r} - \frac{1}{r_S}\right)\right] + T_{pars},$$ (2.44)

for $r_I \le r \le r_S$,

$$T_{par}(r) = \frac{q_f''' r_f^3}{3}\left[\frac{1}{k_O}\left(\frac{1}{r} - \frac{1}{r_O}\right)\right] + T_{pars},$$ (2.45)

for $r_S \le r \le r_O$,

where

T_{pars} is the particle surface temperature at the location within the pebble where the particle resides,

q_f''' is the volumetric heat generation rate in the particle, and

r_f, r_b, r_g, r_I, r_S, r_O are the radii of the outer surfaces of kernel, buffer layer, gap, IPyC layer, SiC layer, and OPyC layer.

The thermal conductivity data for UO_2 and UCO, dense and buffer pyrocarbon, unirradiated and irradiated SiC, and helium as a function of temperature are from El-Wakil [31], Dobranich [28], Price [32], and Mills [29], respectively, and they are summarized in Table 2-5, Table 2-6, and Table 2-7. The thermal conductivity for matrix graphite is given by Kania and Nickel [36] as

$$k_{fgm} = 47.4\left(1.0 - 9.7556 \times 10^{-4}(T - 100)\exp\left(-6.036 \times 10^{-4}T\right)\right), \qquad (2.46)$$

where T is the temperature in °C.

Table 2-5. Thermal Conductivity of UO_2 and UCO

Temperature (°C)	UO_2 Thermal Conductivity (W/m-°C)	Temperature (°C)	UCO Thermal Conductivity (W/m-°C)
92.96	7.79	92.96	25.56
204.07	6.06	148.52	24.35
315.18	4.85	204.07	23.33
426.29	4.33	259.63	22.53
537.41	3.81	315.18	21.93
648.52	3.46	370.74	21.44
759.63	2.77	426.29	21.1
870.74	2.6	481.85	20.8
981.85	2.42	537.41	20.61
1092.96	2.25	648.52	20.46
1204.07	2.08	759.68	20.35
1315.18	1.90	870.74	20.25
1426.29	1.90	981.85	20.2
1537.41	1.90	1092.96	20.02
1648.52	1.90	1300	20.02
1759.63	1.90	1600	20.02

Table 2-6. Thermal Conductivity of Dense and Buffer Pyrocarbon

Temperature (°C)	Dense PyC Thermal Conductivity (W/m-°C)	Buffer PyC Thermal Conductivity (W/m-°C)
76.85	9.2	2.3
116.85	7.5	1.88
216.85	6.7	1.68
326.85	5.9	1.48
456.85	5.4	1.35
556.85	5.2	1.3
1100	5.2	1.3
1600	5.2	1.3

Table 2-7. Thermal Conductivity of Pyrolytic β-SiC

Temperature (°C)	Un-irradiated β-SiC Thermal Conductivity [*] (W/m-°C)	Irradiated β-SiC Thermal Conductivity [†] (W/m-°C)
500	39.8	19.9
900	36.5	18.3
1100	35.7	17.9
1300	35.5	17.8
1600	35.5	17.8

([*]: Unirradiated SiC thermal conductivity values are from Price [32]. [†]: Irradiated values are assumed to be 50% of the unirradiated values.)

Due to lack of data, the thermal conductivities of these materials except for SiC are assumed to be independent of neutron fluence for the time being. The thermal conductivity of the porous pyrocarbon buffer layer is assumed to be 25% of that of dense pyrocarbon [28]. Within the temperature range of available data, a linear interpolation is used, and beyond the temperature range, no dependence on temperature is assumed, i.e. the curve is flat. The thermal conductivity of SiC is known to decrease with increasing temperature with the decreasing rate slowing down at higher temperature. Figure 2-5 from Price [32] clearly shows such a relationship with temperature for β-silicon carbide made from pyrolysis. An extrapolation in temperature was made in Figure 2-5 by Ho [37] and the values are listed in Table 2-7.
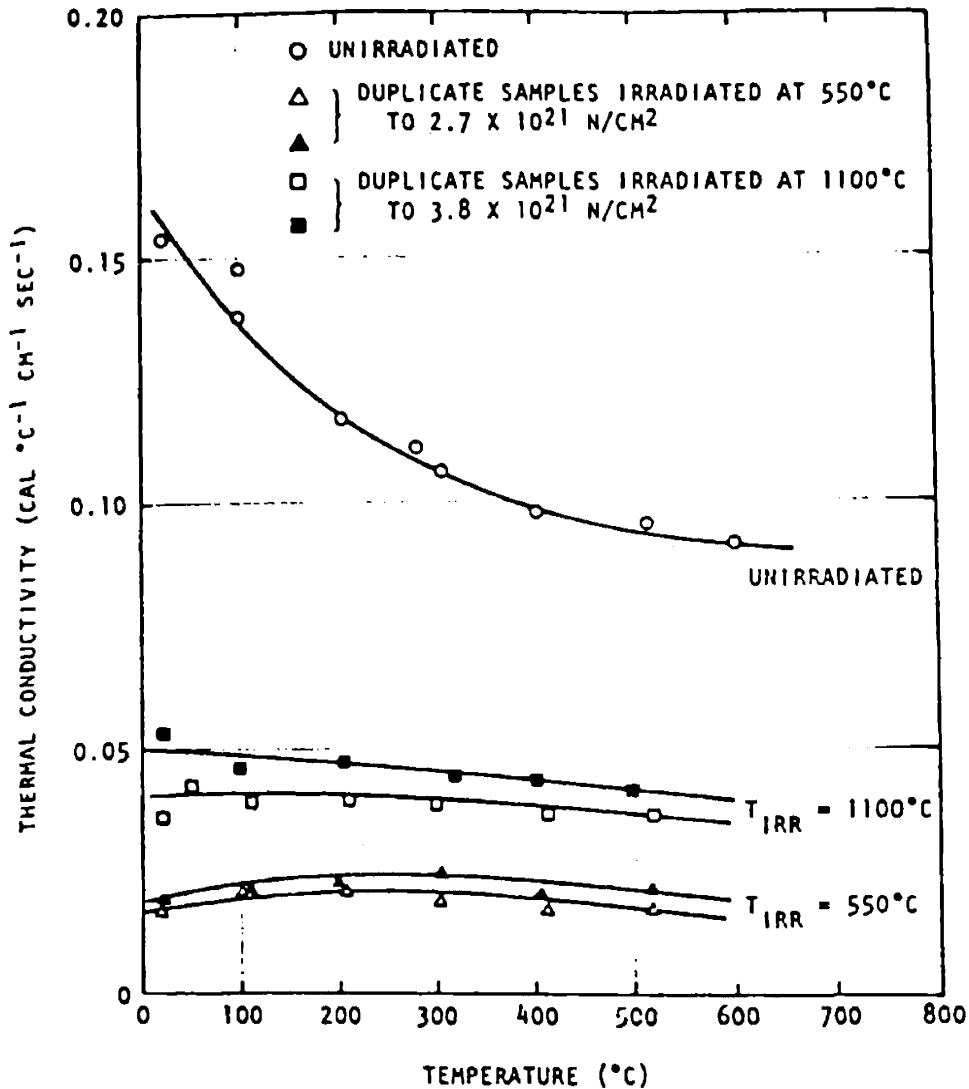
Figure 2-5. Thermal conductivities of unirradiated and neutron-irradiated pyrolytic β-silicon carbide, deposited at 1400°C, as a function of measurement temperature (from Price [32])

Molecular dynamic simulation on perfect β-silicon carbide was performed by Li et al. [33], and the results compare very well with experimental data at temperatures above 400K, as in Figure 2-6. The plot indicates similar trend with respect to temperature as in the case of pyrolytic β-SiC. If we convert the unit of thermal conductivity in Figure 2-5 to W/m.K, we will see the thermal conductivities in pyrolytic β-SiC are about 30% of those in perfect crystal, due to the effects of grain boundaries and defects.

51
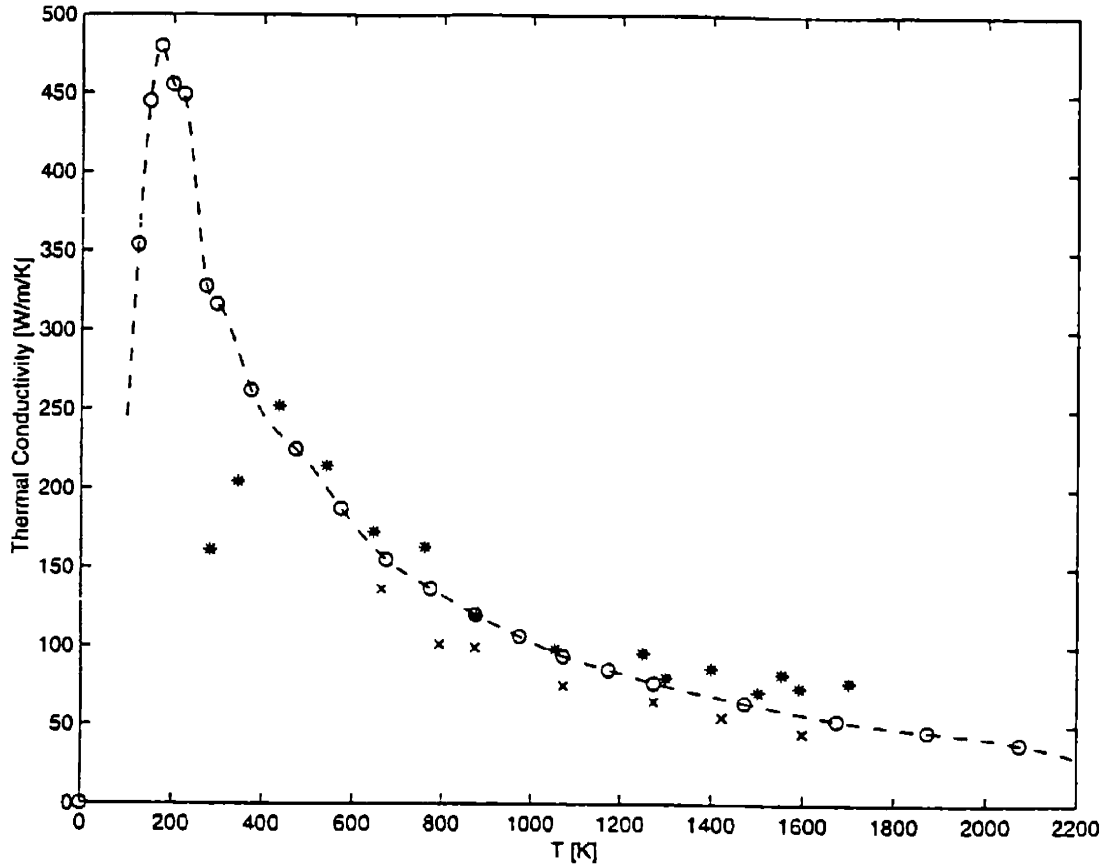
Figure 2-6. Comparion of calculated thermal conductivity for perfect crystal β-SiC with experiments at various temperatures. The circles are experimental results from Taylor et al. [34], the dashed line being its spline fit. Experimental results from Senor et al. [35] are plotted in crosses. The stars are calculated results. (From Li et al. [33])

Neutron irradiation rapidly reduces the thermal conductivity of SiC. For pyrolytic β-SiC irradiated at 1100°C to a fluence of 3.8×10^{21} n/cm^2 (E > 0.18 MeV), it is reduced by 50% to 70%, depending on measurement temperature [32], as shown in Figure 2-5. The effects of irradiation was also studied by Li et al. [33] by introducing point defects into perfect β-SiC crystal, and they show similar reduction in thermal conductivity, as shown in Figure 2-7. From Figure 2-5 and Figure 2-7, we also find that the irradiated thermal conductivity is insensitive to the measurement temperature, decreasing only slightly with increasing measurement temperature.

In the typical irradiation temperature range of 500°C to 1300°C for coated fuel particles in High Temperature Gas Cooled Reactors, we assume a 50% reduction in thermal conductivity of pyrolytic β-SiC induced by modest amount of fast neutron

irradiation, and the values are shown in Table 2-7. Later on in Figure 2-9 to Figure 2-16, we will see that this simplication is acceptable, because in a coated particle, the buffer pyrocarbon layer is of the lowest thermal conductivity and most of the temperature rise across the layers will occur there. The temperature difference from one side of the SiC layer to another side is generally within one degree centigrade, so a coarse treatment for the purpose the particle thermal calculations is not bad.
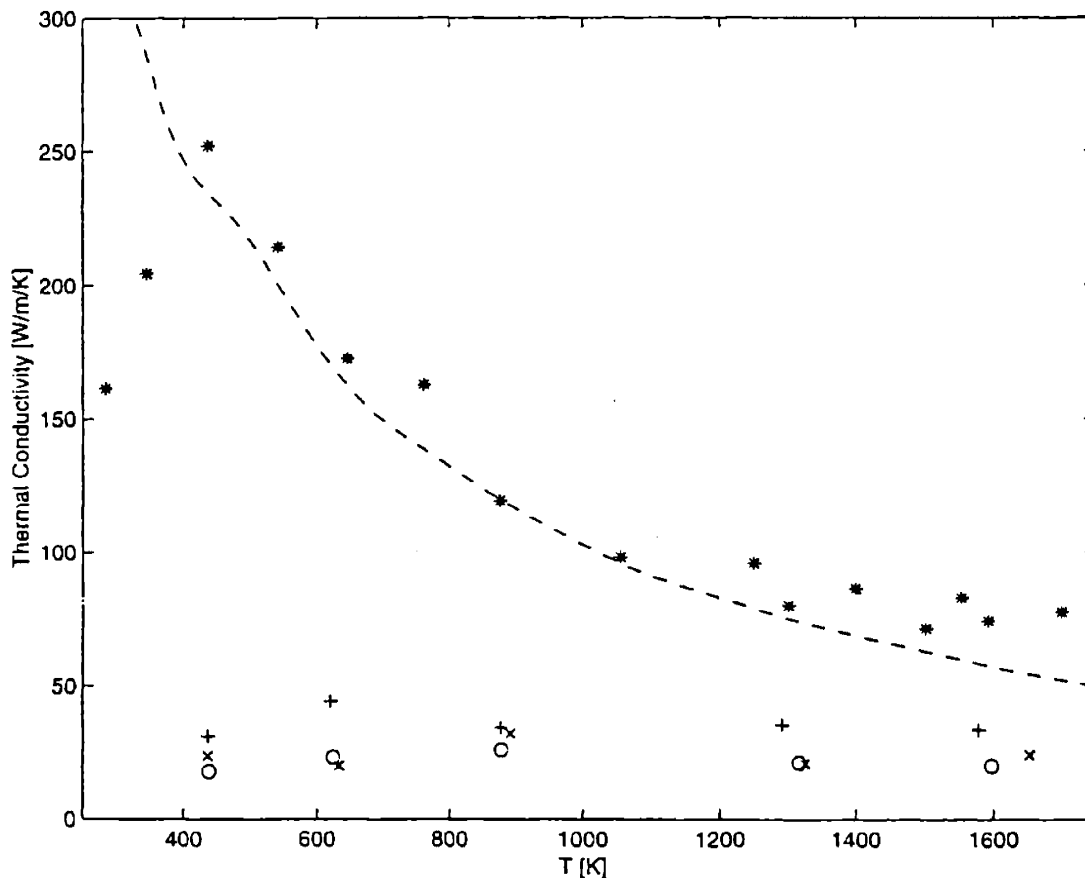
Figure 2-7. Thermal conductivity as a function of temperature. Experimental values for perfect crystal are plotted in dashed line. Results from calculations: perfect crystal (*), 0.5% concentration of carbon vacancy (+), 0.5% concentration of carbon antisite (×), 0.5% concentration of silicon vacancy (∘). (From Li et al. [33])

The thermal conductivity data for fuel related materials are collected and plotted in Figure 2-8 for comparison.
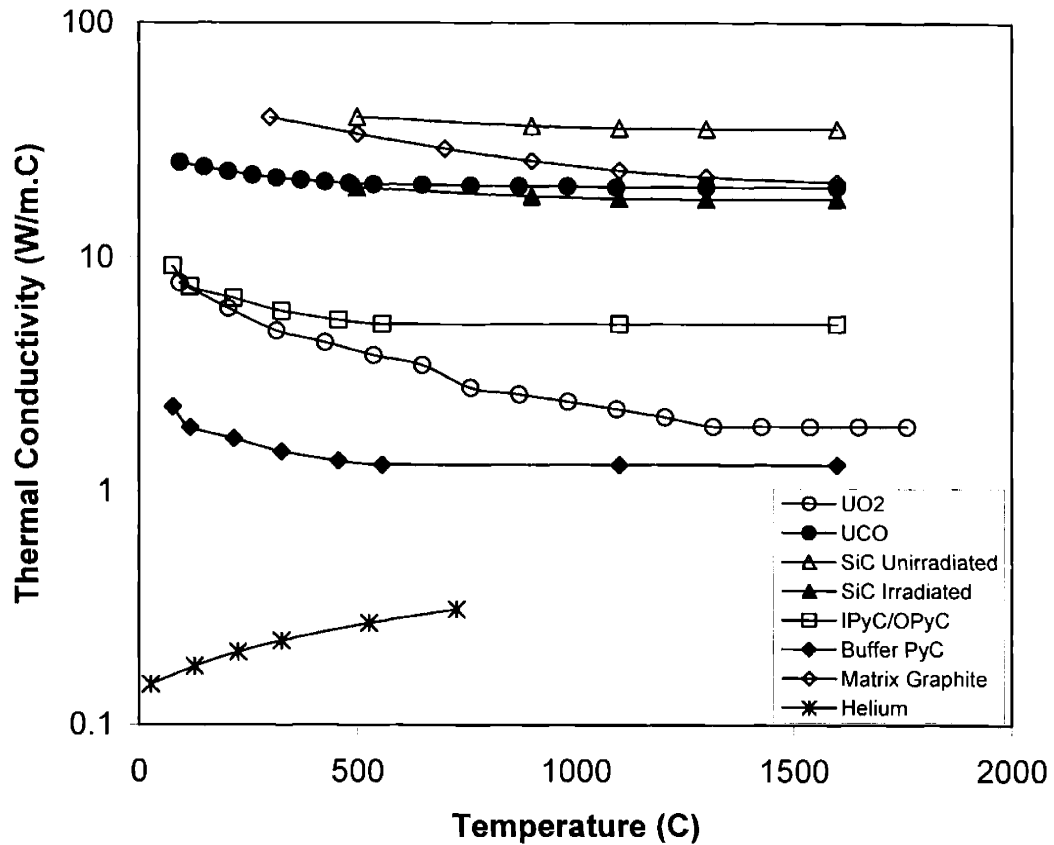
Figure 2-8. Thermal conductivities of fuel related materials (symbols for clarity)

Table 2-8. Typical Pebble Bed Reactor Core Parameters

Parameter	Value	Parameter	Value
Core Height (m)	10.0	Coolant Mass Flow Rate (kg/s)	118
Core Radius (m)	1.75	No. Pebbles in core	360,000
Thermal power (MW)	250	No. Particles per Pebble	11,000
Average Power Density (MW/m³)	3.652	Pebble Fuel Zone Radius (mm)	25.0
Coolant Inlet Temperature (°C)	450	Pebble Radius (mm)	30.0
Coolant Outlet Temperature (°C)	850		

The temperature model was implemented and chedked independently. Several cases for a typical pebble bed reactor core were analyzed. The specifications in for these cases are given in Table 2-8. The intention was to investigate the temperatures of different types of coated fuel particles at different power levels and locations in the reactor core. We choose two types of fuel particles: one with a small fuel kernel and another with a big fuel kernel as in Table 2-1, and the dimensions are given in Table 2-9.

Table 2-9. Dimensions of Particles Used in Thermal Calculations

Parameter	Type 1 (P1)	Type 2 (P2)
Fuel Type	UCO	UO_2
Kernel Diameter (μm)	195	500
Buffer Thickness (μm)	100	100
IPyC Thickness (μm)	53	40
SiC Thickness (μm)	35	35
OPyC Thickness (μm)	43	40

We would like to see the temperature distributions of pebbles and particles in pebbles under various conditions, and the following matrix for thermal calculation is constructed.

Table 2-10. Case Matrix for Thermal Calculations

Particle Type	Conditions			
	C1	C2	C3	C4
Type 1 (P1)	Average power at outlet, PF = 1	High power at outlet, PF = 2.74	Peak power at outlet, PF = 5.27	Average power at inlet, PF = 1
Type 2 (P2)	Average power at outlet, PF = 1	High power at outlet, PF = 2.74	Peak power at outlet, PF = 5.27	Average power at inlet, PF = 1

(Note: PF stands for power peaking factor.)

For example, P1C1 means a pebble containing 11,000 Type 1 particles is sitting at the outlet of the reactor core where the helium temperature is 850°C, and experiencing average power density of 3.652 MW/m^3, and we want the temperature distribution in this pebble and in a particle at the center of the pebble. It will be shown later in Section 2.6 that a PF of 5.27 is the highest peaking factor of an old core design for the Modular Pebble Bed Reactor, and a PF of 2.74 is the highest peaking factor of a newer MPBR design. The resulting temperature plots are shown in Figure 2-9 through Figure 2-16.
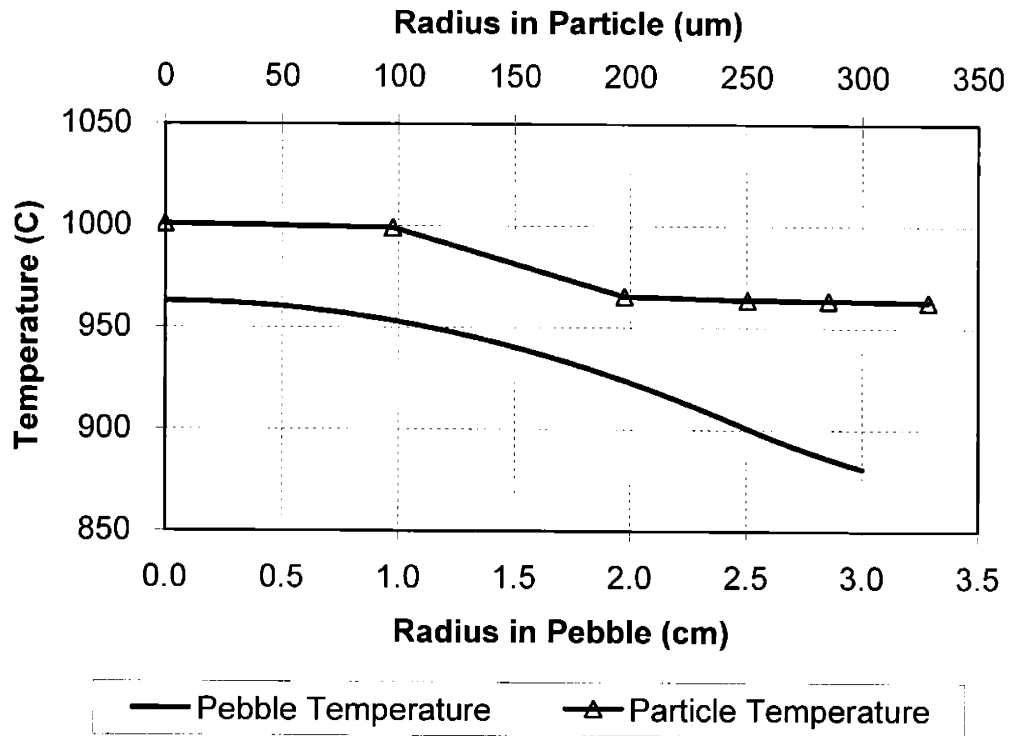
Figure 2-9. Pebble and particle temperature distribution (Case P1C1)
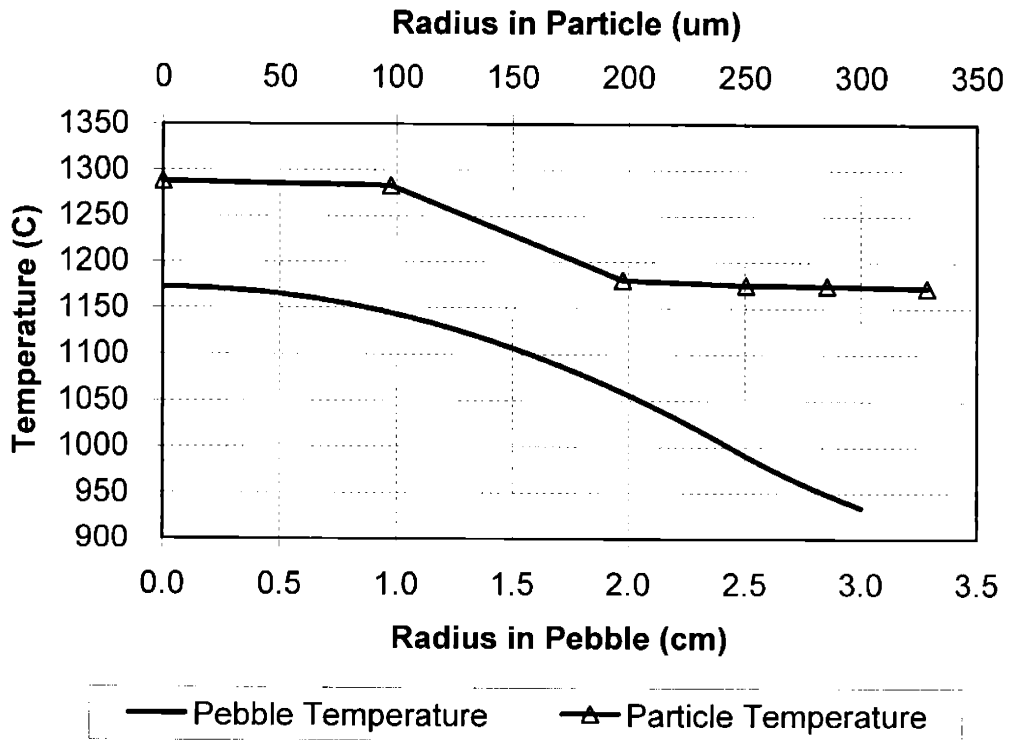
Figure 2-10. Pebble and particle temperature distribution (Case P1C2)
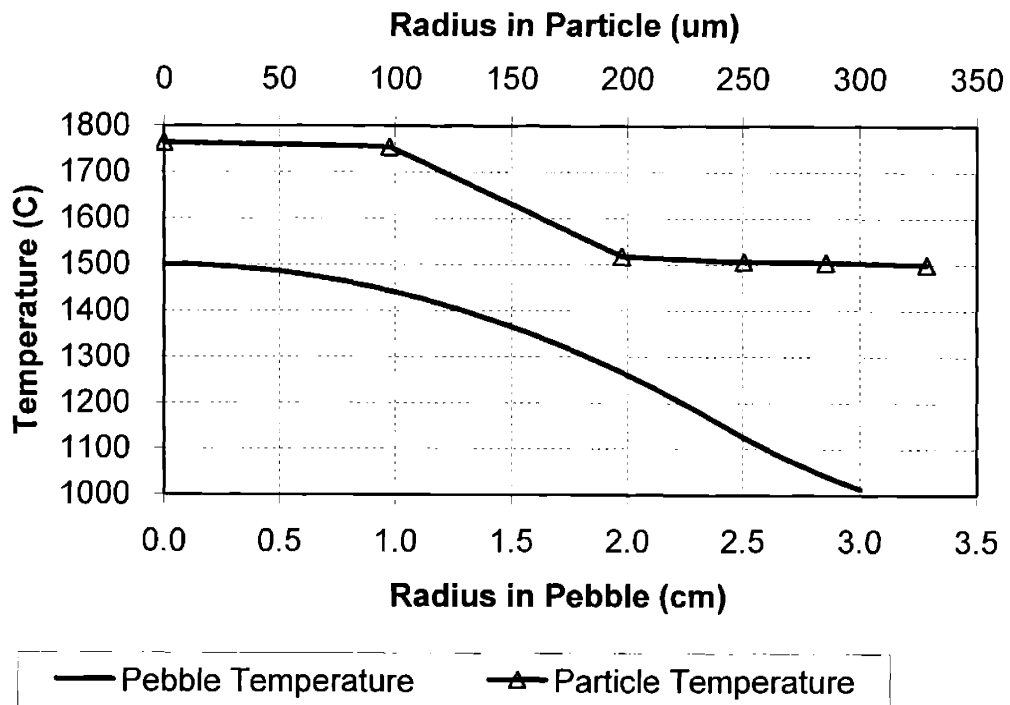
Figure 2-11. Pebble and particle temperature distribution (Case P1C3)
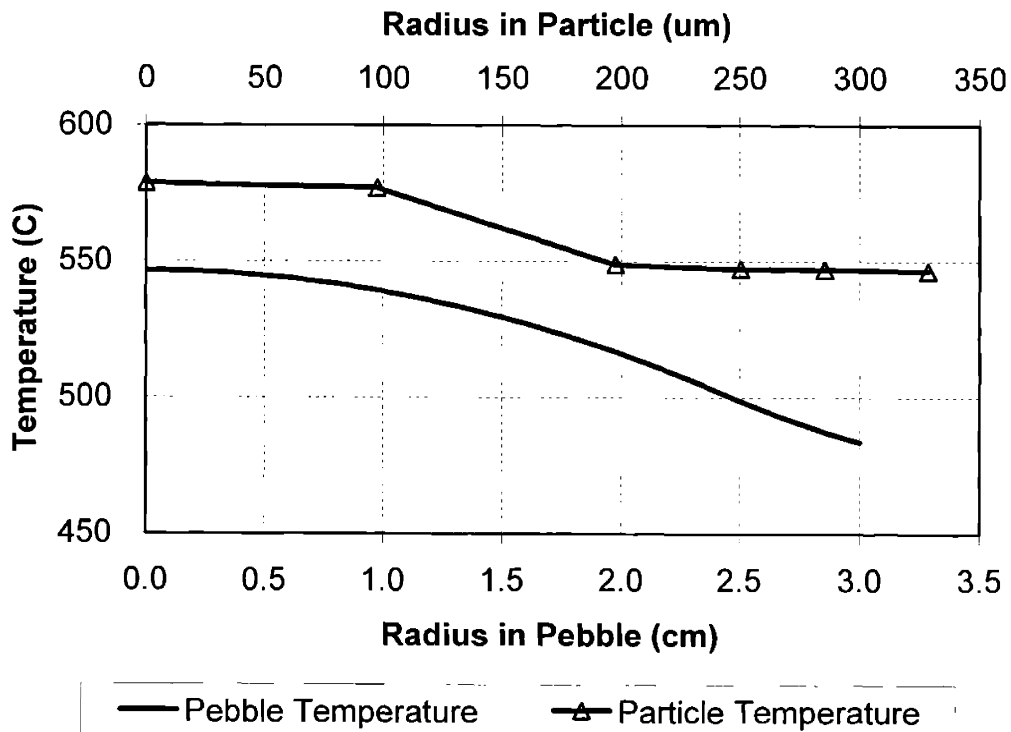
Figure 2-12. Pebble and particle temperature distribution (Case P1C4)
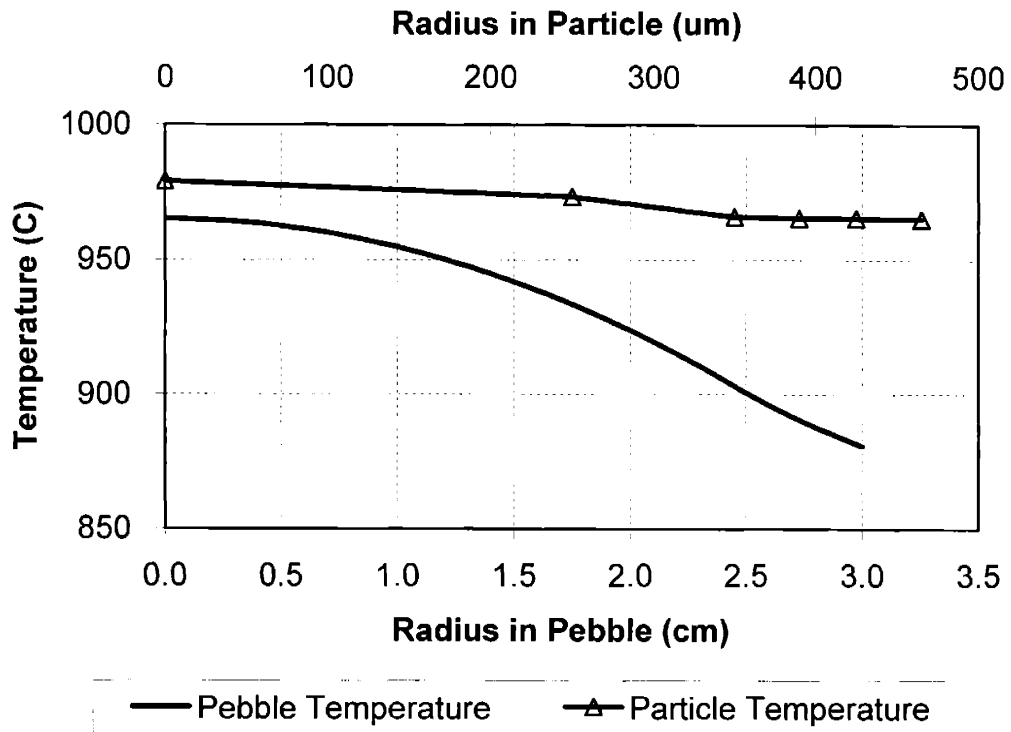
Figure 2-13. Pebble and particle temperature distribution (Case P2C1)
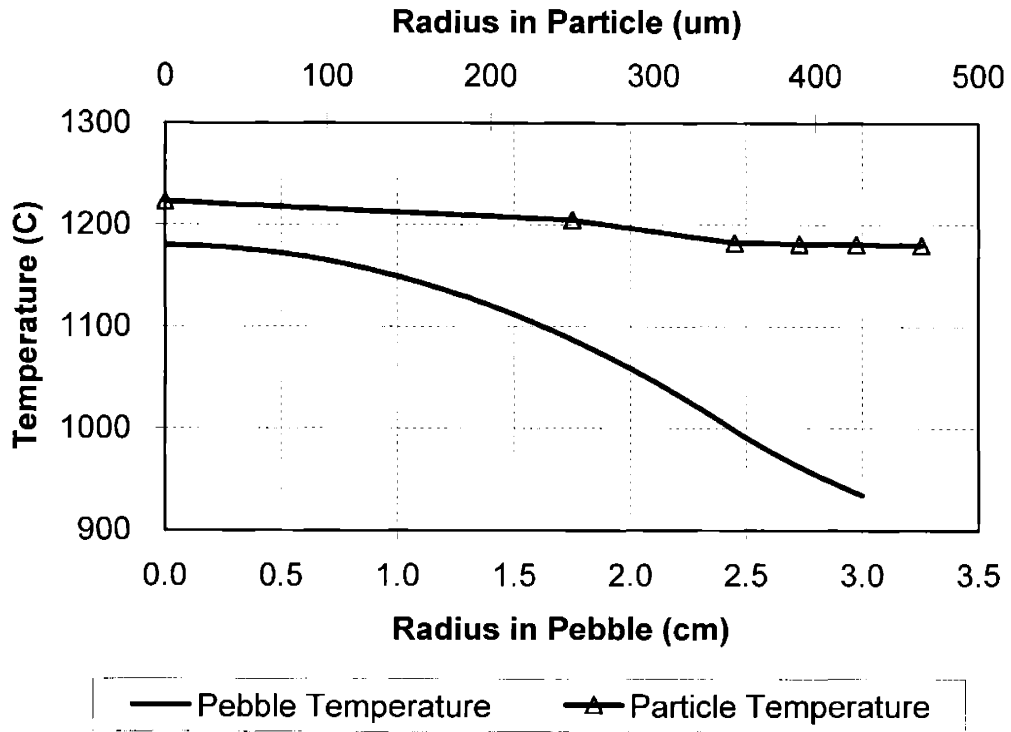
Figure 2-14. Pebble and particle temperature distribution (Case P2C2)
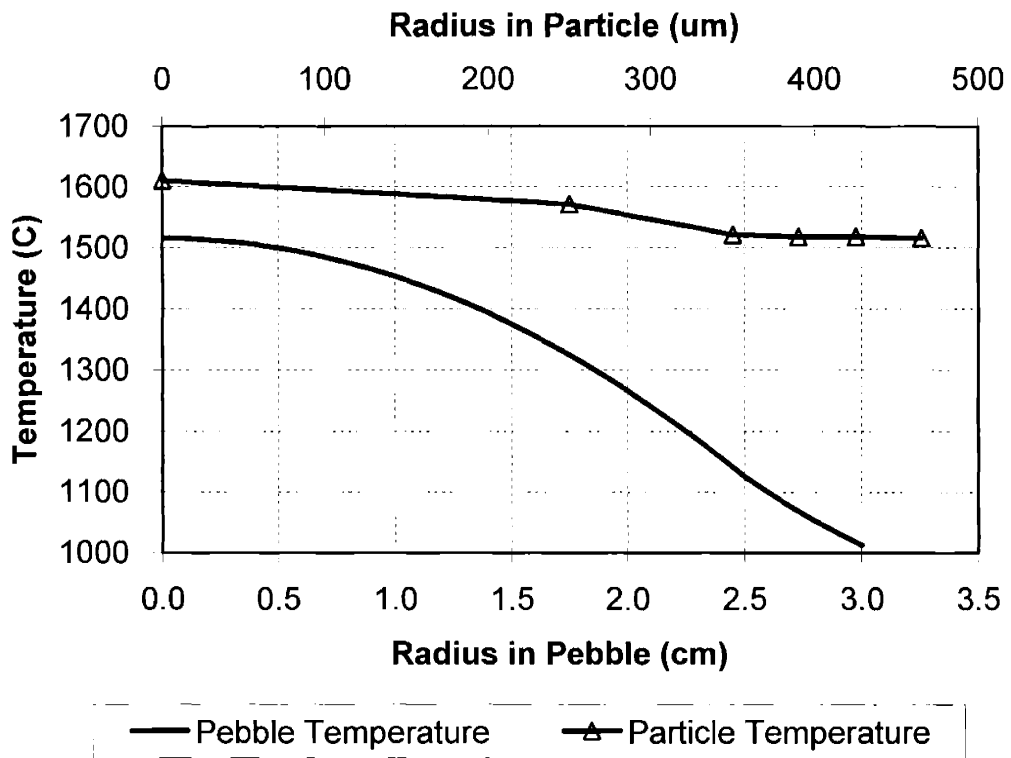
Figure 2-15. Pebble and particle temperature distribution (Case P2C3)
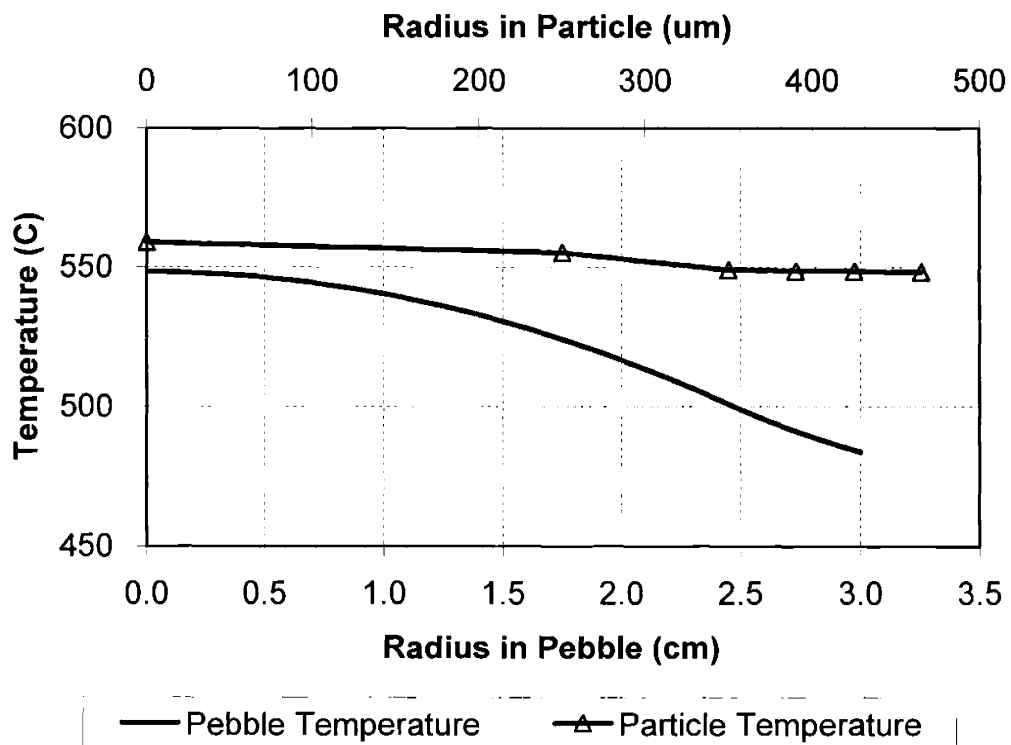
Figure 2-16. Pebble and particle temperature distribution (Case P2C4)

Table 2-11. Calculated Thermal Conditions for Two Types of Coated Fuel Particles

Case	$T_{particle\ center}$ (°C)	$\Delta T_{across\ particle}$ (°C)	$T_{pebble\ center}$ (°C)	$\Delta T_{across\ pebble}$ (°C)	$\Delta T_{across\ three\ structural\ layers}$ (°C)
P1C1	1000.8	38.1	962.7	81.9	2.6
P1C2	1288.0	115.7	1172.3	237.9	7.9
P1C3	1764.2	264.0	1500.2	488.0	17.5
P1C4	578.7	32.2	546.5	62.9	2.2
P2C1	979.2	14.0	965.2	84.0	0.9
P2C2	1223.0	43.2	1180.0	245.2	2.6
P2C3	1610.7	95.1	1515.6	503.3	5.8
P2C4	559.0	10.6	548.4	64.8	0.7

(Note: the three structural layers are IPyC, SiC, and OPyC layers)

The symbols in Figure 2-9 to Figure 2-16 are for clarity purpose only and do not represent experimental data points. Some key values are collected and presented in Table 2-11, and we have the following observations.

(1) The pebble temperature profiles are very similar for the two pebbles with two different types of particles embedded in them, because the power and dimension of the pebbles are the same, but the average thermal conductivity of the fueled region makes a little difference due to different weights of the mixture of materials.

(2) The particle center temperature and the temperature drop across a particle are higher for a Type 1 particle than for a Type 2 particle, because for a Type 1 particle, the fuel kernel volumetric heat generation rate and heat flux are higher due to the smaller fuel kernel and overall particle dimensions, as can be seen in eqs. (2.37) and (2.39). It should be noted that the particle center temperature would be even lower in Type 2 particle if UCO fuel kernel is used in place of UO_2, because the thermal conductivity of UCO is a lot higher than that of UO_2 as in Figure 2-8.

(3) The power peaking factor of 5.27 is from a graphite/fuel pebble mixing zone in an early MPBR design, and it is unrealistically high. It could be an artifact of numerical methods to compensate for the fast neutron flux equilibrium in the mixing zone, and will be discussed later in Section 2.6. Be it as it may, we include it in our exercise and the particle center temperature reaches 1764°C in the case of P1C3 and 1611°C in the

case of P2C3. These two cases are for comparison purposes. In all other cases, the particle center temperatures do not exceed 1300°C.

(4) The temperature drop across the three structural layers is typically several degrees even with wide variations in particle dimensions and power densities, therefore differential thermal expansion will induce little stress in each individual layers.

2.4. Mechanical Analysis

The task of the mechanical analysis is to provide stresses and strains in coated fuel particles under possible normal operating and accidental conditions in HTGRs. To do a credible job, all major stress contributors need to be included in the analysis. It is the general view of the gas reactor community that the total mechanical strain ε is the result of irradiation strain ε_i, creep strain ε_c, elastic strain ε_e, and thermal strain ε_{th}, expressed as

$$\varepsilon = \varepsilon_i + \varepsilon_c + \varepsilon_e + \varepsilon_{th}. \tag{2.47}$$

The following sections 2.4.1 to 2.4.5 discuss material properties and physical phenomena associated with each component above, which are largely based on the material review by Ho [37]. In order to be incorporated in the mechanical analysis, most of these properties need to be abstracted and represented with assumptions, namely, modeled. The material models that follow generally consider dependencies on irradiation temperature, fast neutron fluence, material density and anisotropy, and they construct an indispensable bridge between material properties and behavior.

2.4.1. Bacon Anisotropy Factor (BAF)

Before we delve into the mechanical properties of coating materials, the Bacon Anisotropy Factor (BAF) needs to be introduced as a measure of the degree of preferred crystallographic orientation, which will be used for pyrolytic carbon (pyrocarbon for short). Pyrocarbon is of turbostratic structure and is in many ways similar to polycrystalline graphite. However, pyrocarbon deposits can have any of a variety of complex structures. In these structures, most of the carbon atoms are arranged in planar

hexagonal arrays linked together by strong covalent bonds. The layers vary in perfection and are thought to be wrinkled or contain single or multiple vacant lattice sites. Although the layers in most structures are parallel to one another and are bonded by weak van der Waals forces, some structures contain single unassociated layers, a small fraction of amorphous carbon, or substantial amounts of hydrogen [38][39]. Because of the anisotropy of the bonding and variations in the crystallinity and preferred orientation of pyrocarbon, wide variations in properties are expected.
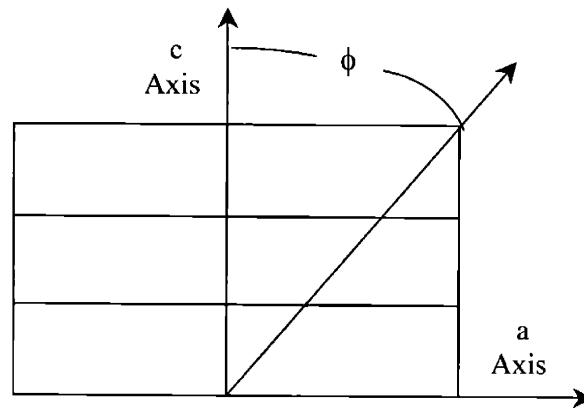
Figure 2-17. Schematic diagram of a turbostratic crystallite (from Bokros [40])

The strong covalent bonding within layers and the weak van der Waals bonding between layers cause certain properties of the crystallites of pyrolytic carbon to be strong functions of the angle ϕ shown in Figure 2-17 but independent of angular position about the principal c-axis.

When the degree of preferred orientation of a deposit is high, the anisotropy of the bulk approaches that of the crystallites. However, when the crystallites in an aggregate are randomly oriented, the anisotropy of the crystallites is perfectly averaged out so that the aggregate is isotropic. Thus, a quantitative measure of the degree of preferred orientation in a deposit is one of the most important factors in its characterization.
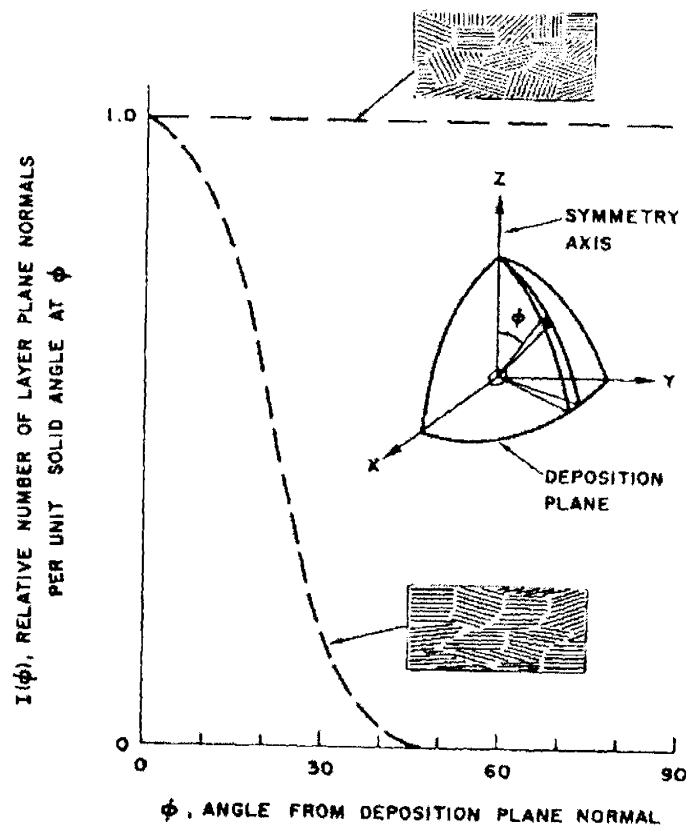
Figure 2-18. Pole figures for a random carbon sample and an oriented sample.
The inset shows the angular relations (from Bokros [40])

When pyrocarbon is deposited on particles in a fluidized bed, there is a natural tendency for the layer planes to become aligned parallel to the deposition plane. Hence the deposits have cylindrical symmetry about the normal to the deposition plane. The degree of preferred orientation for a deposit with symmetry of this type can be conveniently represented by a plot of $I(\phi)$, the relative number of layer plane poles per unit solid angle at angle ϕ versus ϕ. Pole figures for a random specimen and a highly oriented specimen are illustrated in Figure 2-18. The density of layer plane poles has been normalized to unity at $\phi = 0°$ in Figure 2-18.

A parameter which has proved useful in the characterization of the anisotropy of carbon deposited in fluid beds and has special physical significance had evolved from the approach taken by Bacon [41], which is the BAF. Part of Bacon's work is summarized below.

63

Let α_a and α_c be the property coefficients in the a and c directions of a crystallite, respectively. The value of the property in any arbitrary direction inclined at an angle ϕ to the c-axis is

$$\alpha(\phi) = \alpha_a \sin^2 \phi + \alpha_c \cos^2 \phi .$$ (2.48)

The mean value of the contributions of all the crystallites in the aggregate in the z direction in Figure 2-18 is

$$\overline{\alpha_z} = \frac{\int_0^{\pi/2} \alpha(\phi) I(\phi) \sin \phi d\phi}{\int_0^{\pi/2} I(\phi) \sin \phi d\phi} .$$ (2.49)

Plugging eq. (2.48) into eq. (2.49), we get

$$\overline{\alpha_z} = \alpha_a \frac{\int_0^{\pi/2} \alpha(\phi) I(\phi) \sin^3 \phi d\phi}{\int_0^{\pi/2} I(\phi) \sin \phi d\phi} + \alpha_c \left(1 - \frac{\int_0^{\pi/2} I(\phi) \sin^3 \phi d\phi}{\int_0^{\pi/2} I(\phi) \sin \phi d\phi} \right),$$ (2.50)

or

$$\overline{\alpha_z} = \alpha_a R_z + \alpha_c (1 - R_z),$$ (2.51)

where

$$R_z = \frac{\int_0^{\pi/2} I(\phi) \sin^3 \phi d\phi}{\int_0^{\pi/2} I(\phi) \sin \phi d\phi} .$$ (2.52)

Similarly, it can be shown that for directions parallel to the deposition plane,

$$\alpha_{xy} = \alpha_a R_{xy} + \alpha_c (1 - R_{xy}),$$ (2.53)

where

$$R_{xy} = \frac{2 - R_z}{2} .$$ (2.54)

Sometimes R_z is referred to as R_3 or simply R, and R_{xy} as R_1. The Bacon anisotropy factor (BAF) is related to R_z by

$$R_z = R_3 = R = \frac{2}{2 + BAF} .$$ (2.55)

Thus, R_z and BAF are parameters with some physical significance which can be obtained by evaluating eq. (2.52) and (2.55). The evaluation may be done graphically or

by fitting $I(\phi)$ to a suitable empirical approximation and integrating eq. (2.52) analytically. For a random deposit, $R_z = R_{xy} = 2/3$ and BAF=1. For oriented deposits, R_z can take values from 0 to 2/3 and BAF takes corresponding values from 1 to ∞.

2.4.2. Elastic Response of Pyrolytic Carbon (PyC) and Silicon Carbide (SiC)

Now we have introduced the concept of BAF, we can begin to discuss the elastic response of pyrocarbon and silicon carbide. The elastic constants for a material consist of a set of Young's moduli E and Poisson's ratios ν, which link stresses with strains. For pyrocarbon, the properties are axisymmetric with respect to the normal direction of the deposition plane, in the case of coated particles, the radial direction of the spherical configuration. The in-plane direction perpendicular to the radial direction is the tangential direction, or θ direction. This characteristic is called transverse isotropy, and five independent elastic constants are required to describe it, so the following constitutive laws apply to PyC,

$$\varepsilon_{rr} = \frac{1}{E_r}\sigma_{rr} - \frac{2\nu_{\theta r}}{E_\theta}\sigma_{\theta\theta},$$ (2.56)

$$\varepsilon_{\theta\theta} = \frac{1-\nu_{\theta\theta}}{E_\theta}\sigma_{\theta\theta} - \frac{\nu_{r\theta}}{E_r}\sigma_{rr}, \text{ and}$$ (2.57)

$$\frac{\nu_{r\theta}}{E_r} = \frac{\nu_{\theta r}}{E_\theta}.$$ (2.58)

Another elastic constant is the shear modulus, which we don't use because there is no shear deformation in a spherical intact particle. Another notation for the radial and tangential directions is 3 and 1 directions, respectively, which is the same thing.

The silicon carbide used for the coating of fuel particles is of the type β-SiC, which is face-centered-cubic (fcc) structured and isotropic, hence only two independent elastic constants are needed. The corresponding constitutive laws are

$$\varepsilon_{rr} = \frac{1}{E}\sigma_{rr} - \frac{2\nu}{E}\sigma_{\theta\theta}, \text{ and}$$ (2.59)

$$\varepsilon_{\theta\theta} = \frac{1-\nu}{E}\sigma_{\theta\theta} - \frac{\nu}{E}\sigma_{rr}.$$ (2.60)

2.4.2.1. Elastic Constants of Dense Pyrocarbon

The elastic constants have been obtained for graphite single crystals [42] [43], but the measurements for pyrocarbon are limited and show some discrepancies partially due to different manufacturing conditions for the pyrocarbon samples [42] [44] [45]-[48]. The idea is to establish the dependency of elastic constants on a number of parameters over extensive ranges, based on existing data and acceptable engineering approaches. In many cases, assumptions are made because of the absence of experimental data.

The functions for Young's moduli are obtained by assuming the effects of various parameters are multiplicative, because correlations between parameters were not studied. The resulting equations for E_1 (tangential) and E_3 (radial) are given in GPa as [37]

$$E_1(\rho, BAF_0, L_c, \Phi, T) = E_0(0.384 + 0.324\rho)(0.481 + 0.519BAF_0) \times (2.985 - 0.0662L_c)(1 + 0.23\Phi)(1 + 0.00015(T - 20)) \text{, and} \quad (2.61)$$

$$E_3(\rho, BAF_0, L_c, \Phi, T) = E_0(0.384 + 0.324\rho)(1.463 - 0.463BAF_0) \times (2.985 - 0.0662L_c)(1 + 0.23\Phi)(1 + 0.00015(T - 20)) \quad , \quad (2.62)$$

where

ρ is the pyrocarbon density (g/cm^3),

BAF_0 is the unirradiated BAF, and $BAF_0 < 2.15$ is required for the above two equations,

Lc is the apparent crystallite size (angstrom),

Φ is the fast neutron fluence (10^{21} n/cm^2, E > 0.18MeV),

T is the measurement temperature (°C), and

E_0 is the reference value of 25.5GPa for $\rho = 1.9$g/cm^3, $BAF_0 = 1.0$, Lc = 30angstrom, $\Phi = 0$, and T=20°C.

The dependencies on each parameter in the above two equations are explained below.

The weak temperature dependence is assumed to be identical to that of graphite [49] up to 2000°C. E versus fast neutron fluence data from Price and Bokros [44] and Kaae [45] suggest a linear relationship, and this relationship is independent of density for the density range of 1.55 to 2.0 g/cm^3, and irradiation temperature between 650°C to 1250°C. The rate of increase with respect to fluence is between 0.22 to 0.25 (10^{21} n/cm^2)$^{-1}$, and an intermediate value of 0.23 is recommended as in eqs. (2.61) and (2.62). The relationship is assumed to be valid for $1.0 \leq \rho \leq 2.0$ g/cm^3 and $\Phi \leq 4.0 \times 10^{21}$ n/cm^2. As for the

66

dependence on BAF_0, all the measurements are made in the tangential direction because the thin section of the radial direction is not suitable for measurements. Thus the E_3 versus BAF_0 relationship is based on E_1 data and the ratio of E_1/E_3 for graphite crystals, as described by Ho [37], and it is less applicable due to more assumptions being involved. The dependence of E on density, BAF_0, and apparent crystallite size were studied and given by Kaae [48], and it was concluded that the relationships between PyC structure and its mechanical properties can be characterized by these three parameters, meaning PyCs basically show the same mechanical properties if the values of these parameters are the same, no matter whether they are deposited from methane, propane, propylene, or propylene-acetylene mixtures.

For the dense pyrocarbon coatings of fuel particles, BAF is generally in the range of 1.0 to 1.1, which means the coated dense pyrocarbon is not significantly different from isotropic pyrocarbon, and the corresponding E_1/E_3 is not higher than 1.10. Given this fact and that the model for E_3 is largely empirical and differentiating E_1 and E_3 would introduce great level of complexity in stress analysis, we just use the relationship from eq. (2.61) for both radial and tangential directions for the time being.
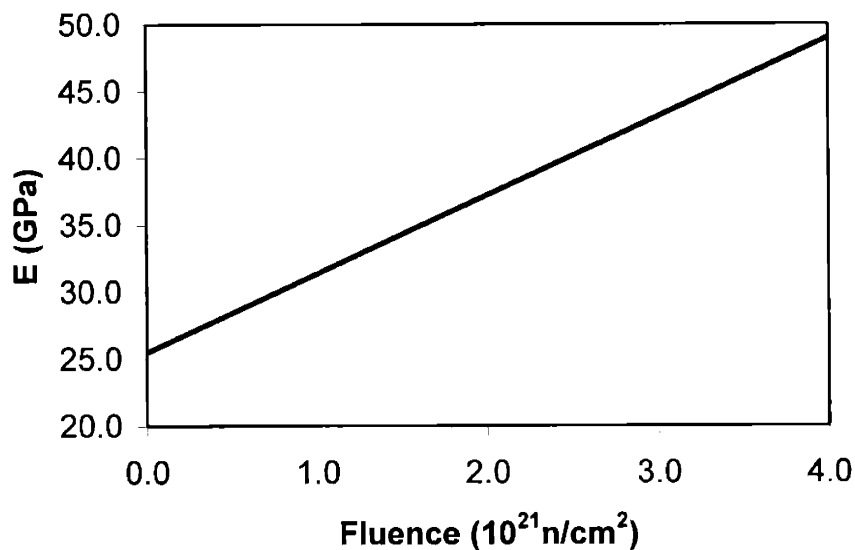
Figure 2-19. Young's modulus of dense PyC versus fast neutron fluence

Fast neutron fluence has the dominant effect on Young's modulus of pyrocarbon, as can be seen from Figure 2-19 if we plot E versus Φ by keeping other parameters at their

reference values. Other parameters will not change the value of E dramatically in the range in interest.

The dependence of Poisson's ratio ν on density, temperature, and neutron fluence is largely unknown. The dependence of ν on anisotropy is given by Ho [37] based on the data given by Price and Kaae [50] as

$$\nu_{\theta\theta} = 0.766R - 0.275, \tag{2.63}$$

$$\nu_{\theta r} = -0.89R + 0.825, \text{ and} \tag{2.64}$$

$$\nu_{r\theta} = \nu_{\theta r} E_r / E_\theta, \tag{2.65}$$

where again R is given by eq. (2.55).

Due to the complexity of including anisotropic elastic constants of pyrocarbon in the general mechanical analysis, we just use the isotropic value of Poisson's ratio, which is chosen to be a constant value of 0.235, for all directions. In the thermal stress analysis as we will show later in Section 2.4.6, we are able to employ the whole set of anisotropic elastic constants for pyrocarbons.

2.4.2.2. Elastic Constants of Silicon Carbide

It has been mentioned that the SiC coating layer for fuel particles is predominantly of β phase, which is isotropic. The Young's moduli of SiC in the literature were derived from three-point or four-point bend tests on strip samples and diametral compression tests on brittle rings, and some room temperature values are summarized in Table 2-12.

Table 2-12. Young's Modulus of β-SiC at room temperature

E (GPa)	E (10^6 psi)	Source	Test Method
427	62	Price [51]	Three-point bend
427	62	Gulden [52]	Four-point bend
282 – 365	41 – 53	Bongartz et al. [53]	Brittle ring compression
200 – 600	29 – 87	Bongartz et al. [54]	Brittle ring compression
282 – 413	41 – 60	Wallura et al. [55]	Brittle ring compression
431	62.5	Yavuz & Tressler [56]	Four-point bend

It seems that 427GPa can be used as the room temperature value of Young's modulus of β-SiC, and the following temperature dependence reported by Gulden [52] are used in

our model. No significant changes in Young's modulus due to irradiation are observed from the work by Price [7].

Table 2-13. Young's Modulus of β-SiC v.s. temperature

T (°C)	25	940	1215	1400
E (GPa)	427	375	340	271
E (10^6 psi)	62	54.4	49.3	39.4

Poisson's ratio for SiC is given as 0.18 by Gibson [57]. A value of 0.13 ± 0.02 was reported by Yavuz and Tressler [56]. We use 0.13 in our model.

2.4.3. Irradiation Induced Dimensional Changes in Pyrolytic Carbon (PyC)

The irradiation induced dimensional changes in pyrocarbon is a very complicated phenomenon, because pyrocarbon is a mixture of constituting anisotropic graphite crystallites of all orientations with crystallite boundaries, cross links, vacancies, voids, defects and many other microstructures. Fast neutron irradiation leads to energetic knock-on carbon atoms which displace other carbon atoms in the structure and annihilate vacancies and defects. Before we get to the quantitative facts of irradiation dimensional changes, we would like to qualitatively explain what is going on in pyrocarbon with the aid of Figure 2-20.
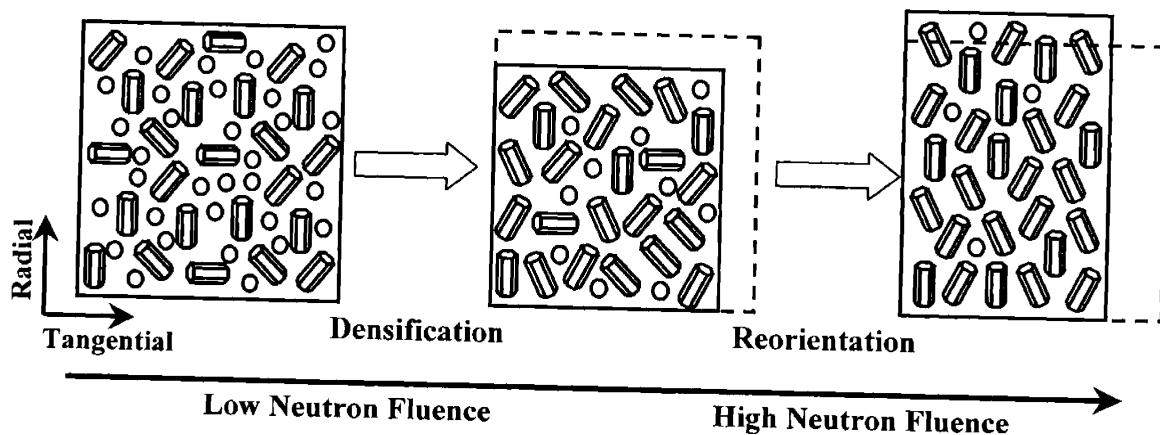
Figure 2-20. Schematic of irradiation dimensional change mechanisms in PyC (hexagonal bars represent graphite growth features, and circles represent vacancies and defects)

We know that the graphite crystallites are highly anisotropic and have a preferred orientation of crystallites. Micrographs show graphite growth features of all orientations, which are bases for the graphite crystallites to deposit on. It was determined that the carbon-layer planes of the crystallites (planes that 'a' direction in Figure 2-17 resides in) were always parallel to the surface of the growth features and that the preferred orientation of crystallites in small regions within the growth features was very high [58]. The left box in Figure 2-20 shows the essentially random dispersion of graphite growth features in the as-deposited pyrocarbon, hence its macroscopic behavior is isotropic. The effect of fast neutron irradiation is that neutrons displace carbon atoms so that they can re-distribute and find their favorite sites. One consequence is that many atoms fill in the previously existing vacancies and defects in between the growth features so that the material free boundary shrinks toward the bulk material. This is the process of densification. Another consequence is that graphite crystallites can re-orient in their preferred direction, and as a result, the grow features tend to re-orient uniformly in one direction, which is the normal of the coating plane. This is the process of reorientation. These two processes take place simultaneously. However, at early stage of irradiation, if the pyrocarbon is of low density, densification will outplay reorientation so that the pyrocarbon exhibits shrinkage in both radial and tangential directions. Later on as irradiation continues, there is not much space for densification and reorientation becomes the leading mechanism, so the dimensional change in the radial direction shows a turnaround point after which the material begins to expand in this direction. We can imagine reorientation will cause the macroscopic anisotropy of pyrocarbons to increase as a function of neutron fluence. Experimental results from Kaae [58] seem to support the above description. After irradiation at 950°C to a fluence of 2.1×10^{21} n/cm^2, the low density pyrocarbon had an increase in density from 1.62 to 1.99g/cm^3 and shrinkage strains of 7.5% and 6.0% in the directions parallel and perpendicular to the coating plane, respectively. From micrographs the original growth features were much more uniform in appearance, and those regions appeared similar to the as-deposited growth features in the high density pyrocarbon. Moreover, it was evident that a strong increase in crystallite size occurred. The as-deposited high density pyrocarbon also subjected to considerable

crystallite growth during irradiation, and the crystallite size increase in this case was larger. Figure 2-21 from Kaae [58] clearly show the two processes described above. In the figure, the bifurcation of two curves indicates the ongoing of reorientation, and densification is more apparent in the low density pyrocarbon.
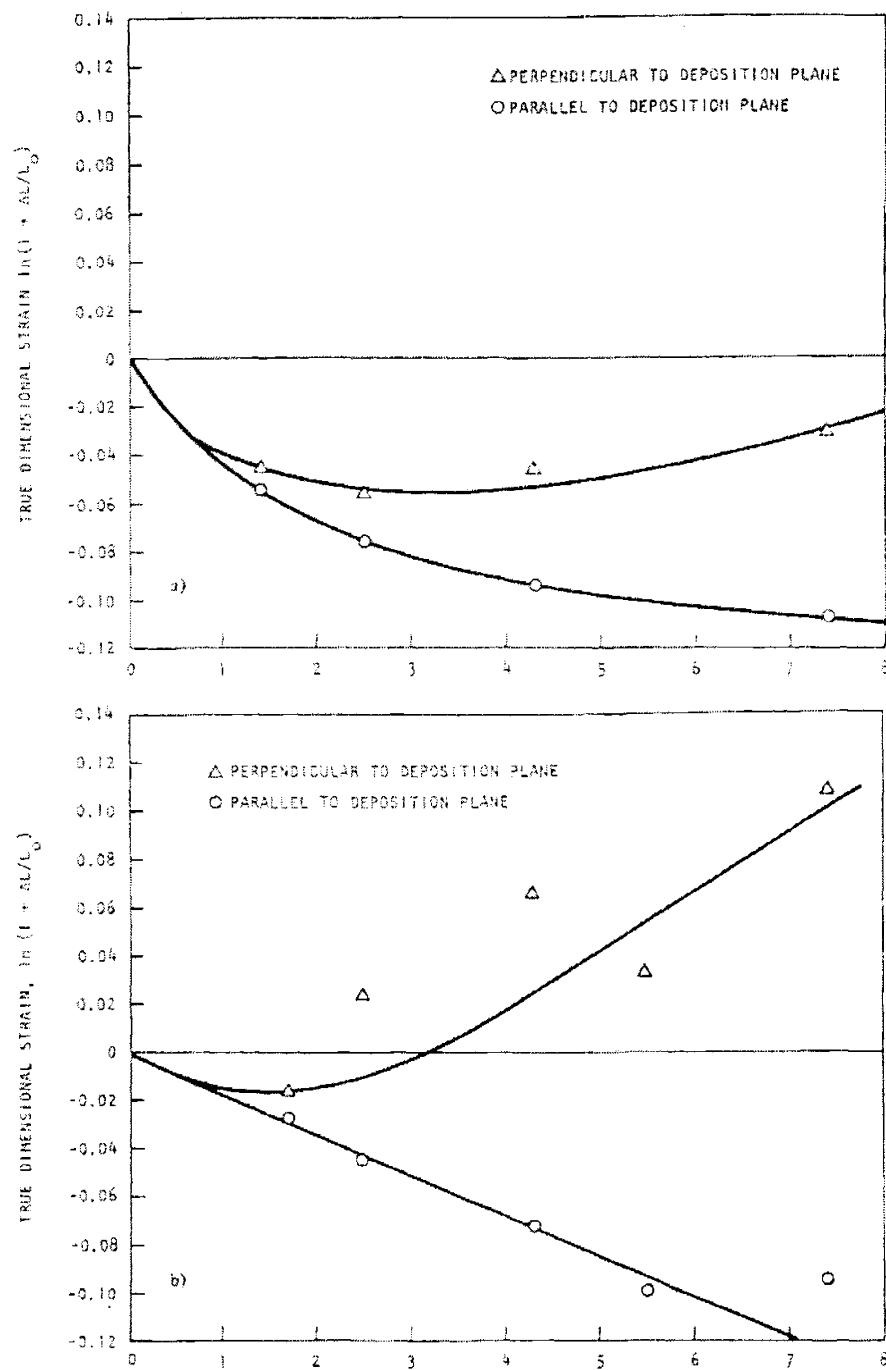
Figure 2-21. Dimensional changes of isotropic pyrolytic carbons during irradiation at 1000°C; (a) low density carbon, (b) high density carbon. Abscissas in (a) and (b): fast neutron fluence in 10^{21} n/cm^2 E > 0.18 MeV. (from Kaae [58])

We now develop the quantitative model for irradiation-induced dimensional changes ε_{ir} (radial direction) and ε_{it} (tangential direction) for pyrocarbons. We desire the dependency of ε_{ir} and ε_{it} on ρ, BAF_0, T, and Φ, but again some assumptions and interpolations have to be made due to insufficiency of data even though considerable work has been done to evaluate the dimensional changes.

2.4.3.1. Dimensional Changes of Pyrocarbon with Density of $1.96g/cm^3$
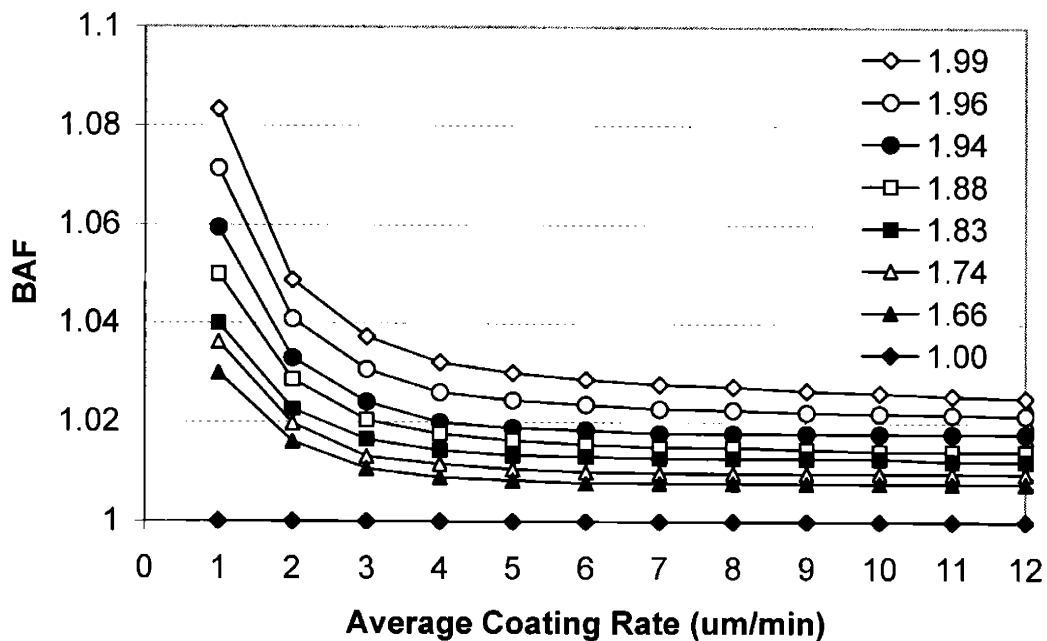
Figure 2-22. Variation of the as-deposited BAF with coating rate, reproduced based on Figure 1 from Kaae [47] and added two curves for $\rho=1.96g/cm^3$ and $\rho=1.00g/cm^3$ for interpolation purposes

Since we do not have the complete set of data with respect to arbitrary ρ, BAF_0, T, and Φ, we start with a series of data which cover as many parameters as possible. The dimensional change curves presented in reference [57] for two coating rates, 1 and 2.5 μm/min are the model based curves. For each coating rate and the density of $1.96g/cm^3$, curves as a function of fast neutron fluence were given at temperatures of 930 - 1150°C (or median of 1032°C [37]) and 1350°C. Since coating rate is not considered as an independent parameter, because it has strong correlation with density and BAF_0, the two

coating rates were converted to BAF_0 at $\rho=1.96g/cm^3$ based on Figure 2-22, and turned out to be BAF_0 of 1.063 and 1.036, respectively.

In the figure above, a curve for $\rho=1.96g/cm^3$ is added by interpolation because it is for the reference density. Another curve for $\rho=1.00g/cm^3$ is appended by assuming pyrocarbon at this density is isotropic, and this curve simply serves as a bottom line for modeling. It can be seen that coating rate appears to have strong effect at low coating rate, and the effect vanishes at intermediate and high coating rates. It should also be noted that for a specified density of pyrocarbon, certain value of BAF may not be possible, which is reasonable because good packing and orientation of graphite crystallites are required to achieve high density. For example, the BAF of a pyrocarbon coating with density of $\rho=1.99g/cm^3$ is above 1.02 based on the figure.

In reference [37], some other data source were employed and fitting was used to get curves at 600°C for BAF_0 of 1.063 and 1.036, then we get

$$\varepsilon_{ir}\left(\rho=1.96, BAF_0=(1.036,1.063), T=(600,1032,1350), \Phi\right) \text{ and}$$

$$\varepsilon_{it}\left(\rho=1.96, BAF_0=(1.036,1.063), T=(600,1032,1350), \Phi\right).$$

2.4.3.2. Dependence of Dimensional Changes of Pyrocarbon on Density

Now we would like to extend the curves obtained in the last section to a wider range of density and BAF_0. References that have shown the dependence of ε_{ir} and ε_{it} on density with the end-of-life fluence and irradiation temperature are summarized in Table 2-14.

Table 2-14. References for Irradiation Dimensional Changes of PyC versus Density

References	Temperature (°C)	Fluence ($10^{21}n/cm^2$)
Figure 3(c) in Ref. [59]	1220 – 1270	1.8 – 2.1
Figure 3(b) in Ref. [60]	1000	2.1 – 2.3
Figure 3(b) in Ref. [61]	1000	3.85
Figure 1(b) in Ref. [45]	650 – 1250	3.7
Figure 1 in Ref. [62]	1010 – 1140	2.5, 4.3
Figure 2(a) in Ref. [62]	1235	3.6
Figure 3(a) in Ref. [63]	650 - 900	3.7

(Note: This table is copied from reference [37])

73

All of the curves presented in the references above were superimposed in one figure and two average curves for the radial and tangential directions as a function of density were estimated by Ho [37] and redrawn in Figure 2-23. Also the averaged temperature and fluence for the two curves were approximated to be about 1100°C and 3.7×10^{21} n/cm^2, respectively. It was observed that two curves merge at a low density of 1.0g/cm^3, namely, PyC is more and more isotropic with the decrease of density, which agrees with our discussion at the beginning of Section 2.4.3.
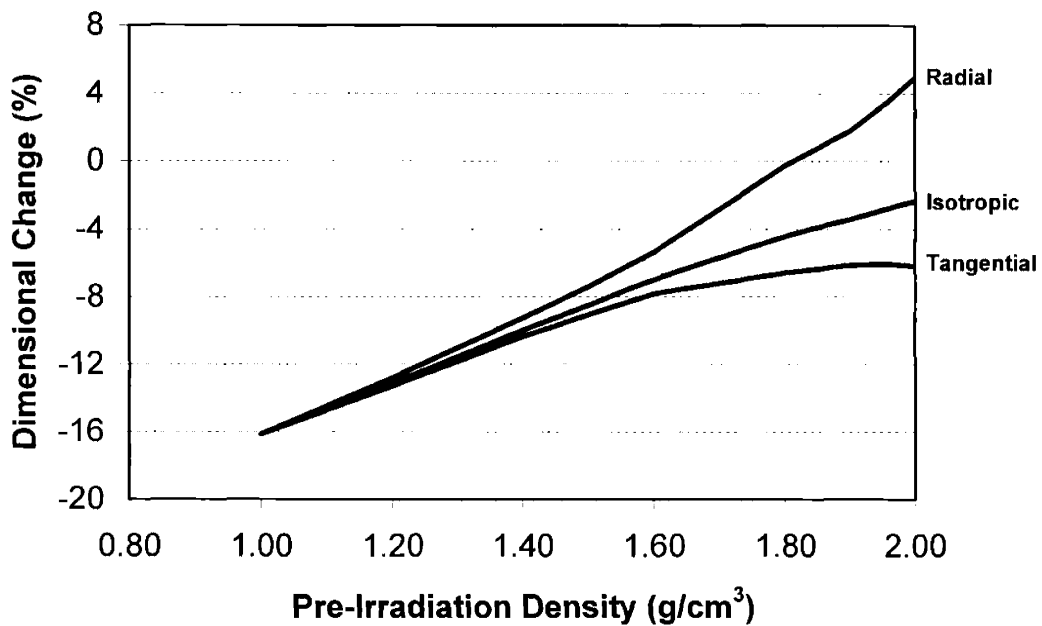
Figure 2-23. Constructed irradiation induced dimensional changes versus density for PyC irradiated at 1100°C to 3.7×10^{21} n/cm^2

We could also construct an artificial curve for isotropic PyC at the same irradiation conditions from the radial and tangential curves according to

$$\varepsilon_{iISO} = 1 - (1 - \varepsilon_{it})^{2/3}(1 - \varepsilon_{ir})^{1/3},$$ (2.66)

meaning picking out the densification information and disregarding the reorientation information carried by the radial and tangential curves. Figure 2-23 is the reference for our modeling of the dependence of irradiation induced dimensional changes on density. The isotropic curve gives the effect of irradiation induced densification on PyC density,

74

and the difference between the radial curve and the tangential curve gives the dependence of anisotropy on density. These values are tabulated in Table 2-15, which will be used to correct for density difference on the dimensional changes we obtained in Section 2.4.3.1.

Table 2-15. Irradiation Dimensional Changes of PyC at 1100°C to 3.7×10^{21} n/cm^2

ρ (g/cm^3)	1.0	1.2	1.4	1.5	1.6	1.8	1.9	1.96	2.0
ε_{iISO} (%)	-16.15	-13.11	-9.98	-8.50	-6.97	-4.42	-3.41	-2.75	-2.33
$\varepsilon_{ir} - \varepsilon_{it}$ (%)	0.0	0.50	1.10	1.65	2.45	6.31	7.90	9.60	11.10

Based on eq. (2.66), curves for $\varepsilon_{iISO}(\rho = 1.96, BAF_0 = 1, T = (600,1032,1350), \Phi)$ can be obtained from $\varepsilon_{ir}(\rho = 1.96, BAF_0 = (1.036,1.063), T = (600,1032,1350), \Phi)$ and $\varepsilon_{it}(\rho = 1.96, BAF_0 = (1.036,1.063), T = (600,1032,1350), \Phi)$. The curves can be fitted to a fourth order polynomials of fluence in the form of

$$\varepsilon_{iISO}(\%) = a_1\Phi + a_2\Phi^2 + a_3\Phi^3 + a_4\Phi^4, \tag{2.67}$$

with very good accounting for variance (~99%), where Φ has the dimension of 10^{21}n/cm^2. The fitting coefficients are presented in Table 2-16.

Table 2-16. Coefficients of the Polynomials for Irradiation Induced Dimensional Changes of Isotropic PyC at ρ=1.96g/cm^3

		Polynomial Coefficients			
T (°C)	BAF	a_1	a_2	a_3	a_4
1350	1.0	-1.8886	0.38982	-0.03691	0.00130
1032	1.0	-1.7111	0.38139	-0.03674	0.00135
600	1.0	-1.4764	0.29487	-0.02790	0.00105

2.4.3.3. Dependence of Dimensional Changes of Pyrocarbon on Anisotropy

One more task is to extend what we have to other BAF_0 values by fitting and extrapolation. Table 2-16 in Section 2.4.3.2 gives ε_{iISO} at $BAF_0 = 1$, and ε_{ir} and ε_{it} were obtained at $BAF_0 = 1.036$ and 1.063 in Section 2.4.3.3. Because one BAF_0 corresponds to two R values according to eqs. (2.54) and (2.55), we can get more data points by using Rs, and they are R = 0.6530, 0.6588, 2/3, 0.6706, 0.6735.

Points at these values were plotted at fluences of 0.7, 1, 2, 3, and 4×10^{21} n/cm^2, then at each fluence, smooth curves were fitted to the points of changing R values and extrapolated to R of 0.6 and 0.7 in two directions. The shape of the smooth curves and extrapolations were based on experimental evidence of the effect of R on irradiation induced dimensional changes of pyrocarbon in references [59] and [64]. Then the data points at selected R values were again fitted into polynomials of eq. (2.67) with good accounting for variance (~99%) and the coefficients are presented in Table 2-17 and Table 2-18.

Table 2-17. Coefficients of the Polynomials for Irradiation Induced Radial Dimensional Changes ε_{ir} of PyC at $\rho=1.96$g/cm^3

T (°C)	BAF	Polynomial Coefficients			
		a_1	a_2	a_3	a_4
600	1.0000	-1.24080	0.00175	0.08533	-0.01253
	1.0212	-1.10640	-0.03128	0.09184	-0.01220
	1.0488	-0.94333	-0.03589	0.08184	-0.00958
	1.0769	-0.78045	-0.02975	0.06655	-0.00626
	1.1746	-0.15714	-0.14889	0.07546	-0.00293
	1.2787	0.40265	-0.16501	0.03676	0.00706
1032	1.0000	-1.52390	0.13048	0.06299	-0.01072
	1.0212	-2.07520	1.37845	-0.48993	0.06602
	1.0488	-2.00470	1.30380	-0.37280	0.04538
	1.0769	-1.81690	1.10850	-0.23868	0.02484
	1.1746	-1.18540	0.64995	0.01380	-0.01284
	1.2787	-0.45900	0.51172	-0.03245	-0.00142
1350	1.0000	-1.42840	-0.19563	0.18991	-0.02591
	1.0212	-1.54330	0.59804	-0.09997	0.00978
	1.0488	-1.49640	1.16621	-0.30106	0.03475
	1.0769	-0.89522	0.80331	-0.09009	0.00467
	1.1746	1.20930	-0.53861	0.43114	-0.05590
	1.2787	3.71620	-2.70420	1.17990	-0.13910

Table 2-18. Coefficients of the Polynomials for Irradiation Induced Tangential
Dimensional Changes ε_{it} of PyC at ρ=1.96g/cm^3

T (°C)	BAF	Polynomial Coefficients			
		a_1	a_2	a_3	a_4
600	1.0000	-1.24080	0.00175	0.08533	-0.01253
	1.0303	-1.38550	0.05307	0.07620	-0.01245
	1.0769	-1.46790	-0.02836	0.12139	-0.01948
	1.1250	-1.64660	0.03928	0.10067	-0.01764
	1.2258	-1.84990	-0.09358	0.18119	-0.03036
	1.3333	-2.19190	0.02675	0.15352	-0.02972
1032	1.0000	-1.52390	0.13048	0.06299	-0.01072
	1.0303	-1.57590	0.09019	0.05306	-0.00815
	1.0769	-1.32200	-0.51928	0.27603	-0.03465
	1.1250	-1.18700	-0.90635	0.41046	-0.05067
	1.2258	-0.96963	-1.59110	0.64689	-0.07682
	1.3333	-0.81239	-2.20760	0.88496	-0.10457
1350	1.0000	-1.42840	-0.19563	0.18991	-0.02591
	1.0303	-2.24680	0.48243	-0.07687	0.00464
	1.0769	-2.82930	0.76088	-0.22314	0.02431
	1.1250	-3.25550	0.90423	-0.33175	0.04329
	1.2258	-4.44780	1.60320	-0.58683	0.07458
	1.3333	-5.67140	2.41920	-0.86155	0.10668

2.4.3.4. The Procedure of Obtaining ε_{ir} and ε_{it} at given ρ, BAF_0, T, and Φ

Based on the descriptions in the three sub-sections above, the steps for obtaining the radial and tangential irradiation induced dimensional changes of pyrocarbon at given density ρ', unirradiated BAF_0', irradiation temperature T' and fast neutron fluence Φ' is summarized below.

(1) Get $\varepsilon_{iISO}(\rho = 1.96, BAF_0 = 1, T', \Phi')$ from Table 2-16. Interpolation is used for T' other than the specified temperatures in the table.

(2) Adjust for density difference to get $\varepsilon_{iISO}(\rho', BAF_0 = 1, T', \Phi')$ based on Table 2-15. For example, if ρ' = 1.6 g/cm^3, then the factor is -6.97/-2.75 = 2.535, meaning

77

$\varepsilon_{iISO}(\rho', BAF_0 = 1, T', \Phi') / \varepsilon_{iISO}(\rho = 1.96, BAF_0 = 1, T', \Phi') = 2.535$. The assumption is that the relative densification effect with respect to density is independent of T and Φ.

(3) The given ρ' and BAF_0' are converted to a pair of $\rho = 1.96$ g/cm^3 and BAF_0'' from Figure 2-22 by assuming the same coating rate.

(4) $\varepsilon_{ir}(\rho = 1.96, BAF_0'', T', \Phi')$ and $\varepsilon_{it}(\rho = 1.96, BAF_0'', T', \Phi')$ are obtained from Table 2-17 and Table 2-18, and $\Delta\varepsilon_i(\rho = 1.96, BAF_0'', T', \Phi') = \varepsilon_{ir} - \varepsilon_{it}$ is calculated. Interpolations on T' and BAF_0'' may be necessary.

(5) Adjust for density difference to get $\Delta\varepsilon_i(\rho', BAF_0', T', \Phi')$ based on Table 2-15. Similarly to step (2), the relative effect of density on anisotropy is assumed to be independent of T and Φ.

(6) Use $\varepsilon_{iISO}(\rho', BAF_0 = 1, T', \Phi')$ and $\Delta\varepsilon_i(\rho', BAF_0', T', \Phi')$ to derive $\varepsilon_{ir}(\rho', BAF_0', T', \Phi')$ and $\varepsilon_{it}(\rho', BAF_0', T', \Phi')$ according to eq. (2.66), which are what we need.
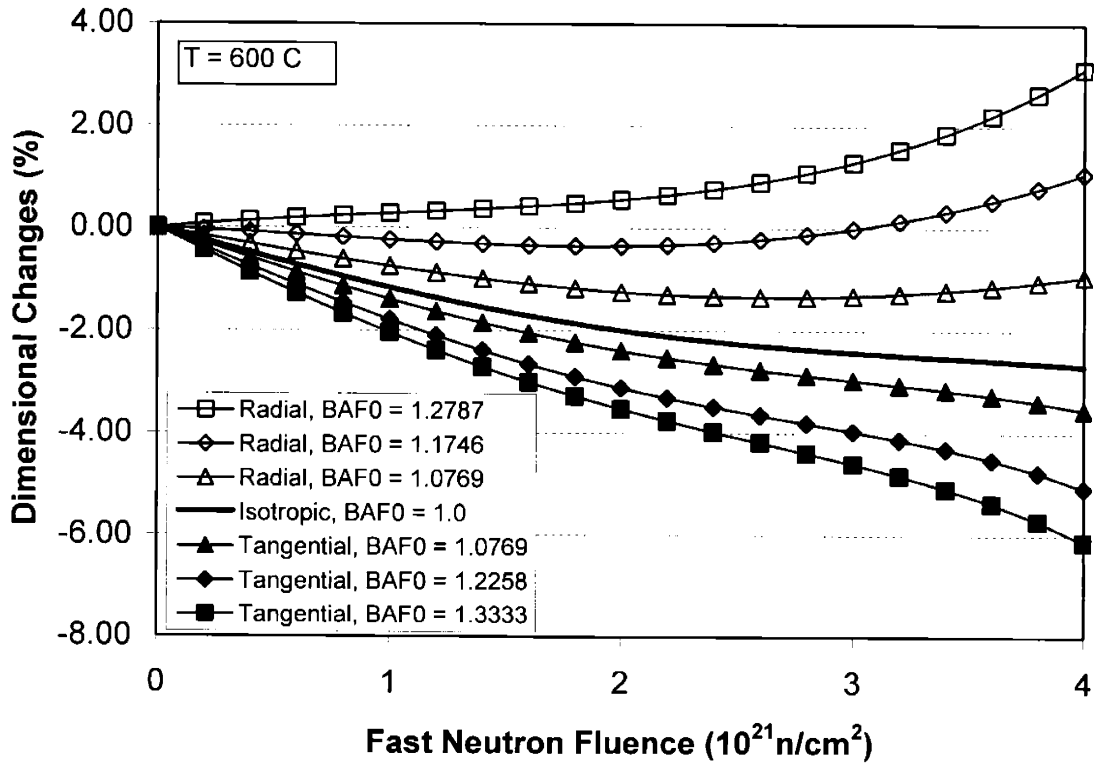
Figure 2-24. Irradiation induced dimensional changes of PyC of density 1.96g/cm^3 irradiated at 600°C (symbols for clarity)
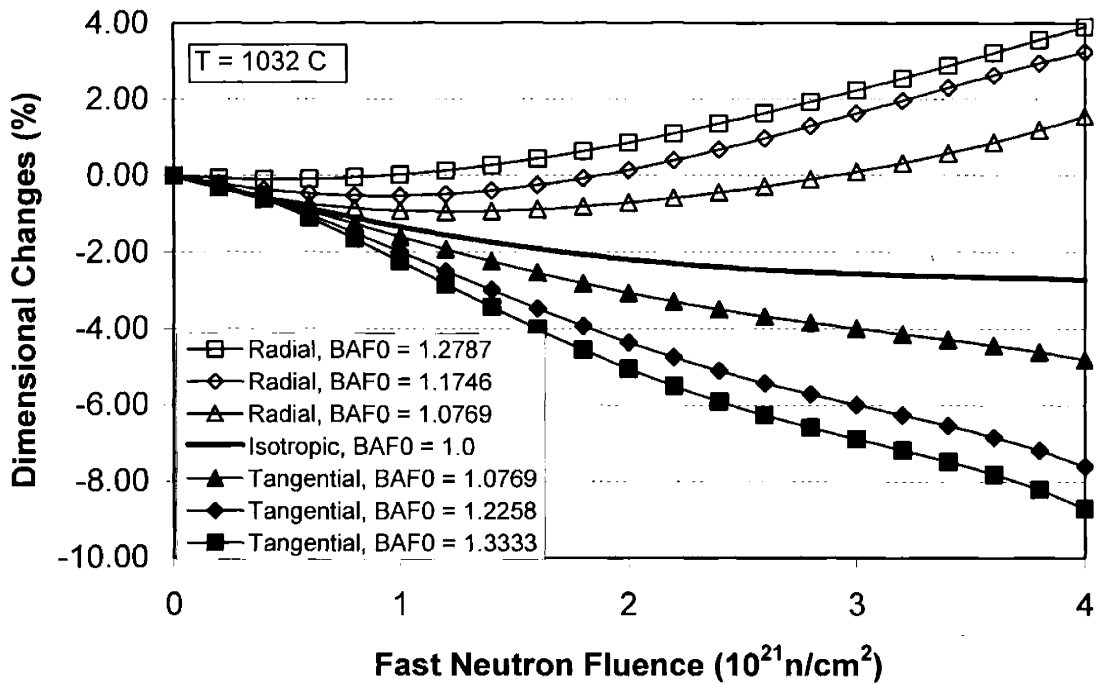
Figure 2-25. Irradiation induced dimensional changes of PyC of density 1.96g/cm^3 irradiated at 1032°C (symbols for clarity)
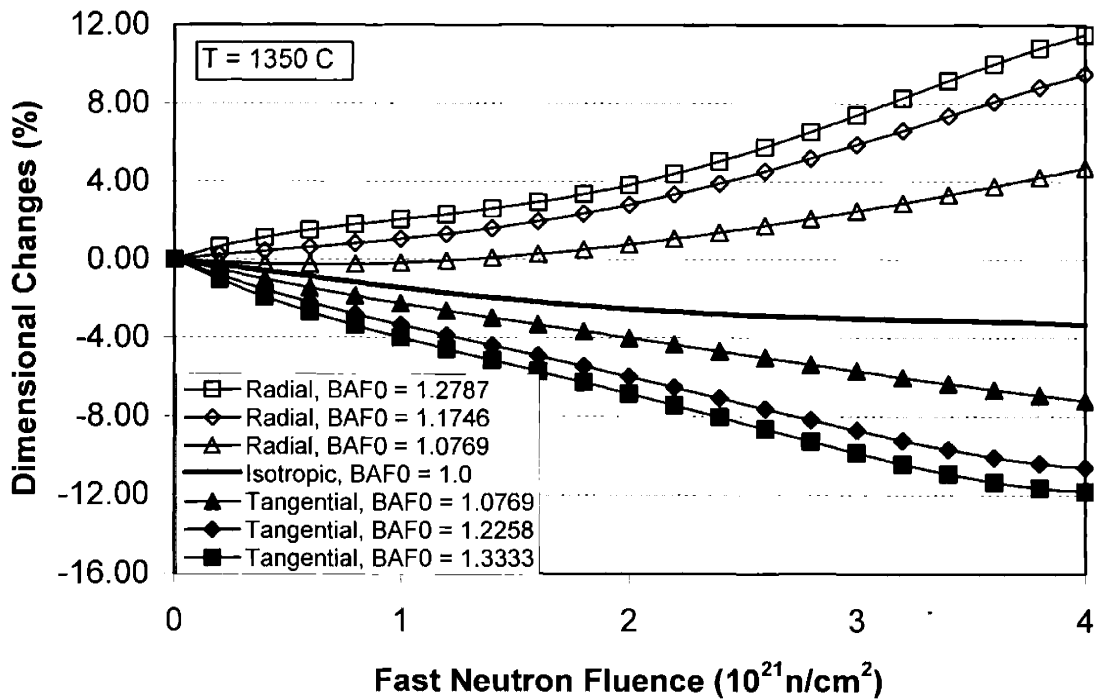
Figure 2-26. Irradiation induced dimensional changes of PyC of density 1.96g/cm^3 irradiated at 1350°C (symbols for clarity)

For illustration purposes, selected curves from Table 2-17 and Table 2-18 are plotted in Figure 2-24, Figure 2-25, and Figure 2-26 at three temperatures.

It is clearly shown in the figures that higher irradiation temperature and anisotropy cause wider separation of the radial and tangential curves, and leads to earlier turnaround points in the radial dimensional changes. From Figure 2-26, with BAF_0 of about 1.30 the magnitude of dimensiona changes of pyrocarbon exceeds 10% in both directions at irradiation temperature of 1350°C.

2.4.3.5. Non-isothermal and Restrained Conditions

As has been discussed in the Introduction and Thermal Model sections, the fuel pebbles and particles will not be subject to constant irradiation temperatures in most cases, so a way to deal with irradiation induced dimensional changes of pyrocarbon with non-isothermal irradiation temperature history has to be introduced. Let's say at fluence of 1×10^{21} n/cm^2 irradiation temperature changes from 800°C to 1000°C, a reasonable way is to sample the dimensional change rate instead of dimensional change itself from the 1000°C curve at 1×10^{21} n/cm^2, because the rate represents the driving force of dimensional changes at the new condition. What we get from this scheme is a curve of dimensional change rate associated with a specific temperature history, and the absolute dimensional change curve is obtained by integrating the rate curve. Some error would be introduced because beside temperature and fluence, the rate also depends on the damage which is already made to the material, but this is the best we can do from modeling point of view and the error is believed to be small.

Another issue is that dimensional changes will be different under mechanical restraint conditions. Under stresses and irradiation, pyrocarbon will creep which enhances the BAF of the pyrocarbon. This effect will be factored in through the following procedure. According to Kaae [46] and our discussion at the beginning of this section 2.4.3, ε_i can be decomposed into a volume conserving reorientation component ε_{ia} and a densification component ε_{ib}, so

$$\varepsilon_{ir} = \varepsilon_{ira} + \varepsilon_{irb} \text{, and} \qquad (2.68)$$

$$\varepsilon_{it} = \varepsilon_{ita} + \varepsilon_{itb} \text{,} \qquad (2.69)$$

satisfying

$\varepsilon_{ira} = -2\varepsilon_{ita}$ (volume conservation), and $\qquad\qquad$ (2.70)

$\varepsilon_{irb} = \varepsilon_{itb}$ (isotropic densification). $\qquad\qquad$ (2.71)

From eqs. (2.68) - (2.71), we get

$$\varepsilon_{ira} = -2\varepsilon_{ita} = \frac{2}{3}(\varepsilon_{ir} - \varepsilon_{it}), \text{ and} \qquad\qquad (2.72)$$

$$\varepsilon_{irb} = \varepsilon_{itb} = \frac{1}{3}(\varepsilon_{ir} + 2\varepsilon_{it}). \qquad\qquad (2.73)$$

The components ε_{ira} and ε_{ita} can be further expresses as [46]

$$\varepsilon_{ira} = R_i X_a + (1 - R_i) X_c, \text{ and} \qquad\qquad (2.74)$$

$$\varepsilon_{ita} = (1 - R_i / 2) X_a + (R_i / 2) X_c, \qquad\qquad (2.75)$$

where X_a and X_c are dimensional strains of the crystallites in the a and c directions, and R_i is the parameter in eq. (2.55), associated with BAF_i which is the irradiated BAF.

From eqs. (2.72) - (2.75), we can have

$$X_a = \frac{2}{3(2 - 3R_i)}(\varepsilon_{it} - \varepsilon_{ir}), \text{ and} \qquad\qquad (2.76)$$

$$X_c = \frac{4}{3(2 - 3R_i)}(\varepsilon_{ir} - \varepsilon_{it}). \qquad\qquad (2.77)$$

The remaining task is to first back out X_a and X_c which are not influenced by irradiation creep, then update BAF_i and R_i and plug them back into eqs. (2.76) and (2.77) to get restrained ε_{ir} and ε_{it}. This procedure has been used in codes TRISO [57] and PISA [65].

The irradiated BAF as a function of fluence is from [37] and given below.

Table 2-19. Irradiated BAF for PyC of $BAF_0 = 1.05$ and $\rho = 1.9$ g/cm^3

Φ (10^{21}n/cm^2)	0	1	2	3	3.5	4	4.5	≥ 5
BAF_i	1.05	1.052	1.062	1.073	1.08	1.084	1.088	1.09

The BAF as a function of apparent creep strain was given in [46], but the presented BAF values are very high which would lead to unrealistically big dimensional changes based on our database, therefore this relationship is not implemented now. We think shear strain may be more effective in changing pyrocarbon crystallite alignment, so we

recommend looking at the effect of octahedral-shear creep strain instead of apparent creep strain on dimensional changes.

2.4.4. Irradiation Induced Creep in Pyrolytic Carbon (PyC)

The irradiation induced creep in PyC has both a transient component and a steady state component. Because transient creep strain is much smaller than steady state creep strain, and few data are available, transient creep is not included in the model. For a transversely isotropic material like PyC, steady state creep are described by four independent constants, but since all measurements were made in the in-plane (tangential) direction, only two constants were given, and we have to use isotropic creep model. Fortunately this is not too bad because the pyrocarbons we deal with is nearly isotropic.

The governing equations for irradiation induced steady state creep in PyC in the radial and tangential directions are

$$\varepsilon_{cr} = c(\sigma_{rr} - 2\nu_c \sigma_{\theta\theta})\Phi, \text{ and} \tag{2.78}$$

$$\varepsilon_{ct} = c((1 - \nu_c)\sigma_{\theta\theta} - \nu_c \sigma_{rr})\Phi, \tag{2.79}$$

where

c is steady state creep coefficient $(MPa.10^{21} \text{ n/cm}^2)^{-1}$,

ν_c is Poisson's ratio in steady state creep, and

Φ is fast neutron fluence (10^{21} n/cm^2).

For simplicity, we will say creep instead of irradiation induced steady state creep from now on.

The following relation is given for c by Ho [37] to be

$$c = (2.193 \times 10^{-4} - 4.85 \times 10^{-7}T + 4.0147 \times 10^{-10}T^2)(1 + 2.38 \times (1.9 - \rho)), \tag{2.80}$$

which gives a quadratic relationship with respect to T in °C and a linear relationship with respect to ρ in g/cm^3. The equation was derived from a set of data discussed in [37], which exhibits a trend of increasing creep with increasing temperature (for T ≥ 600°C) and of decreasing creep with increasing density, and this is consistent with the behavior of graphite. The creep coefficient c is assumed to be independent of fast neutron fluence, as indicated in all of the published literature.

Based on the author's knowledge, all of the previous coated particle fuel performance models use 0.5 as the value of Poisson's ratio in creep v_c, which means the creep behavior is volume conservative, like the flow of incompressible fluid. Kaae has suggested that the value of v_c appears to depend on the effective or octahedral shear creep strain, independent of structure, density, and irradiation temperature of the pyrocarbon [66], as shown in Figure 2-27.
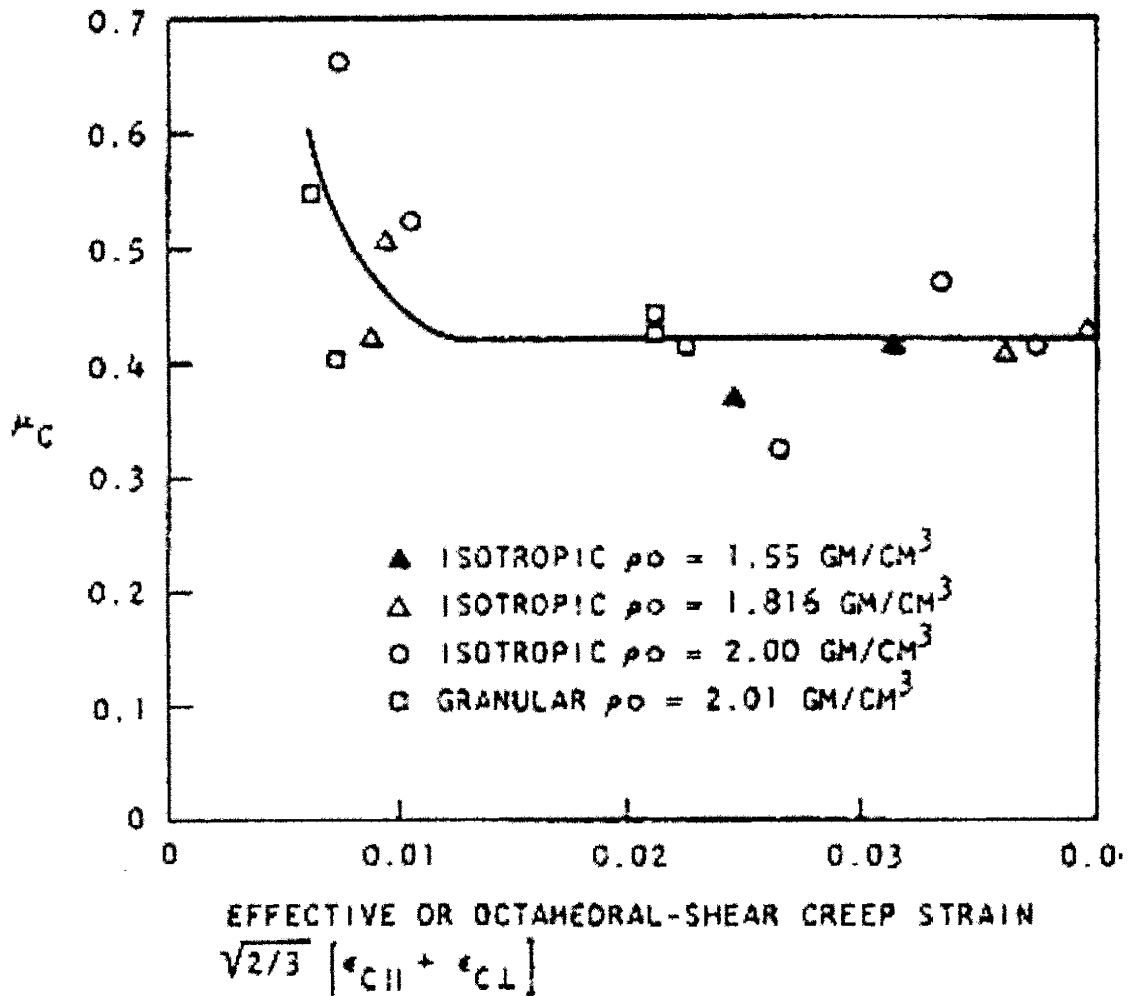
Figure 2-27. Poisson's ratio in irradiation creep as function of effective creep strain (from Kaae [66])

The effective creep strain is calculated as

$$\varepsilon_c^{eff} = \sqrt{\frac{2}{3}\left(\varepsilon_{cr} + \varepsilon_{ct}\right)}.$$ (2.81)

At low strains, v_c is near or above the constant-volume value of 0.5, but beyond strain of 0.01, it rapidly decreases to about 0.4 and remains constant over a wide range of strains. This means creep is happening with an increase in volume, possibly due to the growth of micro-cracks. It will be shown later in our stress analysis that this makes a significant difference in terms of stress condition and fuel performance by relaxing the constraint of fixing v_c at 0.5.

The creep coefficients represented by eq. (2.80) are plotted in Figure 2-28.
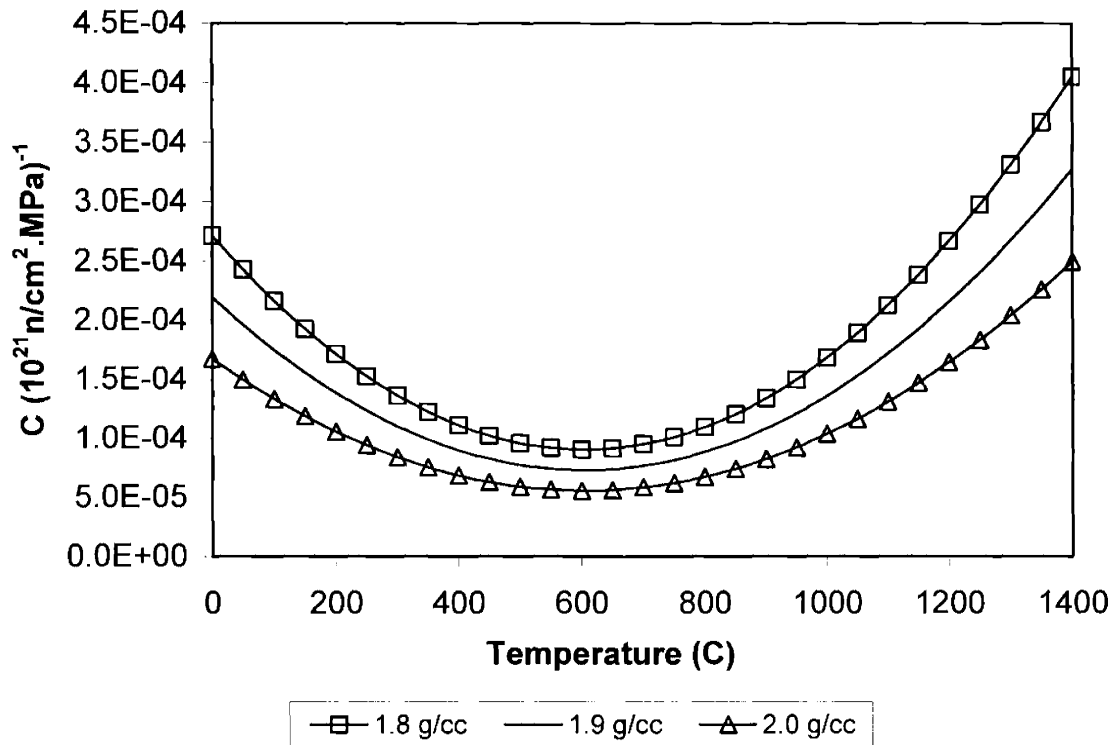
Figure 2-28. Creep coefficient of pyrocarbon as function of temperature and density (symbols for clarity)

2.4.5. Thermal Expansion of Pyrolytic Carbon (PyC) and Silicon Carbide (SiC)

2.4.5.1. Thermal Expansion of Pyrolytic Carbon

The thermal expansion of pyrocarbon has been shown in the literature to depend primarily on the degree of preferred orientation of graphite crystallites, and a simple Bacon relation gives the thermal expansion coefficient in a particular direction to be

$$\alpha = R\alpha_a + (1 - R)\alpha_c ,$$ (2.82)

where R is the orientation parameter introduced before for that direction, and α_a and α_c are the thermal expansion coefficients in the a and c directions of graphite crystallite. Some data of α_a and α_c are presented in Figure 2-29.
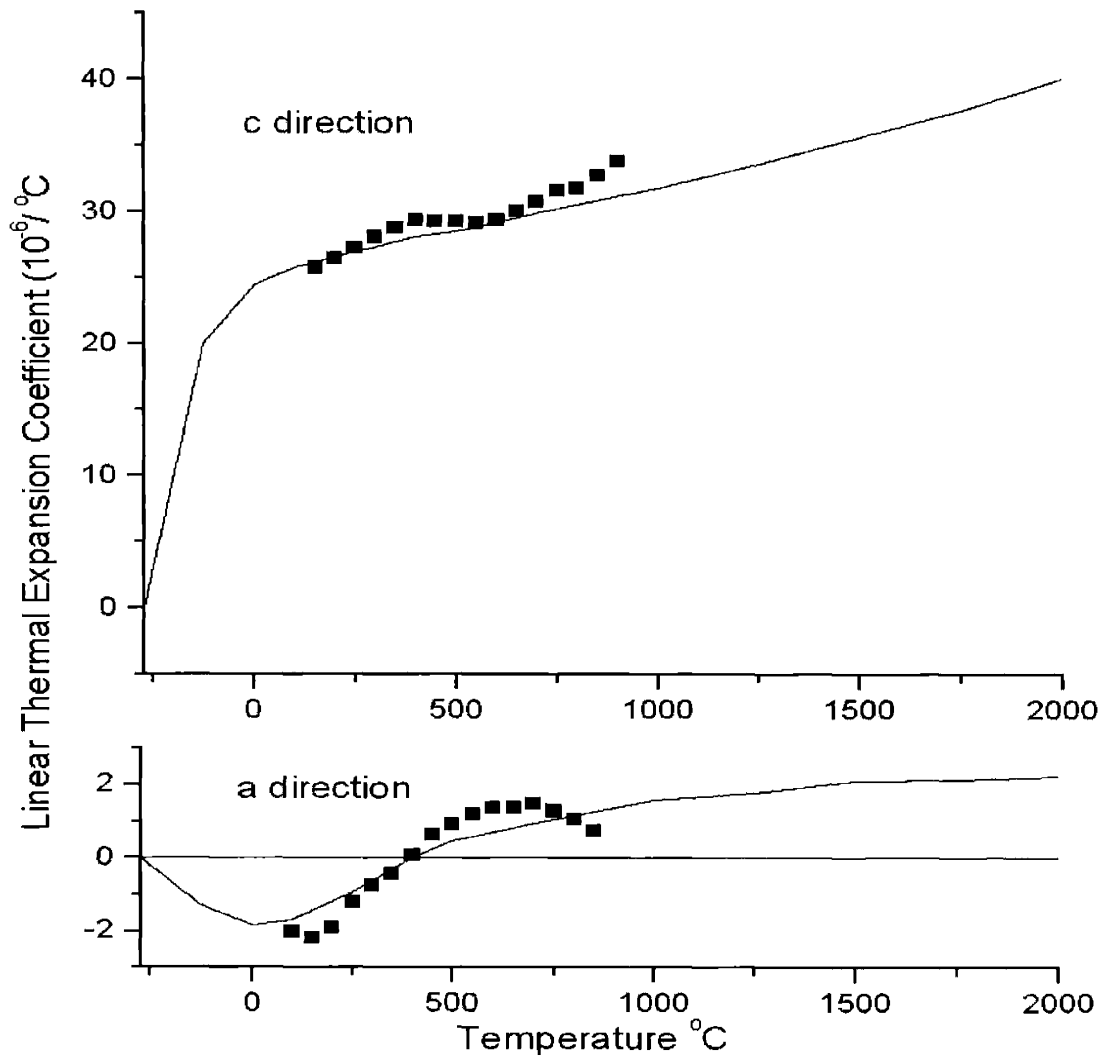
Figure 2-29. Thermal expansion of the graphite crystal in the a and c directions (Solid line: experimental data from Pierson [67]; squares: derived data from Bokros [40])

We see that the thermal expansion in the normal direction of graphite basal plane is much higher than that in the plane. At 1100°C, α_c is about 31×10^{-6}/°C from Pierson [67],

$28.8 \times 10^{-6}/°C$ from Ho [68], and $27 \times 10^{-6}/°C$ from Gebhardt and Berry [69], and α_c is about $1.7 \times 10^{-6}/°C$ from Pierson [67], and $1.5 \times 10^{-6}/°C$ from Gebhardt and Berry [69].

The actual thermal expansion of pyrocarbon deviates some from the Bacon relation. The thermal expansion coefficients of various pyrocarbon at 400°C are given in Figure 2-30 taken from Bokros [40] as a function of orientation parameter R.
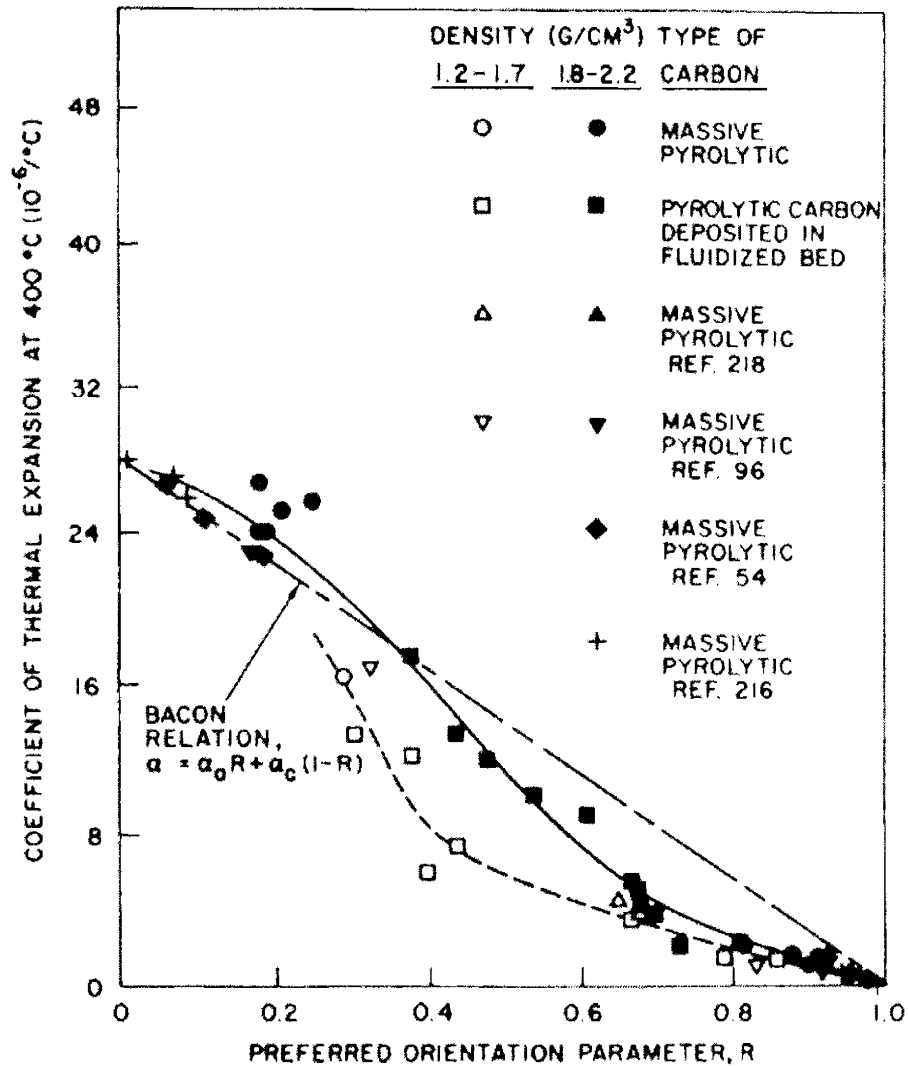
Figure 2-30. Thermal expansion coefficient at 400°C versus preferred-orientation parameter R for various pyrolytic carbons. At 400°C, $\alpha_a = 0$. (from Bokros [40])

Typical pyrocarbons used as fuel particle coatings have BAFs close to 1.0. If fitting is performed in the range of BAF less than 3 (so $R_3 > 0.4$ and $R_1 < 0.8$ with R_3 and R_1 defined in eqs. (2.54) and (2.55), respectively), the following relationship is obtained for

1100°C by adjusting the data in Figure 2-30 with the percentage increase which would be predicted by Bacon relation from 400°C to 1100°C,

$$\alpha_r = \alpha_3 = \frac{-125R_3}{3} + \frac{100}{3}, \text{ and} \qquad (2.83)$$

$$\alpha_t = \alpha_1 = 40(R_1 - 1)^2 + \frac{10}{9}. \qquad (2.84)$$

These two equations are used in the model. The reason of making the adjustment to 1100°C is to bring the thermal expansion coefficients into high temperature range in HTGRs. Notice that when BAF = 1, so $R_3 = R_1 = 2/3$, $\alpha_r = \alpha_t = 5.56 \times 10^{-6}/°C$.

2.4.5.2. Thermal Expansion of Silicon Carbide
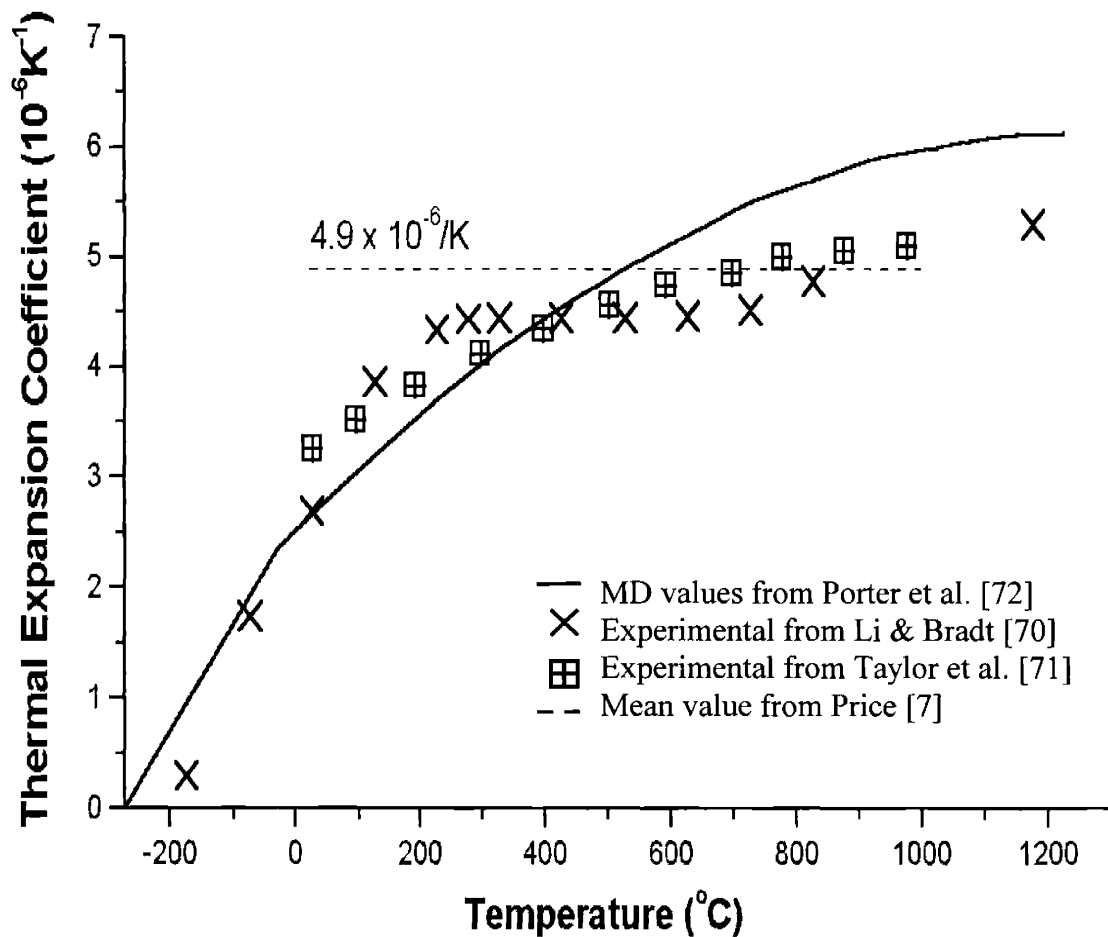
Figure 2-31. Thermal expansion coefficient for β-SiC as a function of temperature

A collection of thermal expansion coefficients for β-SiC is presented in Figure 2-31. The solid line is a Molecular Dynamics simulation result by Porter et al. [72], which shows fairly good agreement with experimental data. For now it is acceptable to use the constant value of $4.9 \times 10^{-6}/°C$. Thermal expansion of β-SiC is found to show no systematic dependence on the deposition temperature and is not affected by neutron irradiation.

2.4.6. The Formulation of Mechanical Analysis

Efforts on the mechanical analysis of coated fuel particles have been ongoing for forty years. It has evolved from one pyrocarbon shell model by Prados and Scott [73] to the IPyC/SiC/OPyC model that most people are using today, with the inclusion of irradiation induced dimensional changes, irradiation induced steady state creep, thermal expansion, and elastic response of materials.

The detailed formulation of our mechanical model is given in Appendix A. In our model, the thermal stress calculation is separated as a stand alone solution because four anisotropic elastic constants as discussed in Section 2.4.2.1 can be fully used. The general mechanical solutions using series solution technique would not give us a closed form solution if four elastic constants were included, hence we use two isotropic elastic constants. Furthermore, the thermal stress calculation is needed under accident conditions of HTGR systems when quick temperature rise occurs. Here we summarize the mechanical analysis which takes into account irradiation effects.

The constitutive equations for pyrocarbon layers in the radial and tangential directions expressed in spherical coordinates are

$$\frac{\partial \varepsilon_r}{\partial t} = \frac{1}{E}\left(\frac{\partial \sigma_r}{\partial t} - 2\nu \frac{\partial \sigma_\theta}{\partial t} \right) + c(\sigma_r - 2\nu_c \sigma_\theta) + \dot{S}_r, \text{ and} \tag{2.85}$$

$$\frac{\partial \varepsilon_\theta}{\partial t} = \frac{1}{E}\left[(1-\nu)\frac{\partial \sigma_\theta}{\partial t} - \nu \frac{\partial \sigma_r}{\partial t} \right] + c[(1-\nu_c)\sigma_\theta - \nu_c \sigma_r] + \dot{S}_\theta. \tag{2.86}$$

where the tangential direction is denoted by θ instead of t to avoid confusion with the time t. Time t in our language here is equivalent to fast neutron fluence in $10^{21} n/cm^2$.

Other symbols have been introduced in previous sections and are clearly defined in Appendix A.

Table 2-20. Parameters of Coated Fuel Particles for Stress Analysis

Parameter	Type 1	Type 2
Fuel Type	UCO	UO_2
Carbon to Uranium ratio	0.36	0
Oxygen to Uranium ratio	1.51	2
U235 Enrichment (%)	93.15	10.0
End-of-life Burnup (%FIMA)	10.0	10.0
End-of-life Fluence (10^{21}n/cm^2)	3.0	3.0
Irradiation Temperature (°C)	1000	1000
Irradiation Time (EFPD)	1000	1000
Ambient Pressure (MPa)	6.38	0.10
Kernel Density (g/cm^3)	10.52	10.80
Buffer Density (g/cm^3)	0.95	0.95
IPyC/OPyC Density (g/cm^3)	1.90	1.90
IPyC/OPyC BAF_0	1.03	1.03
Kernel Diameter (μm)	195	500
Buffer Thickness (μm)	100	100
IPyC Thickness (μm)	53	40
SiC Thickness (μm)	35	35
OPyC Thickness (μm)	43	40

We use series solutions to solve for stresses, strains, and displacements, as shown in Appendix A. The SiC layer is treated as an elastic medium with no irradiation induced deformation. We now show some results for two cases in Table 2-20, which give the same particle dimensions as those in Table 2-9, to explain the general mechanical behavior of fuel particles under irradiation conditions.

Figure 2-32 and Figure 2-33 show the radial and tangential stress distributions in the Type 1 particle at a fast neutron fluence of 0.9×10^{21}n/cm^2, when the stresses are the highest in this case. Although particles can have different dimensions, fuel types, and irradiation conditions, the stress patterns given in these two figures are very robust over a wide range of neutron fluence levels. Here are the common features of stress distributions.
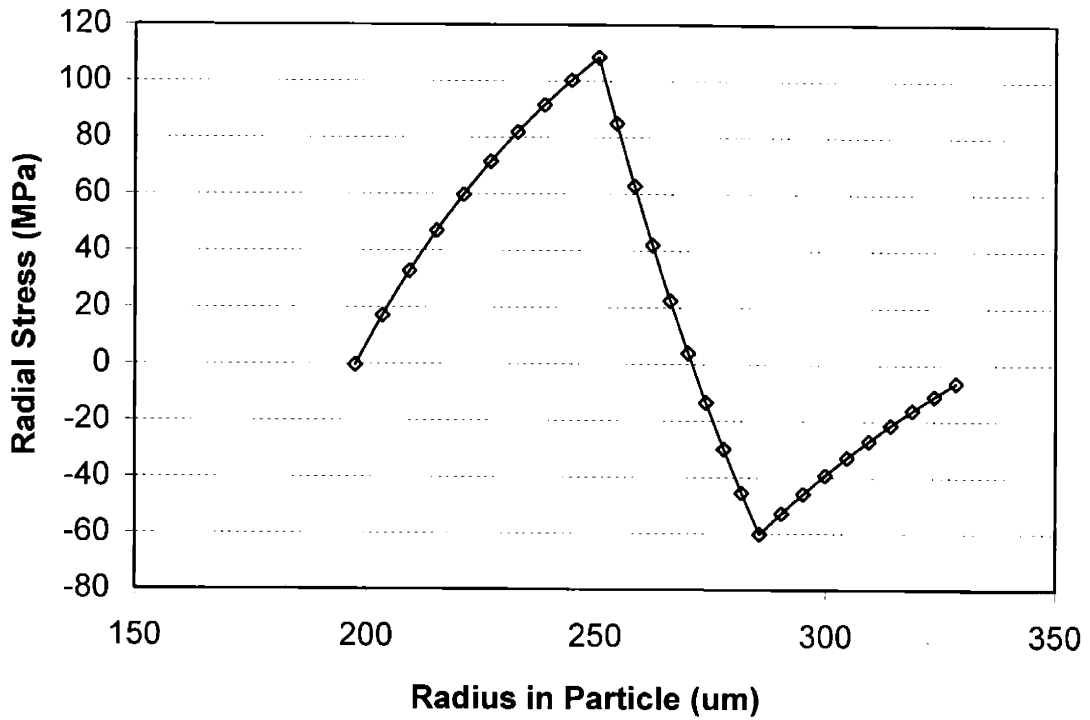
Figure 2-32. Radial stress distribution in Type 1 particle at fluence of $0.9 \times 10^{21} \text{n/cm}^2$ (symbols for clarity)
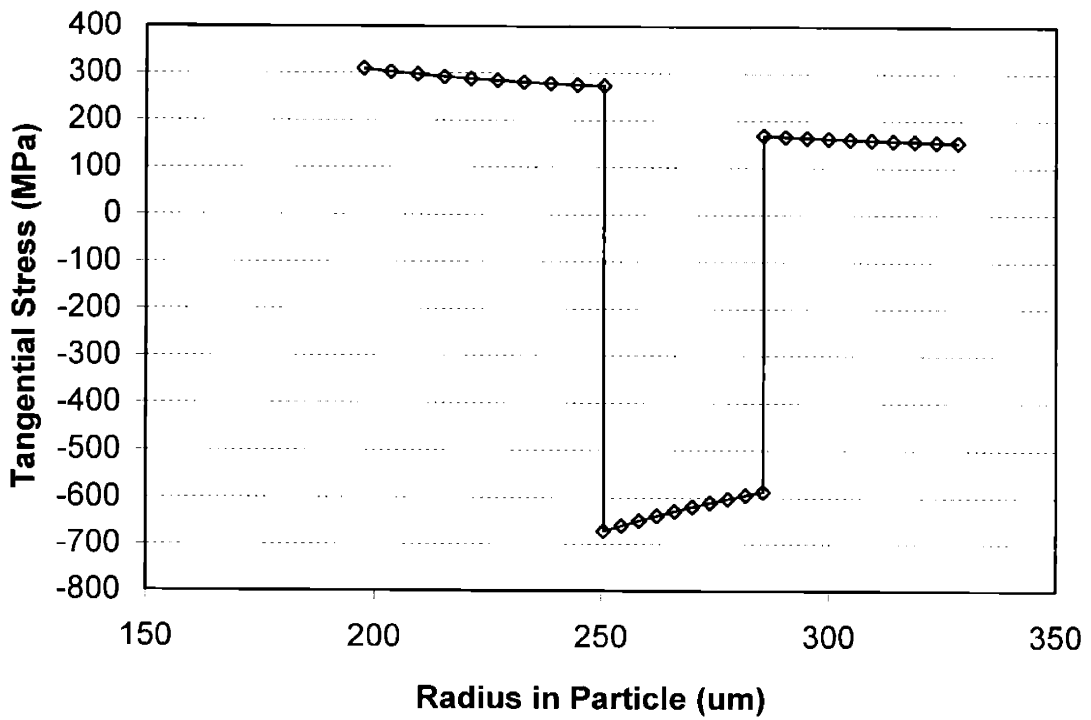
Figure 2-33. Tangential stress distribution in Type 1 particle at fluence of $0.9 \times 10^{21} \text{n/cm}^2$ (symbols for clarity)
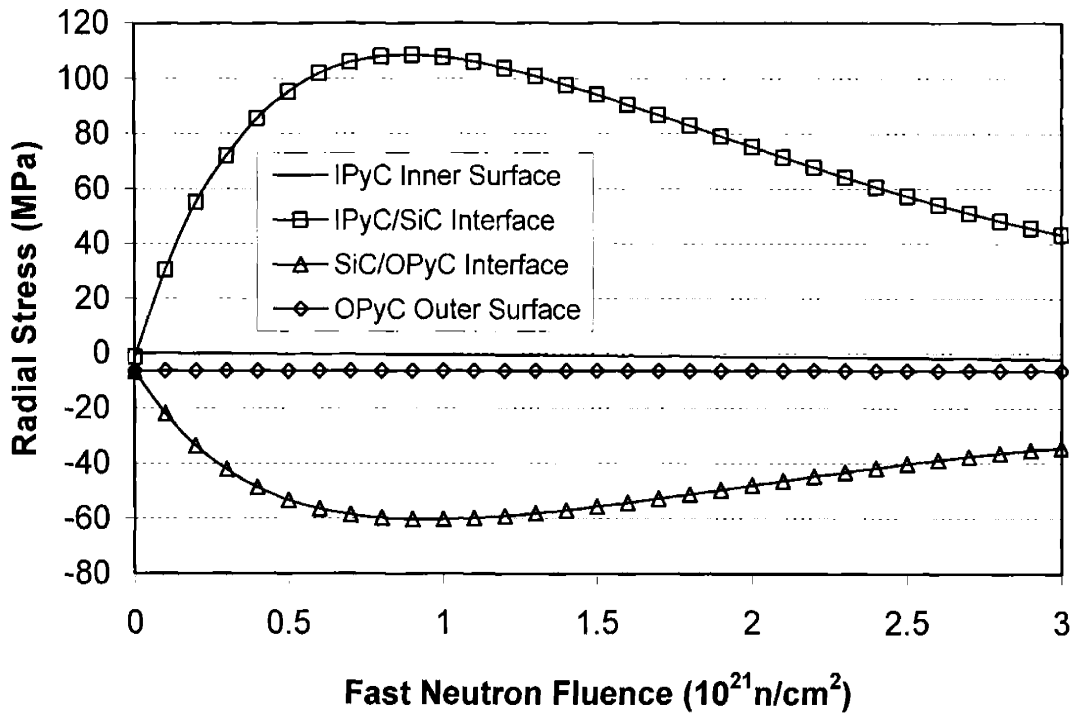
Figure 2-34. Radial stress history in Type 1 particle (symbols for clarity)
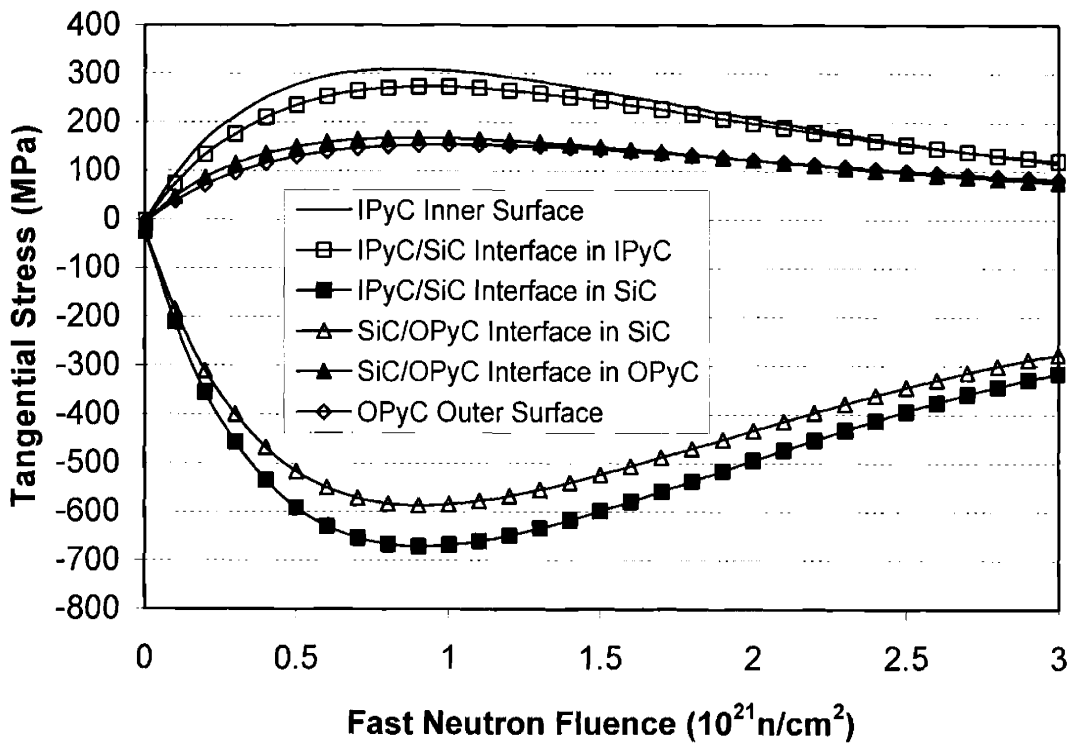
Figure 2-35. Tangential stress history in Type 1 particle (symbols for clarity)

91
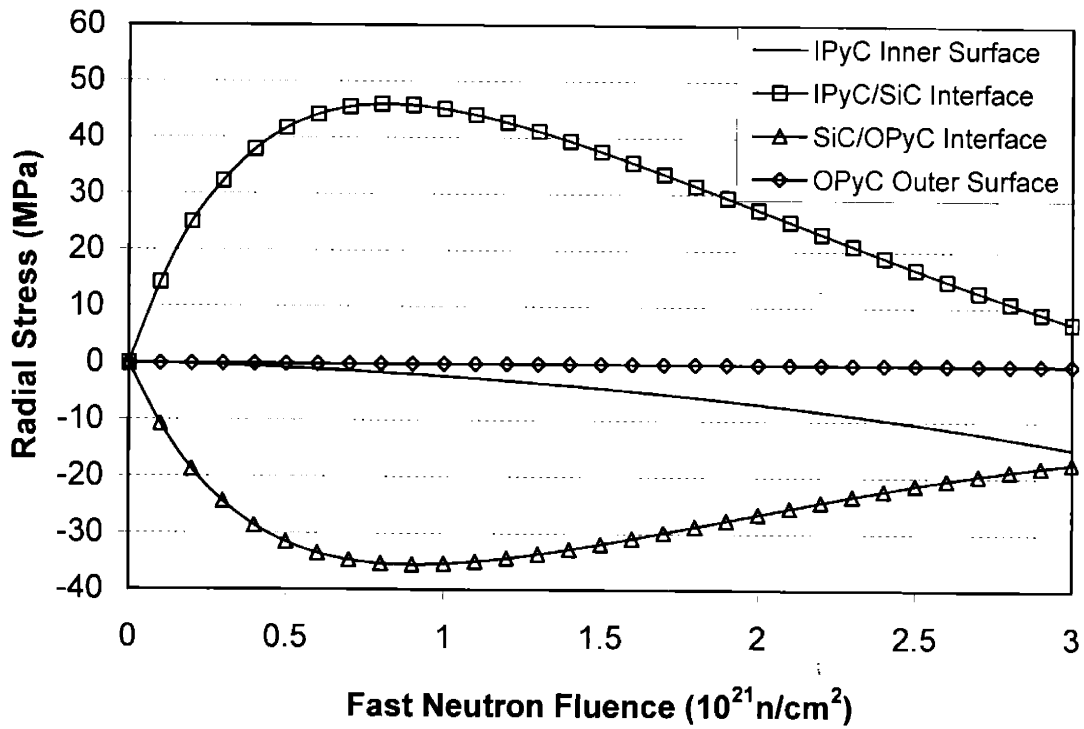
Figure 2-36. Radial stress history in Type 2 particle (symbols for clarity)
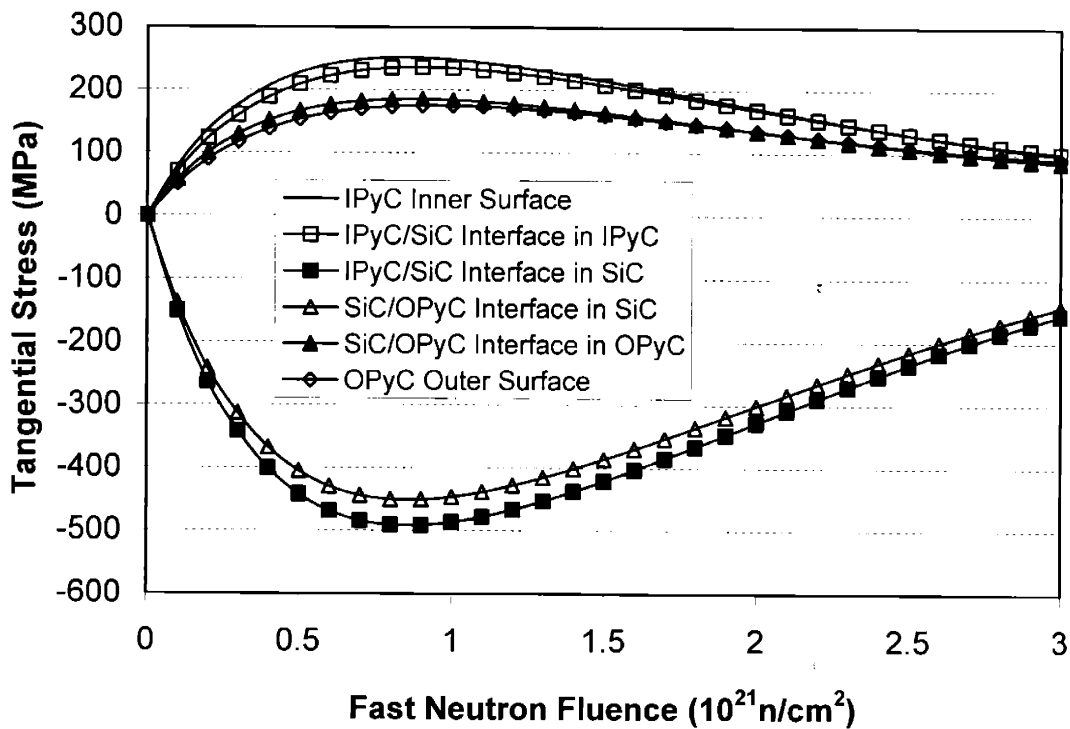
Figure 2-37. Tangential stress history in Type 2 particle (symbols for clarity)
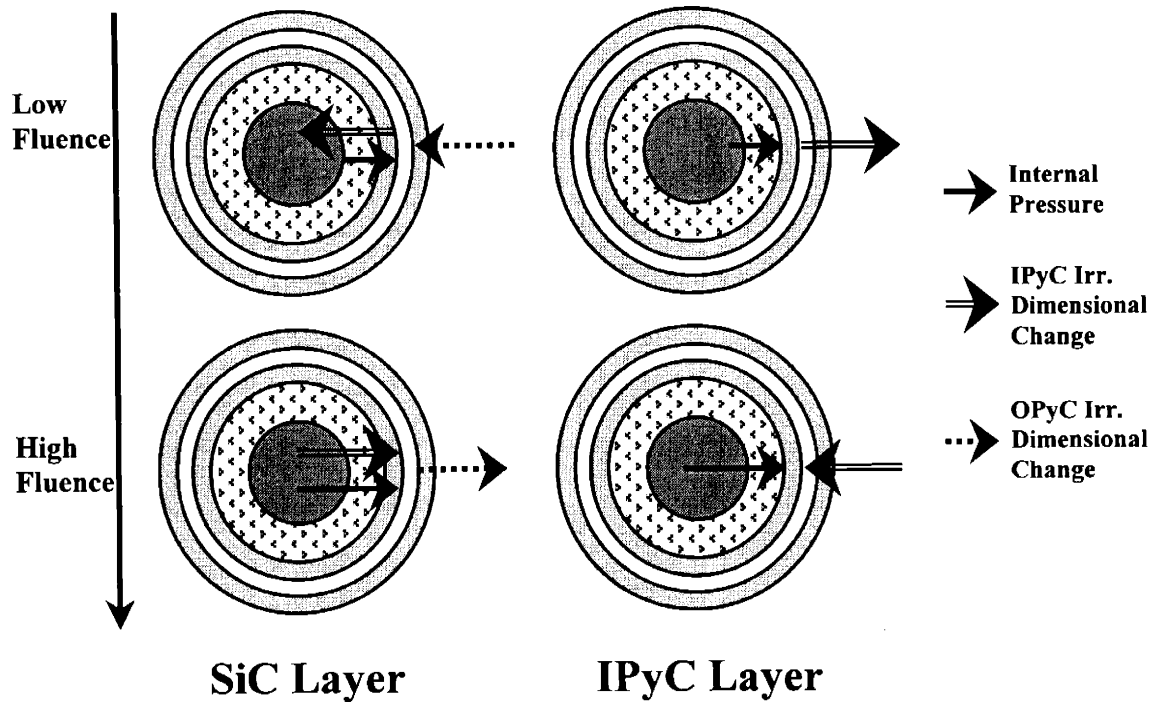
Figure 2-38. Schematic of some stress contributors in a coated fuel particle

(1) In the radial direction, the stress at the inner surface of IPyC layer is equal to the internal pressure from fission gases, as we discussed in Section 2.2, and the stress at outer surface of OPyC layer is equal to the ambient or external pressure provided by the packing of fuel elements. The radial stress profile is continuous due to the equality of action and reaction forces. We see from Figure 2-25 that pyrocarbon shrinks in both radial and tangential directions at the early stage of irradiation but silicon carbide does not, so IPyC layer tends to depart from SiC layer and induces tension in itself, and the shrinkage of OPyC layer is resisted by the presence of high modulus SiC layer which produces radial compression in OPyC layer, as we can see with the help of Figure 2-38. In the SiC layer, the stress changes from high tension at IPyC/SiC interface sharply to high compression at SiC/OPyC interface. The whole stress distribution is like the one shown in Figure 2-32. At very high radiation dose, if pyrocarbon turns into net expansion, the stress condition is reversed.

(2) In the tangential direction, we observe high tensile stresses in the IPyC and OPyC layer and high compressive stresses in the SiC layer, as shown in Figure 2-33. The tangential stresses are discontinuous at the two interfaces of structural layers. There is

no continuity requirement for the tangential stresses, and they are balanced by the radial stresses and the gradient of radial stresses, as can be concluded from the equations of equilibrium in Appendix A. Because the Young's modulus of SiC is one order of magnitude bigger than of PyC, we can think of SiC layer as being rigid for simplicity. At early stage of irradiation, the IPyC layer shrinks down to a smaller radius to find a new relaxed state, but the SiC layer holds it back to its original position. This radius increasing force creates tension in the IPyC layer. Similarly, the SiC layer pushes the OPyC layer outward and thus puts tension in it. The reaction of these forces is that the IPyC layer pulls inward on the SiC layer and the OPyC layer presses on the SiC layer so that the compression in the SiC layer is tremendous. At high fluence and burnup, the reverse process of PyC dimensional changes can put the SiC layer into tension. Meanwhile, internal pressure will act in the same direction to create tension in the particle. It should be noted that the tangential stresses in each layer is fairly uniform. Therefore, an average stress is a good estimate of tangential stress state. We also notice that the tensile stress in the OPyC layer is generally lower than in the IPyC layer if they are of the same material properties.

Now instead of looking at the cross-sectional information of stresses, we examine the evolution of stresses. Figure 2-34 and Figure 2-35 show the radial and tangential stress histories of a Type 1 particle. Typically stresses are intensified up to a fluence of about $1 \times 10^{21} n/cm^2$ and then relaxed, so there is a peak stress point around that fluence level. The quick rising of stresses is due to pyrocarbon shrinkage, and the gradual stress relaxation is the result of pyrocarbon radially turning around, pyrocarbon creep, and internal pressure. It is seemly counter-intuitive that the internal pressure is a stress relaxing factor. Again we give the explanation with the aid of Figure 2-38. We already know the high stresses, either tensile or compressive, in layers mainly come from the strain mismatch of PyC and SiC. In the upper left drawing of Figure 2-38, internal pressure pushes the IPyC layer in the direction which the SiC layer wants it to go, in other words, mitigates the separation potential between IPyC and SiC layer. This is clearly demonstrated if we also take a look at the stresses of Type 2 particle in Figure 2-36 and Figure 2-37. Type 1 and Type 2 particles have the same density and anisotropy

94

for pyrocarbon and the same irradiation condition, but Type 2 particle has a much bigger fuel kernel which produces more fission gases. From Figure 2-36, we see the internal pressure (radial stress at IPyC inner surface) grows higher than that of a Type 1 particle, which alleviates the stresses in a Type 2 particle. We can then conclude that factors such as high temperature, big fuel kernel, and thin buffer layer which contribute to high internal pressure are favorable at early stage of irradiation from stress point of view. The effects of various parameters on fuel performance will be discussed in great detail in Chapter 4. Another point we want to make is that the SiC layer is a strong shielding layer. From Figure 2-35 and Figure 2-37 we find the tangential stresses in the OPyC layer is essentially unaffected by what is going on inside the SiC layer, and vice versa as we will see later in other studies.

Finally we take a little time to study thermal stresses in Type 1 particle if it experiences a temperature rise of $1000°C$ from $20°C$ to $1020°C$. Suppose the particle is a fresh one, i.e. as-fabricated fuel particle, and the density of IPyC and OPyC layers is $1.9g/cm^3$. According to the formulations of thermal stress presented in Appendix A, we are able to use anisotropic elastic constants of pyrocarbon here. The elastic constants and thermal expansion coefficients are listed in Table 2-21 as a function of BAF_0 for the IPyC and OPyC layers. The values are obtained via the formula and approaches given in Sections 2.4.2 and 2.4.5, and for temperature dependent Young's moduli, we use the values at average temperature of $520°C$. The Young's modulus of SiC turns out to be $398.9GPa$.

Table 2-21. Material Properties of IPyC/OPyC for Thermal Stress Analysis

Property	BAF_0				
	1.0	1.1	1.2	1.3	1.4
E_θ (GPa)	27.40	28.82	30.25	31.67	33.09
E_r (GPa)	27.40	26.13	24.86	23.60	22.33
$\nu_{\theta r}$	0.235	0.251	0.269	0.286	0.301
$\nu_{\theta\theta}$	0.235	0.219	0.204	0.189	0.176
$\nu_{r\theta}$	0.235	0.227	0.221	0.213	0.203
α_θ ($10^{-6}/°C$)	5.56	5.27	5.02	4.78	4.57
α_r ($10^{-6}/°C$)	5.56	6.45	7.29	8.08	8.82

The thermal stresses are plotted in Figure 2-39 and Figure 2-40. Firstly in the case of isotropic pyrocarbon layers and a sudden temperature rise of 1000°C, the magnitude of thermal stresses is about 10% of the overall stresses. Secondly, thermal stresses with positive temperature change generally counteract the overall stresses, if we compare these two figures with Figure 2-32 and Figure 2-33, therefore lower the maximum stresses in layers. Thirdly, we find that as IPyC and OPyC become more and more anisotropic, the thermal stresses in layers tend to reduce and flip over. This is the consequence of self-induced stresses in pyrocarbon layers due to anisotropic thermal expansion and the interaction between SiC and PyC layers. When the PyC layers are isotropic ($\alpha = 5.56 \times 10^{-6}/°C$), they thermally expand more than the SiC layer ($\alpha = 4.9 \times 10^{-6}/°C$). Therefore, the IPyC layer is radially compressed and the OPyC layers is radially stretched, as we see in Figure 2-39. But at BAF_0 of 1.4, if we look at the IPyC layer alone, it tried to expand more radially than tangentially, as a result, it is self-stressed with radial restriction and tangential stretch and the resultant thermal expansion could be less than that of the SiC layer, which causes the flipping of the whole interaction situation.
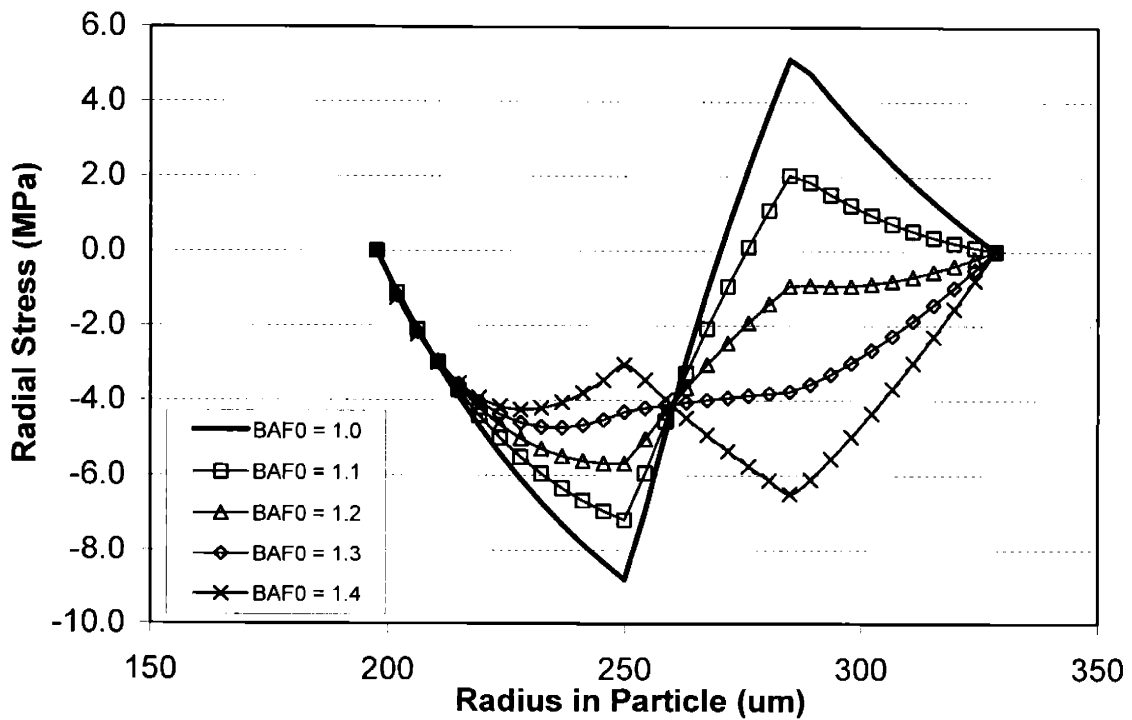
Figure 2-39. Radial thermal stress distribution in Type 1 particle with ΔT of 1000°C (symbols for clarity)
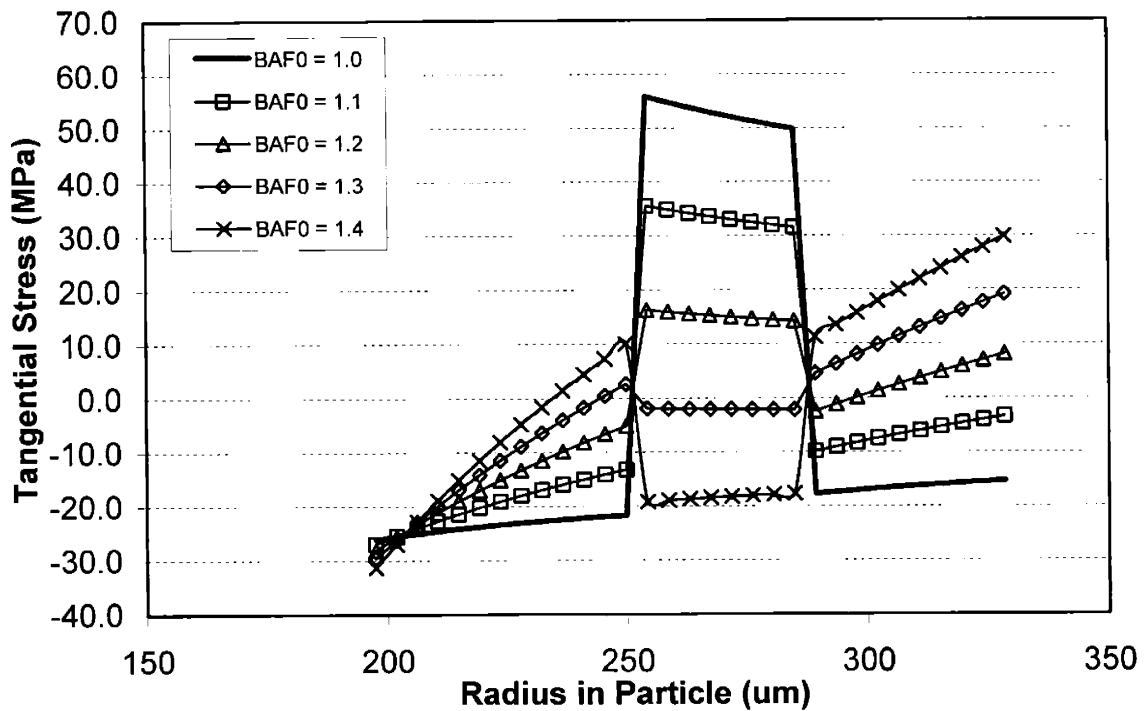
Figure 2-40. Tangential thermal stress distribution in Type 1 particle with ΔT of 1000°C (symbols for clarity)

2.5. Mechanical Fuel Failure Model

2.5.1. Pressure Vessel Model and Weibull Strength Theory

In Chapter 1, we have reviewed the coated fuel particle failure mechanisms. The most popular mechanical fuel failure model that everyone has been using is the pressure vessel model. Its idea is fairly simple as the evaluation of pressure vessel failure. When the internal pressure in a pressure vessel is high enough so that the induced tensile stress in the wall of the vessel exceeds its fracture strength, the rupture of the wall will occur. Here for coated fuel particles, this model works in conjunction with the Weibull strength theory.

The Weibull statistical strength theory is established based on the weakest link hypothesis, which says the weakest link in a structure determines the strength of it. The idea is that when there is a population of flaws in a material, their sizes are likely to fall

into a certain statistical distribution which is characterized by some material properties or parameters, and such distribution implies a distribution of strengths. Weibull theory is used to link the probability of incipient failure to the relative position of stress state on that strength distribution. The conventional form of the two parameter Weibull strength theory if assuming volume flaws is as follows [74][75]

$$P_f = 1 - \exp\left[-\int\left(\frac{\sigma}{\sigma_0}\right)^\beta dV\right],$$ (2.87)

where

P_f is the probability of incipient failure,

σ is the distributed uniaxial stress (MPa),

σ_0 is characteristic strength (MPa.m$^{3/\beta}$), and

β is Weibull modulus.

This theory has been quite successful in predicting the strengths of brittle materials [76]. The flaw types that the theory can treat include volume, surface, and edge flows, but usually volume flaws are assumed for fuel particle coatings because data are not sufficient for other types. Weibull theory does not consider slow crack growth and propagation, and that is why incipient failure is specified and it is suitable for brittle materials in which catastrophic failure occur.

When there are mutliaxial stresses, the principle of independent action [77] is used with Weibull theory to give

$$P_s(\sigma_1, \sigma_2, \sigma_3) = 1 - P_f = P_s(\sigma_1)P_s(\sigma_2)P_s(\sigma_3),$$ (2.88)

where P_s is the probability of survival, and σ_1, σ_2, σ_3 are principal stresses.

Another thing we need to address is that Weibull theory is applicable when microscopic cracks or flaws prevail, but if there is a macroscopic crack created previously or intentionally introduced such as in fracture mechanics test specimen, it is not applicable any more because the special crack does not obey the distribution of flaw sizes. In that case we must consider fracture mechanics for solutions, which is exactly what the crack induced fuel failure model, developed in this research, is based on.

The characteristic strength is apparently dependent on structural properties such as porosity and grain size. The strength of a brittle material is known to depend negative

exponentially on porosity according to Ryshkewith [78] and Duckworth [79], and on the inverse square root of grain size based on the studies of Orowan [80], Petch [81], and Knudsen [82].

2.5.1.1. Weibull Strengths of Pyrolytic Carbon and Silicon Carbide

(1) Pyrolytic Carbon

Based on the three-point bend strength test data from Kaae [47], regression analysis on Weibull modulus was performed by Ho [37] with respect to BAF_0 to get

$$\beta = 10.1 - 0.587 BAF_0,$$ (2.89)

which accounted for 83% of the variance in data. β is not sensitive to BAF_0, at least for the nearly isotropic pyrocarbons we encounter as structural coatings of fuel particles, so for practical purpose, it is assumed that

$$\beta = 9.5,$$ (2.90)

independent of other parameters, including irradiation temperature and neutron fluence.

Similarly, the relationship of σ_0 to BAF_0 at ρ of $1.9 g/cm^3$ is obtained by Ho [37] as

$$\sigma_0(\rho = 1.9) = 154.46 BAF_0^2 - 141.1 BAF_0 \ (MPa.m^{3/9.5}), \text{ when } \beta = 9.5,$$ (2.91)

which accounted for 96.4% of the variance. This relationship is based on the BAF_0 range of 1.007 to 1.041 in [47]. The strength remains constant in the density range of 1.8 to $2.0 g/cm^3$, and decreases when the density is less than $1.8 g/cm^3$ [48]. The following density dependence is obtained,

$$\sigma_0 = \sigma_0(\rho = 1.9), \qquad\qquad 1.8 \leq \rho \leq 2.0 g/cm^3,$$ (2.92)

$$\sigma_0 = (1.241\rho - 1.234)\sigma_0(\rho = 1.9), \quad 1.1 \leq \rho < 1.8 g/cm^3,$$

$$\sigma_0 = (0.644\rho - 0.577)\sigma_0(\rho = 1.9), \quad 1.0 < \rho < 1.1 g/cm^3,$$

$$\sigma_0 = 0.0667\sigma_0(\rho = 1.9), \qquad\qquad \rho = 1.0 g/cm^3.$$

The dependence of characteristic strength on temperature and irradiation is assumed to be related to the corresponding dependence of Young's modulus by

$$\frac{\sigma_{0i}}{\sigma_0} = \left(\frac{E_i}{E}\right)^{1/2},$$ (2.93)

according to the assumption of constant strain energy at failure.

In modeling practice, it is not very convenient to use characteristic strength due to its special dimension. When dealing with individual particles, we prefer to use fracture strength that can be compared to stresses directly. Unlike the characteristic strength, the fracture strength depends on the volume and stress state of a component, so it is not a property. The fracture strength σ_f is defined by

$$P_f = 1 - \exp\left[-\left(\frac{\sigma}{\sigma_f}\right)^\beta\right],$$

(2.94)

so in multiaxial stress state, from eqs. (2.87), (2.88), and (2.94) we get

$$\left(\frac{\sigma}{\sigma_f}\right)^\beta = 2\int\left(\frac{\sigma_\theta}{\sigma_0}\right)^\beta dV + \int\left(\frac{\sigma_r}{\sigma_0}\right)^\beta dV,$$

(2.95)

where σ_r and σ_θ are stresses in radial and tangential directions in certain layer, respectively. Generally we omit the radial component term because the average radial stress in layers is much lower than the tangential stresses as shown in Figure 2-32, so the contribution to the above equation is small. We then substitute σ with $\overline{\sigma}_\theta$ in the above equation and derive

$$\sigma_f = \frac{\sigma_0 \cdot \overline{\sigma}_\theta}{\left(2\int\sigma_\theta{}^\beta dV\right)^{1/\beta}}.$$

(2.96)

If the stresses are uniform in a layer, then we have a simpler form of

$$\sigma_f = \frac{\sigma_0}{(2V)^{1/\beta}}.$$

(2.97)

We take a Type 2 particle as given in Table 2-20, assume uniform stresses in each layer, and calculate the strengths of its IPyC and OPyC layers. The results are shown in Figure 2-41. Here the IPyC strength is slightly higher than the OPyC strength because the OPyC layer has a larger volume, which provides more probability of including a larger flaw. We see that the strength rises quickly with BAF_0, which is reasonable because better alignment of graphite crystallites inherits higher strength from the strong covalent bonds of in-plane direction in graphite. The dependence on BAF_0 may not be able to extrapolate to BAF_0 of 1.2 as in Figure 2-41, but it should be applicable when BAF_0 is below 1.1.
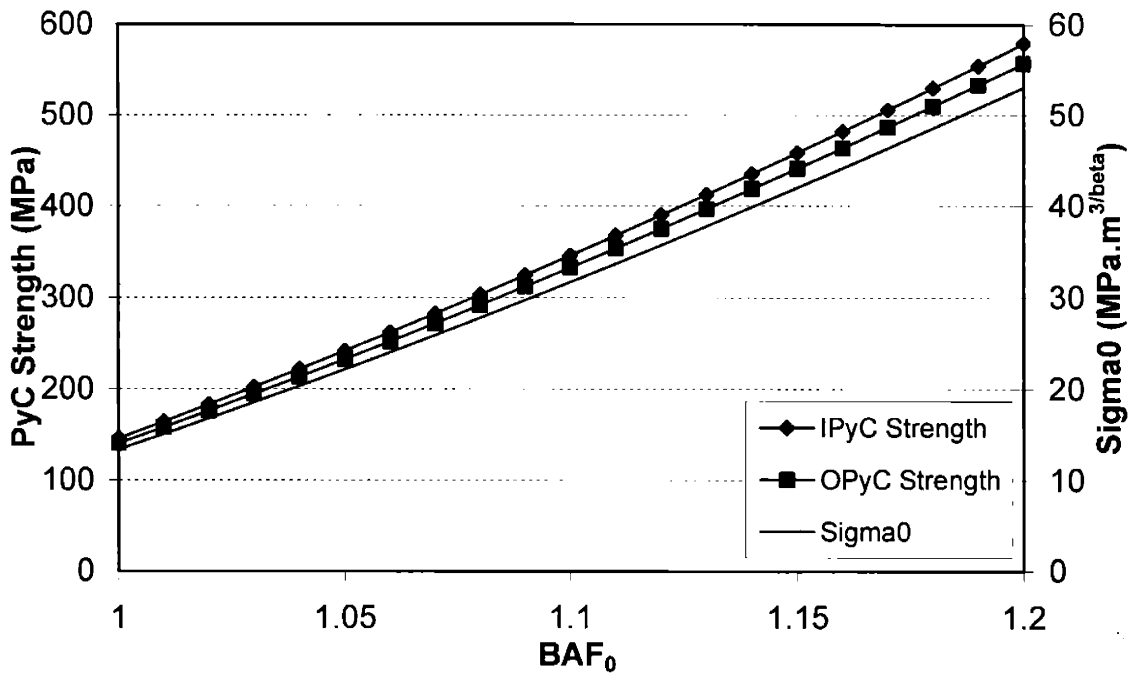
Figure 2-41. The strength of PyC layers in Type 2 particle at room temperature and zero fluence (symbols for clarity)

(2) Silicon Carbide

For silicon carbide, a Weibull modulus β of 6 is recommended by Ho [37] based on data from Evans (3 to 8) [83], Briggs et al. (6.6 to 8.4) [84], Bongartz et al. (4 to 9.4) [54], Bullock (9) [85], Ketterer (5.4 ± 0.8) [86], and Nemeth et al. (6.6) [87]. High temperature SiC strength data from Gulden [52] and Yavuz and Tressler [56] indicated that the strength variation measured by Weibull modulus is not dependent on test temperature up to about 1250°C, so a constant value of β is assumed in this work.

For a β of 6, the characteristic strength of SiC is given by [37]

$$\sigma_0 = 9.64 MPa \cdot m^{3/\beta} .$$
(2.98)

Due to the discrepancy in data with varying temperature and irradiation conditions, the temperature and irradiation effects on characteristic strength of SiC is not considered.

101

2.5.2. Crack Induced Fuel Failure Model (CIFM)

Failure of a coated fuel particle occurs when all three structural layers of it are failed. In Figure 2-35, we see that tensile stresses in IPyC and OPyC layers may be high enough to fail these two layers, and the pressure vessel failure model is able to capture that. However, the SiC layer is in compression most of the time, and pressure vessel failure will not occur. Yet, experiments showed whole particle failures which were not accounted for by the pressure vessel model and Weibull theory. One typical example is the irradiation program for the New Production-Modular High Temperature Gas Cooled Reactor (NP-MHTGR) conducted in early 1990s [88]. In the 1980s, the United States and Germany began to exchange information on techniques for fuel fabrication and fuel performance modeling for gas reactors. The U.S. fuel performance models were assessed based on the German performance database, and at that time it was believed that all the fuel manufacturing problems had been corrected and U.S. could make high-quality fuel like the German fuel which had shown superior performance. Three capsules called NPR1, NPR2, and NPR1A were made and believed basically to be the same as the German fuel. However, from the 221,136 particles in the three NPR capsules that were irradiated, about 700 particles failed at fairly early stage of irradiation, which amounted to 0.32% of the irradiated particles. The U.S. fuel performance models, based on the pressure vessel failure model, predicted no failures in any of the capsules. Although closer examination of NPR fuel and German fuel revealed differences in the fabrication and irradiation of the two types of fuel which affect the strength and layer interaction of the particle [89], it is certain that the pressure vessel model misses something. In fact, it was stated in [88] that the most probable of the causes was mechanical failure of the SiC layer induced by the concentration of tensile stresses in the SiC in the vicinity of cracks in the IPyC layer. In compact metallography, IPyC failures were observed without SiC failures, but all through-wall cracks in the SiC were found to be in the vicinity of IPyC cracks, as shown in Figure 2-42.

It was not until recently that people began to model this phenomenon. G. Miller et al. [90] used a finite element method to calculate the maximum principal stress in the SiC layer at the tip of a preset through-IPyC crack. The stress turned out to be tensile and was

fed into the Weibull theory to predict SiC failure probability. However, this approach has some problems. Firstly, the crack tip stresses are very sensitive to the type of finite elements and mesh size. Actually special finite elements are needed for the crack tip [91] - [93], but the authors didn't specify in their paper whether such treatment was given. Secondly, to initiate failure, stress not only needs to exceed the critical stress of the material but also needs to span enough number of grains, so using the maximum stress at one point is not very convincing. Thirdly, as discussed before, Weibull statistical theory is not applicable in this case. These problems are exactly what a fracture mechanics approach could solve. Therefore, in the model developed here, we use fracture mechanics to model the failure induced by pyrocarbon cracks.
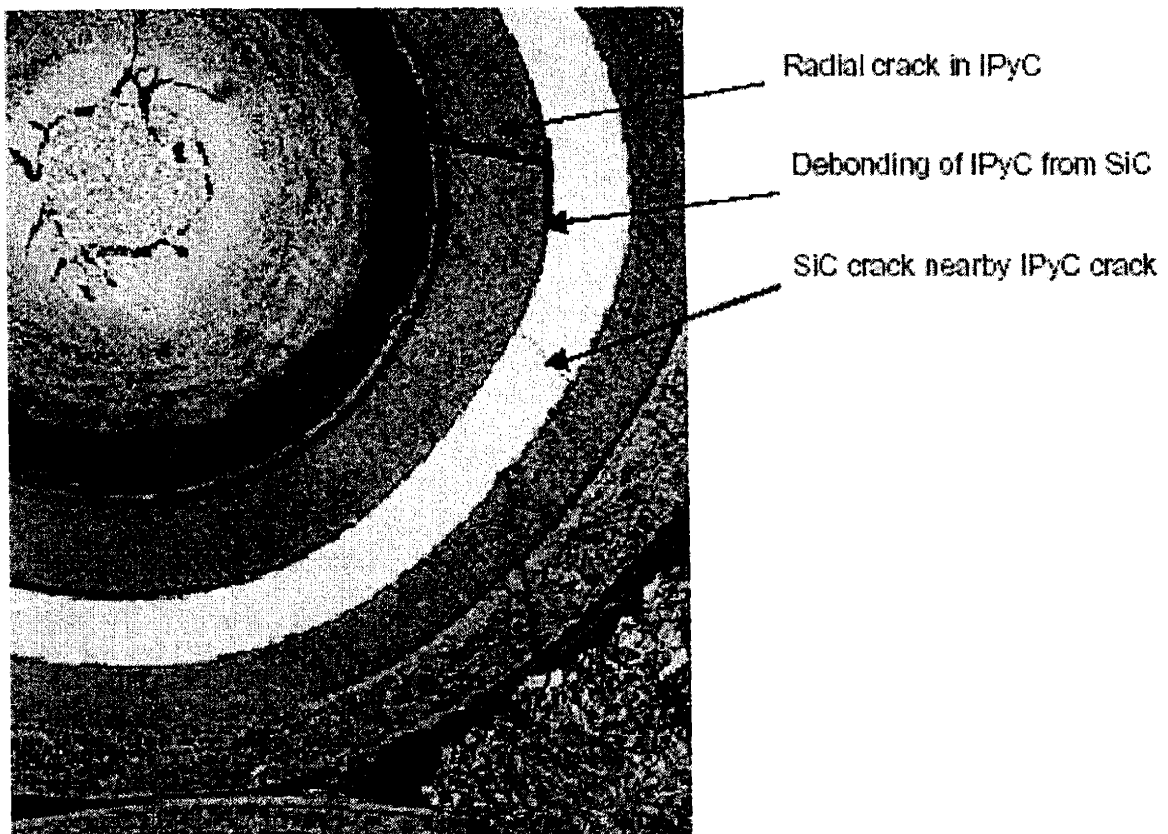
Figure 2-42. Radial cracks in the SiC layer near a crack in the IPyC layer (from Hobbins [88])

2.5.2.1. Simplified Crack Induced Fuel Failure Model
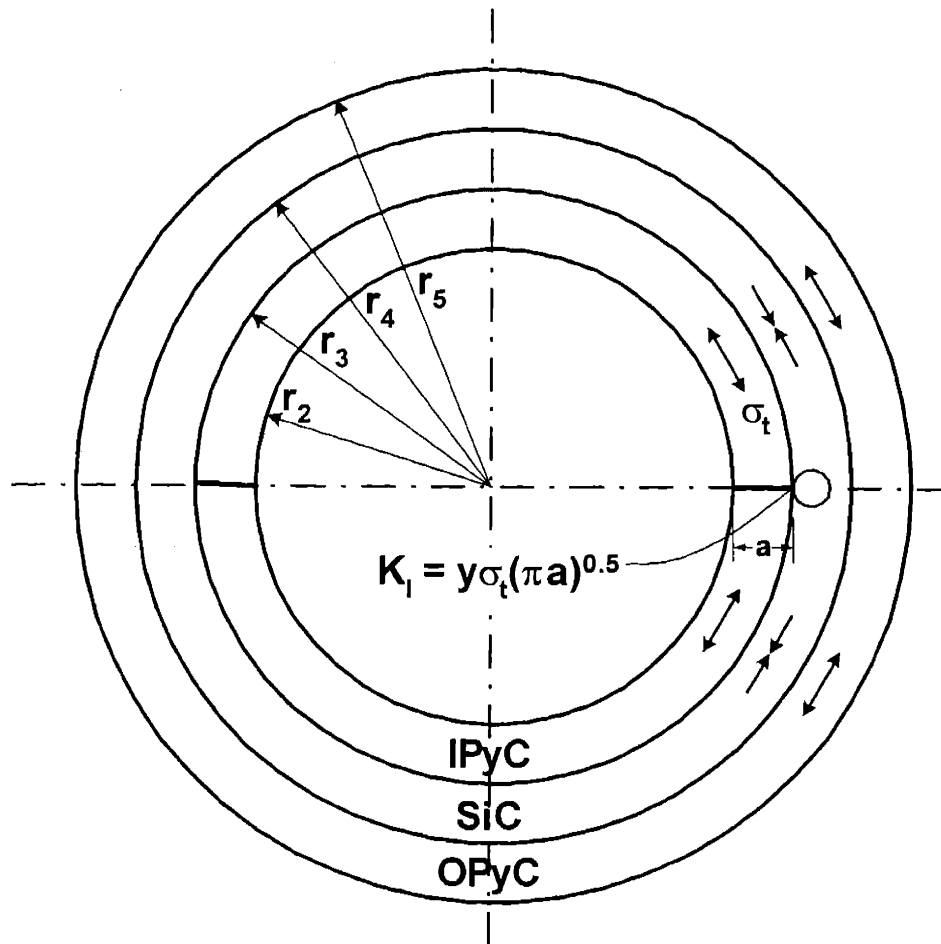
Figure 2-43. Schematic of a coated particle with instantaneous through-IPyC crack

The crack induced failure model is based on the sequential propagation of cracks through pyrocarbon layers and then through the SiC layer. A crack initiated in one of the pyrocarbon layers induces a local stress concentration in the SiC layer. If the local stress concentrator results in a value of crack tip stress intensity that exceeds the fracture toughness of the SiC layer then failure is assumed to occur. In this section we develop first a simplified failure model based on instantaneous stresses and then extend the model to more realistic conditions.

As a first attempt to model a through-thickness crack in pyrocarbon layers adjacent to the SiC layer, we use linear elastic fracture mechanics (LEFM) with the following simplifications. We denote this model CIFM1. The validity of LEFM is supported by the

fact that brittle materials like pyrocarbon and silicon carbide would rather crack than undergo plastic flow when loads increase to a certain extent. The configuration of a particle with an instantaneous through-IPyC crack is shown in Figure 2-43.

(1) We use the IPyC layer for example. Suppose that stresses induced by internal pressure and pyrocarbon shrinkage result in the failure of the IPyC layer, which is captured by the pressure vessel failure model. Then we assume a radial crack is formed due to high tangential stresses and propagates catastrophically through the IPyC thickness and circumferentially until it forms a cracked ring as shown in the figure. Fracture in brittle materials and some particle micrographs support the view that nothing will stop the cracking in the circumferential direction. The first simplification in this initial model is that we do not to allow stress relaxation and redistribution after initial PyC cracking though cracking consumes strain energy and the IPyC layer loses its strength as a structural layer. This treatment alone would overestimate the stress concentration and the overall particle failure probability.

(2) Secondly, the evaluation of stress concentration due to IPyC crack is instantaneous. That is to say IPyC cracking is like a spike to the SiC layer. If the spike does not break the SiC layer, it will not happen later and we no longer keep track of this particle. This obviously cut off the failures of the SiC layer after IPyC failure, and will underestimate the overall particle failure probability.

(3) At a crack tip, a stress singularity exists and the stress is not an appropriate indicator. The stress intensity factor K is a measurement of stress concentration around a crack tip in fracture mechanics, and for the opening mode (mode I) with which the load is perpendicular to the crack surface, the associated stress intensity factor is called K_I, given by [94]

$$K_I = y\sigma\sqrt{\pi a},$$
(2.99)

as the one shown in Figure 2-43. In this formula, a is the crack length, σ is the far-field stress and y is a shape factor modified by the structure and configuration of the cracked body. K_I has an interesting dimension of $MPa.(\mu m)^{1/2}$.

In a layered structure like the coated fuel particle where materials have elastic mismatch, the expression of K_I will be much more complicated. Also the spherical

shape will add corrections. In this version of crack induced fuel failure model, we use the simplest form of eq. (2.99) with y equal to 1.

(4) When the SiC layer is failed by IPyC or OPyC cracking, it is assumed that the remaining PyC layer is also failed subsequent to crack propagation from the SiC layer. Therefore with this model, the predicted overall particle failure probability will be the same as the predicted SiC layer failure probability.

To evaluate this type of fuel failure, we compare mode I stress intensity factor K_I with fracture toughness K_{IC} of silicon carbide, which quantifies the material's resistance to fracture. K_{IC} will be discussed below in Section 2.5.2.3. If K_I is greater than K_{IC}, then SiC layer is cracked catastrophically at the same time of PyC cracking. One detail of the calculation of K_I is that due to the compressive stress in the SiC layer, we add a correction as

$$K_I = \sigma_t(PyC)\sqrt{\pi a} + \sigma_t(SiC)\sqrt{\pi c},$$

(2.100)

where c is an inherent surface flaw size of the SiC layer. Evans et al. [83] showed that internal flaws in SiC coatings are pores less than 0.5μm in diameter, but scanning electron microscopy shows the largest flaws are nodular irregularities at the surface, which in profile resemble surface cracks with a microscopically sharp tip. These flaws are up to 20μm deep. In actual fuel particles the SiC layer is only about 35μm thick, so the average surface flaw size should be much smaller. Gulden [52] found that the grains in CVD SiC are generally columnar, and their diameters range from 1μm to 15μm depending on deposition temperature. Below deposition temperature of 1600°C, the grain diameter is less than 4μm. If we assume the surface flaw size is comparable to the grain size, the average value of c is estimated to be 1 ~ 2μm.

2.5.2.2. Improved Crack Induced Fuel Failure Model

The development of simplified and improved crack induced fuel failure models reflects the path we take to deal with this type of failure. We call the improved model CIFM2. After the formulation and some exercise that will be shown in Section 3.2.2, we

want to seek solutions closer to the physics of crack growth and propagation in layered structures. First of all let's look at Figure 2-44 taken from Hutchinson and Suo [95].
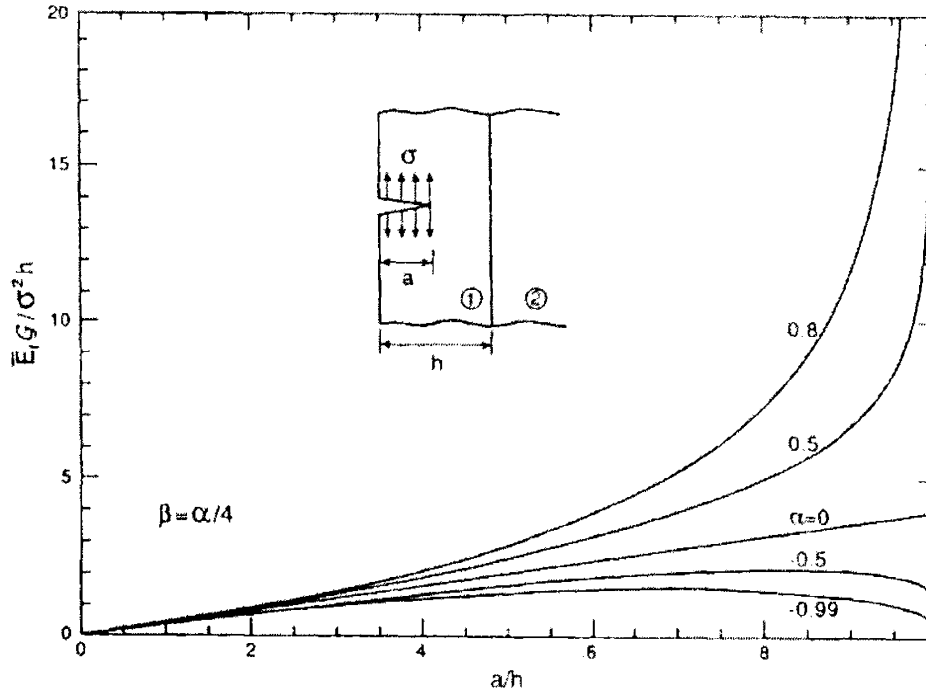
Figure 2-44. Driving force available for an edge crack at various depths a/h (from Hutchinson and Suo [95])

The figure plots the strain energy release rate G (driving force) of an edge crack in material 1 of a bi-material configuration. Two parameters called Dundurs elastic mismatch parameters [96] need to be introduced. The parameter α measures the mismatch in the plane tensile modulus across the interface of two materials, and is given by

$$\alpha = \frac{G_1(\kappa_2 + 1) - G_2(\kappa_1 + 1)}{G_1(\kappa_2 + 1) + G_2(\kappa_1 + 1)},$$ (2.101)

where

G_1 and G_2 are the shear moduli of material 1 and 2, respectively,

$\kappa = 3 - 4v$ for plane strain and $\kappa = (3 - v)/(1 + v)$ for plane stress.

The parameter β measures the mismatch in the in-plane bulk modulus, and is given by

$$\beta = \frac{G_1(\kappa_2 - 1) - G_2(\kappa_1 - 1)}{G_1(\kappa_2 + 1) + G_2(\kappa_1 + 1)}.$$ (2.102)

107
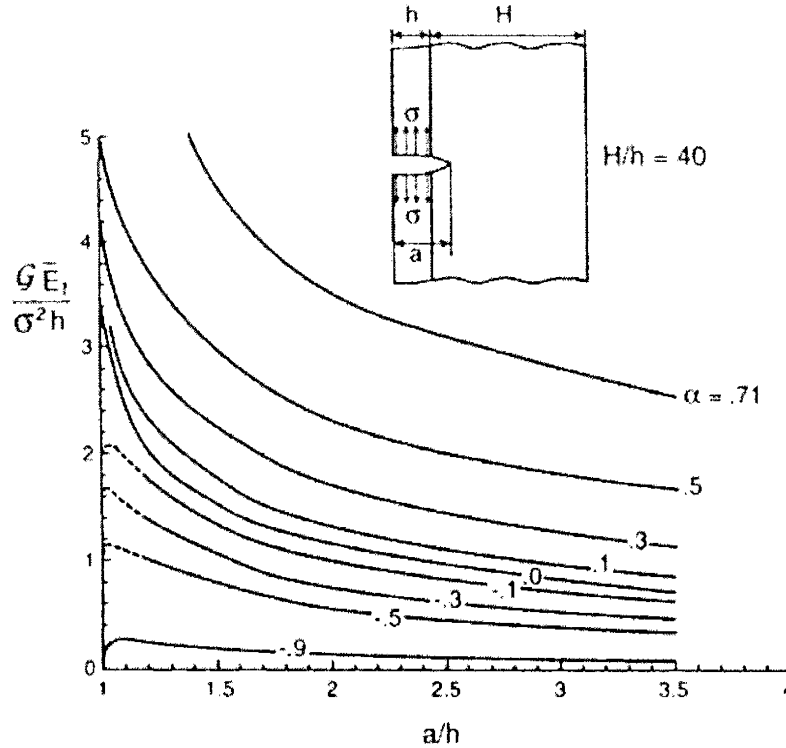
Figure 2-45. Energy release rate for a plane strain crack with the tip in the substrate (from Hutchinson and Suo [95])

Generally if material 1 is harder (higher Young's modulus) than material 2, α is positive; otherwise, α is negative. In our case if material 1 is pyrocarbon and material 2 is silicon carbide, then typical values of α and β are -0.847 and -0.202, respectively, indicating silicon carbide is much harder than pyrocarbon. Looking at Figure 2-44, we see that as the crack approaches the interface of PyC and SiC, the driving force plummets when a is about 99% of the thickness of the PyC layer, which means the crack stops right before it penetrates the entire PyC layer. It would thus appear that the driving force for crack propagation would drop to zero and the crack would stop just before the interface. However, in this case other mechanisms act to allow for further crack advance to the interface. Due to creep crack growth [94] and fatigue loading from environment temperature variation, the remaining small ligament could be broken, and the main crack connects to the surface flaws we have talked about in the SiC layer. Figure 2-45 gives the energy release rate for this scenario. When this happens, the driving force rises again and crack propagation in the SiC layer is made possible. Other scenarios may be possible depending on the magnitude of driving forces. For example, the radial crack in the IPyC

layer may deflect and cause debonding of the interface, and then kink into the SiC layer at another location, as shown in Figure 2-42. Such possibilities will be discussed in Chapter 6 and is beyond the scope of this thesis.

Knowing the above described picture of crack growth and comparing it with the simplified crack failure model CIFM1, we make the following improvements.

(1) Since we know that crack propagation is not instantaneous, we allow for stress relaxation due to crack growth in a PyC layer and stress redistribution because the boundary condition changes when the PyC layer loses its structural strength. The details of estimating stresses in the cracked PyC layer and the stress analysis for intact layers under various boundary conditions are given in Appendix A.

(2) If the cracked PyC layer is tightly bonded to the SiC layer, further irradiation may cause the stress in the cracked layer to rise. So even if the SiC layer is not failed by PyC cracking, failure could occur due to the presence of the crack and higher concentration of stresses as irradiation proceeds. This effect is now included in CIFM2.

(3) Lastly, we implement a better calculation of the stress intensity factor. We find solutions for a cylinder with a crack ring, which is thought to be the closest case to the cracked particle layer, from Tada et al. [97]. For the IPyC layer, the \crack is initiated from its inner surface, then we have

$$K_I(IPyC) = 0.413 \frac{1 + r_2/r_3}{\sqrt{1 - a/(r_3 - r_2)}} \bar{\sigma}_{\theta\theta}^P (r_{IPyC}) \sqrt{\pi a_{IPyC}} , \qquad (2.103)$$

where $\bar{\sigma}_{\theta\theta}^P$ is the average resulting stress in IPyC layer after cracking, and the other variables are shown in Appendix A.

For the OPyC layer, the crack is initiated from its outer surface, then we have

$$K_I(OPyC) = 0.413 \frac{1 + r_5/r_4}{\sqrt{1 - a/(r_5 - r_4)}} \bar{\sigma}_{\theta\theta}^P (r_{OPyC}) \sqrt{\pi a_{OPyC}} . \qquad (2.104)$$

Notice that eqs. (2.103) and (2.104) are for crack tips in the cracked PyC layers, when the IPyC crack joins a surface flaw of the SiC layer, the contribution to the tip of the surface flaw is

$$K_I(IPyC)\sqrt{c/a_{IPyC}} , \qquad (2.105)$$

because the crack tip stress field is continuous and the stress intensity factor is proportional to the square root of crack length. Finally we add a correction due to compressive stress in the SiC layer, as in eq. (2.100), and get

$$K_I(SiC) = K_I(IPyC)\sqrt{c/a_{IPyC}} + \overline{\sigma}_t(SiC)\sqrt{\pi c} ,$$ (2.106)

for a crack initiated from the IPyC layer, and

$$K_I(SiC) = K_I(OPyC)\sqrt{c/a_{OPyC}} + \overline{\sigma}_t(SiC)\sqrt{\pi c} ,$$ (2.107)

for a crack initiated from the OPyC layer.

The model CIFM2 assumes that small ligament takes no time to break, so as soon as a crack is formed in certain PyC layer and relaxed, it connects to SiC surface flaws. The consequence of this assumption is underestimating the time to failure of particles, as will be seen from simulations of NPR experiements in Section 3.2.

2.5.2.3. Fracture Toughness of Silicon Carbide

Before we collect the data for the fracture toughness of silicon carbide, we want to show the relationship between fracture toughness and fracture energy (surface energy for failure). It is known that the material resistance to crack extension G_C is given by

$$G_C = 2\gamma_f ,$$ (2.108)

where γ_f is the surface energy. Also G_C is linked to K_{IC} by

$$G_C = \frac{K_{IC}^2}{E/(1-v^2)} , \text{ for plane strain condition,}$$ (2.109)

then we get

$$K_{IC} = \sqrt{\frac{2E\gamma_f}{1-v^2}} , \text{ for plane strain condition.}$$ (2.110)

Evans et al. [83] estimated the value of γ_f to be $20J/m^2$ for SiC coatings of fuel particles, and concluded that the value is not affected by temperature up to 1300°C. If we take the interpolated value of 367GPa for E at 1000°C from Table 2-13 and plug numbers into eq. (2.110), we get $3864MPa.\mu m^{1/2}$. The following table is a survey of SiC fracture

energy and fracture toughness. When fracture toughness data are not provided, we use the above relationship to calculate them.

Table 2-22. Fracture Toughness Data for SiC

SiC Type	T (°C)	K_{IC} (MPa.μm$^{1/2}$)	γ_f (J/m^2)	Measurement Method	Comment and Reference
β, polycrystal	23	2800	-	ICS	Slavin & Quinn [98]
CVD, polycrystal	23	3728*	16	AMDCB	// direction, Freiman et al. [99]
CVD, polycrystal	23	4271*	21	AMDCB	⊥ direction, Freiman et al. [99]
-	-	3300	-	-	Morton Adv. Mater. [100]
Polycrystal	23	4716*	25.6	SENB	Simpson [101]
	23	3658*	15.4	DCB	Simpson [101]
Polycrystal	23	4746*	27	SENB	E = 410GPa, McLaren et al. [102]
Polycrystal	23	3610*	15	DCB	Matthews et al. [103]
Polycrystal	23	4168*	20	AMDCB	Rice et al. [104]
Polycrystal	23	4372*	22	AMDCB	Rice et al. [104]
Polycrystal	23	3954*	18	AMDCB	Rice et al. [104]
Polycrystal	23	3100	-	ICS	Evans & Charles [105]
Single crystal	23	3300	-	SENB	Henshall et al. [106]

(*: calculated using eq. (2.110). SENB: Single Edge Notched Beam, AMDCB: Applied Moment Double Cantilever Beam, DCB: Double Cantilever Beam, ICS: Indentation Crack Size)

The values in the table range from 2800 to 4746 MPa.μm$^{1/2}$ at room temperature. If we assume K_{IC} scales as the square root of E as in eq. (2.110), then the data fall into the range of 2600 – 4400 MPa.μm$^{1/2}$ at 1000°C, which is about the average irradiation temperature of the SiC layer. Based on this information, we choose to use K_{IC} = 3500 MPa.μm$^{1/2}$ for the temperature range of interest in HTGRs.

2.5.3. Fuel Particle State Diagram

The pyrocarbon crack induced fuel failure models address the issue that the failure of the entire particle experiences a series of stages (states) which are connected by various

failure events in the structural layers, and the occurance of one state depends on the previous state and what happens at that state. To facilitate the modeling of such failure scenarios, we can borrow the idea of a finite state diagram from electrical engineering and construct a fuel particle state diagram that works closely with our failure models. The diagram is shown in Figure 2-46. Each state in an oval box is associated with some analysis and is monitored by a number of flags.
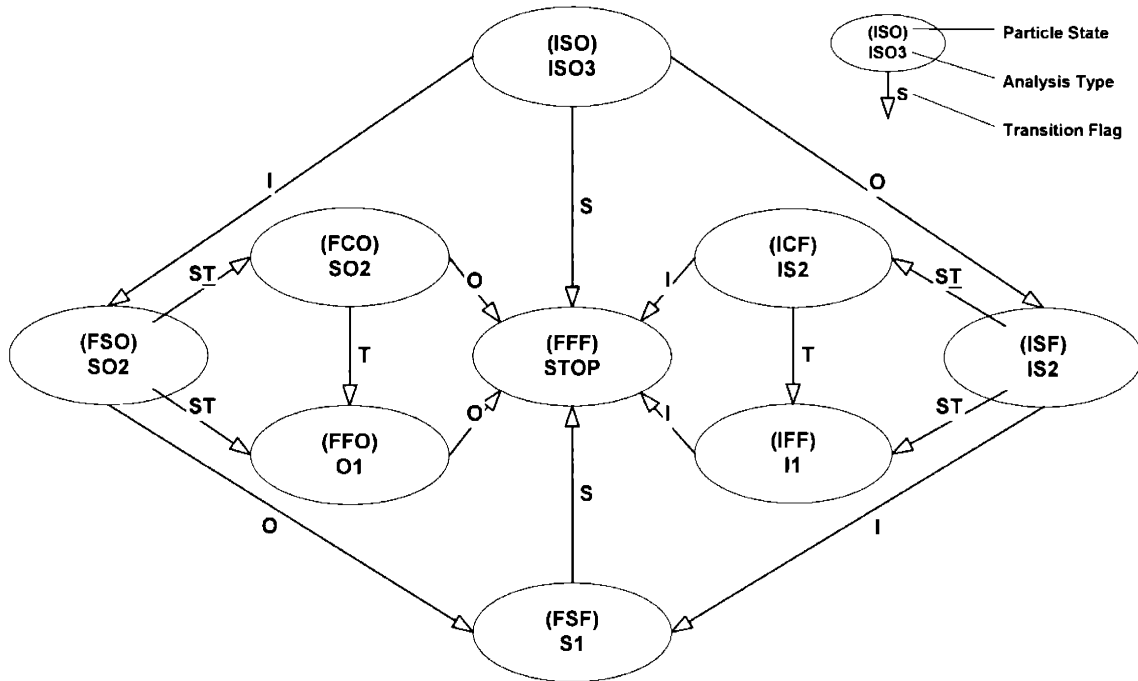
Figure 2-46. Coated fuel particle state diagram

(1) Particle State. The particle state is represented by a three-digit symbol in parenthesis, in the order of IPyC, SiC, and OPyC layer. 'I', 'S', 'O' symbolize the intact state of those layers, respectively. We use 'F' for a mechanically failed layer. We also introduce a symbol 'C' for a cracked but structurally functional layer due to the fact that a cracked layer in compression can behave like an intact layer, which has to be differentiated from a failed layer. From the stress analysis we presented in previous sections, we see that only the SiC layer may fall into this category. For example, (FCO) means the IPyC layer is failed, and the SiC layer is cracked but under compression. (ISO) means all the layers of the particle are fine.

(2) Analysis Type. The whole set of mechanical analyses includes ISO3, IS2, SO2, I1, S1, and O1, which are detailed in Appendix A. ISO3 is the three layer stress analysis.

112

IS2 combines the stress analysis for IPyC and SiC two-layered structure and the stress estimation in failed OPyC layer presented in Appendix B. The remaining analyses are analogous. Right now we don't implement I1 and O1, and we assume when either pyrocarbon layer and the SiC layer are failed, the other pyrocarbon layer is not strong enough to withstand the stresses and hence is also failed. Notice in Figure 2-46 that for the state (FCO) we use analysis SO2, because, as just described, the cracked SiC layer is still able to support the OPyC layer in such a case.

(3) Transition Flag. The flags are by the side of arrows in the figure and are constantly updated by the fuel failure models, both the pressure vessel failure model and the crack induced failure model, during simulations. The flag 'I' (true) indicates the failure of the IPyC layer, and '$\underline{I}$' ('I' is false) indicates the intactness of it. Because of the special 'C' state of the SiC layer, we also introduce a 'T' flag specifically for the SiC layer. 'T' and '$\underline{T}$' stand for tension and compression in the tangential direction of the SiC layer, so (ISF) – S$\underline{T}$ –> (ICF) means the SiC layer is cracked, probably due to stress concentration from OPyC cracking in this case, but the far field stress in SiC is compressive. We omit some implicit flags in Figure 2-46 beside self-pointing arrows for each state. For instance, there should be three flags '$\underline{I}$', '$\underline{S}$' and '$\underline{O}$' for the self-pointing arrow of state (ISO), because when these flags are false, the particle stays at this state.

2.6. Simulation of Refueling Scheme in Pebble Bed Reactors

As discussed at the beginning of this chapter, the analysis requires that we build into the model the capability of simulating the virtual irradiation environment that pebbles and particles would encounter in pebble bed reactor systems. The pebble bed reactor fueling scheme consists of a number of cycles, typically 6-10, where a particular pebble is fed to the top of the core in a random manner. Once the pebble is introduced it will follow a streamline that is defined, to first order, by the location of entry. The core shape can be approximated by a right circular cylinder with a cone-shaped exit region. Fuel pebbles flow through the system in much the same way that sand flows through an hourglass. When a pebble exits the core its burnup and failure status are checked. If the end of life

burnup has not been reached and the pebble contains no failed fuel particles it is recycled to the top of the core where it is introduced once again, as shown in Figure 2-1. However, the ultimate streamline that the pebble follows during a particular pass through the core is independent of the streamline of the previous and subsequent passes. Thus, the actual power history for a particular fuel particle is determined by a random process. Unlike the case of the Light Water Reactor (LWR) where a particular fuel element has a fixed location during each cycle and the fuel manager can shuffle the fuel to optimize performance and reliability, the pebble-bed fueling scheme lacks this flexibility. While from a reliability standpoint it may be advantageous to arrange the exposure such that a fuel element sees a decreasing power density with increased burnup, this is not possible for the pebble-bed reactor. A realistic assessment of pebble-bed fuel reliability thus requires that a fuel performance model be able to accommodate such a fuel management scheme. To do this, the model must have realistic power and neutron flux distributions, which are obtained by running the VSOP code which was developed in Germany for the pebble-bed system [107]. The VSOP code provides power, neutron flux, and burnup distributions as a function of both time and position (both axial and radial) within the pebble-bed core. A pebble (and a selected fuel particle) is randomly re-circulated through the reactor core for the appropriate number of cycles, tracing streamlines determined by the random entry point, thus generating a unique power history for the pebble. At the same time, variables such as neutron fluence, and burnup are accumulated.

Figure 2-47 shows a schematic of the VSOP model for the reactor. The model is a two-dimensional axisymmetric one to represent three-dimensional cylindrical core. Channel 1 is a central graphite reflector. The fuel portion of the model is divided into 4 "channels" (channel 2 to 5) each of which is segmented into 9 to 15 spatial "blocks". Each block is filled with pebbles from 11 "batches", which account for different burnup levels. For example, batch no. 5 consists of pebbles which have passed through the core four times. This mixture of batches in each block accounts for the fact that individual pebbles in a block may have been through the core a different number of cycles. Thus in a steady state core, the space dependent information is provided by the blocks and the time dependent information by batches. VSOP provides power peaking factors, burnup,

114

and fast neutron flux down to the batch level. To obtain the local power within a block, for a given batch of fuel, it is necessary to multiply the core average power by the peaking factor for that batch. To obtain the actual power density for a pebble within a batch (corresponding to a particular burnup) the packing fraction of the pebbles must be taken into consideration. This number is typically about 0.7 in the ideal case but closer to 0.6 in real cases.
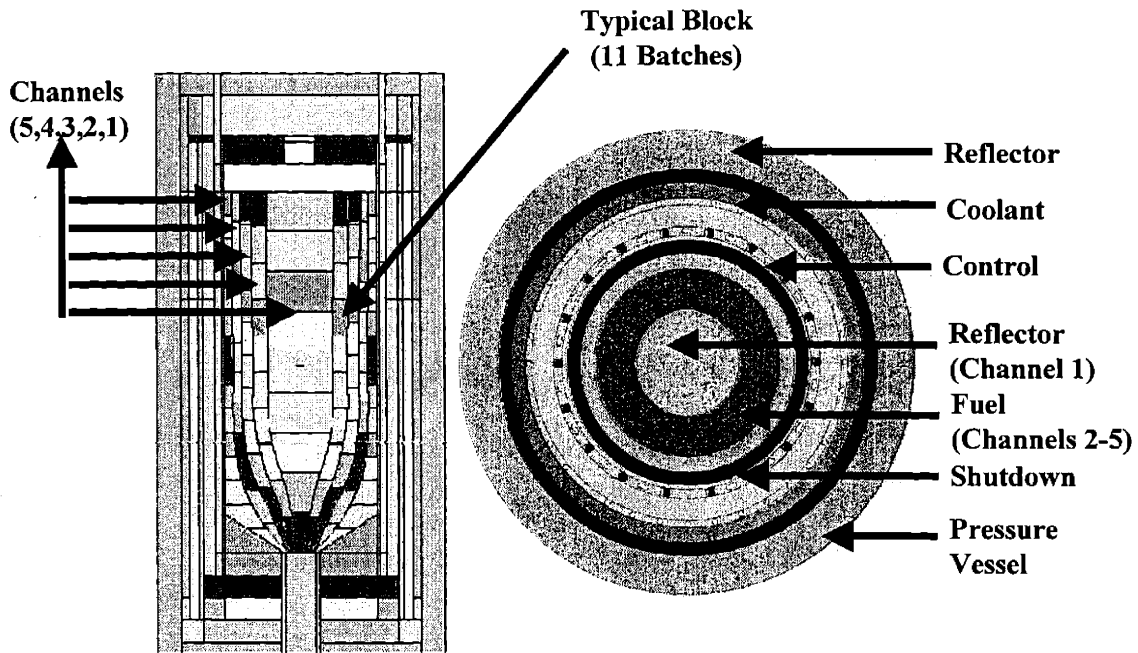
Figure 2-47. VSOP model of a typical pebble bed ractor core

We have obtained two sets of VSOP results on two configurations of pebble bed reactor cores. The first one which we call MPBR1 was shown in Figure 2-47. In this configuration there is a central graphite reflector of about 1.4m in diameter, and a mixing zone modeled by channel 2 of pure graphite pebbles and fuel pebbles is immediately adjacent to the reflector. Only three channels are filled with pure fuel pebbles. In the second configuration which we call MPBR2, the mixing zone is no longer there, and the pebble discharge at the bottom of the core is at a radial position of 1.55m instead of on the central line. The VSOP setup for these two types of cores is shown in Figure 2-48, with the bars marking the positions of blocks.
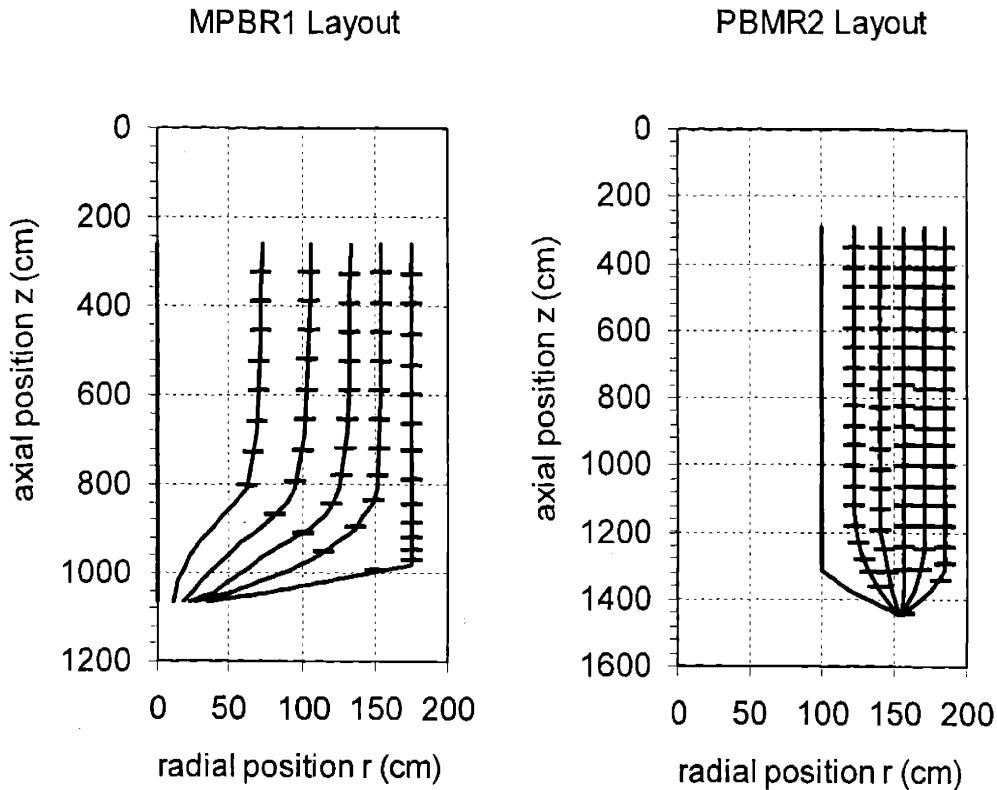
Figure 2-48. VSOP setup of two MPBR cores

Beside the above difference, the specifications of two MPBR cores that VSOP modeled are quite different. They are listed in Table 2-23. Actually the parameters of MPBR1 have already been given in Table 2-8 in the section of thermal model, but here we list them again for comparison purposes.

The power distribution of MPBR2 is shown in Figure 2-49, and the power peaking factor histograms are plotted in Figure 2-50 and Figure 2-51. The power distribution is the volumetric power density in blocks obtained by averaging over 7 batches in blocks. The power peaking factors are down to the batch level. As we have discussed in Section 2.3.3, the high peaking factors in MPBR1 all come from the mixing zone, and they could be an artifact from numerical calculation to find equilibrium of a local position with its surroundings. However, compared with Light Water Reactors, the maximum peaking factor in MPBRs is likely to be higher because of the random introduction of a fresh fuel pebble to a high neutron flux region. Comparing Figure 2-50 to Figure 2-51, we find the

116

peaking factor distribution of MPBR1 is like that of MPBR2 overlapped by a scattering of high peaking factors provided by the mixing zone. However, the shapes of two distributions in the range of 0 – 3 are different due to some reasons.

Table 2-23. Specifications of VSOP Modeled MPBR Cores

Parameter	MPBR1	MPBR2
Core Height (m)	10.0	11.0
Core Radius (m)	1.75	1.85
Thermal Power (MW)	250	400
Coolant	Helium	Helium
Core Inlet Temperature (°C)	450	500
Core Outlet Temperature (°C)	850	900
Average Power Density (MW/m^3)	3.652	4.777
Max. Power Peaking Factor	5.27	2.74
Min. Power Peaking Factor	4.44E-5	2.70E-5
Coolant Mass Flow Rate (kg/s)	118.0	154.6
No. Pebbles in Core	360,000	451,600
No. Particles per Pebble	11,000	15,000
Pebble Cycling Times	10	6
No. VSOP Blocks	57	93
No. VSOP Batches per Block	11 (10 effective*)	7 (6 effective*)
Pebble Fuel Zone Radius (mm)	25.0	25.0
Pebble Radius (mm)	30.0	30.0

(*: one additional batch is added for numerical calculation purpose.)
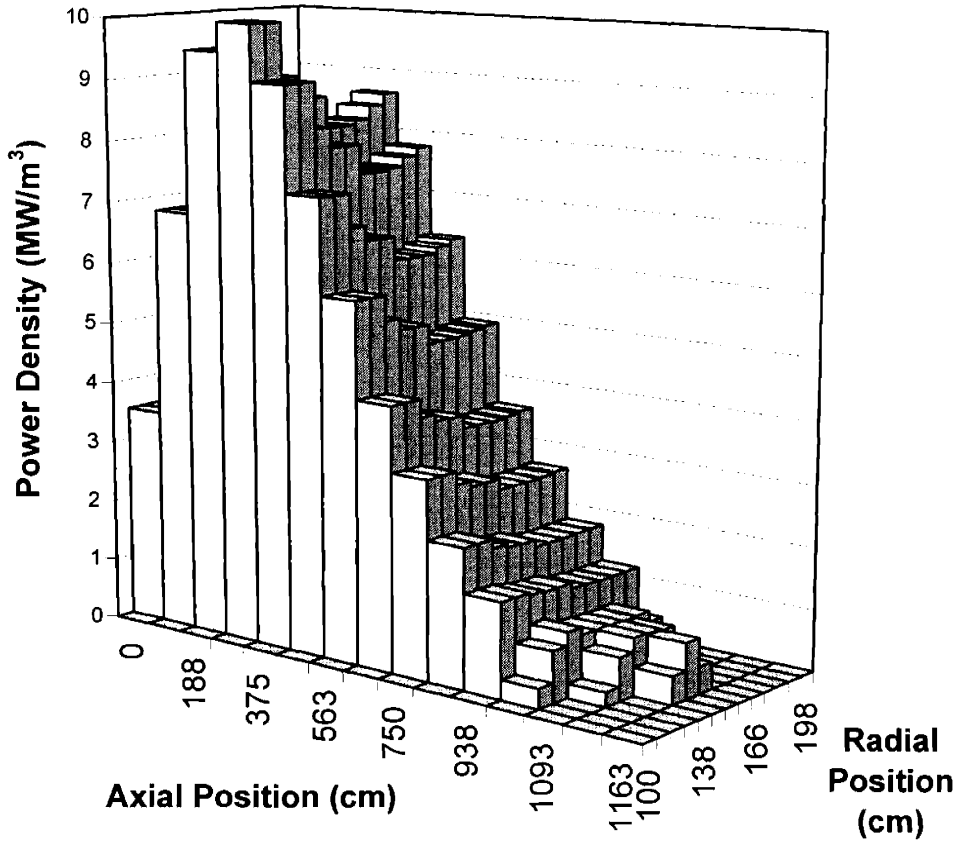
Figure 2-49. VSOP calculated power distribution in MPBR2
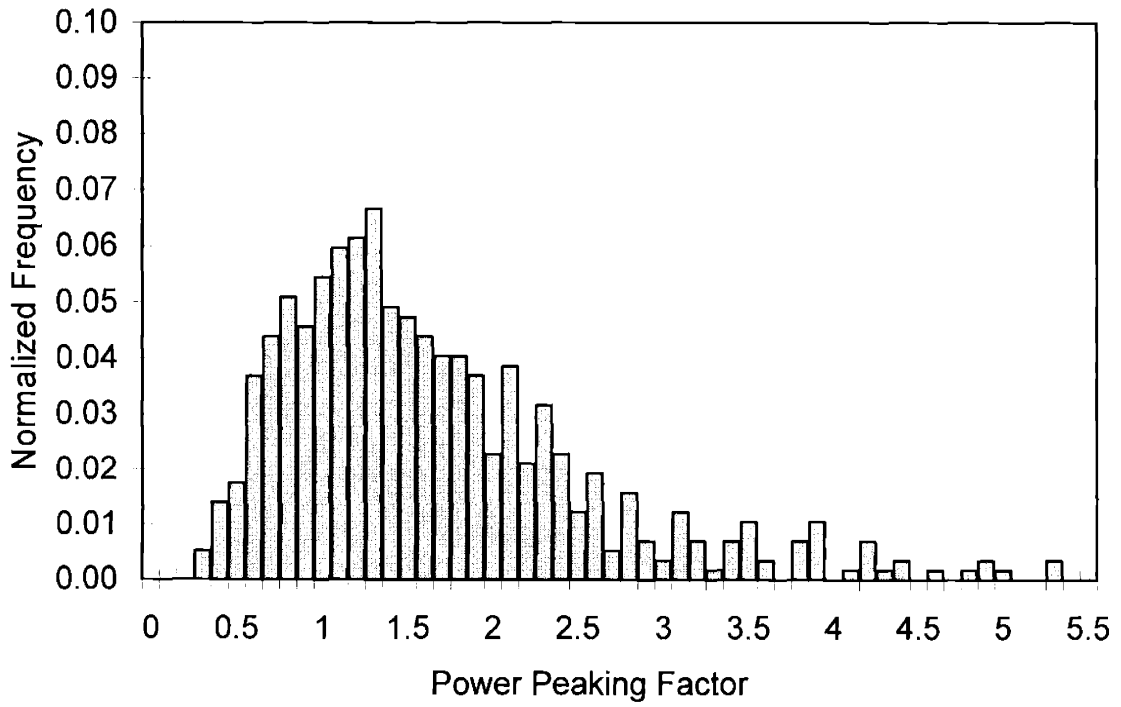
Figure 2-50. VSOP calculated power peaking factor distribution for MPBR1

118
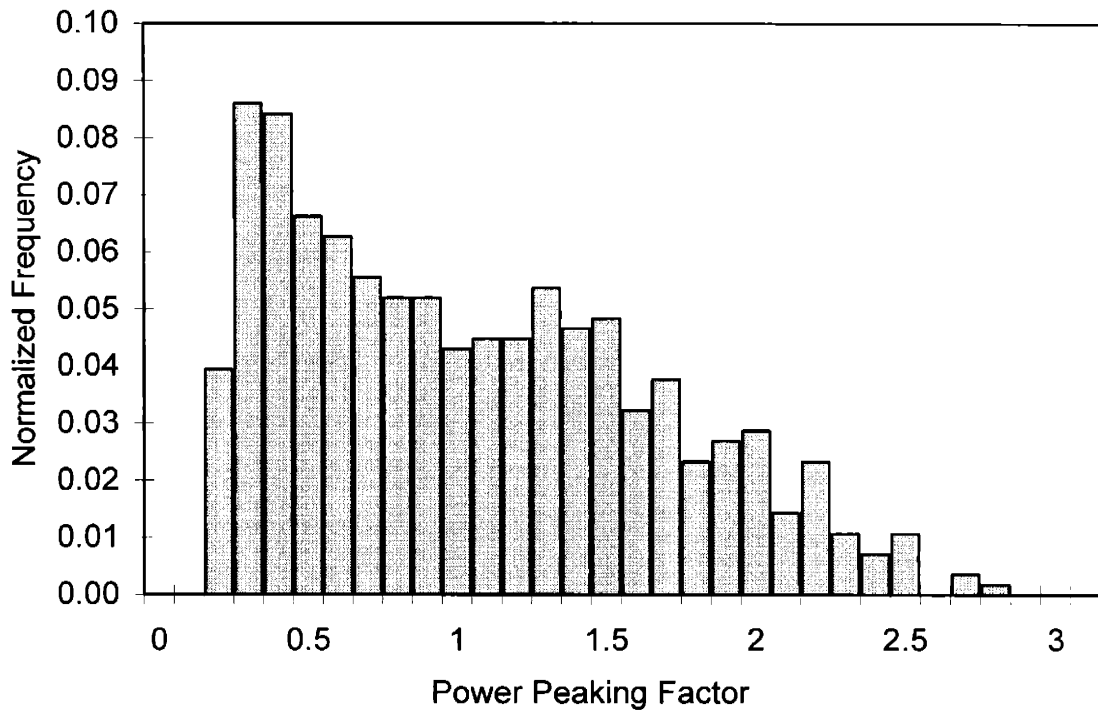
Figure 2-51. VSOP calculated power peaking factor distribution for MPBR2
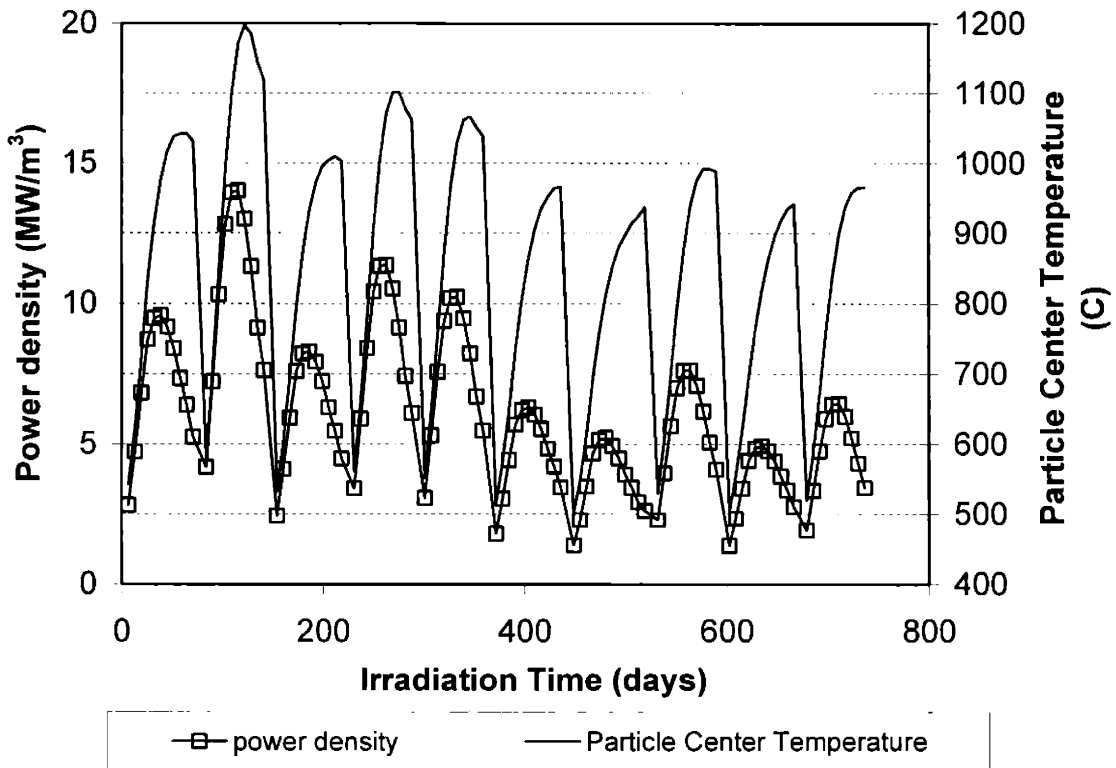
Figure 2-52. A power history and corresponding particle temperature history in MPBR1 (symbols for clarity)

Figure 2-52 shows a sampled power history and the corresponding fuel kernel center temperature history for a Type 2 particle as given in Table 2-20. In a simulation of one million particles, we would get one million power histories like the one in the figure for them. As Figure 2-52 illustrates, the particle experienced ten cycles through MPBR1 core, and the peak power in the particle, while generally decreasing with cycle number due to a reduction in fissionable material, is exposed to a number of cycles where the fuel is "driven" by fresh fuel in the batch. Also, while the average temperature is a generally decreasing function of time, there are cycles where the fuel temperature does not follow this general trend. Such behavior is fundamentally different than what would be the case for a stationary fuel system in a prismatic core and will have a significant effect on fuel reliability.

2.7. Monte Carlo Sampling of Particle Dimensions and Materials Properties

The last piece we need before the particle fuel performance model is fully functional is the Monte Carlo sampling ability. As discussed in Section 1.2, due to the violent coating process in fluidized beds and the small dimensions of coated fuel particles, we could expect variations on particle dimensions and their materials properties among the population of $10^{10} - 10^{11}$ particles in a reactor. Over large samples of this size, the variations can generally be described by some distributions, such as the normal distribution (a.k.a. Gaussian). What this implies is that the model predictions of fuel performance are given in terms of fuel failure probability on a statistically significant set of samples, because we can never be sure whether a specific manufactured fuel particle will fail during operation.

The question is then how many particles we need to sample and where we get the information that describes the distributions. Possibly the most controversial aspect of the pebble bed concept is the contention that the fuel is sufficiently robust to eliminate the need for a containment as it is currently defined for the LWR system. It is argued that the SiC (or ZrC) layer acts as one of the primary boundaries to the release of fission products during an accident. For the SiC layer to serve this purpose the failure probability, among

other requirements, must be less than a value on the order of 1 part in 10^5. As a practical matter, this means that at least a million individual particles for which particle dimensions and properties are assigned by sampling from appropriate distributions should be examined by the model. In the case of LWR fuel it is possible to inspect each fuel pellet to insure that fabrication requirements (enrichment, dimensions, density, etc.) are met. While the outside dimensions of the particles can be checked, the individual layer thickness values, fuel kernel diameter, and layer mechanical and physical properties cannot be individually verified. Complete inspection requires that the particle be destroyed. For this reason, the dimensional data for actual particles will consist of: (1) a distribution of outside diameter values that have been determined by a go, no-go test to insure that the particle outside diameters are between the specified limits and (2) a set of layer dimensional distributions that will have been determined by inspecting a selected number of particles destructively. The distributions of material properties such as densities and BAF_0s are also estimated by inspecting a collection of particles one by one, and it is obvious this collection is much smaller than the number of particles in a reactor core. We have shown in Section 2.5.1.1 that coating material fracture strengths are characterized by the Weibull distribution and the associated parameters are estimated by crushing tests as in references [53] and [84]. For particle dimensions and other material properties, experimental tests generally suggest that a normal distribution apply. But a normal distribution covers the range from $-\infty$ to $+\infty$, which is boundless. We need a choice of finite distributions for a property or characteristic which reflects the fact that, in real life-cases, it is physically impossible for a property or physical characteristic to be outside of some finite range. If one simply uses an unbounded distribution and discards those unaccepted values, the resulting samples will not be normalized and the effect of tails will be overestimated. For this reason we chose bounded triangular distributions for particle dimensions and material properties except for the Weibull strengths of pyrocarbon and SiC. The triangular distribution is both simple and very close to the normal distribution (Gaussian) in terms of data scattering coverage within two standard deviations. For the time being we assume that this is good enough, because the model is not aiming at getting the absolute value of failure probability right, instead, its ultimate goal is to capture that certain type of fuel particles performs better in an application than

others on relative basis. A better distribution, i.e. truncated normalized normal distribution, could be used later as a refinement of the overall model. Nevertheless, we take a little time to discuss the normal distribution.

2.7.1. Normal (Gaussian) Distribution

Many random variables of practical interests obey the normal distribution or at least approximately do. Its probability density function is given by [108]

$$f(x) = \frac{1}{\sqrt{2\pi}\sigma} e^{-\frac{(x-\mu)^2}{2\sigma^2}},$$
(2.111)

where μ is the mean and σ is the standard deviation of the distribution. Figure 2-53 shows the normal distributions of two cases.
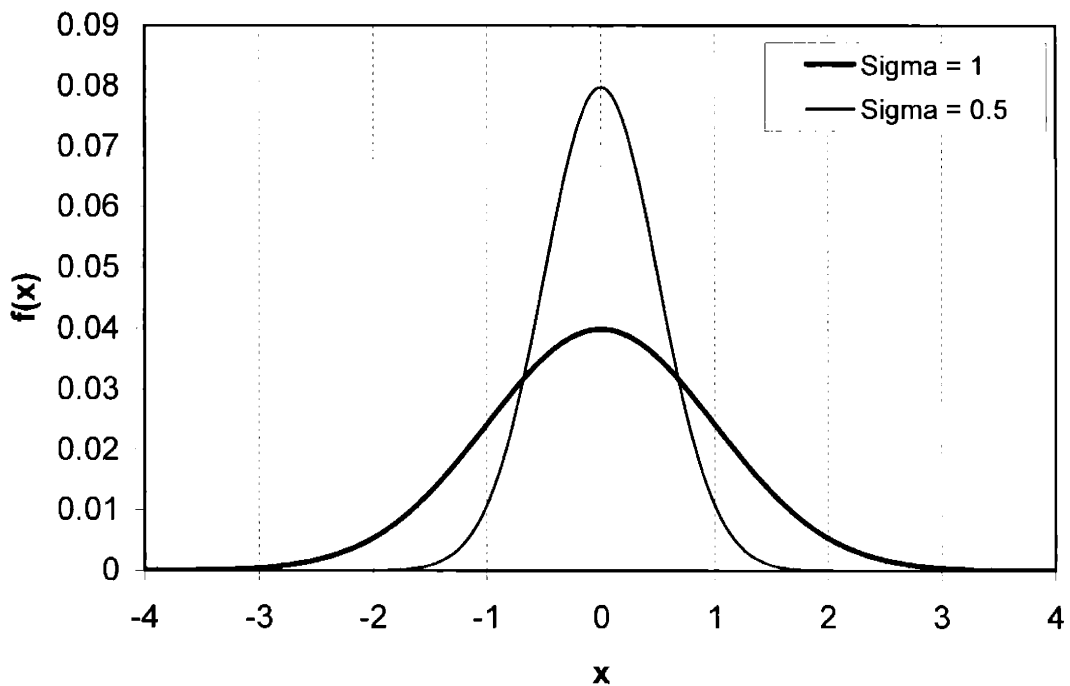
Figure 2-53. Density of the normal distribution with μ of 0 for two values of σ

The normal distribution is symmetric with respect to its mean value and the standard deviation measures its spread. Although the distribution extends from $-\infty$ to $+\infty$, most of the time the variable falls into three standard deviation range from the mean. To run

Monte Carlo sampling on a normal distribution, we need its cumulative distribution function, which is

$$F(x) = \frac{1}{\sqrt{2\pi}\sigma} \int_{-\infty}^{x} e^{-\frac{(s-\mu)^2}{2\sigma^2}} \, ds \,.$$ (2.112)

If we inverse it to get

$$x = F^{-1}(F(x)),$$ (2.113)

and draw uniformly random numbers as F(x) above, it can be shown that the resulting distribution for x is f(x). Since there is no analytical solution for the inversion of eq. (2.112), numerical methods [109] exist to do the sampling of eq. (2.113).

The probability that x falls into the window of (μ - σ, μ + σ) is given by

$$P(\mu - \sigma \le x \le \mu + \sigma) = F(\mu + \sigma) - F(\mu - \sigma) = 68.3\%.$$ (2.114)

Similarly, we can get

$$P(\mu - 2\sigma \le x \le \mu + 2\sigma) = F(\mu + 2\sigma) - F(\mu - 2\sigma) = 95.5\%, \text{ and}$$ (2.115)

$$P(\mu - 3\sigma \le x \le \mu + 3\sigma) = F(\mu + 3\sigma) - F(\mu - 3\sigma) = 99.7\%.$$ (2.116)

According to the normal distribution, a 1,000,000 case sample on fuel kernel diameter with a mean of 500μm and standard deviation of 20μm is shown in Figure 2-54.
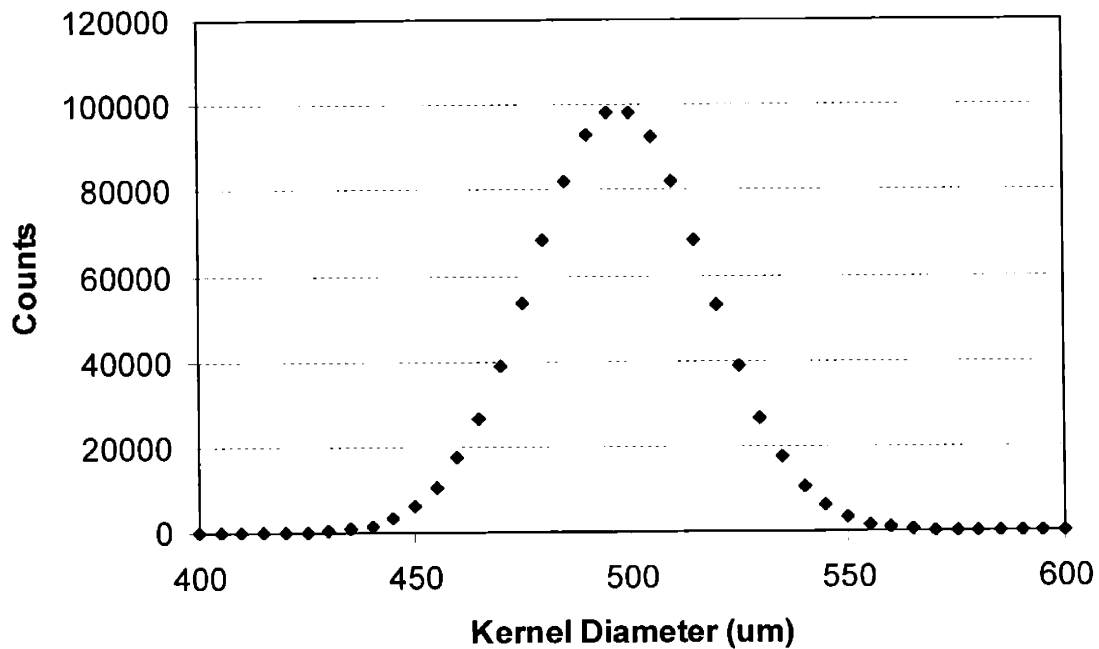
Figure 2-54. Sampling of fuel kernel diameter with μ= 500μm and σ = 20μm

2.7.2. Triangular Distribution

The triangular distribution is given by

$$f(x) = \frac{1}{d^2}(x - \mu + d), \qquad (\mu - d \leq x < \mu),$$

(2.117)

$$f(x) = \frac{1}{d^2}(\mu + d - x), \qquad (\mu \leq x \leq \mu + d).$$

where μ is the mean value and the standard deviation is given by

$$\sigma = \frac{d}{\sqrt{6}}.$$

(2.118)

The cumulative distribution is

$$F(x) = \frac{1}{2d^2}(x - \mu + d)^2, \qquad (\mu - d \leq x < \mu),$$

(2.119)

$$F(x) = 1 - \frac{1}{2d^2}(\mu + d - x)^2, \qquad (\mu \leq x \leq \mu + d).$$

and the inverse of F(x) is

$$x = \mu - d + d\sqrt{2F}, \qquad (0 \leq F \leq 0.5),$$

(2.120)

$$x = \mu + d - d\sqrt{2(1 - F)}, \qquad (0.5 < F \leq 1).$$

As in the normal distribution, F, which is generated by random number generator, is uniformly distributed, then x will fall into a triangular distribution given by eq. (2.117).

It can be calculated that

$$P(\mu - \sigma \leq x \leq \mu + \sigma) = 65.0\%,$$

(2.121)

$$P(\mu - 2\sigma \leq x \leq \mu + 2\sigma) = 96.6\%, \text{ and}$$

(2.122)

$$P(\mu - 3\sigma \leq x \leq \mu + 3\sigma) = 100\%.$$

(2.123)

Now we try a sampling on SiC fracture toughness given in Section 2.5.2.3 with triangular distribution. The mean value is $3500\text{MPa.um}^{1/2}$, and we choose a standard deviation of $530.7\text{MPa.um}^{1/2}$ to safely cover the range of $2200 - 4800\text{MPa.um}^{1/2}$. The result of 1,000,000 cases is shown in Figure 2-55.
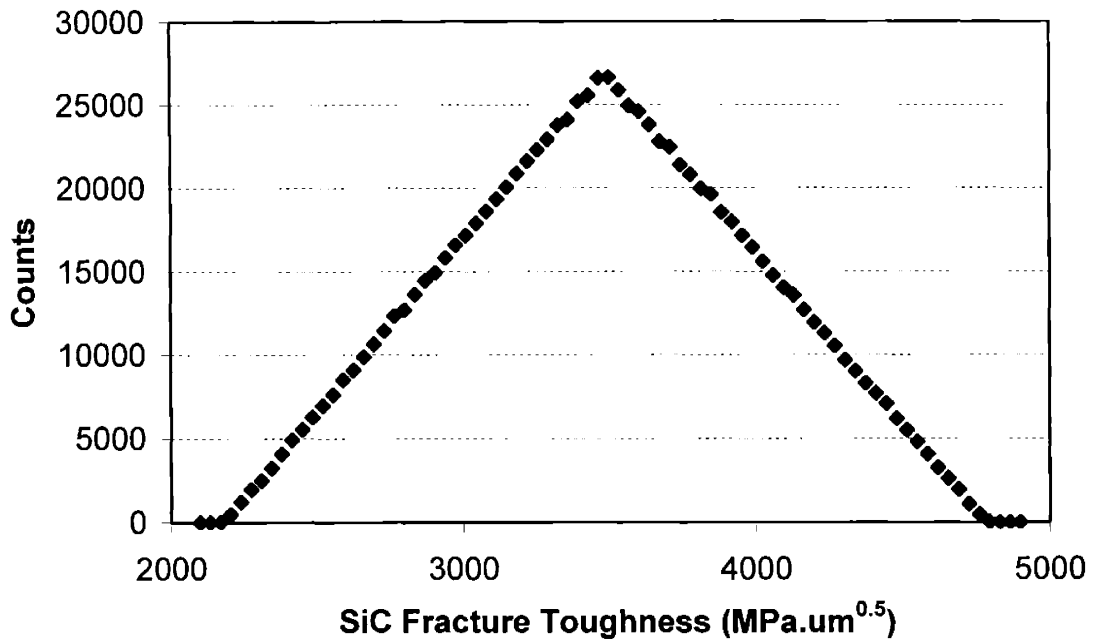
Figure 2-55. Sampling of SiC fracture toughness with μ= 3500MPa.um$^{1/2}$ and σ = 530.7MPa.um$^{1/2}$
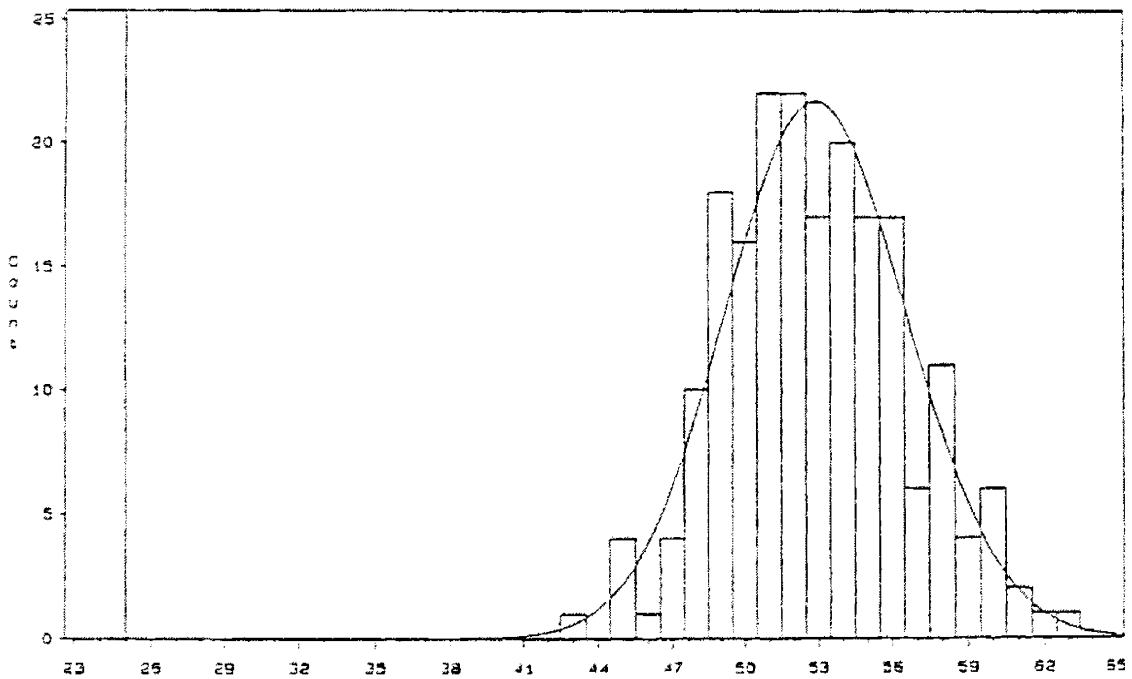
Figure 2-56. Histogram of the measurements on IPyC thickness of NP-MHTGR Performance Test Fuel (from Bryan [110])
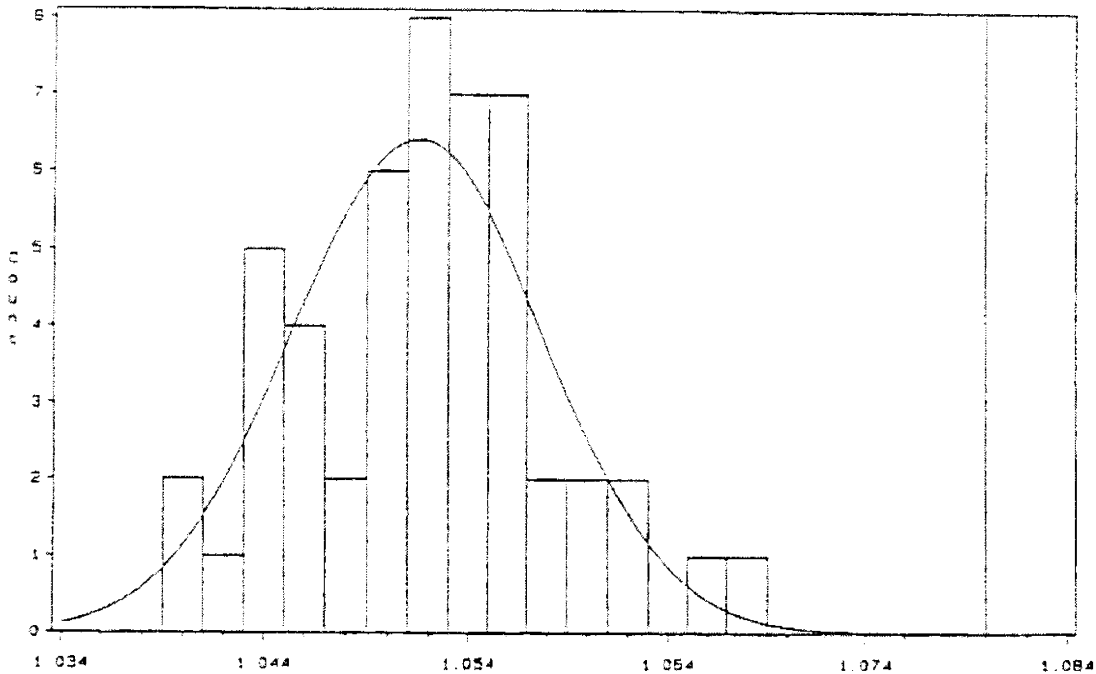
Figure 2-57. Histogram of the measurements on OPyC BAF_0 of NP-MHTGR
Performance Test Fuel (from Bryan [110])

Figure 2-56 gives the measured IPyC thickness from radiographs of 200 NP-MHTGR
Performance Test Fuel particles[1], and Figure 2-57 gives the measured OPyC BAF_0 of 50
particles [110]. The means and standard deviations of IPyC thickness and OPyC BAF_0
are 52.9μm and 3.68μm, and 1.0515 and 0.00622, respectively. The histograms suggest
normal distributions with lower and upper bounds, but applying triangular distribution is
not a bad choice.

2.7.3. Weibull Distribution

The Weibull statistical theory was introduced in Section 2.5.1.1, and here we discuss
how to use it in Monte Carlo sampling. The cumulative Weibull distribution with mean μ
and modulus β is given by

$$C_W(x) = 1 - \exp\left[-\left(\frac{x}{\mu}\right)^\beta\right].$$
(2.124)

---

[1] The New-Production Modular High Temperature Gas Reactor (NP-MHTGR) Performance Test Fuel will
be discussed in Section 3.2.

126

Then eq. (2.124) is inverted to give the variate x as a function of the cumulative distribution:

$$x = \mu \exp\{\log[-\log(1 - C_W)]/\beta\}. \tag{2.125}$$

From eq. (2.125) the Weibull distribution is generated by sampling a uniform distribution for C_W.

Now we choose BAF_0 of 1.05 and density of $1.9g/cm^3$ for pyrocarbon, so the corresponding characteristic strength and Weibull modulus are 22.14 $MPa.m^{3/9.5}$ and 9.5, respectivley, based on the model in Section 2.5.1.1. For SiC, the characteristic strength and Weibull modulus are 9.64 $MPa.m^{3/6}$ and 6, respectively. Then we run Monte Carlo sampling and get the plots in Figure 2-58. It can be seen that Weibull distribution is not symmetric, and it has negative skewness, i.e., bigger tail on the weak side of the distribution. Weibull modulus measures the spread of variables but depends on the mean value. For the same mean value, the higher the modulus is, the narrower the distribution is, as displayed by two curves for SiC.
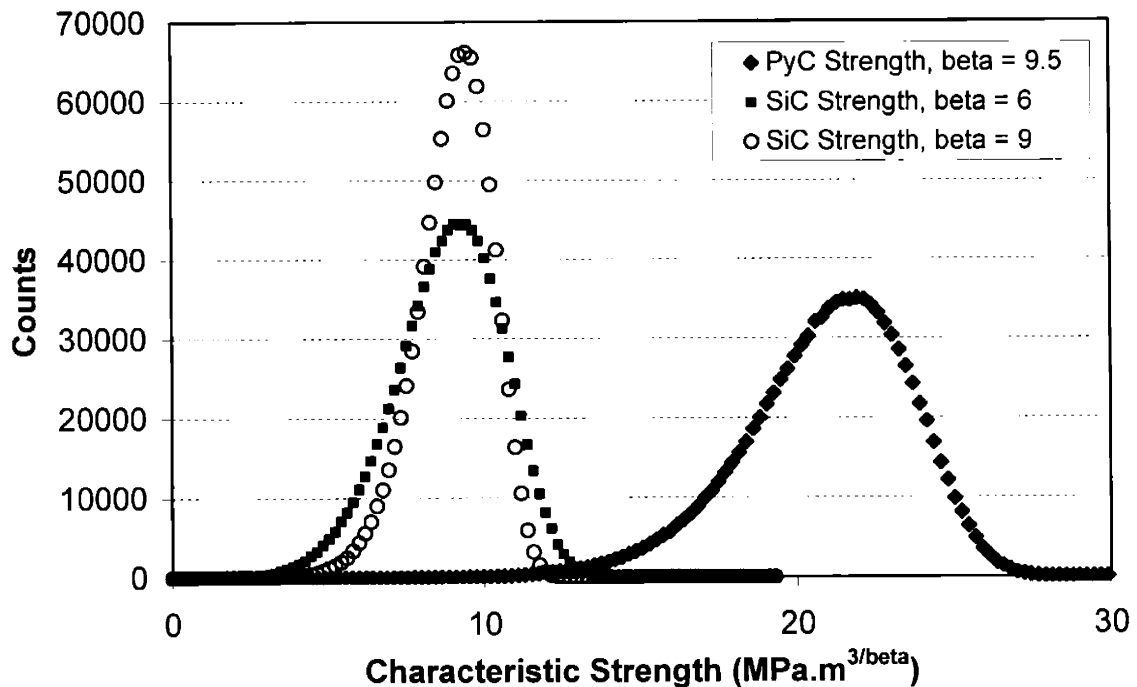
Figure 2-58. Sampling of PyC and SiC characteristic strengths

Chapter 3.

Benchmarking the MIT Fuel Performance Model

The difficulties in fuel performance modeling has been discussed in Chapter 1, and one of them, due to the nature of tiny fuel particles, is that it is impossible to verify the detailed stresses and deformation that occur in an individual particle during irradiation with actual measurement data. What can be provided is the failure history of a big batch of fuel particles in a fuel assembly as indicated by the release of fission gases. Additionally, actual failure data can be provided by post-irradiation examinations of small groups of particles. Typical fuel irradiation experiments are conducted on fuel compacts which consist of thousands of individual fuel particles. Data collected during the irradiation include fission gas and product releases, such as Kr^{85m} and Cs^{137}, from all the particles. Although the monitoring of fission gas release can detect the failure of a single particle, signaled by an upward jump, it is impossible to narrow the measurement down to the individual particle level. In other words, it is impossible to determine which particle has failed. Post irradiation examinations then take some particles, typically on the order of a hundred, from the compacts for detailed measurements. When the particle failure probability is low, this number of closely examined particles is not a good representative of the whole compacts. Nevertheless, this is the place where we can benchmark our model with actual experimental data. From Figure 2-1 we see that before the model predicts fuel failures, it has to go through other calculations, the most important of which is the mechanical analysis, which can only be verified with other existing model predictions and calculations. Given the above mentioned facts, we have chosen a three-tier approach to the validation of our model: (1) to compare our model stress calculations (analytical) with finite element calculations (numerical), (2) to compare our results with other fuel performance models, (3) to compare our model failure predictions to fuel failure probabilities from capsule irradiations where possible.

Tier 1 and 2 are comparisons with calculations, so they are grouped together in Section 3.1. Tier 3 is comparisons with experiments, and it is placed in Section 3.2.

3.1. Benchmarking with Other Model Predictions

3.1.1. Stress Comparisons with FUEL Code

A fuel performance code called FUEL [114] was developed at the Idaho National Engineering & Environmental Laboratory (INEEL) to implement the closed form solutions for stresses in TRISO coated particles derived by Miller et al. [112]. As described in their paper, the radial stresses σ_{rI} and σ_{rO} at the IPyC/SiC and SiC/OPyC interfaces and the tangential stress σ_{tO} at the SiC/OPyC interface are calculated by closed form solution. The value for σ_{tO} is on the OPyC layer side of the interface, because the tangential stress is discontinuous at the interfaces. The FUEL code was exercised, with the same sets of inputs and material models as our model, and the results compared. This purpose of this benchmarking exercise is to validate the analytical series solution that our model implements by the closed form solution that FUEL incorporated under certain conditions.

To make comparisons, we needed to fix the Poisson's ratio in irradiation creep at 0.5 because this is the assumption that the closed form solution in [112] is based on. We then choose to run simulations on Type 1 and Type 2 particles used in previous sections. Their specifications are given in Table 2-20. These two particles have a pyrocarbon density of $1.90g/cm^3$ and BAF_0 of 1.03, and they are irradiated at a temperature of 1000°C. To test our model under a wider range of conditions, we design two more cases derived from Type 1 particle. The first case modifies the pyrocarbon layers of the Type 1 particle to a relatively low density of $1.80g/cm^3$ and isotropic behavior (BAF_0 of 1.0), and irradiate it at high temperature of 1300°C. From Figure 2-22 we see that to produce nearly isotropic pyrocarbon, its density should be generally low and the coating rate should be high. The second cased goes in another direction to change the pyrocarbon layers of the Type 1 particle to a high density of $1.99g/cm^3$ and relatively high BAF_0 of 1.08, and irradiate it at 600°C. The results are shown in Figure 3-1 to Figure 3-4.
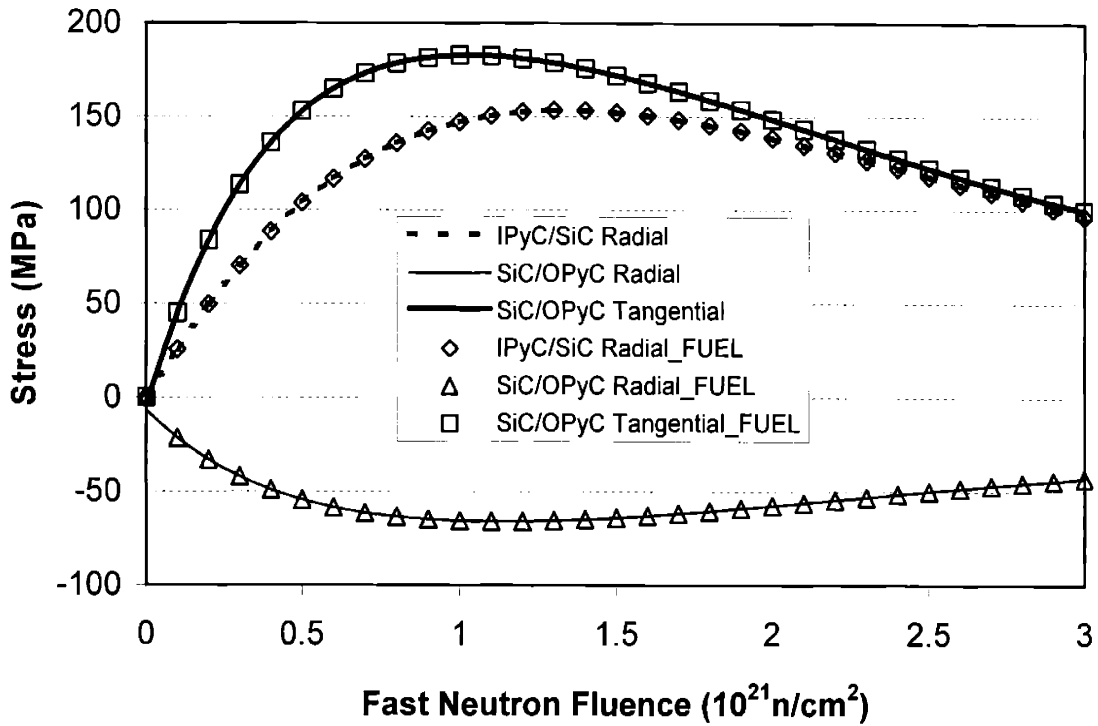
Figure 3-1. Stress Comparison for Type 1 particle (symbols for clarity. T = 1000°C, PyC density = 1.90 g/cm^3, and PyC BAF$_0$ = 1.03.)
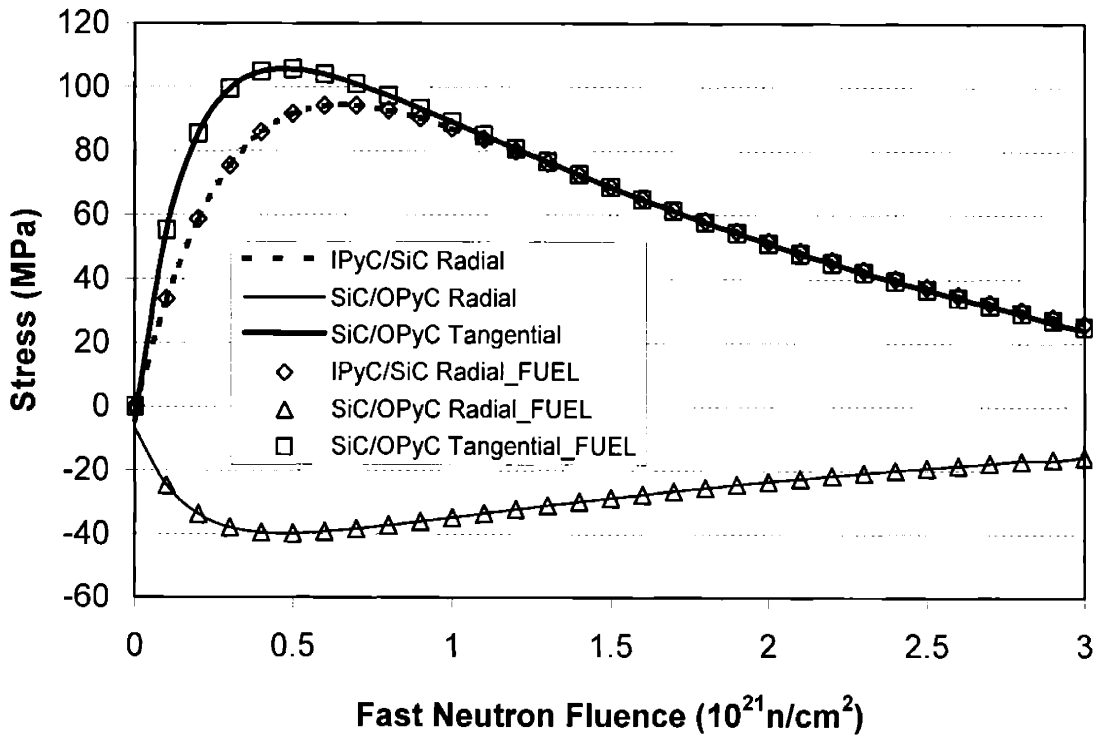
Figure 3-2. Stress Comparison for Type 1 particle (symbols for clarity. T = 1300°C, PyC density = 1.80 g/cm^3, and PyC BAF$_0$ = 1.0.)
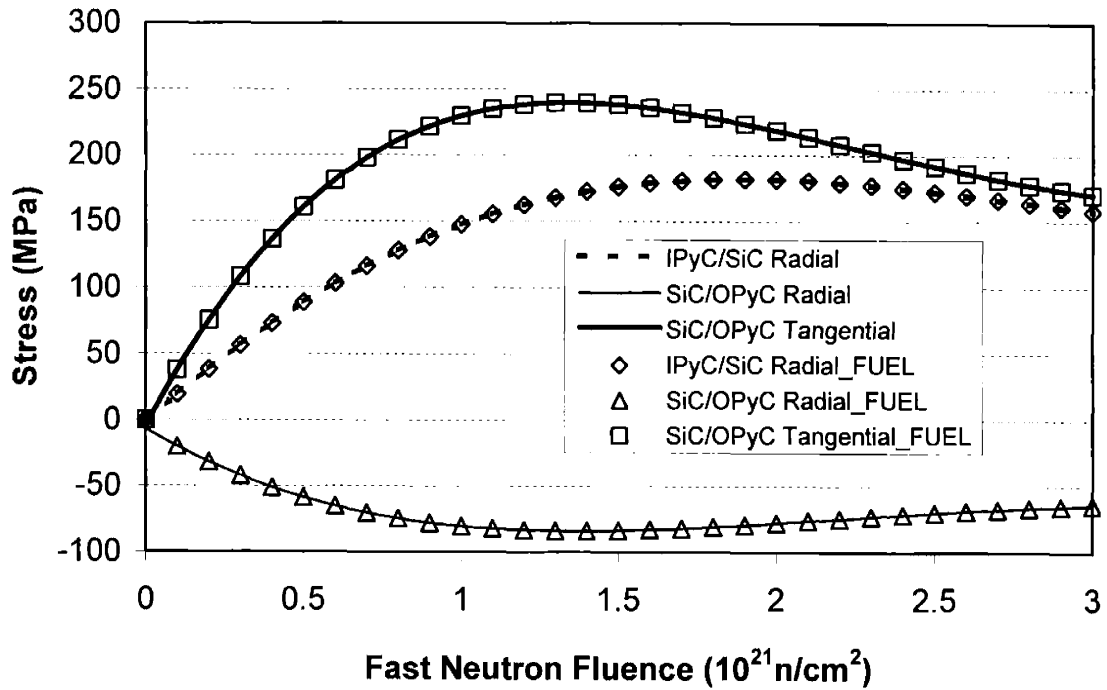
Figure 3-3. Stress Comparison for Type 1 particle (symbols for clarity. T = 600°C, PyC density = 1.99 g/cm^3, and PyC BAF$_0$ = 1.08.)
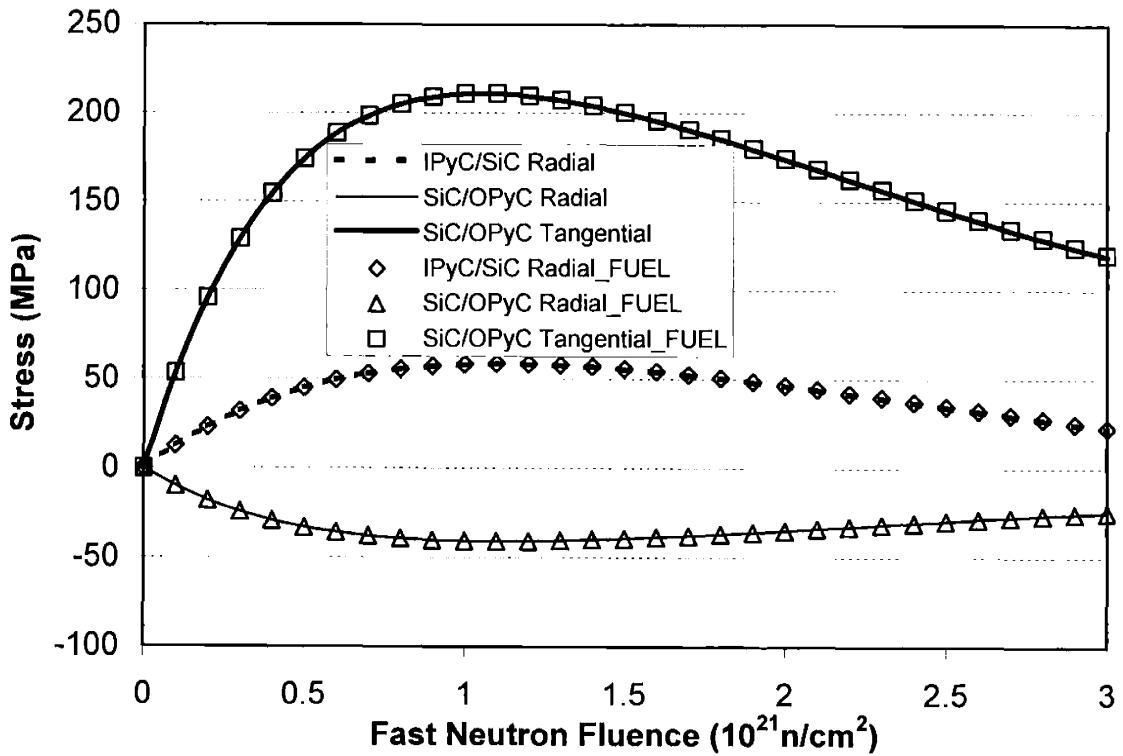
Figure 3-4. Stress Comparison for Type 2 particle (symbols for clarity. T = 1000°C, PyC density = 1.90 g/cm^3, and PyC BAF$_0$ = 1.03.)

From the plots we see that the two solutions are essentially identical in all cases. There are minor differences due to rounding errors and different solution techniques. The series solution keeps adding higher order terms as presented in Appendix A, until it meets its convergence criteria, say 10^{-4} of the summation, therefore the series solution loses some precision compared with the closed form solution. The differences between two sets of results are generally within 0.5%.

When we designed the cases, there was a reason to associate low BAF with high temperature, and high BAF with low temperature, because they work on stresses in the same directions. As will be shown comprehensively later in the parametric study in Section 4.1, stresses go up with higher BAF and lower temperature. The BAF dependency is because the magnitude of irradiation induced dimensional changes is larger with higher BAF, as discussed in Section 2.4.4. The temperature dependency is primarily because the higher creep coefficient induces greater stress relaxation when the temperature is higher. Comparing Figure 3-1, Figure 3-2, and Figure 3-3, we clearly see this trend, and we find earlier stress relaxation as the temperature gets higher. In Figure 3-2, the peak IPyC/SiC interface radial stress happens at about 0.5×10^{21}n/cm^2, and in Figure 3-3, it is about 1.3×10^{21}n/cm^2. Next, if we compare Figure 3-1 and Figure 3-4 with Figure 2-34 to Figure 2-37, we can find the stresses in this exercise are higher due to fixing v_c at 0.5. The effect of v_c is to be discussed further in Section 3.1.2.

From this part of the comparisons we are confident with the correctness of our mechanical formulations and their implementations in our computer code.

3.1.2. Stress Comparisons with Finite Element Calculations by INEEL

As part of collaborative efforts with the INEEL, we performed some comparisons between our analytical stress calculations and the finite element calculations done at INEEL. Both parties agreed to use the same material database and models given by Ho [37]. Two selected cases are listed in Table 3-1. Because there are several interpolations and re-constructions of material data as presented in Section 2.4 of Chapter 2, we chose the first case to be of isotropic pyrocarbon, whose density is 1.96g/cm3, and the irradiation temperature coincides with a temperature at which source data are given, so

132

that a minimal amount of interpolation would be introduced. The predicted stresses at the inner surface of the IPyC layer are plotted in Figure 3-5 and Figure 3-6.

Table 3-1. Parameters for Stress Comparisons with INEEL

Parameter	Case 1	Case 2
Fuel Type	UCO	UCO
Carbon to Uranium ratio	0.36	0.36
Oxygen to Uranium ratio	1.51	1.51
U235 Enrichment (%)	93.15	93.15
End-of-life Burnup (%FIMA)	70.0	70.0
End-of-life Fluence (10^{21}n/cm^2)	3.0	3.0
Irradiation Temperature (°C)	1032	1200
Irradiation Time (EFPD)	1095	1095
Ambient Pressure (MPa)	6.38	6.38
Kernel Density (g/cm^3)	10.52	10.50
Buffer Density (g/cm^3)	0.958	0.958
IPyC/OPyC Density (g/cm^3)	1.96	1.90
IPyC/OPyC BAF$_0$	1.0	1.16
Kernel Diameter (μm)	200	195
Buffer Thickness (μm)	102	100
IPyC Thickness (μm)	53	40
SiC Thickness (μm)	35	35
OPyC Thickness (μm)	39	43

In order to illustrate the effect of varying Poisson's ratio in irradiation creep for pyrocarbon as shown in Figure 2-27, we show our results for Case 1 by using both a fixed Poisson's ratio of 0.5 and varying values essentially according to Figure 2-24. We let it linearly decrease from 0.5 to 0.4 until the effective octahedral shear creep strain reaches 0.01 and stay at 0.4 afterwards. As Figure 3-5 shows, the two methods produce very similar results both in terms of the general trend and the peak stress achieved. A small deviation in the time for peak stress was observed. It is also shown that allowing the Poisson's ratio in irradiation creep for pyrocarbon to change may have dramatic influence on particle stress predictions and, hence, fuel performance predictions. In this case, the stresses differ by about 90MPa, therefore this phenomenon should not be overlooked in modeling efforts. The second case has quite high BAF0 for pyrocarbon layers and the temperature is set higher at 1200°C.
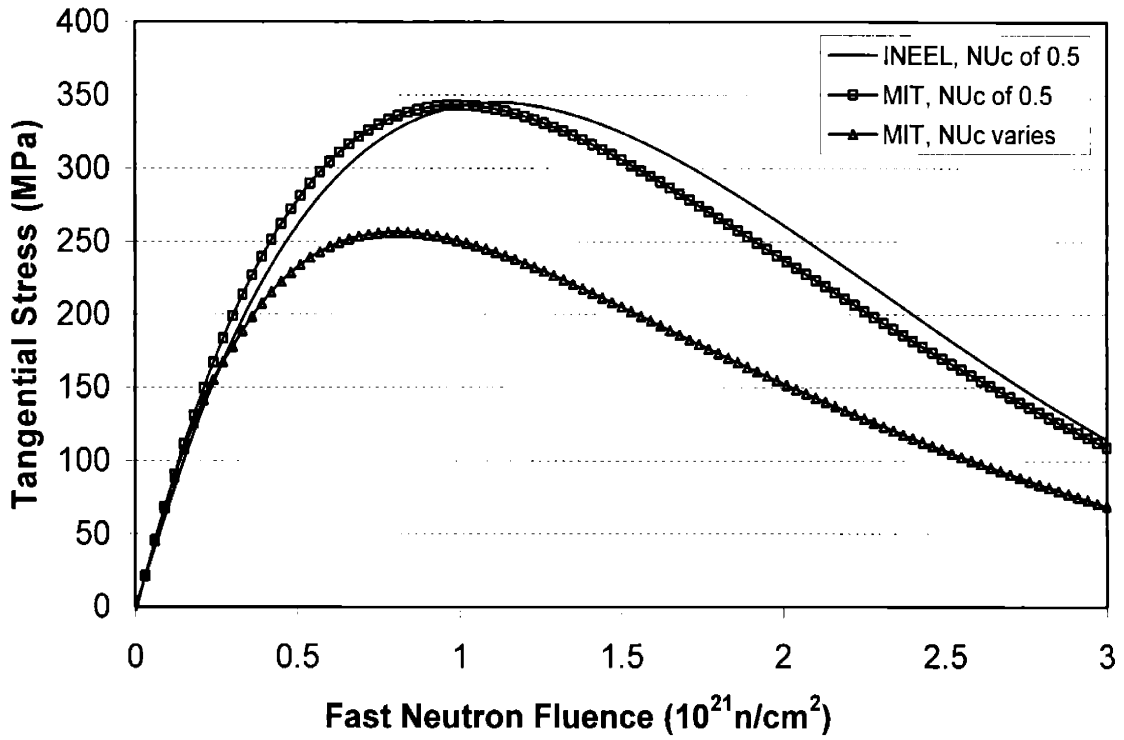
Figure 3-5. Tangential stresses at IPyC inner surface of Case 1 (symbols for clarity)
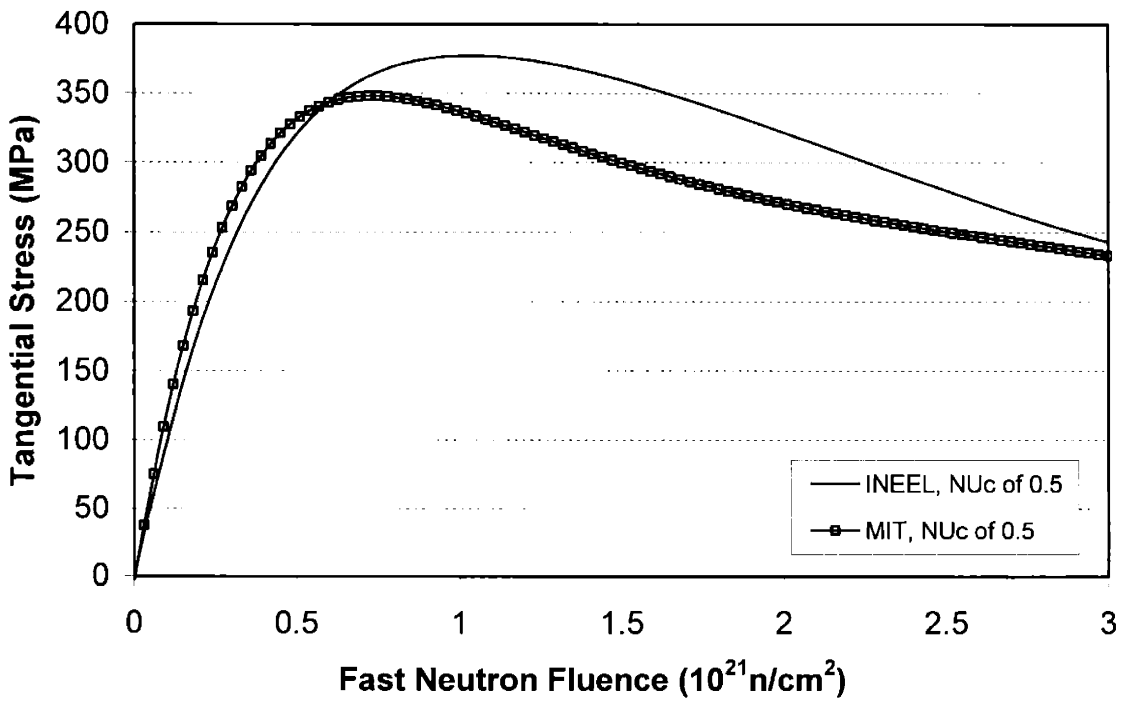
Figure 3-6. Tangential stresses at IPyC inner surface of Case 2 (symbols for clarity)

In Figure 3-6, the agreement is not as good. Our prediction is about 50MPa lower than that of INEEL. It is very hard to say what leads to the difference, but as discussed in Section 2.4.4, to get dimensional change data of pyrocarbons for arbitrary density from the source data at density of $1.96g/cm^3$, we need to go through several steps of adjustments, and the resulting dimensional change data are fitted into polynomials which are then used in our model, so it is beyond our knowledge whether the finite element calculations took the source data the same way. Also, there are many technical details associated with the finite element calculations that we don't know. Therefore we could not trace down the cause of the difference. The comparison for Case 1 should be more informative and we are assertive to say the agreement is not fortuitous.

3.1.3. Stress Comparisons for HTTR First Loading Fuel

Table 3-2. Parameters of HTTR First Loading Fuel Analysis

Parameter	Value
Fuel Type	UO_2*
U235 Enrichment (%)	9.17
End-of-life Burnup (GWd/T)	66.0*
End-of-life Fluence (10^{21}n/cm^2)	3.0*
Irradiation Temperature (°C)	1300*
Irradiation Time (EFPD)	1320*
Ambient Pressure (MPa)	6.38
Kernel Density (g/cm^3)	10.63**
Buffer Density (g/cm^3)	1.1*
IPyC/OPyC Density (g/cm^3)	1.85**
IPyC/OPyC BAF$_0$	1.02
Kernel Diameter (μm)	600*
Buffer Thickness (μm)	60*
IPyC Thickness (μm)	30*
SiC Thickness (μm)	25*
OPyC Thickness (μm)	45*

(*: values provided in reference [116]; **: values provided in reference [115]; chosen otherwise with engineering judgements.)

The High Temperature Engineering Test Reactor (HTTR) is the first high temperature gas-cooled reactor in Japan, and it attained its first criticality in November 1998. The

fabrication of its first loading fuel started in June 1995 [115]. Meanwhile, a coated particle failure model was being developed at Japan Atomic Energy Research Institute (JAERI) to predict the performance of the first loading fuel [116]. Key parameters of HTTR first loading fuel analysis are listed in Table 3-2. Modeling results from Sawa et al. [116] were presented and we plot them together with our model predictions in Figure 3-7. The irradiation induced dimensional changes and creep data and material mechanical properties for pyrocarbon and silicon carbide were not provided by Sawa et al., so we used our own in the calculation.
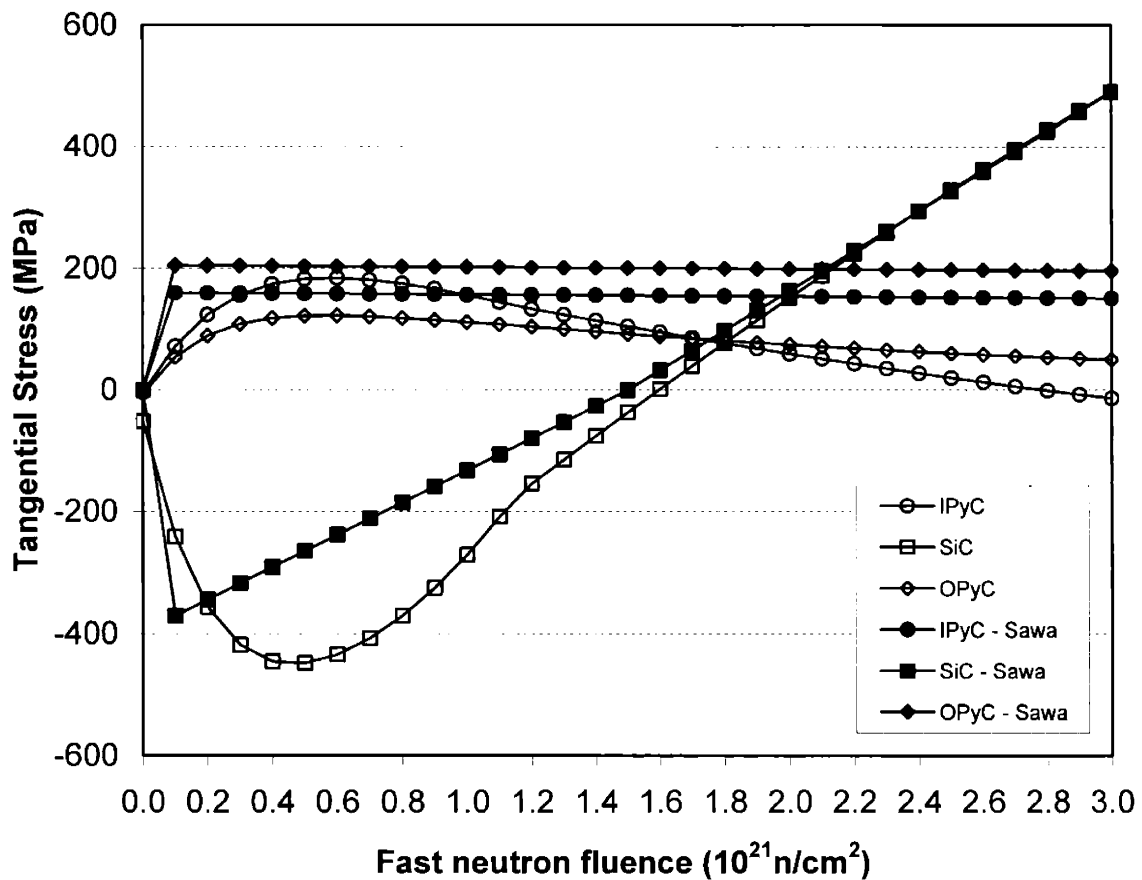
Figure 3-7. Comparison of predicted stresses in a HTTR first loading fuel particle (symbols for clarity)

In Figure 3-7, the lines with open symbols represent our model calculations of tangential stresses in each structural layer. The lines with filled symbols are from Sawa et al. Initially, the SiC is placed in compression due to neutron-induced shrinkage of the

136

adjacent PyC layers. Accordingly, the IPyC and OPyC layers are placed in tension. As the irradiation progresses, the pyrocarbon shrinkage rate gradually decreases. At the same time, fission gas builds up in the buffer layer which results in an increase in the internal pressure and, hence, drives the layer stress in the positive direction. The internal pressure buildup eventually offsets the shrinkage induced compression in the SiC and leads to increasing tensile stress at the end of the exposure. At higher fluence the stress is dominated by the internal pressure in the particle. Our calculation shows the internal pressure at $3 \times 10^{21} \text{n/cm}^2$ reaches 99.8MPa, much higher than the values we saw in Figure 2-34 and Figure 2-36. The reason is that a HTTR first-loading fuel particle has a large fuel kernel but a thin buffer layer, so there is less free volume to accommodate more fission gases generated from the kernel. Due to this end-of-life high internal pressure, the particle could indeed be failed by pressure vessel failure, which, as we discussed, would not happen in common cases. The model calculations for the SiC layer agree with each other quite well at high burnup, whereas our results show a slower relaxation early in the irradiation. The calculations from Sawa et al. exhibit an abrupt change at a fluence of 0.1 $\times 10^{21} \text{n/cm}^2$ and approximately linear behavior afterwards. However, experimental data for PyC shrinkage is not this abrupt and is unlikely to induce stresses such as these. It is likely that the Sawa et al. used some simplifications in modeling PyC dimensional changes and/or creep. The discrepancy between the two stress predictions in the pyrocarbon layers is probably due to the use of different mechanical properties for pyrocarbon. For example, the PyC layers appear to be more rigid in Sawa's results than in ours. In this case, it is even harder for us to make a good comparison than the case in Section 3.1.2, simply because a lot more input data need to be specified. Nevertheless, the stress evolution in the pyrocarbon layers follows the same trend.

3.2. Benchmarking with NPR Experimental Results

3.2.1. Review of NPR Irradiation Program

As mentioned in Section 2.5.2, the New Production-Modular High Temperature Gas Cooled Reactor (NPR in short) irradiation program, whose results are not well-

understood none-the-less represent a significant source of benchmarking data. In this section of benchmarking, we compare our model predictions with the experimental data. In addition, as part of this effort we explore the effect of power history detail on predictions and demonstrate the necessity of incorporating detailed irradiation histories for coated fuel particles. We also show the effects of our crack induced failure models CIFM1 and CIFM2 on fuel performance prediction. We first review the fuel design, capsule irradiations, and post-irradiation examinations of the program.

The designed NP-MHTGR fuel particles have the following characteristics, some of which are different from general TRISO fuel particles. (1) The fuel kernel is quite small (~200μm in diameter), and contains high-enrichment UCO. This is similar to the Type 1 particle we have been using in this thesis. (2) A low density protective PyC layer (PPyC) was added onto the outer surface of OPyC layer to reduce mechanical damage of particles during compacting[2]. (3) Extra dense thin pyrocarbon layers called seal coats were added to both sides of PPyC and between the buffer layer and IPyC. Fuel particles were cast into graphite matrix compacts, 12.5mm diameter by 49.5mm long to provide appropriate reactor core fuel density. The quality and performance requirements for NP-MHTGR fuel are presented in Table 3-3 [88].

Table 3-3. Quality and Performance Requirements for NP-MHTGR Fuel

Quality Requirements	Fraction of particles	
	Mean	95% Confidence
Defective SiC	$\leq 5.0 \times 10^{-5}$	$\leq 1.0 \times 10^{-4}$
Total Heavy Metal Contamination	$\leq 1.0 \times 10^{-5}$	$\leq 2.0 \times 10^{-5}$
Total Fraction of Heavy Metal Outside Intact SiC	$\leq 6.0 \times 10^{-5}$	$\leq 1.2 \times 10^{-4}$
Missing or Defective Buffer	$\leq 5.0 \times 10^{-5}$	$\leq 2.0 \times 10^{-4}$
Missing or Defective IPyC	$\leq 4.0 \times 10^{-5}$	$\leq 1.0 \times 10^{-4}$
Missing or Defective OPyC	$\leq 1.0 \times 10^{-5}$	$\leq 1.0 \times 10^{-3}$
Performance Requirements		
Fuel Failure during Normal Operation	$\leq 1.0 \times 10^{-4}$	$\leq 4.0 \times 10^{-4}$
Incremental Fuel Failure During Accidents	$\leq 3.0 \times 10^{-4}$	$\leq 1.2 \times 10^{-3}$

The Performance Test Fuel (PTF) for this program was manufactured by General Atomics and their subcontractors, and it met the fuel product specifications and had the

---

[2] The fuel particles and graphite pitch and graphite shim particles are hot pressed into 12.5mm diameter by 49.5mm long cylinders designated compacts and sealed at the top. This process is called compacting.

best as manufactured particle fuel quality ever produced in the United States [88]. The specifications and as-fabricated values for PTF are listed in Table 3-4.

Table 3-4. Specifications and Values of Performance Test Fuel for NP-MHTGR

	Thickness		Density	
	Spec. (μm)	As Fabricated (μm)	Spec. (g/cm^3)	As Fabricated (g/cm^3)
UCO Kernel	145-205	200	>10.3	10.51
Buffer	90-110	102	0.8-1.1	0.96
IPyC + seal coat	40-60	53	1.85-1.95	1.92
SiC	30-40	35	$\geq$3.18	3.23
IPyC + seal coat	30-50	39	1.80-1.95	1.86
PPyC + seal coat	40-60	47	0.80-1.10	1.06

Three fuel capsules, each of which was installed with a number of compacts, were designed and manufactured by May 1991. Capsule NPR1 was designed to demonstrate maximum service life conditions of temperature, burnup, and fast neutron fluence. Capsule NPR2 was to be more representative of core average fuel temperatures. These two capsules were irradiated in the High Flux Isotope Reactor (HFIR) at Oak Ridge National Laboratory (ORNL). The third capsule NPR1A was included as a backup test for NPR1 test, and it was irradiated in the Advanced Test Reactor (ATR) at INEEL. The major goal of the experiments was to provide fuel performance data by measuring fission gases release during irradiation, e.g. Kr^{85m}. The Release-to-Birth ratio (R/B), which is the measured fission gas release rate divided by calculated fission gas birth rate, is a measure of fuel performance. Increase in the readings of R/B for a given fission gas would indicate fuel failure. This approach has been used historically for in-pile fuel tests [117]. Key experimental parameters for the three capsules are listed in Table 3-5.

Table 3-5. Key Experiment Parameters for NPR Capsules

	Average T ($^\circ$C)	Peak T ($^\circ$C)	Peak Fluence (10^{21}n/cm^2)	Peak Burnup (%FIMA)	Number of Particles
NPR1	974	1246	3.7	79	77,500
NPR1A	977	1219	2.0	64	75,360
NPR2	753	1024	3.7	79	77,500
NPR core	600	1250	3.7	75	1.8×10^{10}

A schematic of the capsule NPR1A is shown in Figure 3-8.

139
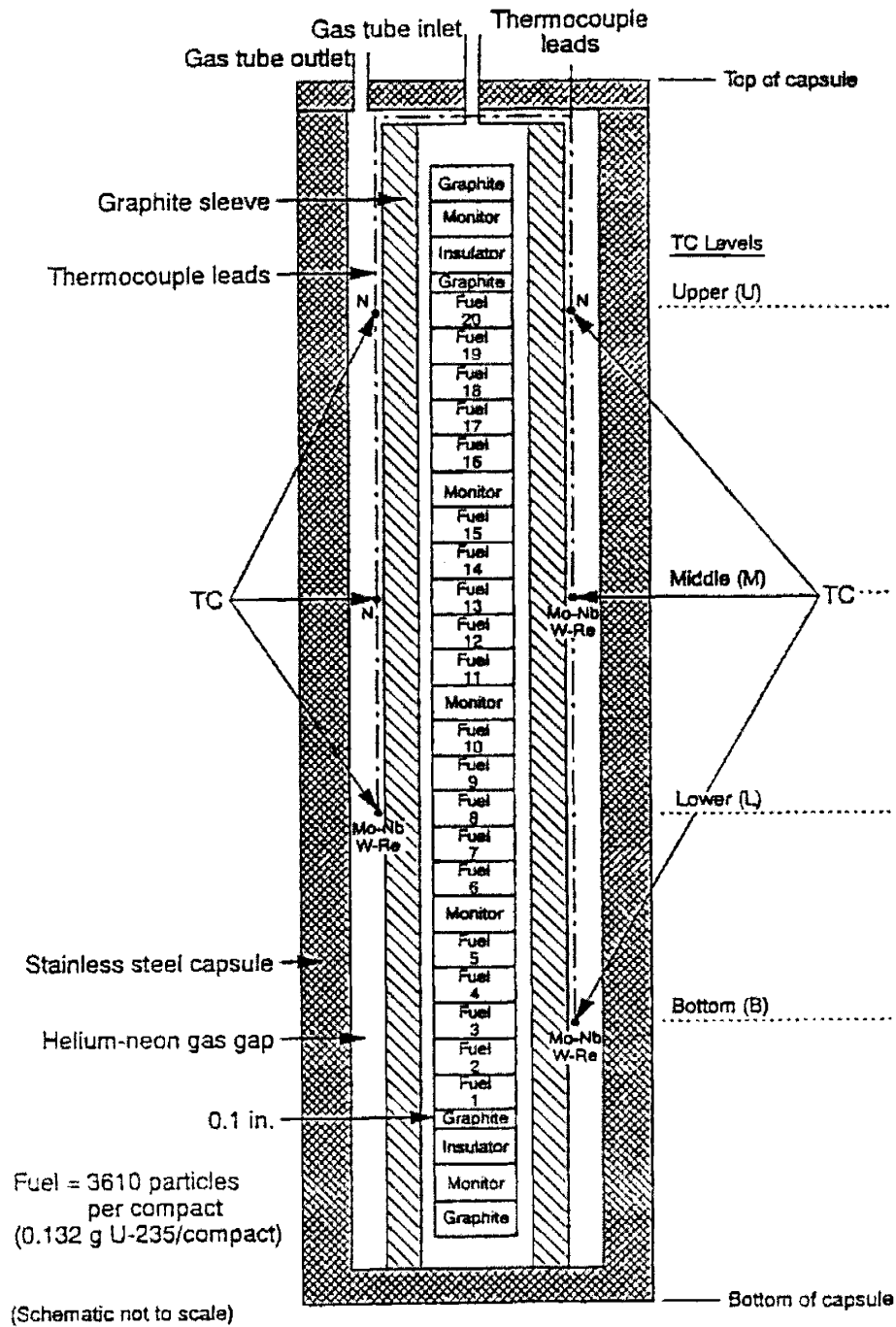
Figure 3-8. Schematic of NPR1A Capsule (from Hobbins et al. [88])

The capsule NPR1A contained 20 compacts, each with about 3610 particles. The fuel compact stack was about 122cm long and 1.7cm in diameter, and contained five neutron fluence monitoring packages, two insulator pellets, and four graphite spacers as shown in the figure. The fuel compact stack was placed within a graphite sleeve housed in an outer

140

stainless steel capsule. The sleeve was instrumented with thermocouples, from which data were collected for thermal analysis to calculated temperatures at various axial and azimuthal locations in the capsule. A sweep gas entered the top of the capsule, flowed down the outside of the compact stack, and up around the compacts to sweep out fission products released from the compacts. The gas also maintained the temperature of the capsule relatively constant during irradiation. The fission product monitoring system consisted of an on-line gamma-ray spectrometer and a sodium iodide detector, and it provided almost instantaneous data on fission gas release during irradiation.

Irradiation of NPR1A began on October 2, 1991 and was terminated after 64.2 full power days due to an unexpected high failure rate. The Kr^{85m} R/B remained low during the first 42 full power days, but on December 12, 1991, it increased from $\sim 5 \times 10^{-9}$ to 3.8×10^{-7}, indicating first particle failure. Then the Kr^{85m} R/B continued to rise to a peak value of 1.79×10^{-5}. Based on these data, the total number of particle failures in NPR1A was estimated as

$$\text{Number of failures} = \left(1.79 \times 10^{-5} - 5 \times 10^{-9}\right)/\left(3.8 \times 10^{-7} - 5 \times 10^{-9}\right) = 48. \qquad (3.1)$$

Capsules NPR1 and NPR2 were identical, and the schematic of them is shown in Figure 3-9. Each capsule contained 16 fuel compacts surrounded by H-451 graphite fuel bodies, and the fuel particle loadings in compacts were varied to compensate for the axial cosine-shaped flux distribution in HFIR to produce relatively uniform heat generation across the capsules. The capsules were instrumented in a similar way for data acquisition. In NPR1, the system included two ionization chambers. In NPR2, two gamma spectrometers were used, which were sensitive enough to detect single particle failures. Irradiation of NPR1 began on July 25, 1991, and was completed on May 29, 1992. The Kr^{85m} R/B remained low during the first 120 full power days, but on January 2, 1992, the R/B increased to 1.7×10^{-7} at a peak fluence[3] of $1.7 \times 10^{21} n/cm^2$, indicating a particle failure. The R/B continued to increase until a final value of about 1.0×10^{-4} in the end. Based on eq. (3.1) and activity spikes recorded by the ionization chambers, 625 and 526 particles were estimated to have failed, respectively. Irradiation of NPR2 began in August 1991 and was completed on May 29, 1992. The first particle failure was observed on

---

[3] The peak fluence refers to the highest achieved fluence somewhere in the capsule at that point.

141

February 11, 1992 at a peak fluence of $2.0 \times 10^{21} \text{n/cm}^2$, when the Kr^{85m} R/B jumped to 7.0×10^{-7}. The final value of the R/B was about 2.0×10^{-5}, and the estimated number of failed particles was 135.

Top of capsule

Compact A1		Compact B1
Compact A2		Compact B2
Compact A3		Compact B3
Compact A4		Compact B4

HFIR
horizontal
midplane

Compact A5		Compact B5
Compact A6		Compact B6
Compact A7		Compact B7
Compact A8		Compact B8

Bottom of capsule
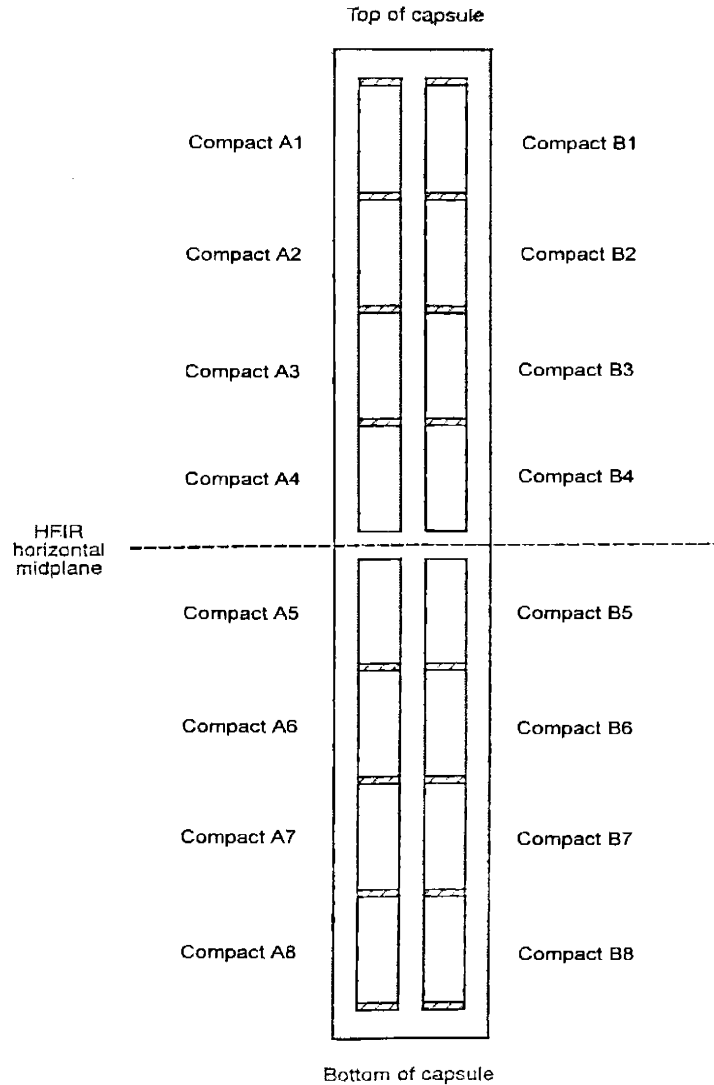
Figure 3-9. Schematic of NPR1 and NPR2 Capsules (from Baldwin et al. [118])

The total number of particle failures was about 700, accounting for 0.32% of 221,136 particles contained in three capsules. This is much higher than the performance requirements in Table 3-3, but the U.S. models predicted no failures in all three capsules. In the sections below, we will discuss our modeling results on the entire NPR1 capsule, one NPR2 compact (NPR2-A4 which was at the center of NPR2 as shown in Figure 3-9), and one NPR1A compact (NPR1A-A9 which was a little below the mid-plane of NPR1A

142

in Figure 3-8). Because of the symmetric arrangements and loadings of NPR1-B1 to NPR1-B8 compacts and NPR1-A1 to NPR1-A8 compacts, it is reasonable to assume two groups would see the same irradiation conditions, therefore modeling eight compacts NPR1-A1 to NPR1-A8 is sufficient. More specifics about NPR irradiations will be mentioned as we elaborate on our modeling results. We actually conducted three rounds of simulations on the above mentioned ten compacts, one using the simplified crack induced failure model (CIFM1) with simplified irradiation histories, one using CIFM1 but with detailed irradiation histories, and one using the improved crack induced failure model (CIFM2) with detailed irradiation histories. Firstly we will discuss the crack induced failure model results contrasting to the pressure vessel failure model, as well as the impact of employing detailed irradiation histories in fuel performance modeling.

3.2.2. Simulations with Different Irradiation Histories

For each compact, simulations can be run with a time averaged irradiation temperature and constant neutron fluence rate and burnup rate, which is the approach that most fuel particle performance models take. Table 3-6 shows the irradiated conditions for simulated NPR compacts. We can also use the detailed temperature histories obtained from thermal calculations based on thermal couple measurements, and they are presented in two separate plots, Figure 3-10 and Figure 3-11, for clarity.

Table 3-6. Irradiation Conditions for NPR Compacts

Compact ID	# Particle Loaded	Time Averaged T (°C)	End-of-life Fluence (10^{21}n/cm^2)	End-of-life Burnup (%FIMA)
NPR1-A1	6126	874	2.4	74.0
NPR1-A2	5266	1050	3.0	77.0
NPR1-A3	4228	1036	3.5	78.5
NPR1-A4	3755	993	3.8	79.0
NPR1-A5	3755	987	3.8	79.0
NPR1-A6	4228	1001	3.5	78.5
NPR1-A7	5266	1003	3.0	77.0
NPR1-A8	6126	845	2.4	72.0
NPR2-A4	3755	746	3.8	79.0
NPR1A-A9	3610	1052	1.9	64.0
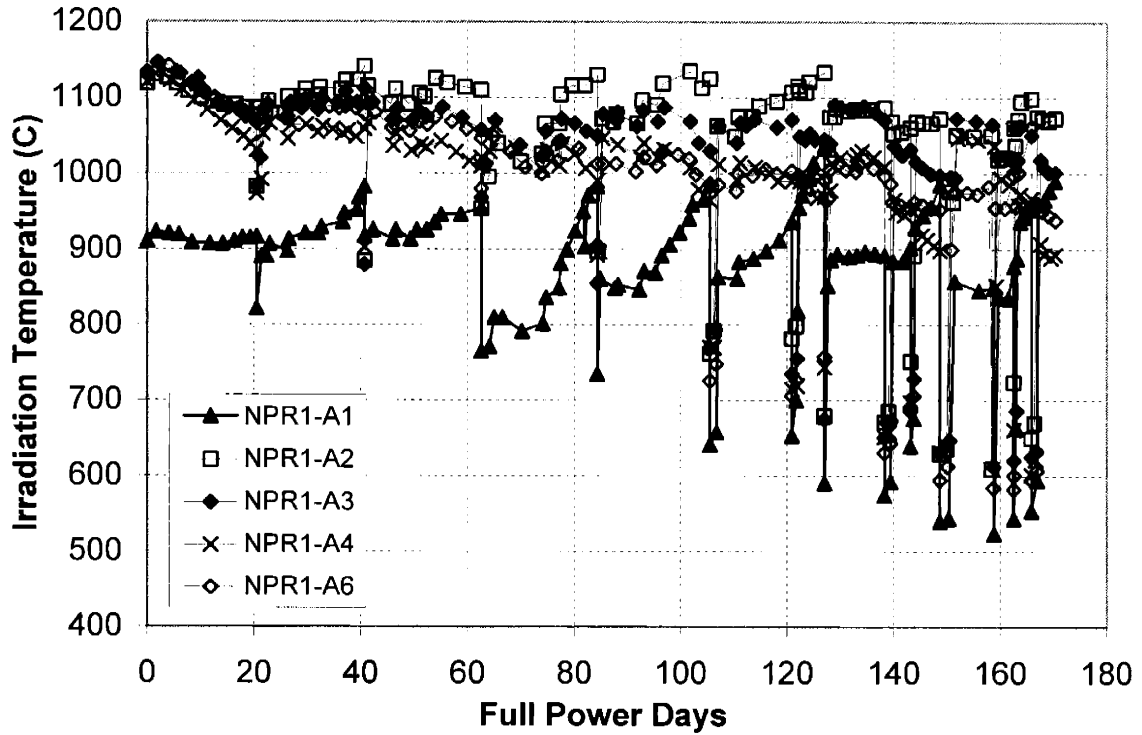
Figure 3-10. Irradiation temperature histories for selected NPR compacts (1)
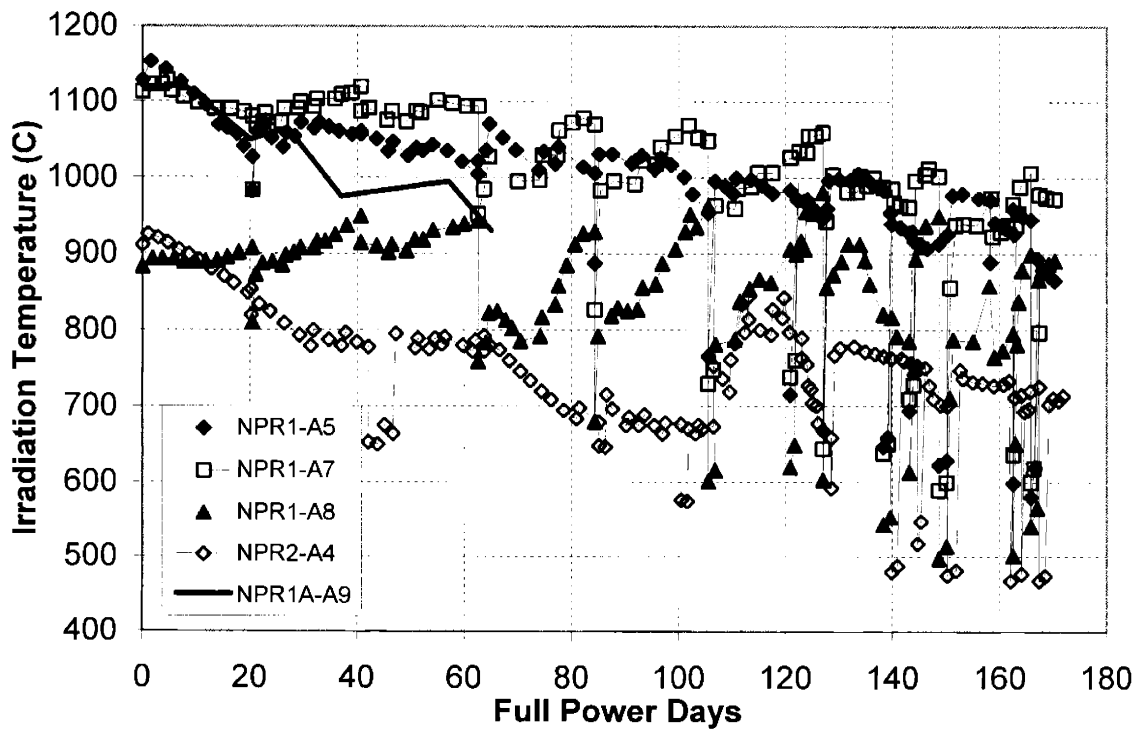
Figure 3-11. Irradiation temperature histories for selected NPR compacts (2)

144

The NPR1 and NPR2 capsules were irradiated for eight cycles, and in each cycle, temperature variations could be as high as 150°C. In general, temperatures decreased with time due to the depletion of fuel materials and hence decreasing energy generation rate, but the temperatures in some compacts such as NPR1-A2 and NPR1-A3 remained quite constant throughout the irradiation. Also in each irradiation cycle, the temperature variations were downward sloping in some cases but upward sloping in others like NPR1-A1 and NPR1-A8, which were at both ends of the NPR1 capsule, as shown in Figure 3-9. These compact specific temperature histories will lead to differentiated fuel performance that models with simplified temperature histories won't be able to tell.

Beside the temperature histories, the neutron fluence and burnup histories for the NPR1 and NPR2 capsules were significantly different from the simplified scenarios. When we say irradiation history, we mean the whole set of temperature, neutron fluence and burnup histories. The burnup versus fast neutron fluence curves are plotted in Figure 3-12 and Figure 3-13. These irradiation history data were extracted with the aid of a computer program from the source curves in reference [88] and [118].
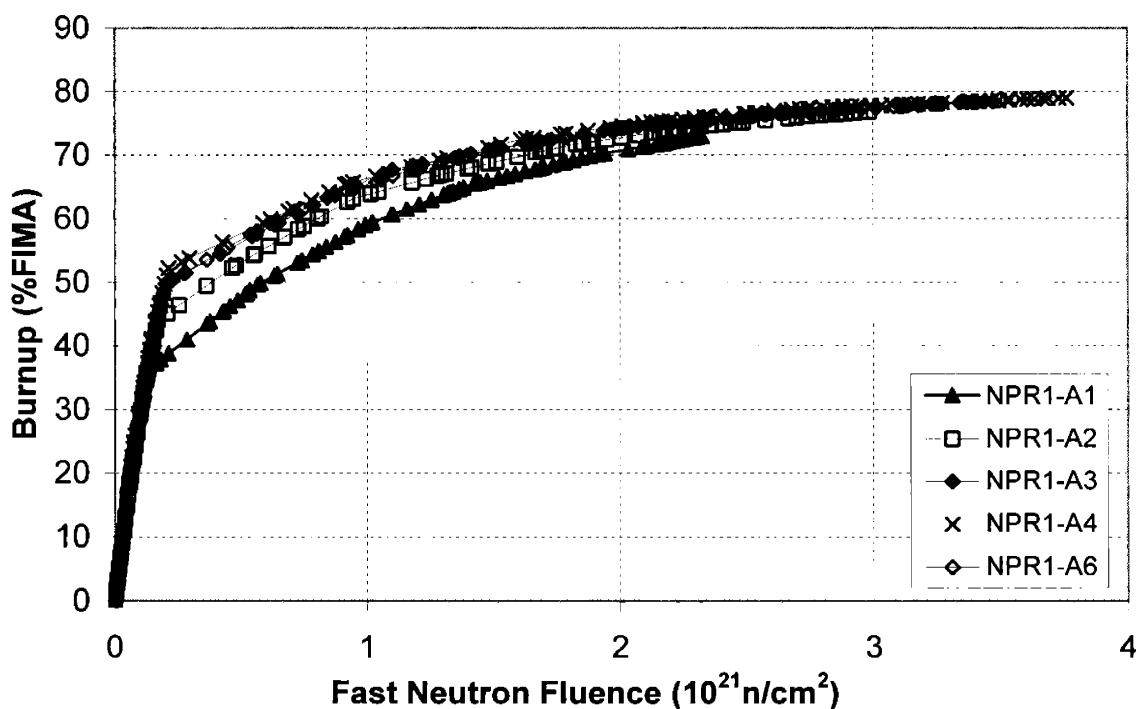
Figure 3-12. Burnup versus fast neutron fluence for selected NPR compacts (1)

145
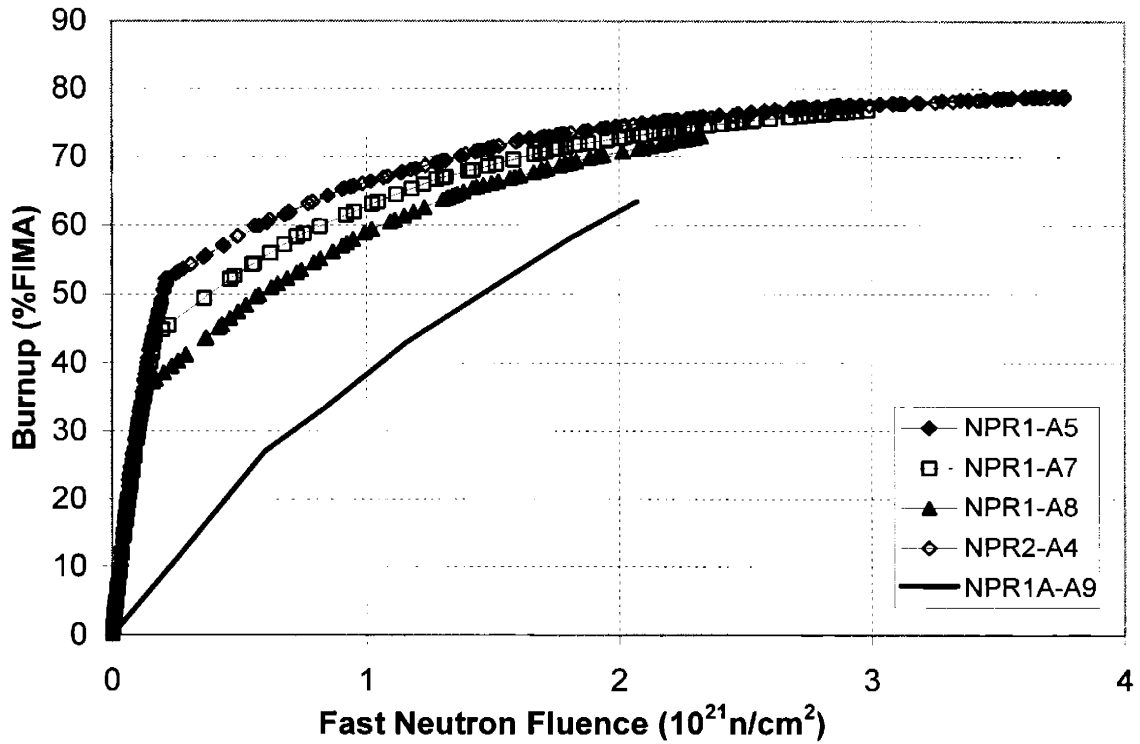
Figure 3-13. Burnup versus fast neutron fluence for selected NPR compacts (2)
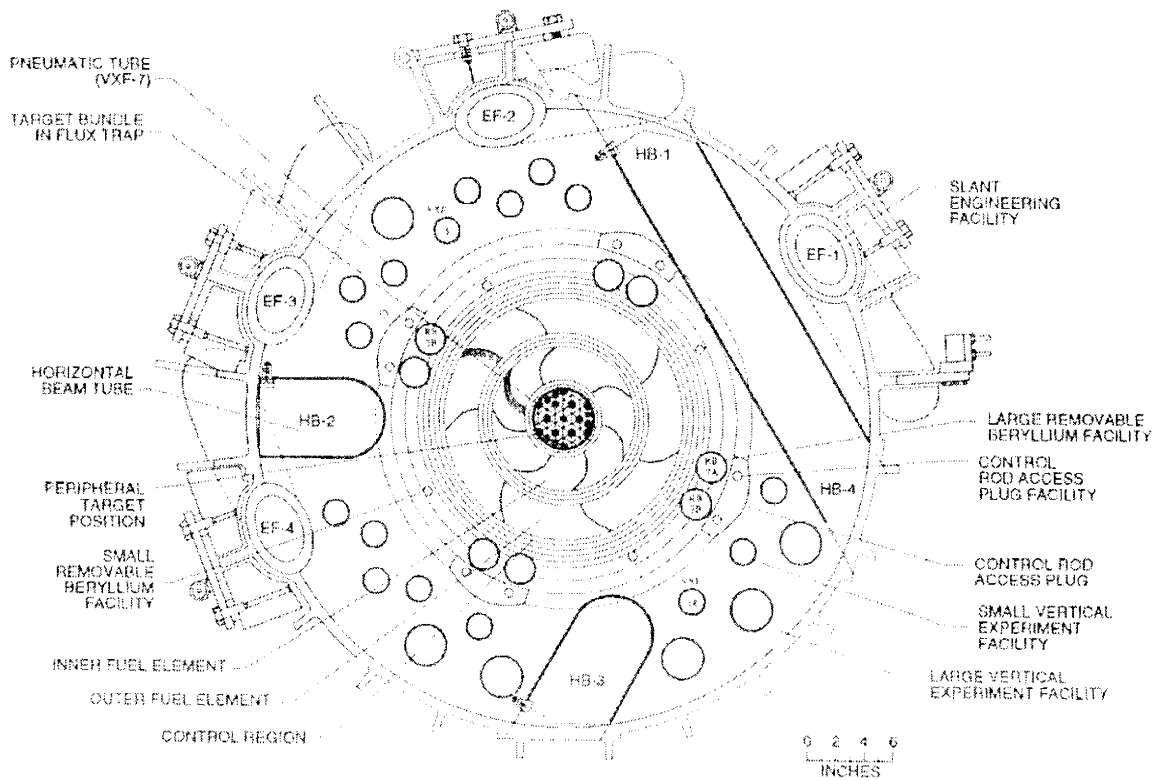
Figure 3-14. Cross section view of the HFIR core at the horizontal midplane (from Baldwin et al. [118])

146

We see the burnup buildup in NPR1A-A9 was roughly linear with respect to fast neutron fluence, but NPR1 and NPR2 compacts achieved 40% to 50% of their burnups before accumulating only $0.2 \times 10^{21} \text{n/cm}^2$ (E>0.18MeV) of fast neutron fluence. Figure 3-14 shows the cross section of HFIR core at its horizontal midplane. The NPR1 capsule was irradiated at position VXF-5 for three cycles, RB-7A for four cycles, and RB-7B for one cycle. The NPR2 capsule was irradiated at VXF-18 for three cycles, and then RB-3A for five cycles. The VXF positions are away from the central high fast neutron flux region in HFIR, but fuel burnup can be driven up quickly there. The RA and RB positions see very high fast neutron flux but contribute less to fuel burnup. Later, when we compare failure predictions, we will see how this can make a difference in fuel performance. The simulations were run and the key input parameters are listed in Table 3-7.

Table 3-7. Key Input Parameters for NPR Fuel Particle Modeling

Parameter	Mean Value	Standard Deviation	Distribution Type
Fuel Type	UCO	-	-
C:U Ratio, O:U Ratio	0.36, 1.51	-	-
Ambient Pressure (MPa)	0.1	-	-
U235 Enrichment (%)	93.15	0.01	Triangular
Kernel Diameter (μm)	200	5.2	Triangular
Buffer Thickness (μm)	102	10.2	Triangular
IPyC Thickness (μm)	53	3.68	Triangular
SiC Thickness (μm)	35	3.12	Triangular
OPyC Thickness (μm)	39	4.01	Triangular
Kernel Density (g/cm^3)	10.51	0.01	Triangular
Buffer Density (g/cm^3)	0.96	0.05	Triangular
IPyC Density (g/cm^3)	1.923	-	-
OPyC Density (g/cm^3)	1.855	-	-
IPyC BAF$_0$	1.05788	0.00543	Triangular
OPyC BAF$_0$	1.05154	0.00622	Triangular
IPyC σ_0 (MPa.m$^{3/\beta}$)	23.6[*]	9.5 (β)	Weibull
OPyC σ_0 (MPa.m$^{3/\beta}$)	22.4[*]	9.5 (β)	Weibull
SiC σ_0 (MPa.m$^{3/\beta}$)	9.64[*]	6.0 (β)	Weibull
SiC K_{IC} (MPa. μm$^{0.5}$)	3500[†]	530	Triangular

([*]: These are initial characteristic strength at room temperature given in Section 2.5.1; [†]: For the simulations with CIFM1, we used earlier choice of 3300 MPa.μm$^{0.5}$.)

One million particles were sampled for each compact. Firstly we look at the end-of-life failure predictions on NPR compacts. The data are listed in Table 3-8.

Table 3-8. Comparison of Model Calculations with PIE Results (Part I)

Compact ID	Failure Fraction (%)	95% Confidence (%)	Detailed History, CIFM1 (%)	Simple History, CIFM1 (%)
IPyC Layer Failures				
NPR1-A1	-	-	47.4	84.2
NPR1-A2	-	-	6.44	16.7
NPR1-A3	-	-	15.0	19.4
NPR1-A4	-	-	33.5	33.9
NPR1-A5	31	17<p<47	26.6	36.3
NPR1-A6	-	-	24.4	30.3
NPR1-A7	-	-	15.6	29.1
NPR1-A8	6	2<p<16	60.7	91.7
NPR2-A4	65	54<p<76	99.6	99.5
NPR1A-A9	18	5<p<42	23.9	19.0
SiC Layer Failures				
NPR1-A1	-	-	1.61	8.32
NPR1-A2	-	-	1.00×10^{-4}	0.0380
NPR1-A3	-	-	0.0250	0.0740
NPR1-A4	-	-	0.857	0.613
NPR1-A5	0.6	0<p<3	0.358	0.790
NPR1-A6	-	-	0.272	0.400
NPR1-A7	-	-	0.0683	0.337
NPR1-A8	0	0<p<2	2.74	9.64
NPR2-A4	3	2<p<6	13.9	12.8
NPR1A-A9	1	0<p<5	0.492	0.0750

(-: Not measured by Post-Irradiation Examination (PIE).)

The Post-Irradiation Examination (PIE) results in the tables were obtained by optical metallography. Four compacts were measured. In this technique a fuel compact is cut through its cross section and slices open the coated particles on the way. Frequently the number of particles examined in cross sections of a compact is about 100. Metallography can characterize the condition of kernel and coating layers, and measure failure fractions of PyC and SiC layers. In addition, a leach-burn-leach (LBL) procedure and individual microsphere gamma analyzer (IMGA) can also measure SiC layer failure fraction [88].

As in the table, our model predictions compare very favorably with PIE results both in the ratio of IPyC layer failure to SiC layer failure and in absolute values. The fact that

PyC layer failures are much higher than SiC layer failures is consistent with the direct result of applying the pyrocarbon induced failure model. Moreover, metallography found no occurrence of failed SiC without failed IPyC or OPyC, which supports this proposed failure mechanism. Discussions on these results are summarized below.

(1) Given the great variations on material properties, particle dimensions, and PIE measurements, the agreements in IPyC layer failures and SiC layer failures are very encouraging. In general, compacts irradiated at lower temperature would have more PyC layer failures which induce more SiC layer failures, as shown by both PIE and model results. The time averaged irradiation temperatures are given in Table 3-6. According to the irradiation creep model for pyrocarbon that we are using, lower temperatures imply less stress relaxation in PyC layers, so they are more liable to failures. The odd one which doesn't seem to follow this trend based on PIE is NPR1-A8. Based on the inverse relationship between failure probability and irradiation temperature, its failure should be between NPR1-A5 and NPR2-A4. It is possible that there were some material property deviations on it, or some other mechanisms which we don't understand, which is not surprising. Later in this section we will see whether irradiation temperature uncertainty can explain it.

(2) Generally the predicted failure probabilities with detailed irradiation histories are lower than those with simplified histories, but the case is reversed in NPR1A-A9 and is marginal in NPR2-A4. Let's proceed with explanations. The general trend results from two factors which reduce stresses in coated particles when detailed histories are used. The first one is that the time averaged irradiation temperatures in the first three irradiation cycles are higher than the overall time averaged temperatures, which leads to more creep-induced stress relaxation at early irradiation stage when the stresses in pyrocarbon layers are critical, as shown in Figure 2-35. The second one is that NPR1 and NPR2 capsules gained much of their burnups before irradiation induced dimensional changes and creep take place, as discussed with Figure 3-12 and Figure 3-13. Then, the built-up internal pressures offset some of the irradiation-induced stresses at early stage of irradiation, as we emphasized in Section 2.4.6. However, since the internal pressure in these small-kernel-big-buffer particles is not very high (Refer to Figure 2-34), this effect is secondary.

149
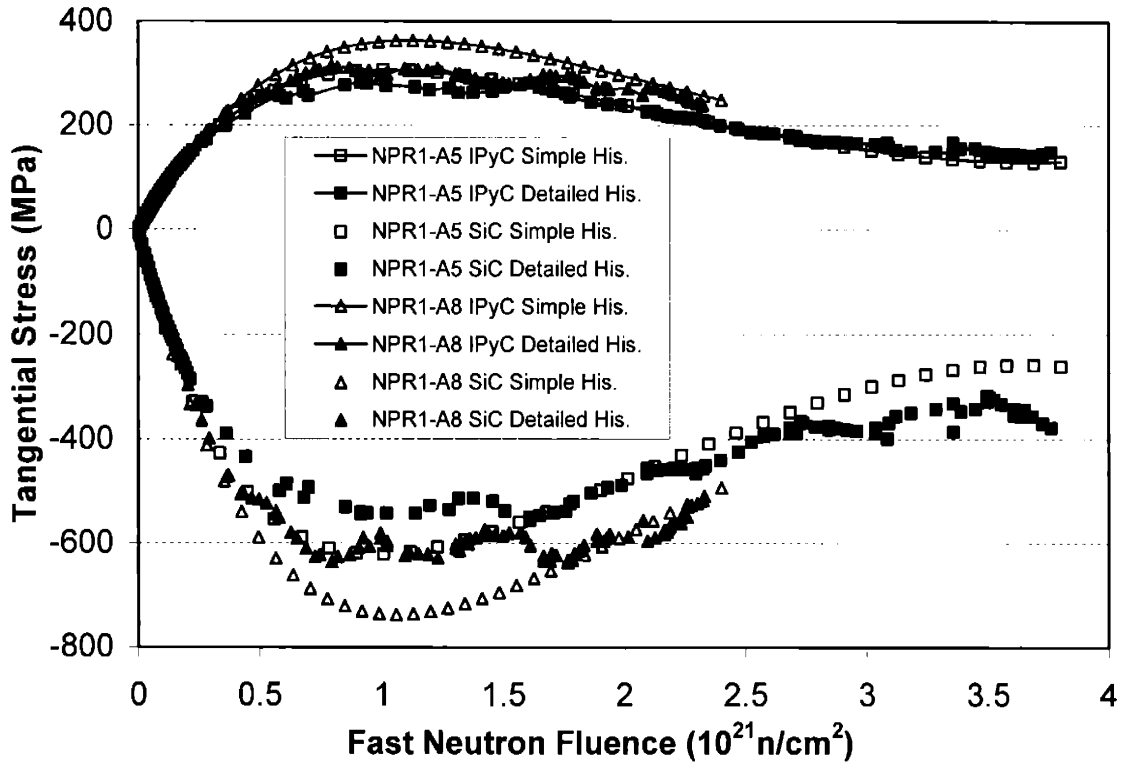
Figure 3-15. Stresses in four PIE examined NPR compacts (1) (symbols for clarity)
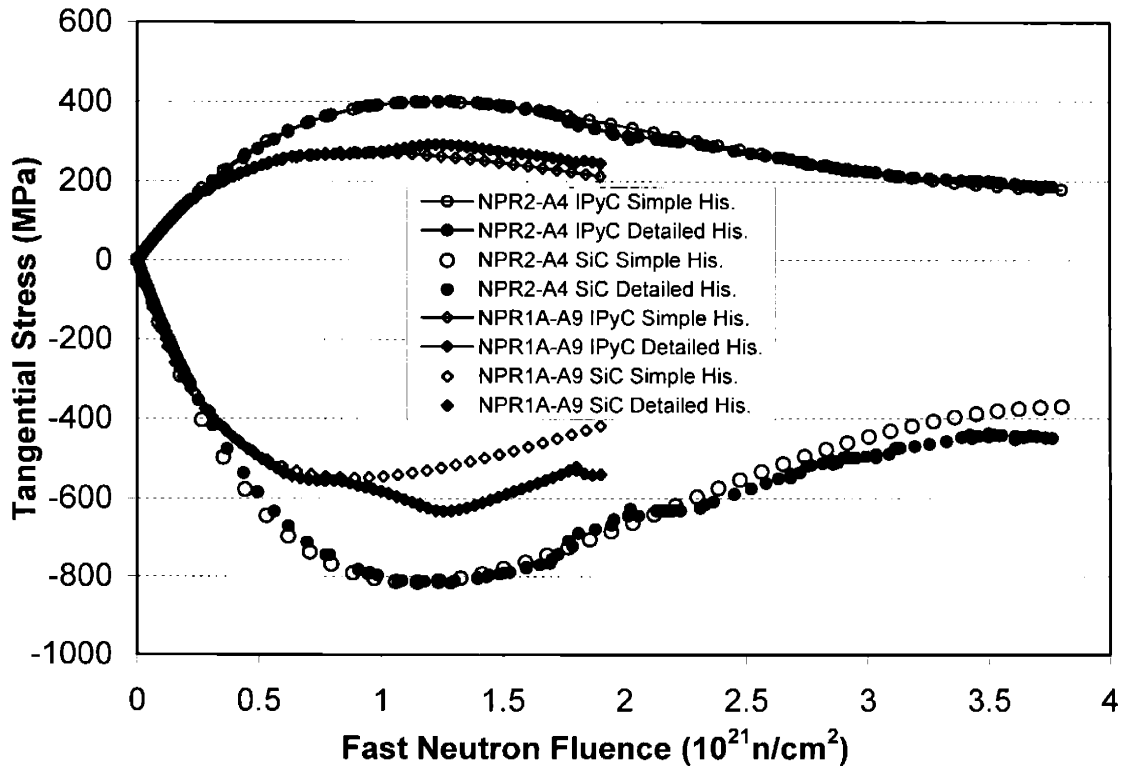
Figure 3-16. Stress in four PIE examined NPR compacts (2) (symbols for clarity)

150

Now we look at the stresses in four PIE examined compacts. They are plotted in Figure 3-15 and Figure 3-16, and again the symbols are for clarity and do not represent actual data points. In NPR1-A5 and NPR1-A8 compacts, using detailed irradiation histories causes lower stresses, which lowers the end-of-life particle failure probabilities and delays the point of initial failure. In Figure 2-28 for creep coefficient, we find the slope of creep coefficient goes up with temperature when the temperatures are higher than 600°C. In the range of about 600°C to 800°C, creep is not sensitive to temperature fluctuations, therefore in NPR2-A4 we don't see much difference in stresses whether or not detailed irradiation history is used. In NPR1A-A9, we see from Figure 3-11 that its irradiation temperature dropped from 1065°C to 975°C after 30 full power days (about $1.0 \times 10^{21} \text{n/cm}^2$), and induced a stress bump as shown in Figure 3-16, which produced a second wave of failure predictions in this compact. We can clearly see this from a failure history plot of NPR1A-A9 in Figure 3-17. In this part of predictions, the particle failure probability equates the SiC layer failure probability, because the assumption of CIFM1 is that once the SiC layer fails, the whole particles fails.
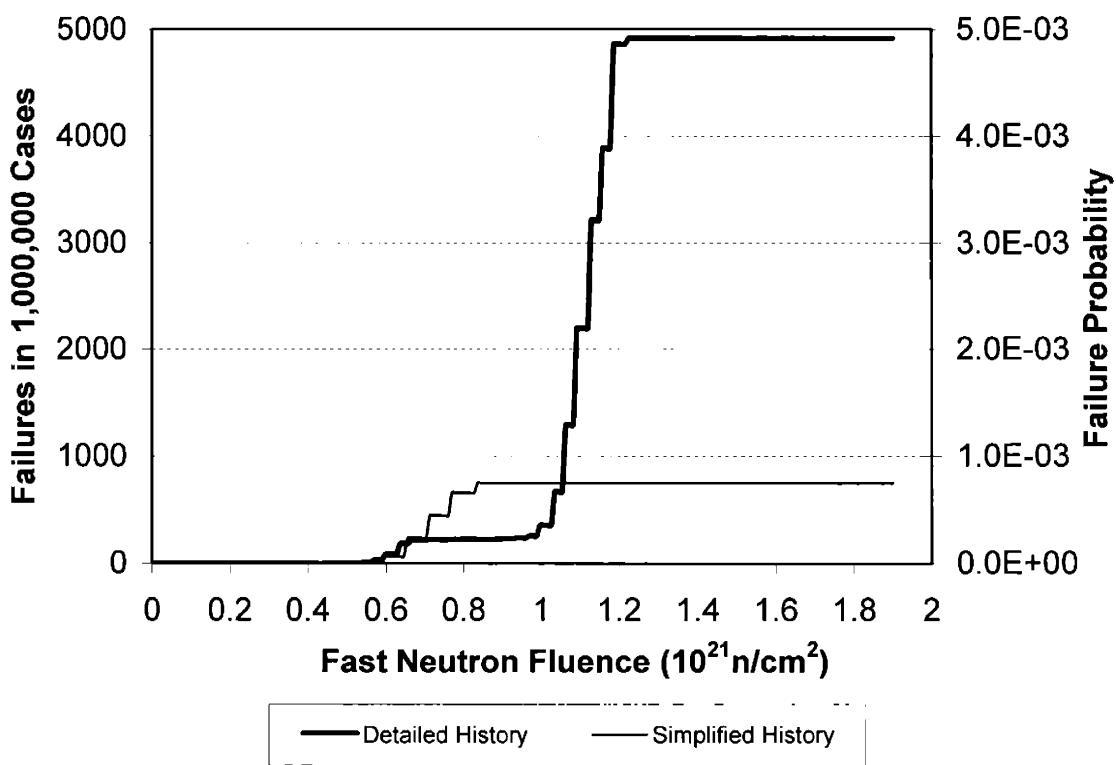
Figure 3-17. Particle failure history for NPR1A-A9

151

The experimental Kr^{85m} R/B curve provides information about the failure histories of the NPR capsules. In our case, since we modeled eight NPR1 compacts (effectively all sixteen compacts), we can construct a predicted R/B curve for NPR1 using the equations

$$\text{Number of failures} = N_i P_{fi}, \text{ and} \tag{3.2}$$

$$Kr^{85m} \text{ R/B} = \text{Number of failures} \times \text{R/B}_{\text{one failure}} + \text{R/B}_{\text{background}}, \tag{3.3}$$

where

N_i is the number of particles in each NPR1 compact, given in Table 3-6,

P_{fi} is the particle failure probability of each NPR1 compact,

$\text{R/B}_{\text{one failure}}$ is the amount of release for one particle failure, 1.7×10^{-7} for NPR1, and

$\text{R/B}_{\text{background}}$ is the background radiation, 1.0×10^{-8} for NPR1.

We then make a comparison with real R/B curve in Figure 3-18.
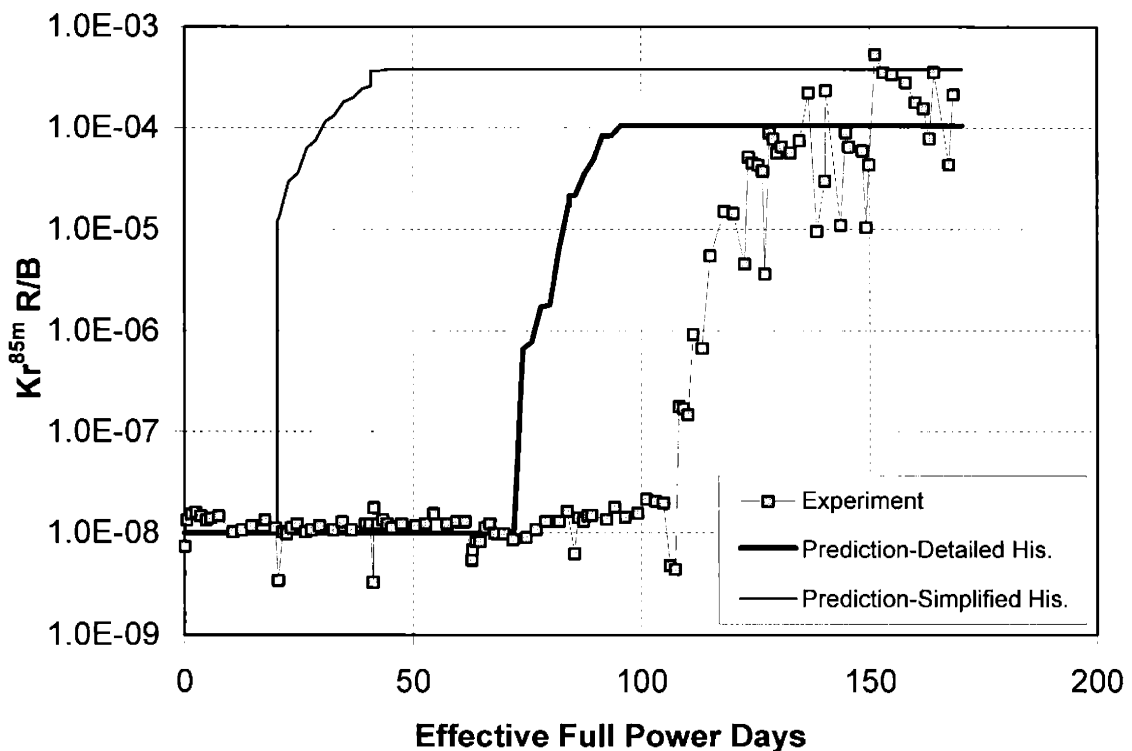
Figure 3-18. Kr^{85m} R/B for NPR1 capsule (Part I)

The prediction with detailed history compares much better than that with simplified history, both in terms of the end-of-life level of failures and the development of failures. Some statistics are given in Table 3-9. This emphasizes again the importance of including

irradiation histories in modeling particle fuel performance. However, our prediction with detailed histories is still earlier than actual failure development. Some thoughts on this discrepancy are given in the next section.

Table 3-9. Overall statistics for Capsule NPR1 (Part I)

	Actual	Prediction – Detailed History	Prediction – Simplified History
# Particles	77,500	77,500	77,500
# Failed Particles	625/526[†]	656	2384
Failure Probability	0.806%/0.679%[†]	0.846%	3.076%
Peak Fluence at Initial Failure (10^{21}n/cm^2)	1.7	0.59	0.071
Peak Burnup at Initial Failure (%FIMA)	72%	59%	24%
Effective Full Power Days at Initial Failure	108	74	20
Peak Temperature at Initial Failure (°C)	1123	1025	1086

([†]: estimated from Kr^{85m} R/B/estimated from ionization chamber spikes.)

Our last attempt in this section is to explore the effect of temperature uncertainty on NPR1-A8 compact. The uncertainty comes from thermal couple measurements, then the standard deviations on the calculated irradiation temperatures are derived [118]. We simply apply twice of the standard deviations on nominal temperatures to create a 95% confidence window, then we run simulations on NPR1-A8 with the upper and lower 95% bound temperature histories. The temperature histories are shown in Figure 3-19, and the resulting failure histories are in Figure 3-20. Based on this study, the failure probability of IPyC layers in NPR1-A8 could range from 32.3% to 83.0% (nominal 60.7%) and that of SiC layers from 0.38% to 6.74%, which overlaps the 95% confidence interval of SiC failure fraction from PIE results in Table 3-8. Although temperature uncertainty might be a factor in accounting for the low failure probability of NPR1-A8, it is definitely not the dominant one, because temperature uncertainty plays a role in any fuel compact. So there are still issues that we don't understand or haven't been able to model.
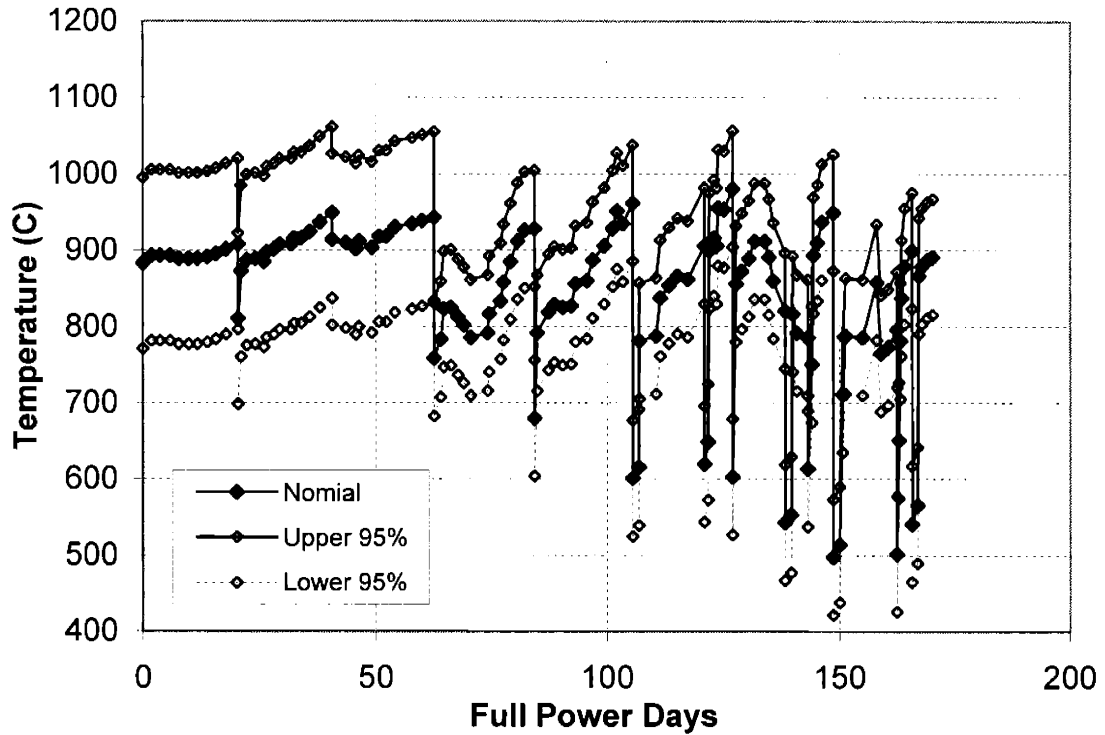
Figure 3-19. Temperature histories for compact NPR1-A8
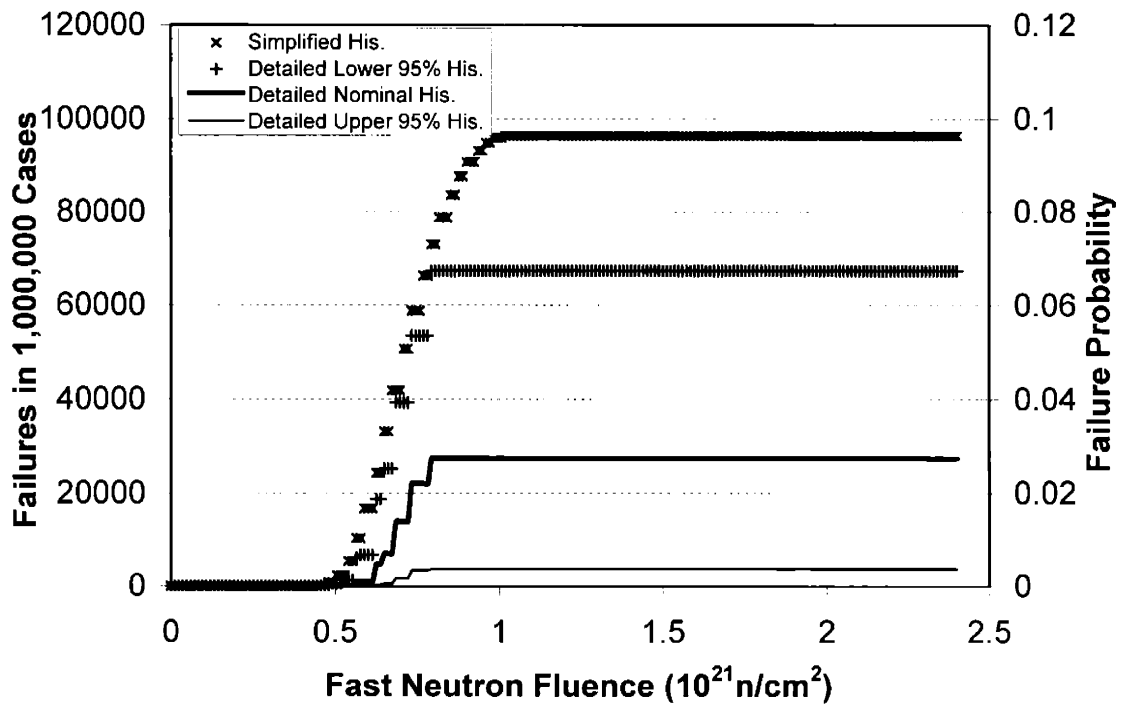
Figure 3-20. Predicted particle failure histories for compact NPR1-A8 (symbols for clarity)

154

3.2.3. Simulations with Improved Crack Induced Fuel Failure Model

After we developed the improved crack induced fuel failure model CIFM2, we used it and performed the second round simulations on the NPR compacts. Again 1,000,000 cases were sampled on each compact and the results are summarized in Table 3-10.

Table 3-10. Comparison of Model Calculations with PIE Results (Part II)

Compact ID	Failure Fraction (%)	95% Confidence (%)	w/ Detailed History, CIFM1 (%)	w/ Detailed History, CIFM2 (%)
IPyC Layer Failures				
NPR1-A1	-	-	47.4	46.9
NPR1-A2	-	-	6.44	6.27
NPR1-A3	-	-	15.0	14.5
NPR1-A4	-	-	33.5	32.8
NPR1-A5	31	17<p<47	26.6	25.9
NPR1-A6	-	-	24.4	23.8
NPR1-A7	-	-	15.6	15.3
NPR1-A8	6	2<p<16	60.7	60.3
NPR2-A4	65	54<p<76	99.6	99.6
NPR1A-A9	18	5<p<42	23.9	21.8
SiC Layer Failures				
NPR1-A1	-	-	1.61	1.21
NPR1-A2	-	-	1.00×10^{-4}	0
NPR1-A3	-	-	0.0250	0.0310
NPR1-A4	-	-	0.857	0.257
NPR1-A5	0.6	0<p<3	0.358	0.122
NPR1-A6	-	-	0.272	0.153
NPR1-A7	-	-	0.0683	0.0383
NPR1-A8	0	0<p<2	2.74	3.01
NPR2-A4	3	2<p<6	13.9	8.84
NPR1A-A9	1	0<p<5	0.492	0.0534

The predictions on IPyC layer failures from the new run are about the same as the old one. The newly predicted SiC layer failures are generally less because we allow for stress relaxation due to PyC cracking, as discussed in Section 2.5.2.2. However, now we also trace down the particles after the initial PyC cracking, unlike the scheme in failure model CIFM1, and by doing so whole particle failures which occur after the point of PyC

cracking could be discovered. These two effects tended to balance each other, and the predictions based on CIFM1 and CIFM2 happen to be quite comparable. Although with CIFM2 the assumption that SiC layer failures infer whole particle failures is dropped, in this round of simulations we found no intact pyrocarbon layers survived the failures of SiC layers, as a result, predicted particle failure probability is still the same as SiC layer failure probability. Now we plot the new Kr85m R/B curve together with the old ones in Figure 3-21.
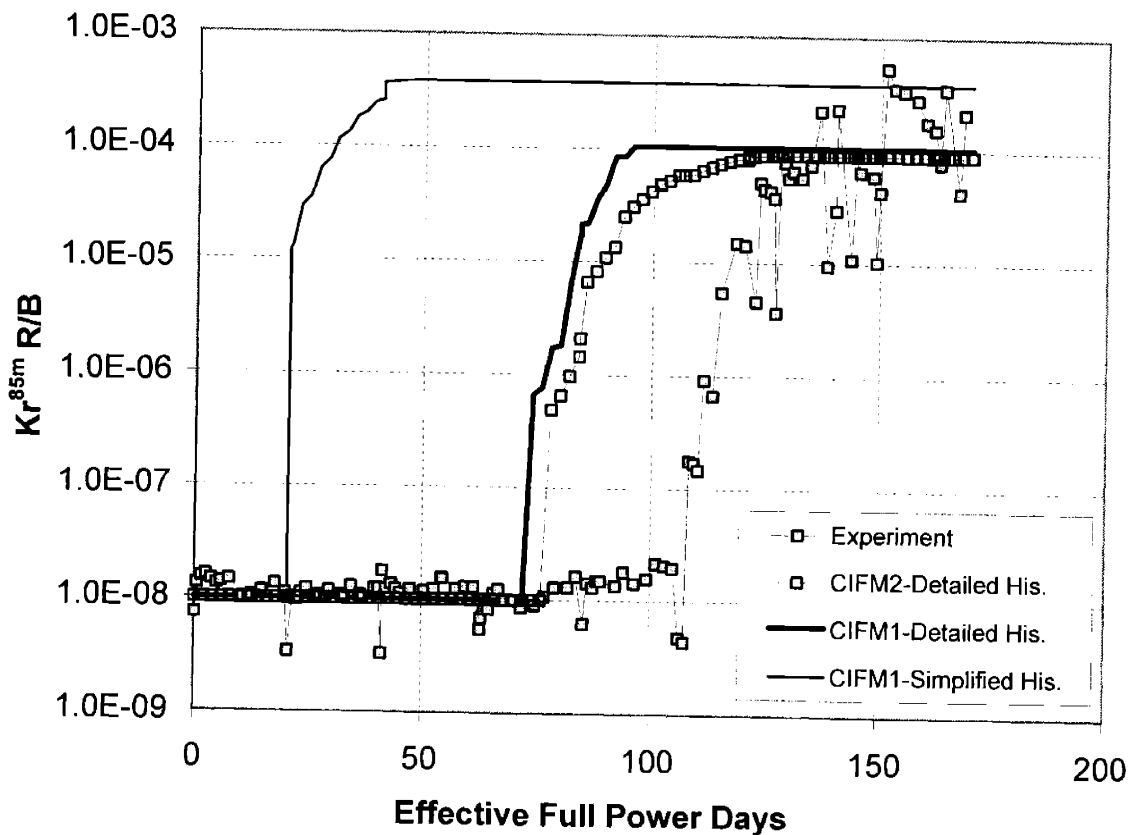
Figure 3-21. Kr^{85m} R/B for NPR1 capsule (Part II)

It can be seen that the main difference the new crack induced failure model CIFM2 makes is that the failure initiation point is delayed a bit because of the inclusion of stress relaxation. Also, the predicted failures occur in a much wider range from 78 full power days to 127 full power days than with CIFM1, which is from 74 full power days to 96 full power days. This is because some particle failures are captured due to further irradiation induced deformation after initial PyC cracking. The slower failure development is more like the real scenario. To illustrate the wider spread of failures predicted by CIFM2, we

156

collect in Table 3-11 the statistics for capsule NPR1 at peak failure rate instead of at initial failure as in Table 3-9.

Table 3-11. Overall statistics for Capsule NPR1 (Part II)

	Actual	CIFM1 – Detailed History	CIFM2 – Detailed History
# Particles	77,500	77,500	77,500
# Failed Particles	625/526[†]	656	565
Failure Probability	0.806%/0.679%[†]	0.846%	0.729%
Peak Fluence at Peak Failure (10^{21}n/cm^2)	2.17	1.08	1.48
Peak Burnup at Peak Failure (%FIMA)	75.3%	67.1%	71.2%
Effective Full Power Days at Peak Failure	124	90	102
Peak Temperature at Peak Failure (°C)	1107	1072	1134

([†]: estimated from Kr^{85m} R/B/estimated from ionization chamber spikes.)

Apparently CIFM2 is doing better in predicting particle failures in NPR1 capsule, but there is still a 30-day gap between model prediction and real data. One reason which leads to the opening of this gap is the existing assumption in CIFM2, which requires zero time for PyC cracks to connect with SiC layer surface irregularities. We have said in Section 2.5.2.2 that actually there will be a small ligament between the PyC crack and SiC surface, and it takes some time to break it.

A couple of mechanisms could contribute to breaking the ligament. The first one is creep crack growth [94]. Due to stresses and irradiation, strains accumulate at a macroscopic crack tip and cause the crack to grow. A quantity called the C* integral was proposed by Landes and Begley [119], Ohji et al. [120], and Nikbin et al. [121] independently after the establishment of the J integral, to characterize crack growth in a material undergoing steady state creep. They applied Hoff's analogy [122] to a visco-elastic body and defined the C* integral by replacing strains and displacements with strain rates and displacement rates in the J contour integral, respectively, and got

157

$$C^* = \int_{\Gamma} \left(\dot{w}dy - \sigma_{ij}n_j \frac{\partial \dot{u}_i}{\partial x} ds \right),$$ (3.4)

where $\dot{w}$ is the strain energy rate, defined as

$$\dot{w} = \int_0^{\dot{\varepsilon}_{kl}} \sigma_{ij} d\dot{\varepsilon}_{ij},$$ (3.5)

$\dot{\varepsilon}_{ij}$ and $\dot{u}_i$ are the strain and displacement rates, respectively,

σ_{ij} are the stress components,

n_j are the normals to unit surface ds along the integrated contour.

Experimental works have shown that creep crack growth rates correlate very well with C* integral in the following form [123],

$$\dot{a} = \gamma \left(C^* \right)^m,$$ (3.6)

where γ and m are material constants. Unfortunately, these constants are not available for pyrocarbons, so we cannot perform a quantitative estimation for now. We suggest that these constant be measured with respect to irradiation creep in pyrocarbons.

Another mechanism which could break the ligament is thermal fatigue cycling. In NPR capsule irradiations, there were eight major cycles and a number of small ones. They could induce fatigue crack growth at the macroscopic crack tip.

Lastly we discuss the types of failures and the failure paths of particles in NPR irradiation simulations.

Table 3-12. Failure types in NPR compacts predicted with CIFM2

Compact ID	# Sampled Particles	PyC Crack Induced Failures	Pressure Vessel Failures
NPR1-A1	1,000,000	12,062	2
NPR1-A2	1,000,000	0	0
NPR1-A3	1,000,000	310	0
NPR1-A4	1,000,000	2565	0
NPR1-A5	1,000,000	1221	1
NPR1-A6	1,000,000	1526	0
NPR1-A7	1,000,000	383	0
NPR1-A8	1,000,000	30,107	0
NPR2-A4	1,000,000	88,427	3
NPR1A-A9	1,000,000	534	0

The particle failures predicted by the new round of simulations with CIFM2 are categorized with failure types in Table 3-12. It can be seen that most of the predicted failures are induced by either IPyC or OPyC cracking. However, Closer inspection of each failed particle revealed that most common failure paths of those failed particles are (ISO) → (FSO) → (FSF) → (FFF) or (ISO) → (ISF) → (FSF) → (FFF) (Refer to Figure 2-46), which means the stress concentration won't be high enough until both structural pyrocarbon layers fail, because when either pyrocarbon layer is intact, the SiC layer is in compression and there is an effective negative stress intensity factor which protects the SiC layer. We plot in Figure 3-22 the stress concentrations in three failed particles from compact NPR1-A1, and their parameters are listed in Table 3-13.

Table 3-13. Parameters of Three Failed Particles in Compact NPR1-A1

Parameter	Particle 1	Particle 2	Particle 3
Failure Type	PyC crack induced	PyC crack induced	Overpressure
Fluence at Failure (10^{21}n/cm^2)	1.256	0.839	1.885
U235 Enrichment (%)	93.15	93.15	93.15
Kernel Diameter (μm)	194.8	196.8	200.8
Buffer Thickness (μm)	80.8	91.5	98.3
IPyC Thickness (μm)	53.6	56.3	60.0
SiC Thickness (μm)	36.4	31.3	36.8
OPyC Thickness (μm)	34.2	42.5	42.4
Kernel Density (g/cm^3)	10.51	10.51	10.51
Buffer Density (g/cm^3)	0.979	0.937	0.953
IPyC BAF$_0$	1.0514	1.0593	1.0553
OPyC BAF$_0$	1.0405	1.0440	1.0430
IPyC σ_0 (MPa.m$^{3/\beta}$)	19.9	16.6	21.2
OPyC σ_0 (MPa.m$^{3/\beta}$)	13.1	13.4	14.1
SiC σ_0 (MPa.m$^{3/\beta}$)	8.33	10.8	1.51
SiC K_{IC} (MPa. μm$^{0.5}$)	3541	3505	3683

In Particle 1, the OPyC layer failed first at 0.535×10^{21}n/cm^2, later the IPyC layer failed at 0.724×10^{21}n/cm^2, and finally the stress concentration from the IPyC layer cracked the SiC layer at 1.256×10^{21}n/cm^2. In Particle 2, the IPyC layer failed first at 0.431×10^{21}n/cm^2, later the OPyC layer failed at 0.535×10^{21}n/cm^2, and finally the stress

concentration from the IPyC layer cracked the SiC layer at 0.839×10^{21}n/cm^2. In Particle 3, the OPyC layer failed first at 0.742×10^{21}n/cm^2, later the IPyC layer failed at 0.784×10^{21}n/cm^2, and finally at 1.885×10^{21}n/cm^2 the tangential stress in the SiC layer exceeded its fracture strength of 74MPa in this case and caused a pressure vessel failure. We see that the probability of pressure vessel failure is very small and in NPR irradiation simulations, such failure might happen when both PyC layers of a particle are failed and this particle has an extremely weak SiC layer.
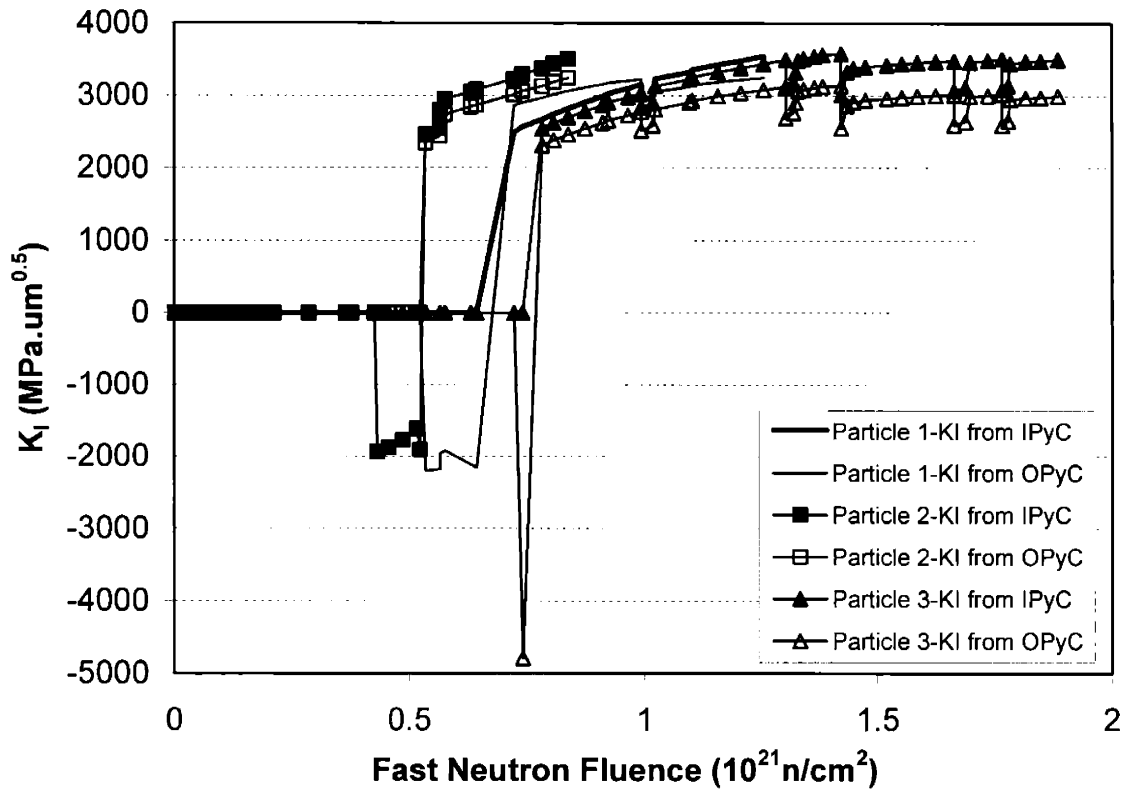
Figure 3-22. Stress concentrations in some failed particles in compact NPR1-A1 (symbols for clarity)

3.2.4. Further Discussion of NPR Irradiation Results

We have shown that the new crack induced fuel failure model is very promising in explaining the higher-than-expected NPR fuel failures, but the model itself doesn't tell why U.S. and German fuel particles had such different performance. Petti et al. [89] discussed the differences in the microstructures of layers of U.S. and German fuel which

probably accounted for their different behaviors. The three major differences were stated to be: pyrocarbon anisotropy and density, IPyC/SiC interface structure, and SiC microstructure.

(1) General Atomics produced pyrocarbon layers generally have laminar structure of high density and anisotropic behavior, resulting from low coating gas concentrations and low deposition rates. However, German fuel manufacturers used higher coating gas concentrations and coating rates, which yielded lower density and more isotropic pyrocarbons. We will see in Chapter 4 that higher anisotropy of pyrocarbon layers leads to higher tangential (hoop) stresses in them, which may lead to higher probability of cracking even though the strength of pyrocarbons also go up with anisotropy, as we discussed in Section 2.5.1. This aspect of pyrocarbons can be accounted for in our new crack induced failure model.

(2) The second important difference between U.S. and German particles is the IPyC/SiC interface. In the German process, each layer of the particles is deposited in the coater in a continuous manner on one pass without any interruption, whereas in the U.S. process, the particles are unloaded after each layer of deposition for QC measurements. As a result, there was a mixing zone of PyC and SiC grains in the German fuel which provided a tight bond between two layers. In fact the coatings of German fuel particles never exhibited debonding under irradiation. However, there existed natural smoother boundaries between PyC and SiC layers in the U.S. fuel particles, which led to less strong bond. Interface debonding as shown in Figure 2-42 happened in U.S. fuel like NPR fuel quite frequently. Debonding generates an interfacial crack which will cause stress concentration in the SiC layer, like a normal radial crack in PyC layer will do. In fact the very possible particle failure pattern in NPR fuel is that firstly a PyC layer cracks radially and it deflects along the PyC/SiC interface and then kinks into the SiC layer at some location. The failure pattern we have talked about in Section 2.5.2.2 is just one scenario, and the crack may choose among various paths depending on available strain energy and local material fracture resistance. In U.S. made fuel where interface bonding is weak, PyC cracks could preferably choose to grow along the interfaces. Hutchinson and Suo [95] discussed the critical driving forces or resistances to various cracking patterns in a film-

substrate configuration. The dimensionless driving force Z is given in Figure 3-23, and we can find the similarities between that system and our case here. In the figure, h and E_f is the thickness and Young's modulus of the film, respectively. The interfacial debonding/cracking in TRISO fuel particles is not ready to be modeled because the interfacial strength of PyC/SiC configuration and its relationship with microstructures are to be determined by experiments.
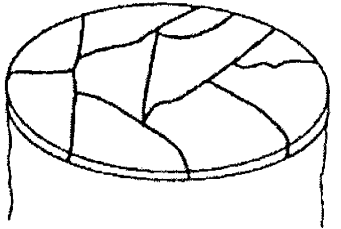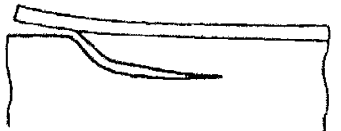
Cracking Patterns $\mathcal{G} = Z\sigma^2 h/\bar{E}_f$

Surface Crack

$Z = 3.951$

Channeling

$Z = 1.976$

Substrate Damage

$Z = 3.951$

Spalling

$Z = 0.343$

Debond

$Z = \begin{cases} 1.028 \text{ (initiation)} \\ 0.5 \text{ (steady - state)} \end{cases}$

Figure 3-23. The dimensionless driving force for various cracking patterns in film-substrate system, assuming each material is elastically homogeneous, and the substrate is infinitely thick (from Hutchinson and Suo [95])

162

(3) The third difference lies in the strength-microstructure correlation of SiC. It was reported by Saurwein and Schilling [124] that NPR fuel particles presented columnar SiC grains as long as 30μm, which is comparable with the thickness of the SiC layer, while only smaller grains about 2μm were found in German fuel particles, as shown in Figure 3-24. The long SiC grains in U.S. fuel are formed in high temperature in the GA process, but the German deposition temperature is lower. As we discussed in Section 2.5.1, the strength of brittle SiC may decrease with increasing grain sizes. Also, bigger grains provide effectively deeper extrusions and intrusions at the SiC layer surface which serve more easily as crack initiation sites. This can be treated with our new crack induced failure model by varying the surface flaw sizes to differentiate U.S. fuel from German fuel.
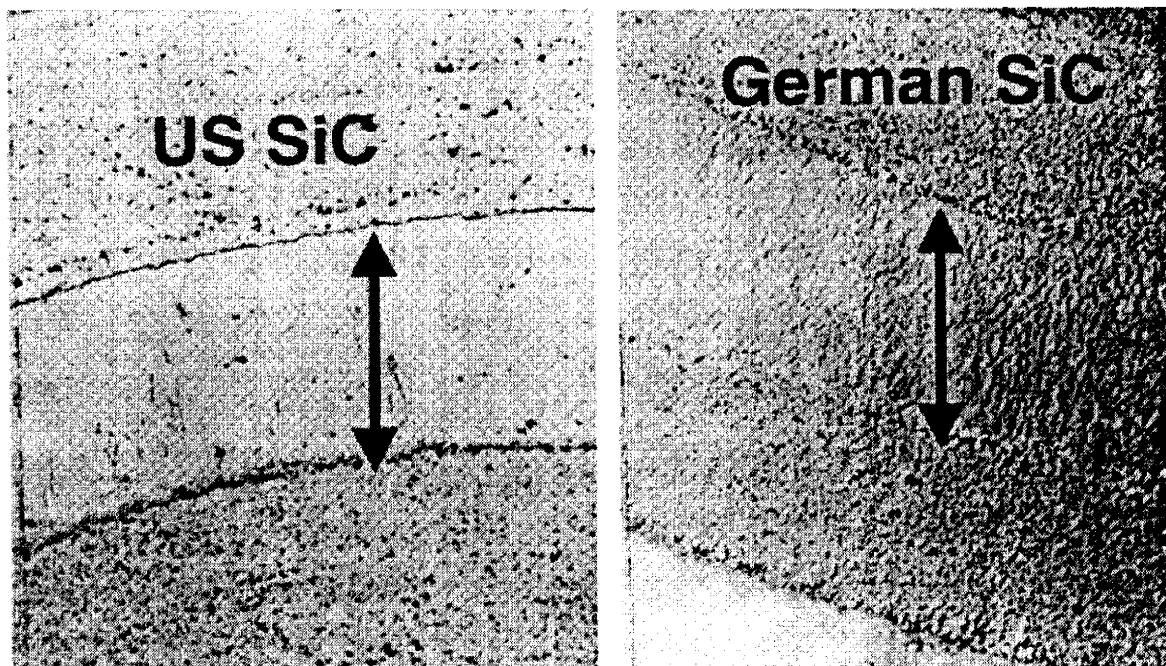
Figure 3-24. Morphology of the SiC layers in U.S. particle (left) and German particle (right) (from Saurwein and Schilling [124])

It is also possible, and the INEEL scientists give significant importance to this, that the interrupted coating process allowed for the introduction of metallic element contamination (from storage containers or inspection using metallic table tops) at the layer interfaces. Recent discussions indicate that individual failures of particles were associated with the presence of metallic element contamination.

163

Chapter 4.

Optimization of Fuel Particles Using the MIT Model

Based on the results of the benchmarking process we now are confident that we can predict, at least in a relative sense, of how coated fuel particles behave under irradiation and what some of the important variables (PyC layer stresses, strengths, etc.) are in determining fuel performance. We also have some knowledge of how certain input parameters affect fuel performance, for example, in Section 2.4.6, we showed in particles with bigger fuel kernels, the stresses in layers are lower because of higher internal pressure. In this chapter, we systematically study the links between input parameters and fuel performance. Suppose we can manufacture a batch of coated fuel particles that match their specifications, our task is to find a set of specifications for particles which would allow for best fuel performance in certain irradiation condition within the scope of our knowledge. The procedure of reaching this goal is called fuel performance optimization.

4.1. Parametric Study

As the first step of fuel performance optimization, we conduct a parametric study on fuel particles. Our developed fuel performance model provides the mapping between input parameters and fuel particle behavior, and here the parametric study looks at how fuel particle behavior changes over a range of input parameters.

Firstly we choose sixteen input parameters to do the parametric study and the ranges of their values are listed in Table 4-1. Some ranges were established based on existing values in the industry, such as SiC layer thickness and buffer density; some ranges are restricted by the current material models, for example, the densities of dense pyrocarbons should be between 1.8 to 2.0g/cm³ because BAFs and irradiation induced dimensional changes data of pyrocarbons were rare out of this range; Some ranges are selected to be reasonable with engineering judgments and modeling esxperience. These parameters can

be grouped into three types: dimensional parameters, material properties, and environmental parameters.

Table 4-1. Value Ranges for Input Parameters in Parametric Study

Parameter	Low	Nominal	High
Kernel Diameter (μm)	100	400	700
Buffer Thickness (μm)	40	120	200
IPyC Thickness (μm)	20	40	60
SiC Thickness (μm)	20	40	60
OPyC Thickness (μm)	20	50	80
U^{235} Enrichment (%)	4	93	96
Kernel Density (g/cm^3)	10.4	10.5	10.6
Buffer Density (g/cm^3)	0.9	1.0	1.1
IPyC Density (g/cm^3)	1.8	1.9	2.0
OPyC Density (g/cm^3)	1.8	1.9	2.0
IPyC BAF$_0$	1.0	1.15	1.30
OPyC BAF$_0$	1.0	1.15	1.30
Irradiation Temperature (°C)	500	900	1300
EOL Fluence (10^{21}n/cm^2)	2.5	3.0	3.5
EOL Burnup (%FIMA)	60	70	80
Ambient Pressure (MPa)	0	6.4	12.8

4.1.1. Perturbation Analysis

We have shown in Section 2.4.6 that the stresses in the three structural layers of fuel particles mainly come from their interactions due to the mismatch in irradiation induced deformation. Therefore when the pyrocarbon layers are in higher tension, the SiC layer will be in higher compression. Meanwhile, since the SiC layer is much more rigid than PyC layers, it is a very good decoupling boundary, which means the behavior of two adjacent PyC layers are roughly independent. Given these practical observations, we choose to primarily monitor the maximum IPyC and OPyC stresses throughout the life of irradiation, which are the critical variables in judging IPyC and OPyC layers failures. Typically the maximum PyC stresses occur at a fluence of around 1.0×10^{21}n/cm^2. We will also look at minimum SiC stress when it needs to be mentioned. Perturbation analysis is performed on each input parameter by fixing other parameters at their nominal values and scanning this specific parameter from its low value to high value.

4.1.1.1. Fuel Kernel Diameter

The results for the perturbation on fuel kernel diameter is shown in Figure 4-1
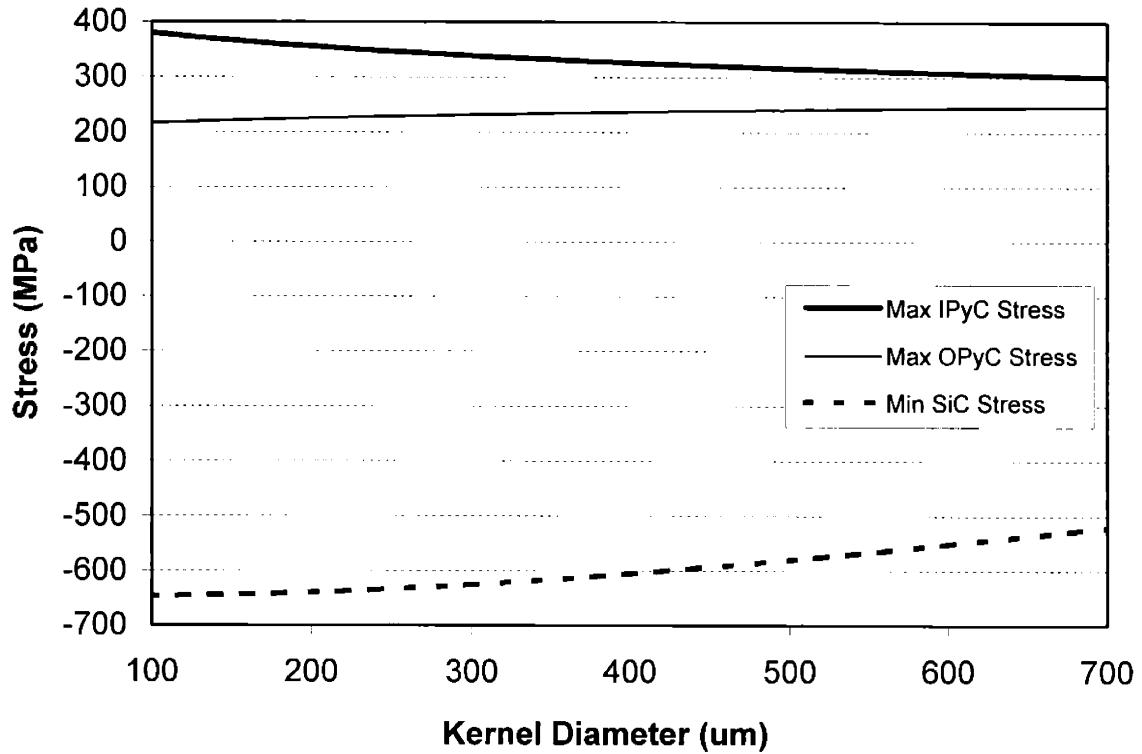
Figure 4-1. Stresses in structural layers versus fuel kernel diameter

Again we remember that the maximum IPyC stress refers to the highest point on the IPyC tangential stress (averaged over its cross section) curve such as is shown in Figure 3-5. The maximum IPyC stress decreases as the kernel diameter increases, because more and more fission gases are generated to produce higher pressure which counteracts the pulling-apart tension at IPyC/SiC interface. Consequently, the compression in the SiC layer is weakened. The effect on the OPyC layer is the reverse to the IPyC layer because the OPyC layer is on another side of the SiC layer, therefore higher internal pressure reinforces the compression at SiC/OPyC interface. From the plot we see the effect on IPyC and SiC is stronger than in the OPyC layer, and conclude that, all other variables being equal, a larger fuel kernel would favor better fuel particle performance within limits.

4.1.1.2. Buffer Thickness

The perturbation results on buffer thickness are shown in Figure 4-2.
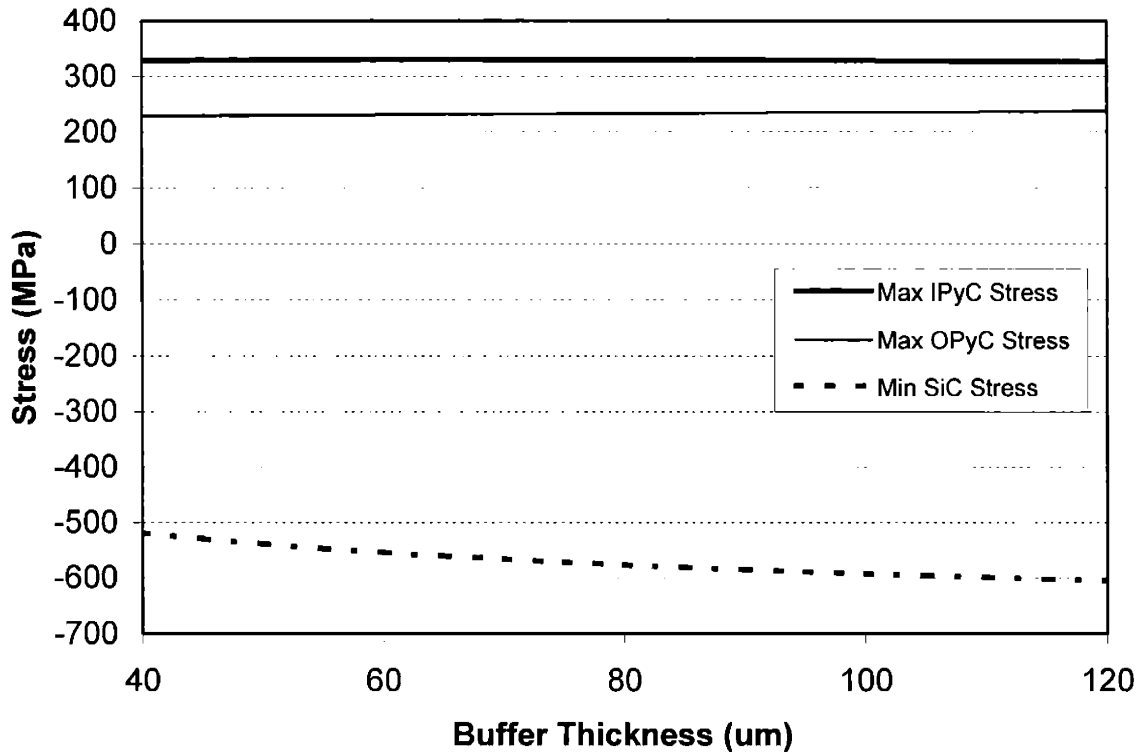
Figure 4-2. Stresses in structural layers versus buffer thickness

The increase of buffer thickness provides more free volume for fission gases, so the internal pressure decreases. The effect is not clearly shown in the IPyC and OPyC layers, but it is magnified in the SiC layer because the Young's modulus of SiC is one order of magnitude higher than that of the PyC. The thickening of the buffer layer also effectively increases the radii of all three structural layers, which influences their stresses in a way that is less obvious. It will be shown later that since the buffer and fuel kernel together determine the internal pressure, their effects should be bound to reveal a general trend.

4.1.1.3. IPyC and OPyC Thicknesses

The perturbation results on IPyC and OPyC thicknesses are shown in Figure 4-3 and Figure 4-4.
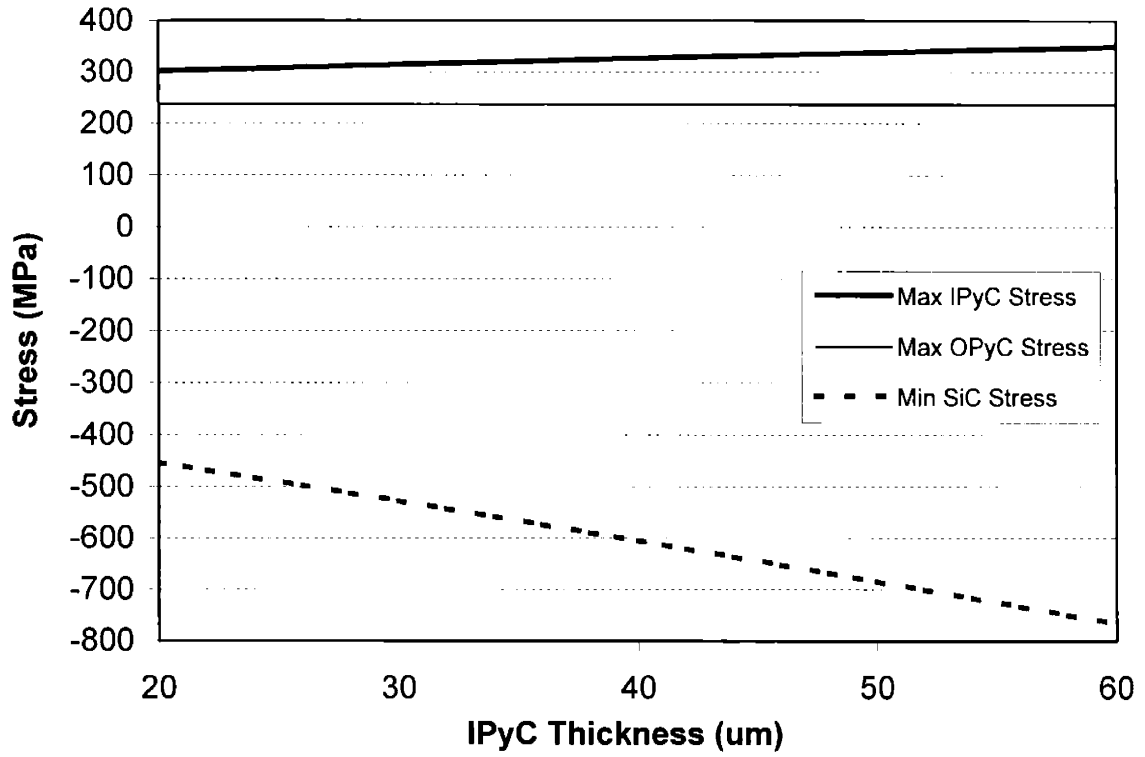
Figure 4-3. Stresses in structural layers versus IPyC thickness
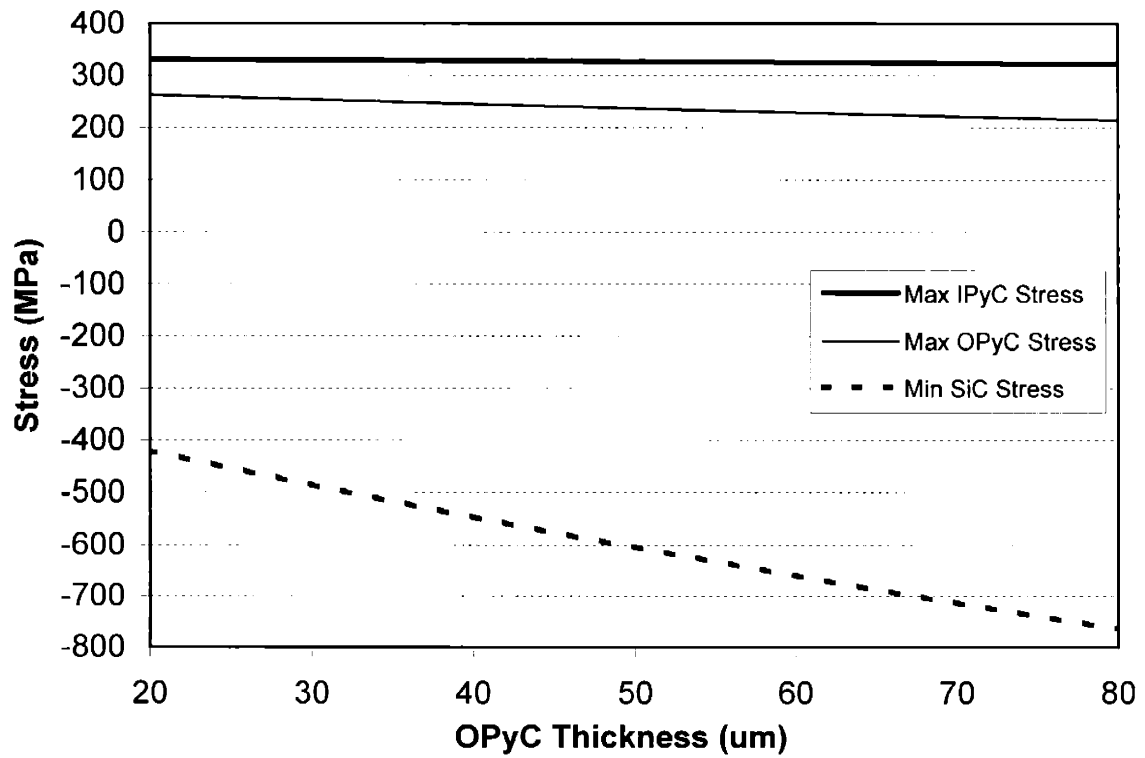
Figure 4-4. Stresses in structural layers versus OPyC thickness

The thickening of the IPyC layer has two results. Firstly it is effectively stronger and more resistant to external forces. Secondly, the radius of IPyC/SiC interface is increased, which brings in the following subtle effect. Suppose the IPyC outer surface is free, the radial displacement at that location is

$$u_r(r = r_3) \cong \int_{r_2}^{r_3} S_r dr,\qquad (4.1)$$

where S_r is the radial irradiation induced dimensional change. Here we need to understand that irradiation induced deformation does not store strain energy in the materials because that is plastic permanent deformation. The elastic interaction between structural layers does. When we attach the SiC layer onto it, it will drag the IPyC/SiC interface back to its original place before irradiation, roughly speaking. According to this, thicker IPyC layer will cause more work to be done and more strain energy to be stored in both IPyC and SiC layers. That explains the behavior we see in Figure 4-3. We also find that the SiC layer basically absorbs the changes to the IPyC layer, so the OPyC layer barely sees any difference. This is what we mean by decoupling.

The case of thickening of the OPyC layer differs in that the position of SiC/OPyC interface is not shifted by it, and the outer surface of the OPyC layer can be regarded as a free surface. The thicker hence stronger OPyC layer compresses more heavily on the SiC layer, as shown in Figure 4-4. Although OPyC outer surface displaces more, that doesn't induce more stress because the surface can move freely. The combined effect is that the OPyC layer has thicker cross section to balance the moderately increased interfacial force from the SiC layer, and the result is the average stress in OPyC is lower. Again in this case the IPyC layer doesn't see much difference because of the shielding from SiC.

Based on the study in this part, we should make IPyC as thin as possible and OPyC as thick as possible.

4.1.1.4. SiC Thickness

The perturbation results on SiC thickness are shown in Figure 4-5. As we said for PyC thicknesses, a thicker SiC implies it is stronger, then it is more resistant to pyrocarbon deformation and leads to higher stresses in IPyC and OPyC. At the same

time, it has more volume itself to accommodate the stronger interactions from PyC layers, so its stress is less negative. When the SiC layer becomes thinner and thinner, the increase in compression accelerates and the layer may reach its buckling strength. From a mechanical point of view, we want the SiC layer to be thin but not too thin. Practically, there are other considerations that put constraints on the SiC thickness. For example, if it is too thin, some fission products may easily permeate through an intact layer.
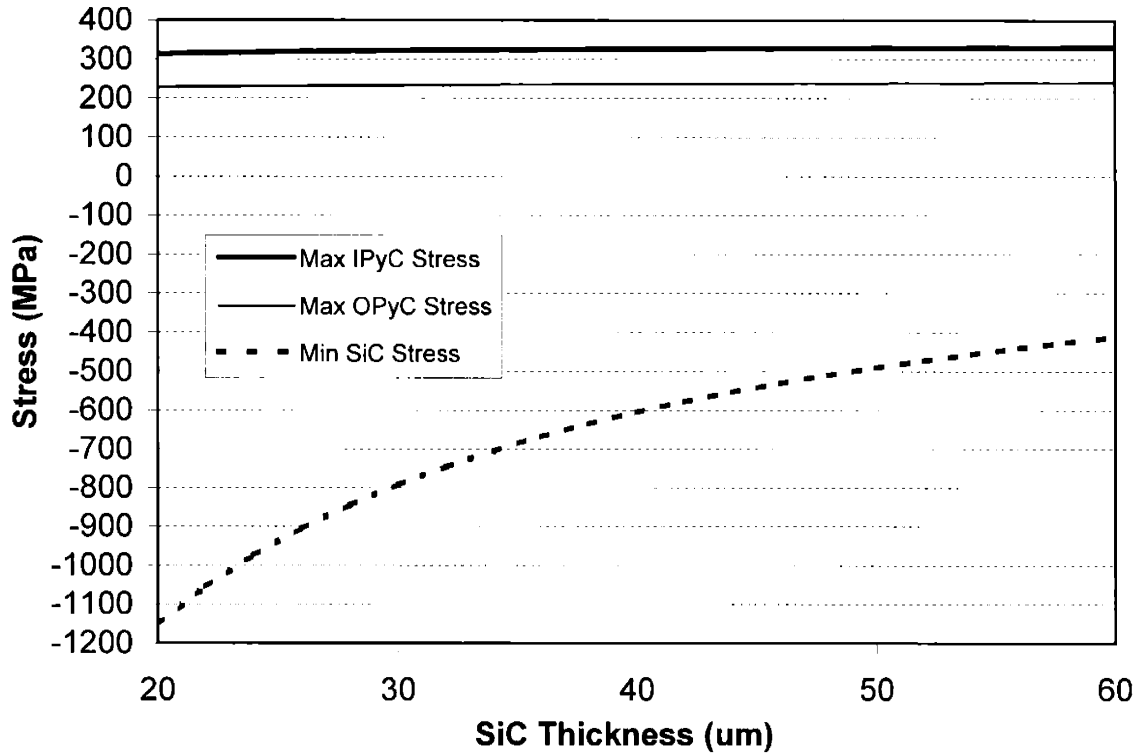
Figure 4-5. Stresses in structural layers versus SiC thickness

4.1.1.5. IPyC and OPyC BAF_0

The perturbation results on IPyC and OPyC BAF_0 are shown in Figure 4-6 and Figure 4-7. As pyrocarbon becomes more and more anisotropic, the magnitude of irradiation induced dimensional changes are bigger, as shown in Figure 2-24, so the stresses in the corresponding PyC layer and the SiC layer are intensified. We find again that the tuning of IPyC BAF_0 does not affect the stress in the OPyC layer, and vice versa.
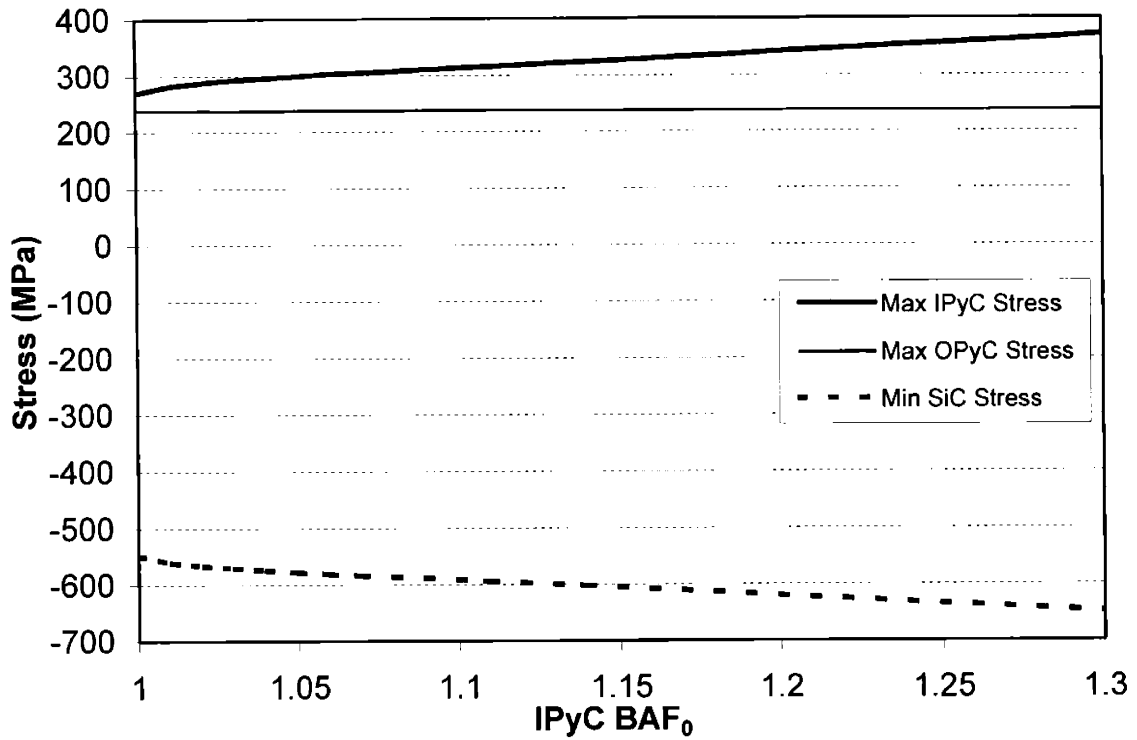
Figure 4-6. Stresses in structural layers versus IPyC BAF_0
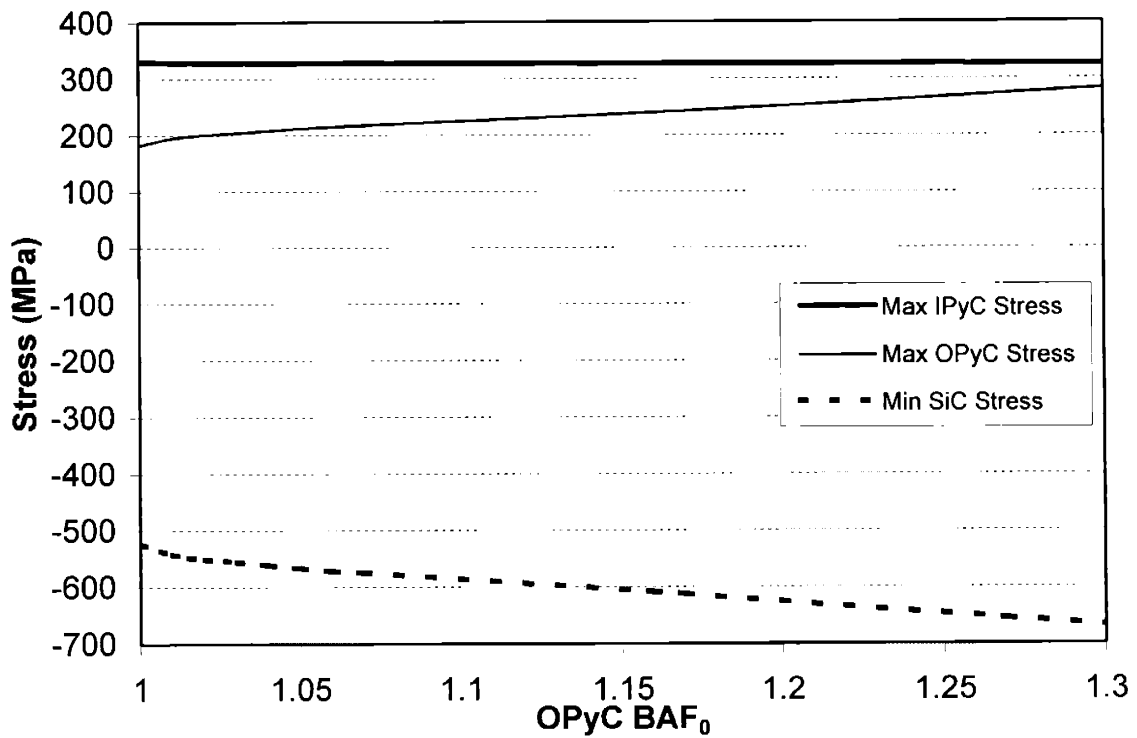
Figure 4-7. Stresses in structural layers versus OPyC BAF_0

4.1.1.6. Fuel Kernel and Buffer Densities

The perturbation results on fuel kernel density are shown in Figure 4-8. Fuel kernel density and buffer density only influence fuel performance through fuel internal pressure, because the closer they get to their theoretical densities, the less free volume they are able to contribute for fission gases. It can be seen that the stresses are almost independent of the kernel density, and we can neglect it from mechanical fuel performance viewpoint. If we plot the stresses as a function of buffer density, it will look the same as Figure 4-8, therefore buffer density is not a parameter of interest as well.
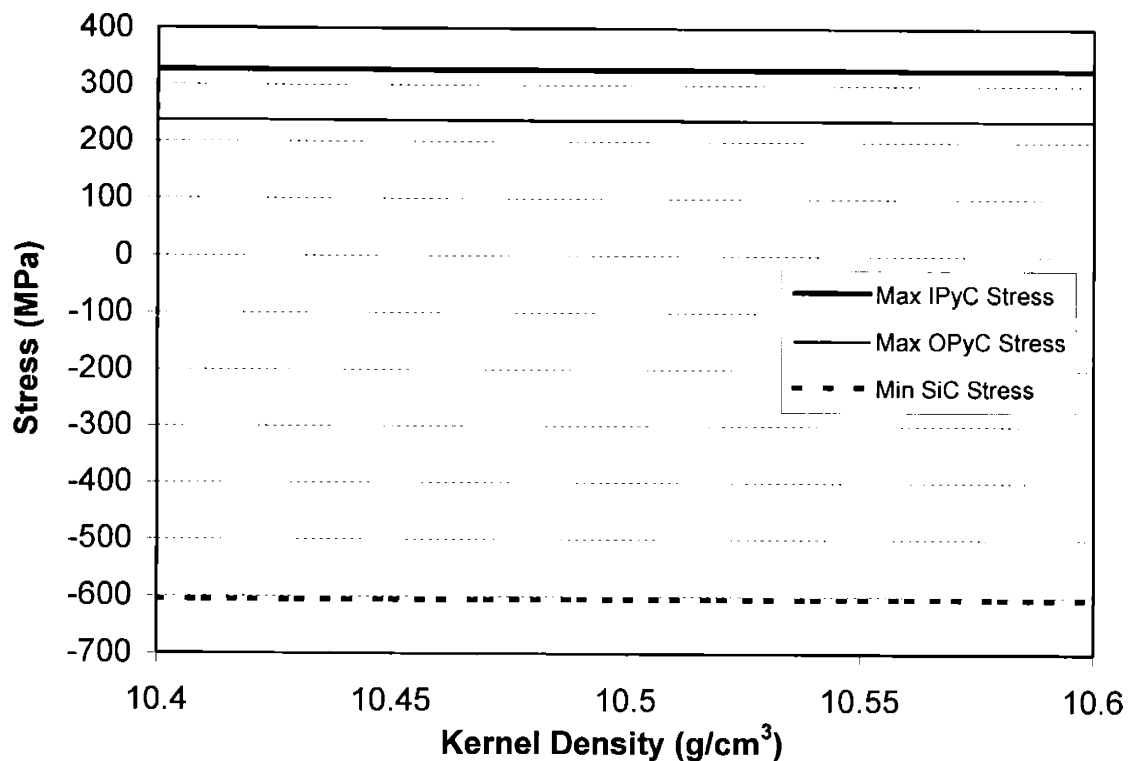
Figure 4-8. Stresses in structural layers versus fuel kernel density

4.1.1.7. IPyC and OPyC Densities

The perturbation results on IPyC and OPyC densities are shown in Figure 4-9 and Figure 4-10. PyC density strongly correlates with PyC BAF_0, and affects fuel performance in a complicated way. But they don't look like major players.
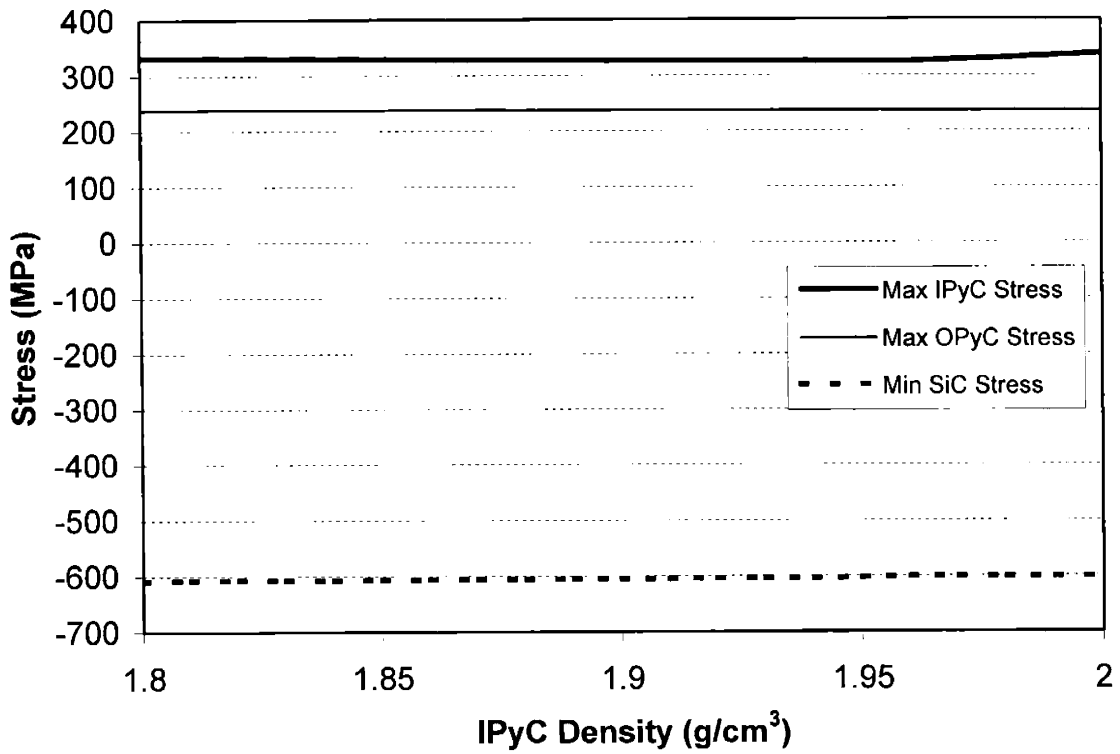
Figure 4-9. Stresses in structural layers versus IPyC density
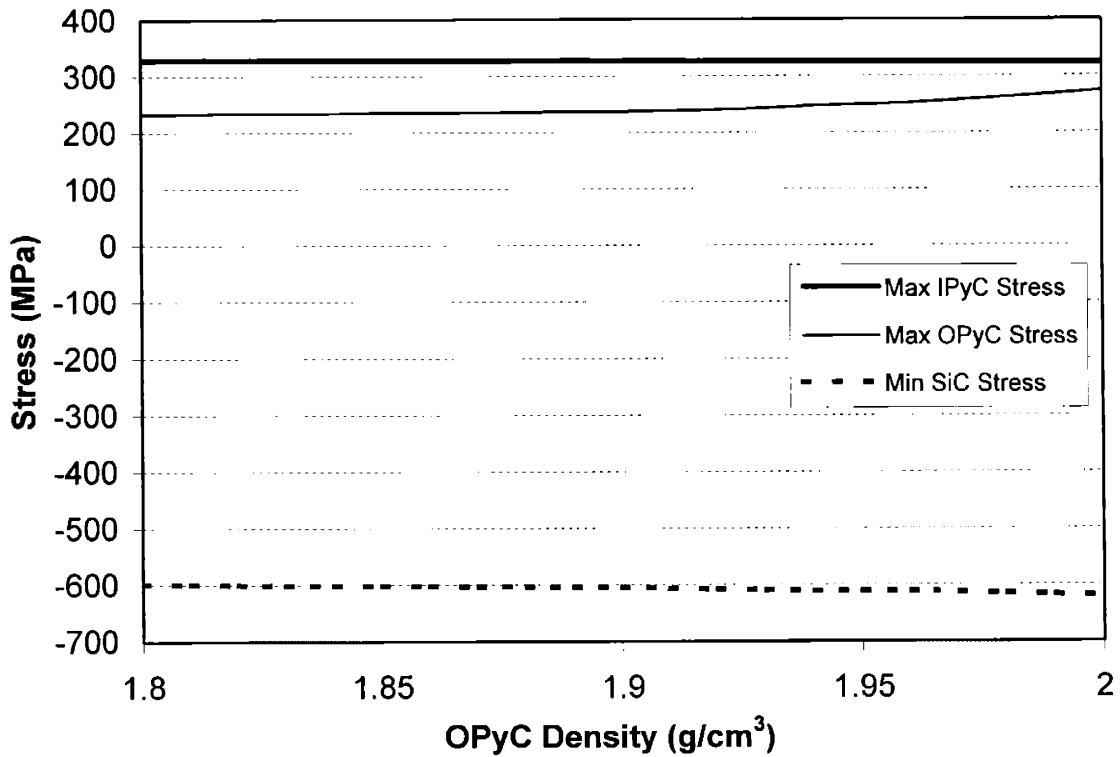
Figure 4-10. Stresses in structural layers versus OPyC density

173

4.1.1.8. Irradiation Temperature

The perturbation results on irradiation temperature are shown in Figure 4-11.
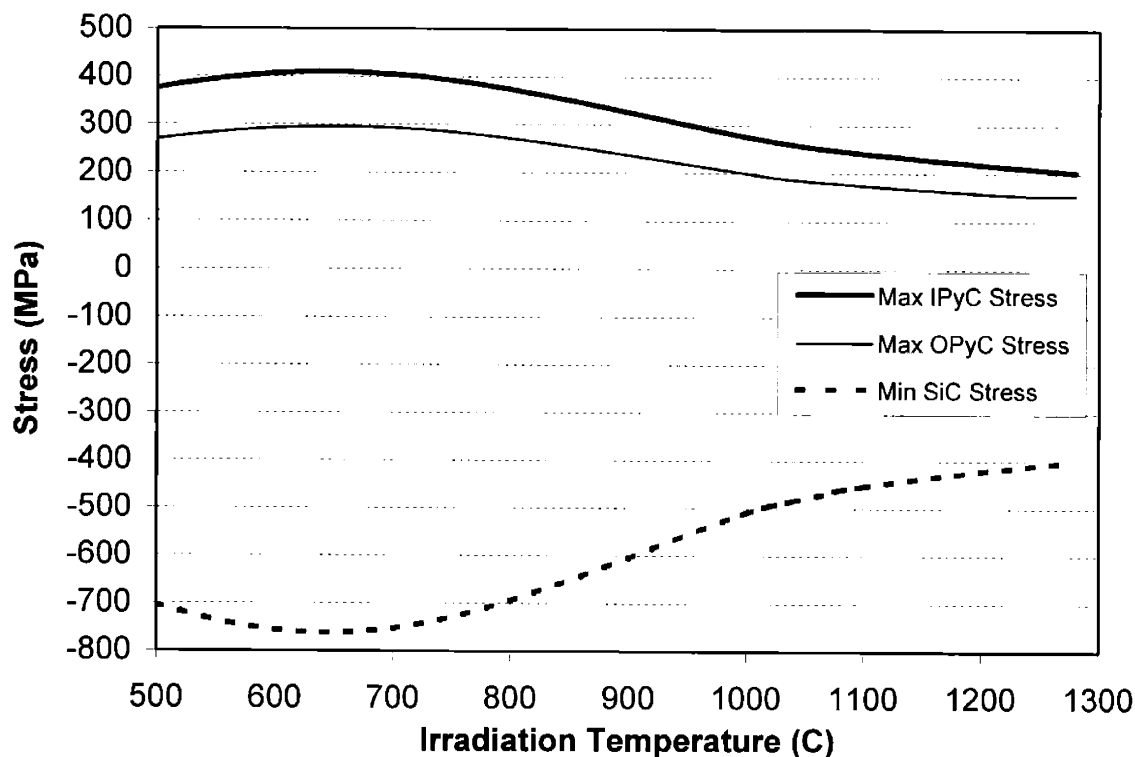
Figure 4-11. Stresses in structural layers versus irradiation temperature

Not surprisingly irradiation temperature dramatically influences stresses in fuel particles in a non-linear way. This comes from the temperature dependent creep coefficient we discussed in Section 2.4.4. According to the pyrocarbon creep model, creep is least active around 600°C. As temperatures rises, more and more stress relaxation takes place and we see the behavior in the above figure. It should be noted that the quadratic temperature dependency of creep coefficient might be a fitting artifact, so we should use it with cautiousness. However, high temperature promotes irradiation creep is supported by many experimental evidences, so the stress-temperature relationship above 600°C is trust-worthy.

4.1.1.9. Ambient Pressure

The perturbation results on ambient pressure are shown in Figure 4-12. Most load from the environment is taken by the SiC layer, and when ambient pressure is higher, the SiC layer is in higher compression. The OPyC layer shows a little less tensile stress when ambient pressure goes up, because ambient pressure helps the OPyC layer to press the SiC layer, so OPyC feels less onerous in the action.
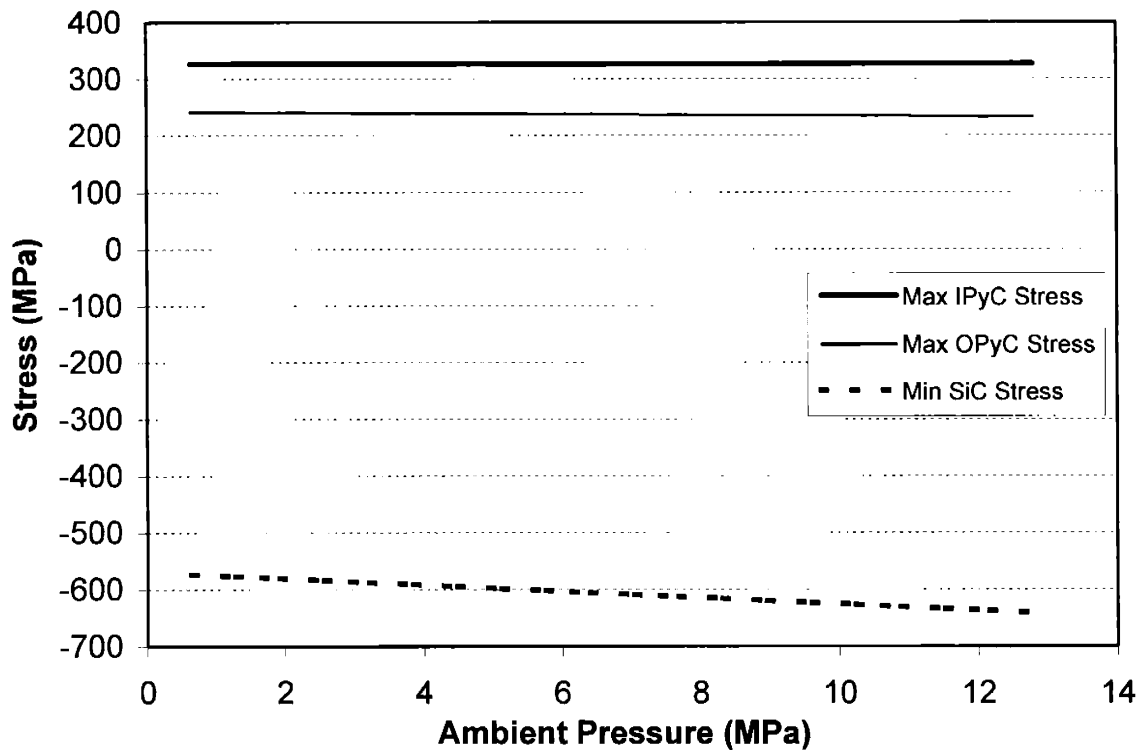
Figure 4-12. Stresses in structural layers versus ambient pressure

4.1.1.10. U^{235} Enrichment

The perturbation results on U^{235} enrichment are shown in Figure 4-13. U^{235} enrichment only affects the atomic weight of Uranium mix in the fuel kernel, which is then used in calculating the moles of Uranium in the kernel. We scanned a wide range of it and its effect is trivial.

175
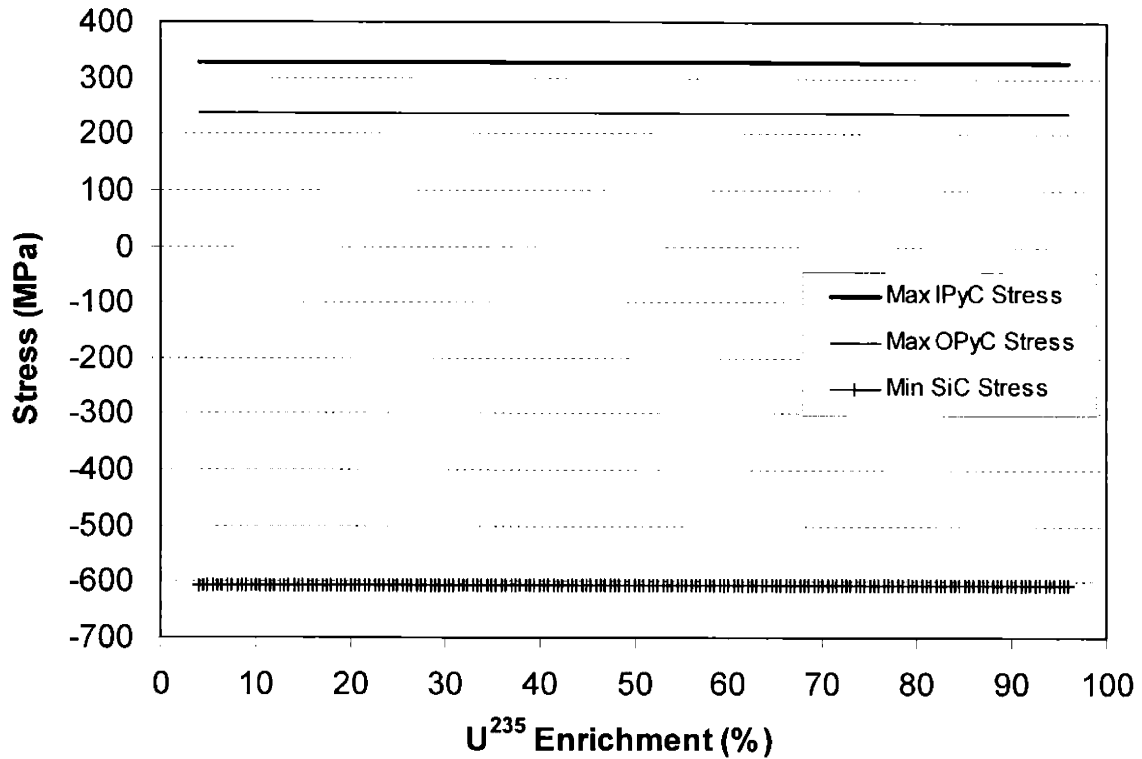
Figure 4-13. Stresses in structural layers versus U^{235} enrichment (symbols for clarity)

4.1.1.11. End-of-life Fast Neutron Fluence and Burnup

In the ranges we choose for end-of-life fast neutron fluence and burnup, these two parameters don't influence the maximum PyC stresses and minimum SiC stresses because they are achieved at early stage of irradiation.

We have seen that for coated fuel particles in HTGRs, pyrocarbon crack induced particle failure is the dominant failure mode. Therefore when it comes to fuel particle design, we should configure the particles to limit the stresses in PyC layers and minimize their cracking rates. We've also seen that the behavior of the IPyC and OPyC layers are quite independent, so we could design them separately. Now we list the stress variations associated with the variation of each input parameter, and rank them based on the amplitude of IPyC stress variation from top down in Table 4-2. The last four parameters are not really important in terms of fuel design. In the remaining ten parameters, temperature, kernel diameter, and SiC thickness are important to all three layers; IPyC BAF_0 and IPyC thickness are important to IPyC and SiC layers; OPyC BAF_0 and OPyC

thickness are important to OPyC and SiC layers; the remaining three parameters IPyC density, OPyC density, and buffer thickness are secondary. We also summarize how stresses change with some parameters in Table 4-3. In next section we look at the inter-dependencies between two parameters.

Table 4-2. Stress Variations in Structural Layers

Parameter	Max. IPyC Stress (MPa)	Min. SiC Stress (MPa)	Max. OPyC Stress (MPa)
Irradiation Temperature (°C)	203.4 – 410.0	-761.9 – -400.2	155.0 – 295.9
IPyC BAF$_0$	269.4 – 381.9	-656.9 – -548.1	236.7 – 238.7
Kernel Diameter (μm)	301.5 – 379.6	-646.5 – -520.9	216.6 – 247.8
IPyC Thickness (μm)	310.9 – 349.8	-765.7 – -453.9	237.0 – 237.2
SiC Thickness (μm)	313.5 – 331.3	-1151.4 – -412.2	228.3 – 241.4
IPyC Density (g/cm^3)	324.7 – 338.2	-607.7 – -601.2	235.6 – 238.3
Buffer Thickness (μm)	319.9 – 330.0	-635.4 – -519.0	228.8 – 243.2
OPyC Thickness (μm)	322.6 – 331.3	-764.3 – -421.4	214.7 – 263.0
OPyC Density (g/cm^3)	323.4 – 328.9	-619.6 – -598.9	233.6 – 273.4
OPyC BAF$_0$	325.2 – 330.6	-679.5 – -522.9	182.3 – 292.2
Buffer Density (g/cm^3)	326.1 – 327.2	-608.7 – -600.6	237.1 – 237.2
Ambient Pressure (MPa)	326.3 – 327.0	-640.7 – -572.7	232.7 – 241.2
Kernel Density (g/cm^3)	326.6 – 326.8	-605.7 – -604.2	237.2 – 237.2
U^{235} Enrichment (%)	326.7 – 326.7	-605.5 – -604.9	237.2 – 237.2

Table 4-3. Stress Changing Direction as Parametric Values Increase

Parameter	Max. IPyC Stress	Min. SiC Stress	Max. OPyC Stress
Irradiation Temperature (°C)	+ → -	- → +	+ → -
IPyC BAF$_0$	+	-	-
Kernel Diameter (μm)	-	+	+
IPyC Thickness (μm)	+	-	+ → -
SiC Thickness (μm)	+	+	+
IPyC Density (g/cm^3)	- → +	+	-
Buffer Thickness (μm)	+ → -	-	+
OPyC Thickness (μm)	-	-	-
OPyC Density (g/cm^3)	-	-	+
OPyC BAF$_0$	-	-	+
Ambient Pressure (MPa)	-	-	-

(+: increase; -: decrease; + → -: increase then decrease; - → +: decrease then increase.)

4.1.2. Parameter Inter-dependency Study

Our task here is to identify some dependent variables such as the maximum IPyC stress as a function of sixteen parameters. Imagine we choose three values for each parameter at which we evaluate the dependent variable, ideally we would need to sample 3^{16} (43 million) points in the multivariate space. To get a better idea of the shape of the function, finer divisions are necessary, which makes the sampling job formidable. On another end of the spectrum, if all sixteen parameters are independent, i.e. the overall function can be decomposed into sixteen functions each of which is a function of one parameter, then we only need 3×16 = 48 sampling points for the same task. The real case is usually somewhere in between. Unfortunately we don't know the independencies among parameters. However, we can make estimations. Perturbation analysis is the first step to help us gain some knowledge on how the dependent variable changes with parameters and how big the influence of each parameter is. In perturbation analysis, we found that some parameters don't have significant effects on the critical stresses in coated fuel particles, so we forgo them in further study. We also observed that the shape of the function is fairly simple and in most cases monotonic. In multivariate space, perturbation with respect to parameter x is like sampling a line parallel to x axis. Now we can scan a plane parallel to the x-y plane to study whether x and y are correlated or dependent. We may call this surface analysis or parameter inter-dependency study. Of course in a sixteen-dimensional space, its 2-D, 3-D, 4-D ... subspaces can be used to sample it, but we assume 2-D surface analysis is good enough in understanding the whole space. Now we use examples to illustrate surface analysis and what information it can provide to fuel optimization.

4.1.2.1. Strongly Dependent Parameters

Figure 4-14 shows the effects of kernel diameter together with buffer thickness on maximum IPyC stress.
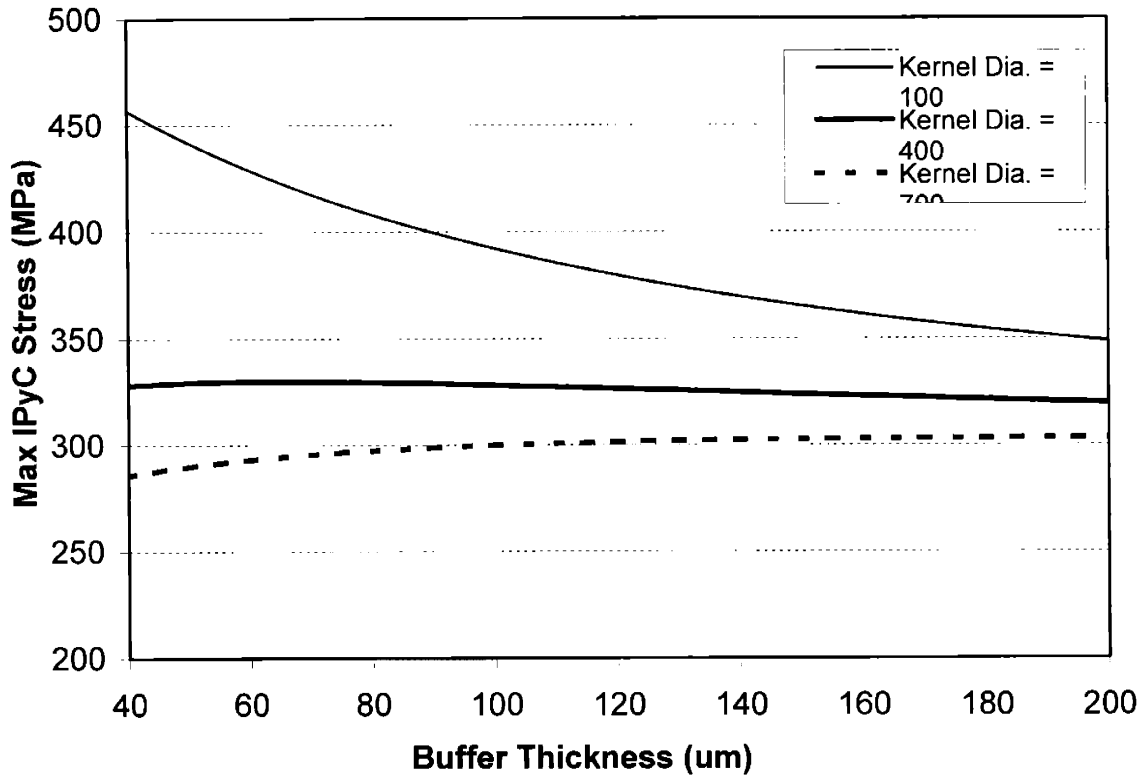
Figure 4-14. Maximum IPyC stress as a function of kernel diameter and buffer thickness

As kernel diameter rises, the dependency of maximum IPyC stress on buffer thickness is gradually modified from monotonically decreasing to increasing. We then say that these two parameters are strongly dependent or correlated because kernel diameter has to be specified before we can determine the dependency of maximum IPyC stress on buffer thickness. The effect shown in Figure 4-14 comes from two aspects: one is internal pressure and another is a geometric effect. As the radius of a certain structural layer increases (the curvature of it decreases), it can be shown from stress analysis that the tangential stress in that layer decreases. The increase of buffer thickness lessens internal pressure, which causes maximum IPyC stress to go up. On the other hand, it effectively increases the radius of IPyC layer, which counteracts the effect of internal pressure. The above figure clearly illustrates the competition between the two. However when we increase kernel diameter, two effects act in the same direction, so the IPyC stress always goes down. Now we know if we want to minimize IPyC stress by merely designing kernel diameter and buffer thickness, we would choose the biggest kernel within permitted range and then scan the whole range of buffer thickness.
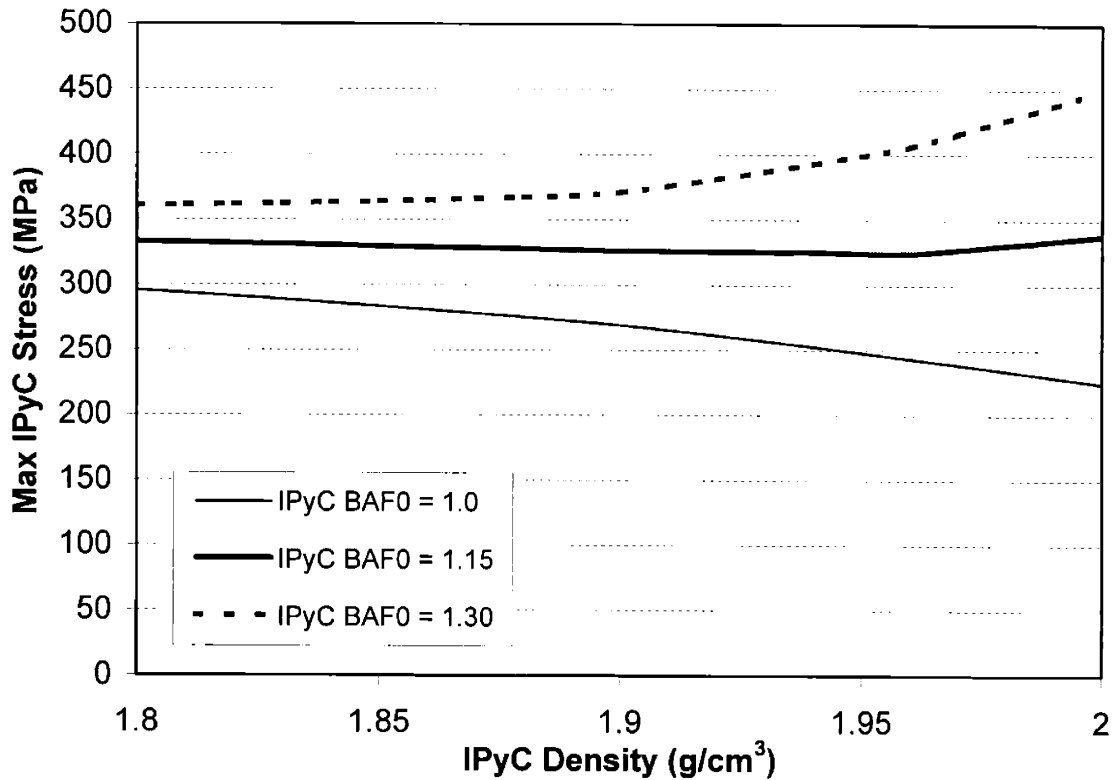
Figure 4-15. Maximum IPyC stress as a function of IPyC BAF_0 and IPyC density

Another example is the strong dependency between IPyC BAF_0 and IPyC density, as shown in Figure 4-15. This is well expected because anisotropy and density of pyrocarbon are correlated with its microstructure. OPyC BAF_0 and OPyC density show similar trend.

4.1.2.2. Independent Parameters

Figure 4-16 shows the effects of IPyC thickness together with SiC thickness on maximum IPyC stress. In the two-dimensional surface, the maximum IPyC stress increases with thicker IPyC and SiC layers, regardless of where in the surface it is evaluated. These two are then called independent parameters, and they can be evaluated individually in fuel design process.
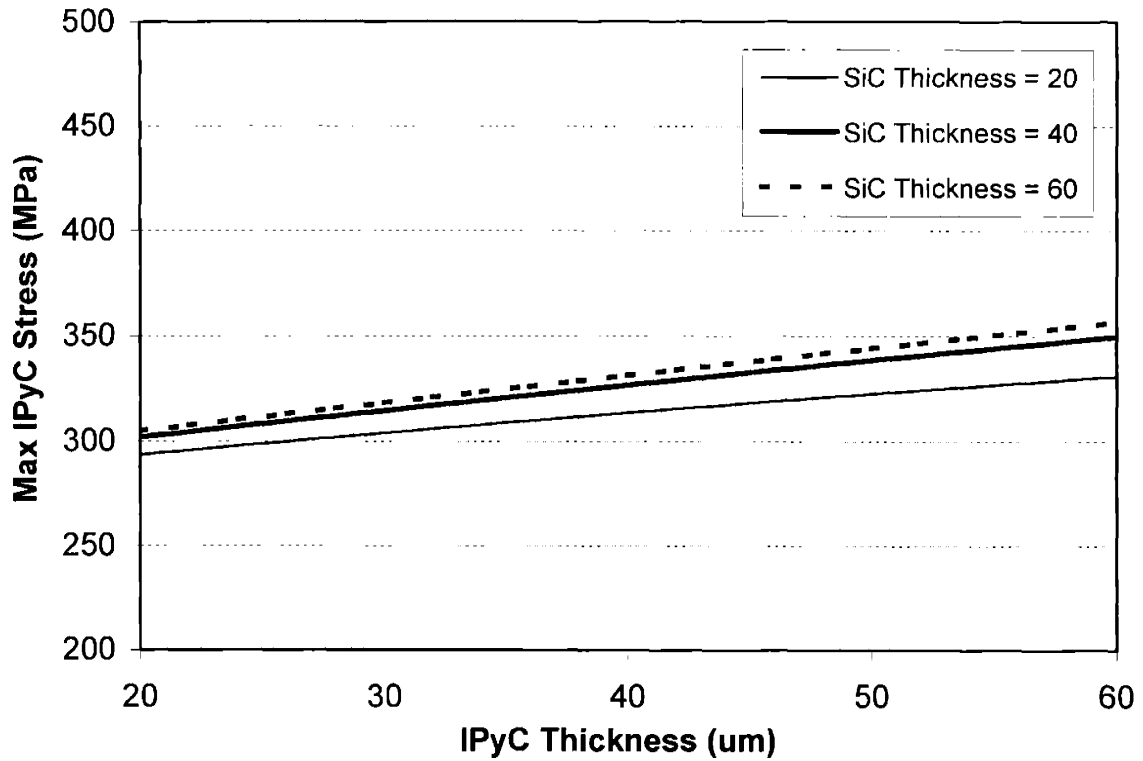
Figure 4-16. Maximum IPyC stress as a function of IPyC thickness and SiC thickness
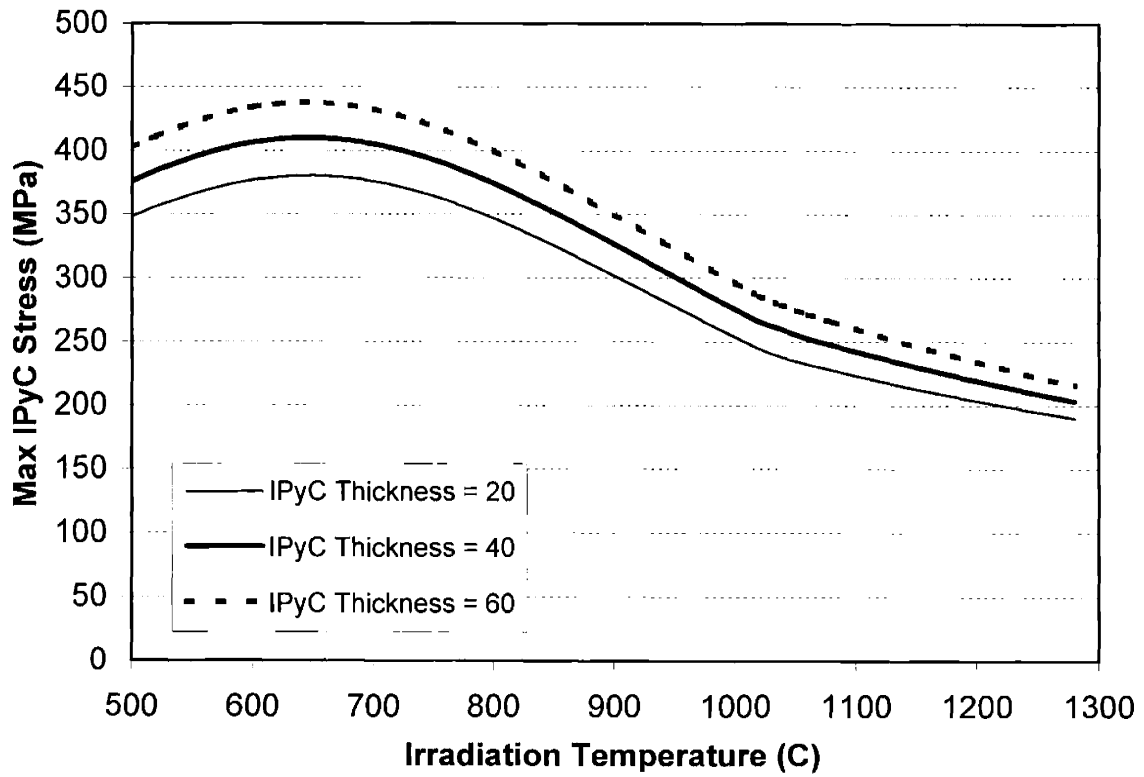
Figure 4-17. Maximum IPyC stress as a function of IPyC thickness and temperature

181

Another example is shown for irradiation temperature and IPyC thickness in Figure 4-17.

4.1.2.3. Weakly Dependent Parameters

If the parameter inter-dependency doesn't fall into the above two categories, we call it weakly dependent. This case happens in those parameters which have small influence on the dependent variable. An example is given in Figure 4-18. When irradiation temperature is 500°C, maximum IPyC stress is the lowest at OPyC BAF_0 of 1.3; when irradiation temperature is 1300°C, maximum IPyC stress is the lowest at OPyC BAF_0 of 1.1, so the changing of irradiation temperature affects the shape of the function of maximum IPyC stress with respect to OPyC BAF_0. Since IPyC stress is barely influenced by OPyC parameters, this weak dependency can be treated as independent.
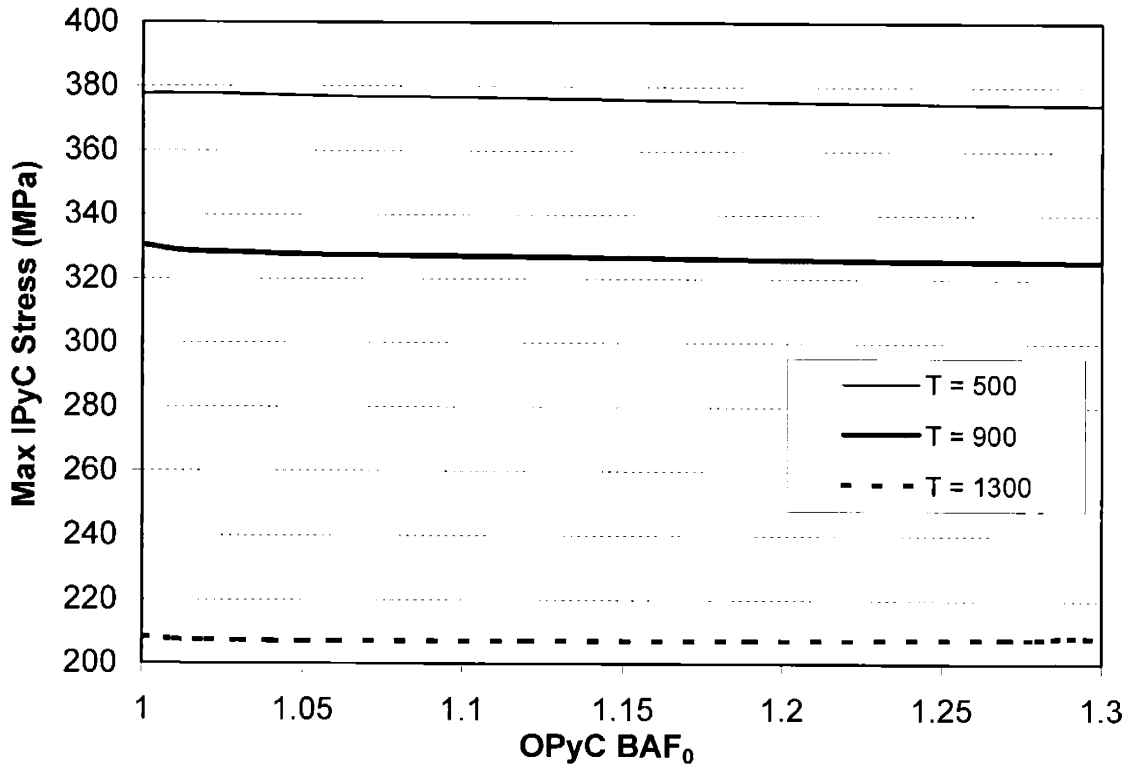
Figure 4-18. Maximum IPyC stress as a function of temperature and OPyC BAF_0

We performed surface analysis for every pair of parameters and present their inter-dependency relationships in Table 4-4.

Table 4-4. Parameter Inter-dependency Table

	T	Kernel Diameter	Buffer Thickness	IPyC Thickness	SiC Thickness	OPyC Thickness	IPyC BAF$_0$	IPyC Density	OPyC BAF$_0$	OPyC Density
T	-	I	WD	I	I	I	WD	WD	WD	WD
Kernel Diameter	I	-	SD	I	I	I	I	I	I	I
Buffer Thickness	WD	SD	-	I	I	I	I	WD	I	I
IPyC Thickness	I	I	I	-	I	I	I	WD	I	I
SiC Thickness	I	I	I	I	-	I	I	WD	I	WD
OPyC Thickness	I	I	I	I	I	-	I	WD	I	WD
IPyC BAF$_0$	WD	I	I	I	I	I	-	SD	I	WD
IPyC Density	WD	I	WD	WD	WD	WD	SD	-	WD	WD
OPyC BAF$_0$	WD	I	I	I	I	I	I	WD	-	SD
OPyC Density	WD	I	I	I	WD	WD	WD	WD	SD	-

(SD: strongly dependent; WD: weakly dependent; I: independent.)

We see in Table 4-4 that the strong dependencies are enclosed in the particle dimensions subspace and material properties subspace, so the subspaces are just weakly dependent, which facilitates our design process.

4.2. Proposed Optimization Procedure

In our terminology, fuel particle optimization means configuring the particles for their best mechanical performance, namely, minimum mechanical fuel failure probability. It has been discussed and demonstrated in Chapter 2 and Chapter 3 that the failure of a whole particle may be triggered by either the cracking of pyrocarbon layers or by the overpressure rupture of all structural layers, especially the SiC layer. This translates to two optimization guidelines: (1) minimizing the failure probability of pyrocarbon layers, (2) minimizing the direct pressure vessel failure of the SiC layer. Our approach to the first guideline is to suppress stresses in PyC layers and lift their strengths. Given that the

average stress in the SiC layer is compressive in most cases, we set the design criterion in responding to the second guideline as controlling the SiC stress to be non-positive at all times.

We now re-define in Table 4-5 a subspace of the one given in Table 4-1 for fuel particle optimization purpose this instead of the parametric study. The parameter ranges chosen here reflect better consideration of practical issues and past fuel manufacture experience. For example, if the fuel kernel is too large, it may depart significantly from spherical shape and increase the failure rate of coated particles, which will be discussed in Chapter 6. Kernel diameter of 600μm was used in HTTR first-loading fuel. The thicknesses of structural layers should be large enough compared with their variations resulting from CVD process and grain sizes. As for pyrocarbon BAF_0, perfectly isotropic pyrocarbons may not be producible, as shown in Figure 2-22, so we select 1.01 as its lower bound.

Table 4-5. Value Ranges for Input Parameters in Fuel Optimization

Parameter	Low	Nominal	High
Kernel Diameter (μm)	200	400	600
Buffer Thickness (μm)	60	90	120
IPyC Thickness (μm)	30	45	60
SiC Thickness (μm)	25	35	45
OPyC Thickness (μm)	30	50	70
IPyC Density (g/cm^3)	1.8	1.9	1.99
OPyC Density (g/cm^3)	1.8	1.9	1.99
IPyC BAF_0	1.01	1.045	1.08
OPyC BAF_0	1.01	1.045	1.08
Irradiation Temperature (°C)	600	900	1200

To optimize the fuel particles, we work in the sequence of temperature, particle dimensions, and pyrocarbon properties. From Table 4-3 we find a sure-gain situation with SiC thickness, OPyC thickness, and ambient pressure, because the stresses in structural layers change in the same direction when each of them changes. Based on all this information gained from perturbation and surface analyses, we propose the following fuel particle optimization procedure.

(1) The irradiation temperature is generally determined by the reactor core specification.

If it is not, higher temperature is better from mechanical fuel performance viewpoint.

184

(2) Minimize SiC thickness and maximize OPyC thickness in given ranges.

(3) Minimize IPyC thickness and maximize kernel diameter for the sake of IPyC layer integrity, but make sure the end-of-life SiC stress is non-positive. This is because their effects on IPyC stress are more significant, and IPyC stress is generally higher than OPyC stress, as shown in previous stress plots, which makes it more liable to failure.

(4) Scan the values for buffer thickness to find the minimal value of the maximum IPyC stress, and again make sure the end-of-life SiC stress is non-positive. In step (3) kernel diameter has been set, so its strongly dependent buffer thickness needs to be scanned in its whole range.

(5) Level up IPyC BAF_0 starting from 1.01 and look for maximum positive gap between IPyC strength and maximum IPyC stress, and then scan the values for IPyC density to find the minimal value of the maximum IPyC stress, but pay attention to acceptable density values according to Figure 2-22. For example, when pyrocarbon BAF_0 equals to 1.02, its density may not go above $1.96g/cm^3$. The idea here is that the wider the gap between IPyC strength and IPyC stress is, the less likely the IPyC layer would be failed.

(6) Choose OPyC BAF_0 and OPyC density for the OPyC layer, as in step (5).

It should be addressed that the proposed fuel optimization procedure is not the only one, and one set of optimization results needs to be taken with the whole pack of material models we have been using. If for instance the relationship between PyC strength and PyC BAF_0 is updated later, we may get a quite different answer, but the optimization procedure still applies.

4.3. Simulations in MPBR with Optimized Particles

In this section we do a systematic exercise on fuel optimization in Modular Pebble Bed Reactor (MPBR) environments. First of all, we demonstrate the simulations of LEU-TRISO fuel, which was the German reference coated particle design and is adopted by ESKOM of South Africa as the fuel design for their Pebble Bed Modular Reactor (PBMR) [125], in two MPBR cores discussed in Section 2.6.

185

4.3.1. Simulations of LEU-TRISO Fuel in MPBR environments

The LEU-TRISO fuel stands for Low-Enriched Uranium TRISO particle fuel which was established as the reference coated fuel particle design in Germany in 1980 [126]. Two series of LEU-TRISO fuel particles were manufactured by German NUKEM plant for irradiation testing under controlled conditions in materials testing reactors. The LEU Phase 1 fuel spheres (pebbles) were manufactured in 1981 and were irradiated under a variety of different conditions in several reactors. The so-called "Proof Test" fuel spheres were manufactured in 1988, and eight spheres were irradiated under conditions simulating the High Temperature Modular Reactor (HTR-Modul) conditions in the HFR Petten materials testing reactor [126][127].

Table 4-6. Specifications for LEU-TRISO Fuel [128][129]

Parameter	Design Specification	As Manufactured
Fuel Type	UO_2	UO_2
U^{235} Enrichment (%)	7.8 ± 0.1	[†]
Kernel Diameter (μm)	500 ± 20	497 ± 14.1
Kernel Density (g/cm^3)	≥ 10.4	10.81 ± 0.01[*]
Buffer Thickness (μm)	90 ± 18	94 ± 10.3
Buffer Density (g/cm^3)	≤ 1.05	1.00 ± 0.05[*]
IPyC Thickness (μm)	40 ± 10	41 ± 4.0
IPyC Density (g/cm^3)	1.90 ± 0.1	Not Measured
SiC Thickness (μm)	35 ± 4.0	36 ± 1.7
SiC Density (g/cm^3)	≥ 3.18	3.20
OPyC Thickness (μm)	40 ± 10	40 ± 2.2
OPyC Density (g/cm^3)	1.90 ± 0.1	1.88
IPyC/OPyC BAF_0	1.058[*] ± 0.00543[*]	1.058[*] ± 0.00543[*]
Defective SiC	$\leq 6 \times 10^{-5}$	3.5×10^{-5}

([*]: Values filled in by author; [†]: Minor deviations in this parameter occur due to technical reasons. We use its design value in simulations.)

Our purpose here is to take use of this fuel design to show simulations in VSOP modeled MPBR cores and to exhibit the effect of fuel optimization. We make no claim that the optimized fuel particles are superior to LEU-TRISO fuel particles, but suggest that according to our current fuel performance model and material database, the predicted

failure probabilities of optimized fuel would be lower in simulated MPBR cores. Our fuel performance model still needs further benchmarking and qualifications and new fuel particles could be manufactured using optimized fuel specifications and tested to verify their performance.

The specifications for reference LEU-TRISO fuel particles are given in Table 4-6 [128][129]. The "Design Specification" column in the table refers to HTR-Modul design values, and the "As Manufactured" column refers to values achieved during manufacture of Type EUO 2308 coated particles. These reference particles were used for all irradiation qualification experiments for Phase 1 [128]. Firstly we look at the behavior of a nominal design-specified LEU-TRISO fuel particle in two MPBR cores described in Section 2.6. The behavior of a nominal as-fabricated LEU-TRISO fuel particle is very similar because the main difference between the two lies in the variations in their properties. Then we run Monte Carlo simulations to predict the failure probabilities of these fuel particles.

Figure 4-19 and Figure 4-20 show the fast neutron fluence and burnup of a nominal LEU-TRISO particle in MPBR environments.
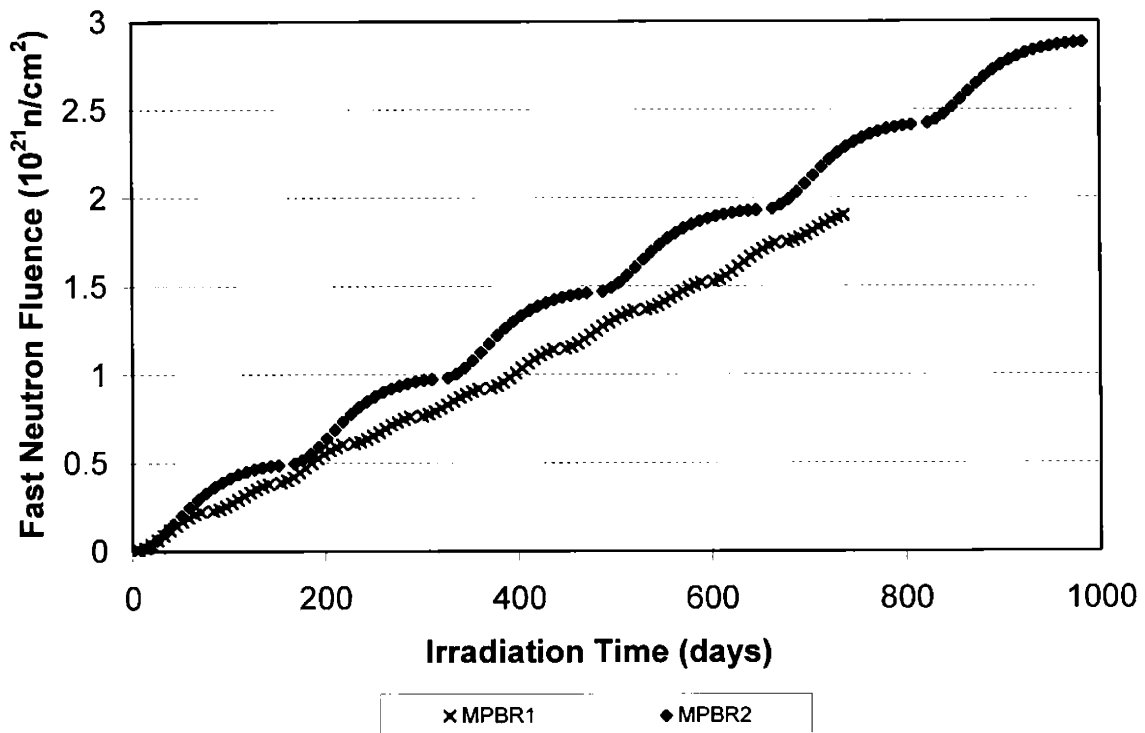
Figure 4-19. Fast neutron fluence received by a nominal LEU-TRISO particle in MPBRs
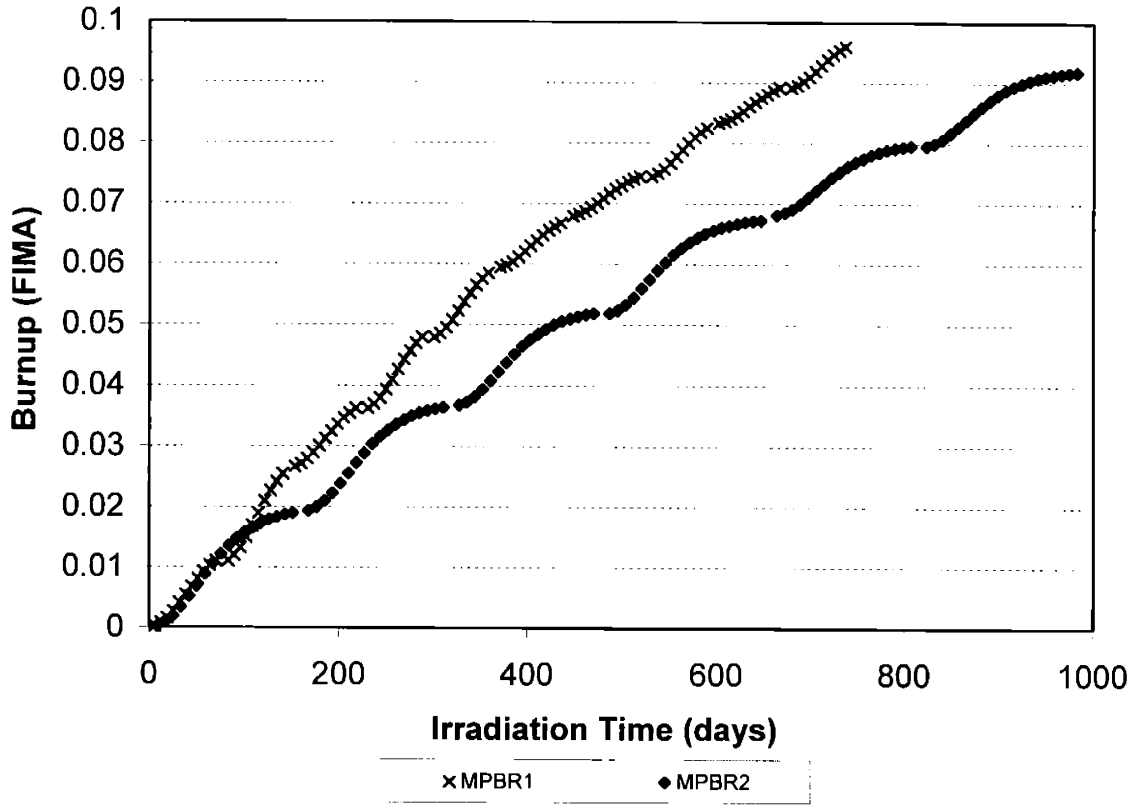
Figure 4-20. Burnup of a nominal LEU-TRISO particle in MPBRs

The particle went through 10 cycles in MPBR1 and 6 cycles in MPBR2. The irradiation time is about 750 days in MPBR1 and 1000 days in MPBR2. The end-of-life fluence and burnup depend on the specific path the particle follows, so the fluence and burnup developments shown in the above two figures are just examples. When we run Monte Carlo simulations, each sampled particle may have a specific path-dependent irradiation history. Roughly speaking, the end-of-life fluence for the particle in MPBR1 and MPBR2 are $1.9 \times 10^{21} \text{n/cm}^2$ and $2.8 \times 10^{21} \text{n/cm}^2$, respectively; the end-of-life burnup is between 9% to 10% FIMA. The accumulation of fluence and burnup in each cycle clearly indicates the cosine-shaped power and fast neutron flux distributions in the axial direction of the reactor cores.

Figure 4-21 shows the power histories of the particle in two reactor cores. Due to the high power peaking factor in the mixing zone of MPBR1, the power history in it shows more fluctuation. The power history in MPBR2 presents better decreasing trend across cycles due to the depletion of fission materials.

188
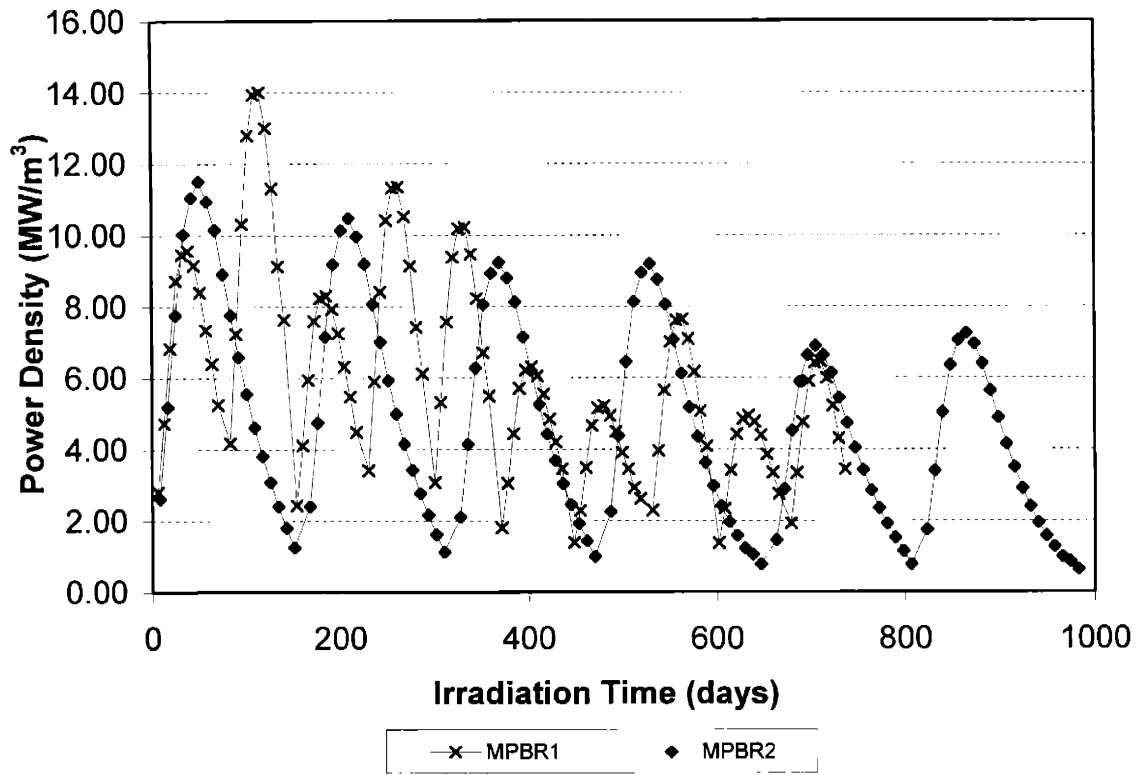
Figure 4-21. Power histories of a nominal LEU-TRISO particle in MPBRs
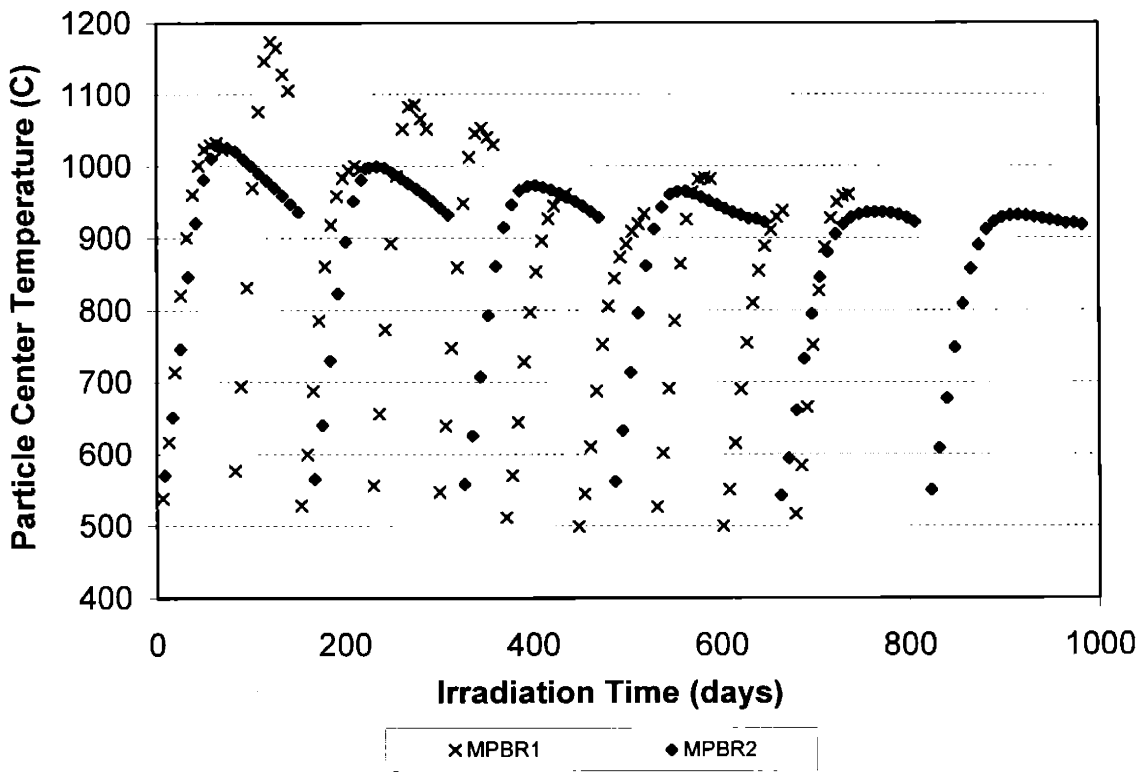
Figure 4-22. Temperature histories of a nominal LEU-TRISO particle in MPBRs

Figure 4-22 shows the temperature histories at the center of the particle corresponding to the irradiation histories. Although the coolant inlet and outlet temperatures of MPBR1 are lower than of MPBR2, as shown in Table 2-23, the fuel temperature in MPBR1 could reach higher in the presence of very high local power density. As a result, the time averaged fuel temperature in MPBR1 may indeed be higher, which leads to lower stresses in structural layers, as plotted in Figure 4-23. The ripples of stress curves are created by thermal cycling in Figure 4-22.
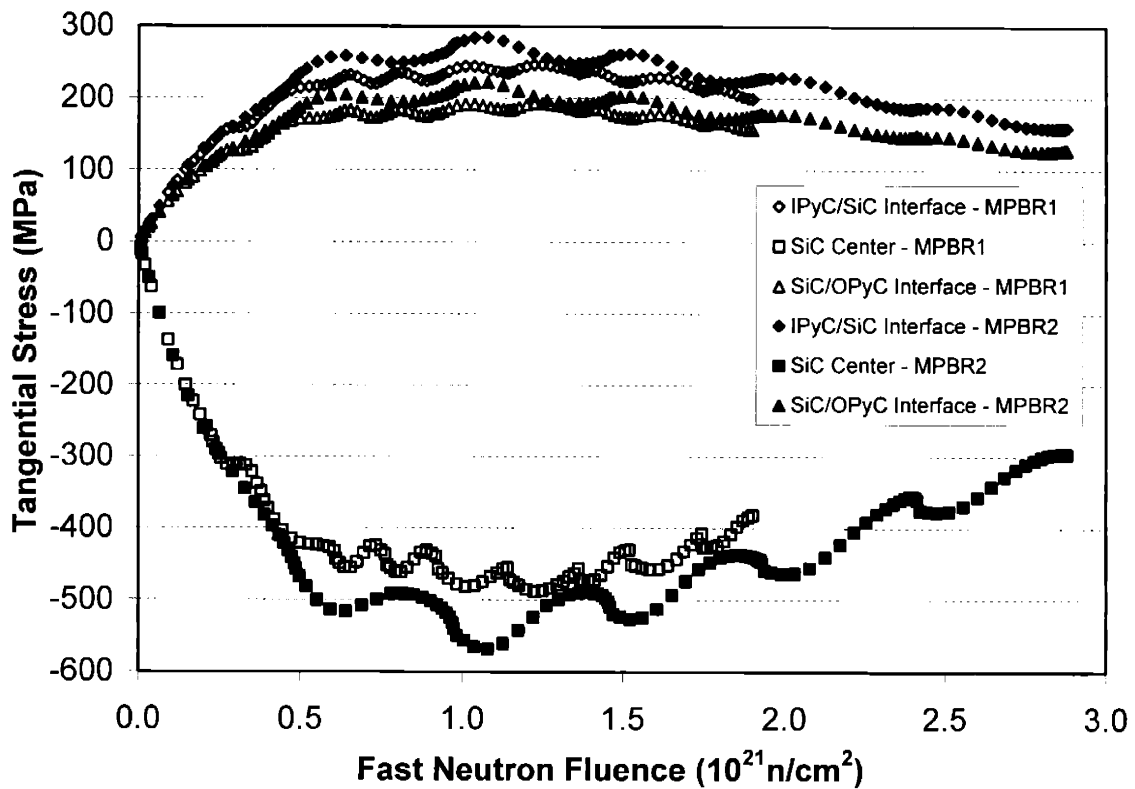
Figure 4-23. Tangential stresses of a nominal LEU-TRISO particle in MPBRs

Since we haven't elaborated on irradiation induced dimensional changes of pyrocarbon layers of particles in pebble bed reactor system, here we give an example in MPBR2. Figure 4-24 shows the dimensional change rates, because they are what we use in non-isothermal simulation environments discussed in Section 2.4.3.5. The way we use dimensional change rates in stress analysis is to fit them into fourth order polynomial as formulated in Appendix A. Because the rates are discontinuous across cycles, we need to

perform stress analysis on each cycle and carry over stresses to next cycle as residual stresses.
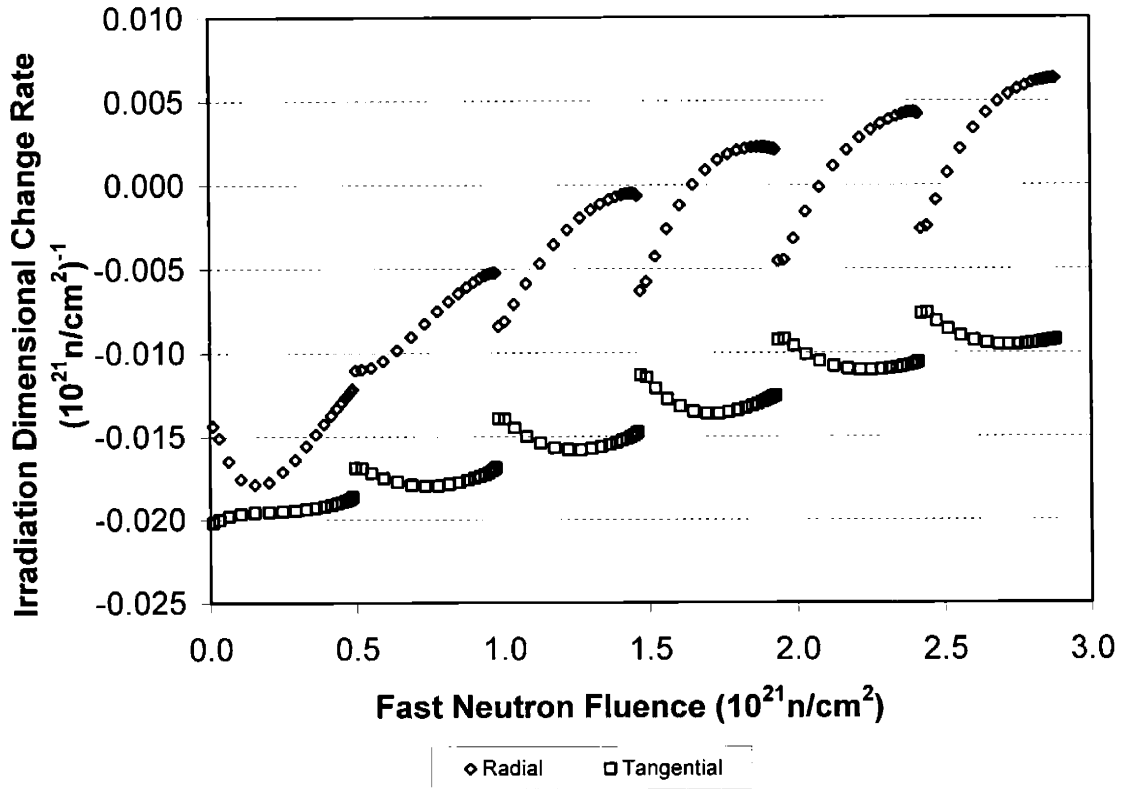
Figure 4-24. Irradiation induced dimensional change rates of PyC layers in MPBR2

Now we simulate the designed specified and as fabricated LEU-TRISO fuel particles in MPBR1 and MPBR2 cores, with 1,000,000 sampling cases each. The failure predictions together with their standard deviations are summarized in Table 4-7. Firstly, because the average fuel temperature in MPBR1 is higher than in MPBR2, the stresses hence the failure probabilities of coated particles are lower in MPBR1. Secondly, comparing the performance of design specified fuel with as fabricated fuel, we find the PyC layer failure probabilities in as fabricated fuel are a little higher but particle failure probability is much lower. This is because the failures of the SiC layer is primarily driven by the extreme particle species on the tails of their dimension distributions, and the narrowing of those distributions in as fabricated fuel particles excludes many of those which could trigger SiC failure. Thirdly, in the simulation of one million as fabricated particles in MPBR1, the standard deviation of particle failure probability (0.00555%) is

higher than itself (0.00340%), meaning the prediction is not significantly different from zero. We then increased the sampling cases to ten million, then the standard deviation decreased to about half of the mean particle failure probability. We see that the predictions of mean values are not improved significantly by increasing sample size, but standard deviations can benefit by a factor of the square root of the times of sample enlargement, in this case, about $\sqrt{10}$. The failure developments in four cases are plotted in Figure 4-25.

Table 4-7. Failure Predictions on LEU-TRISO Particles in MPBR1 and MPBR2

Case	IPyC Failure	OPyC Failure	SiC Failure	Particle Failure
Design Specified in MPBR1	34.37% ± 0.388%	3.66% ± 0.189%	0.104% ± 0.0286%	0.104% ± 0.0286%
As Fabricated in MPBR1 (1M Cases)	35.84% ± 0.456%	3.78% ± 0.196%	0.00340% ± 0.00555%	0.00340% ± 0.00555%
As Fabricated in MPBR1 (10M Cases)	35.93% ± 0.149%	3.80% ± 0.0603%	0.00394% ± 0.00210%	0.00394% ± 0.00210%
Design Specified in MPBR2	52.25% ± 0.498%	6.91% ± 0.259%	0.461% ± 0.0766%	0.461% ± 0.0766%
As Fabricated in MPBR2	55.41% ± 0.522%	7.00% ± 0.239%	0.0645% ± 0.0239%	0.0645% ± 0.0239%
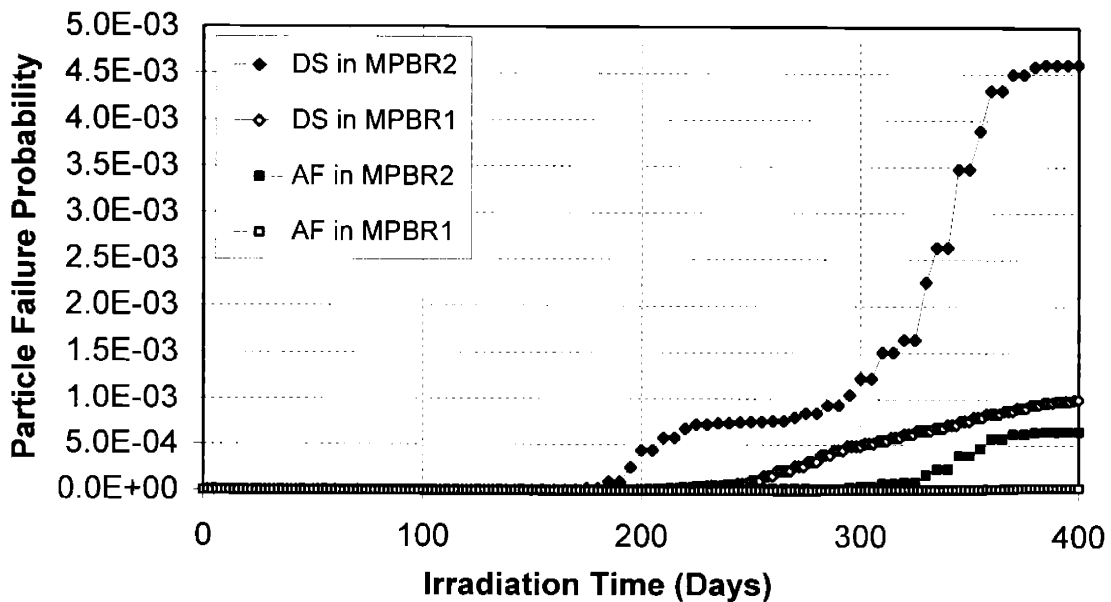
Figure 4-25. Failure developments of LEU-TRISO particles in MPBRs

4.3.2. Simulations of Optimized Fuel in MPBR environments

As described in Section 4.2, if we want to optimize the fuel deployed in the MPBR environments, the first step is to determine the irradiation temperature. Even though particles experience non-isothermal environments in MPBRs, we can define an effective constant irradiation temperature for the purpose of optimization, because the temperature doesn't have strong inter-dependency with other input parameters as shown in Table 4-4. The effective temperature is determined when a nominal particle irradiated under it shows a stress curve which more or less duplicates the wavy stress curve in the real MPBR environment, and the maximum stress is equivalent to that of the wavy stress curve. We will show an example shortly.

We only demonstrate the fuel optimization for MPBR2, and the process is the same for MPBR1 and any other coated particle irradiation environment. The effective irradiation temperature we found is 910°C, then we follow the optimization procedure in Section 4.2 and get the optimized fuel configuration given in Table 4-8. Parameters not listed in the table are chosen to be the same as in design specified LEU-TRISO fuel. It should be noted that we only design the nominal values of parameters. It is intuitive to know the narrower the distributions on parameters, the better, but in practice, tightening of those distributions infers more cost of quality control. The consideration of such issue and chemical aspects of the fuel performance in fuel optimization will be future work.

Table 4-8. Optimized Fuel Configuration for MPBR2

Parameter	Value
Irradiation Temperature (°C)	910
Whole Particle Radius (μm)	545
Kernel Diameter (μm)	600
Buffer Thickness (μm)	120
IPyC Thickness (μm)	30
IPyC Density (g/cm^3)	1.99
IPyC BAF$_0$	1.08
SiC Thickness (μm)	25
OPyC Thickness (μm)	70
OPyC Density (g/cm^3)	1.99
OPyC BAF$_0$	1.08

We see from the table that the optimized fuel particle has big fuel kernel and buffer layer and thin IPyC and SiC layers. The reason we end up with a relatively high BAF_0 value for IPyC and OPyC layers is the gap between PyC strength and stress is the widest at it within the parameter range. This totally depends on the PyC strength model we use, therefore more verification of material models is necessary. The PyC density is chosen according to the optimized BAF_0 and BAF_0-density correlation in Figure 2-22. The stresses in a nominal optimized fuel particle are plotted in Figure 4-26 together with the stresses in original designed specified particle. For clarity we don't put OPyC stresses in the plot. The effect of optimization is to bring down IPyC stress by about 35MPa and increase IPyC strength to broaden their gap. The stress development under effective irradiation temperature replicates that in real pebble bed environment very well, as shown in Figure 4-26.
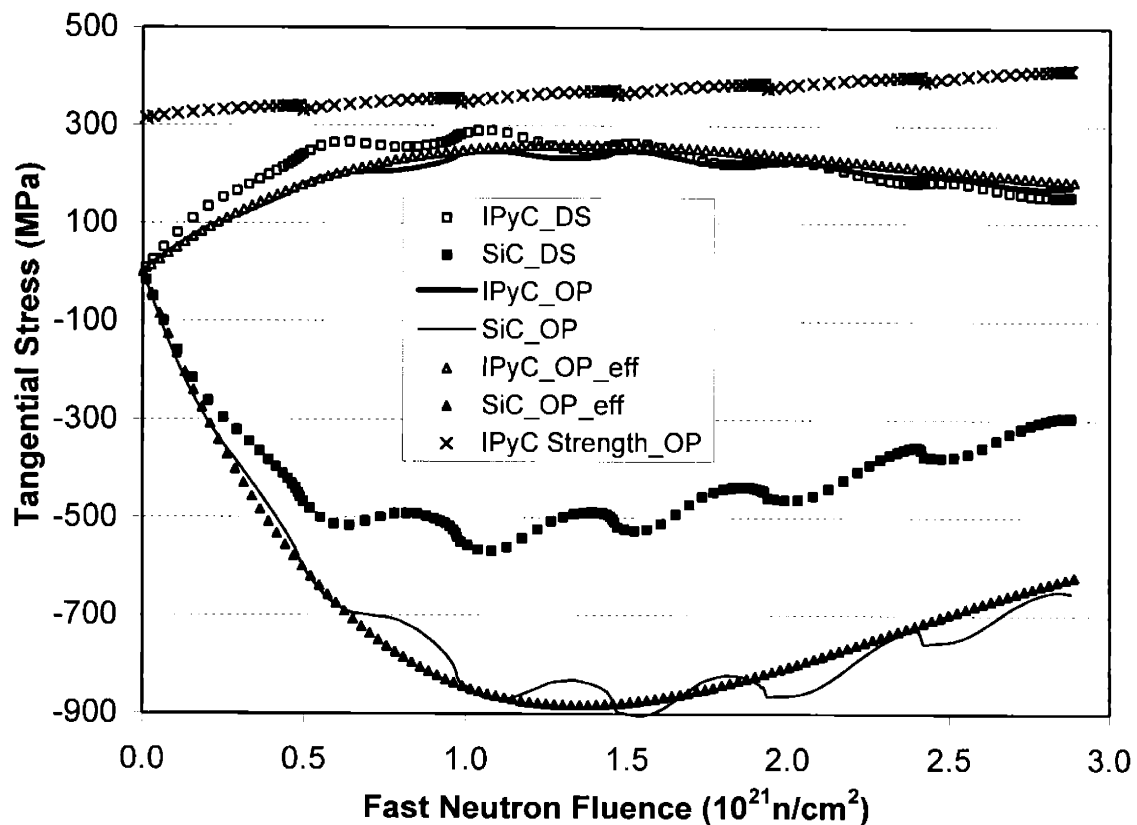
Figure 4-26. Tangential stresses of an optimized particle and a LEU-TRISO particle in MPBR2 (Stresses at the centers of layer thickness are given. 'DS' means designed specified fuel; 'OP' means optimized fuel; 'eff' means effective temperature.)
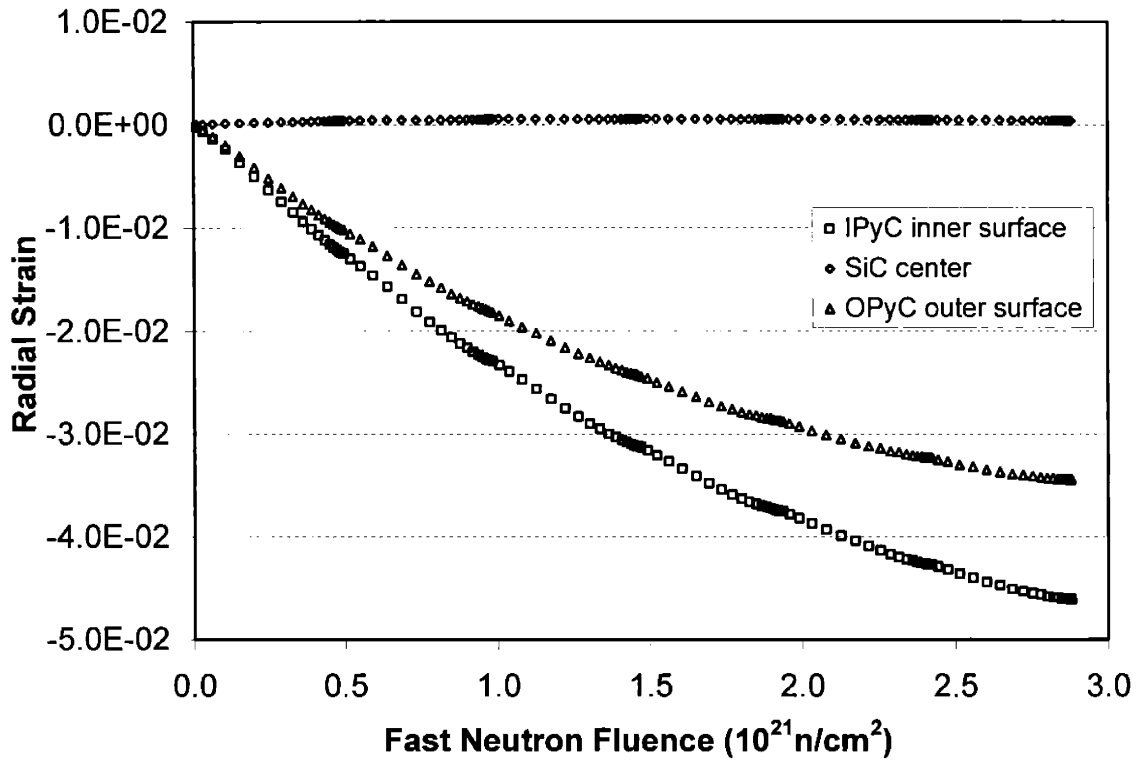
Figure 4-27. Radial strains of an optimized particle in MPBR2
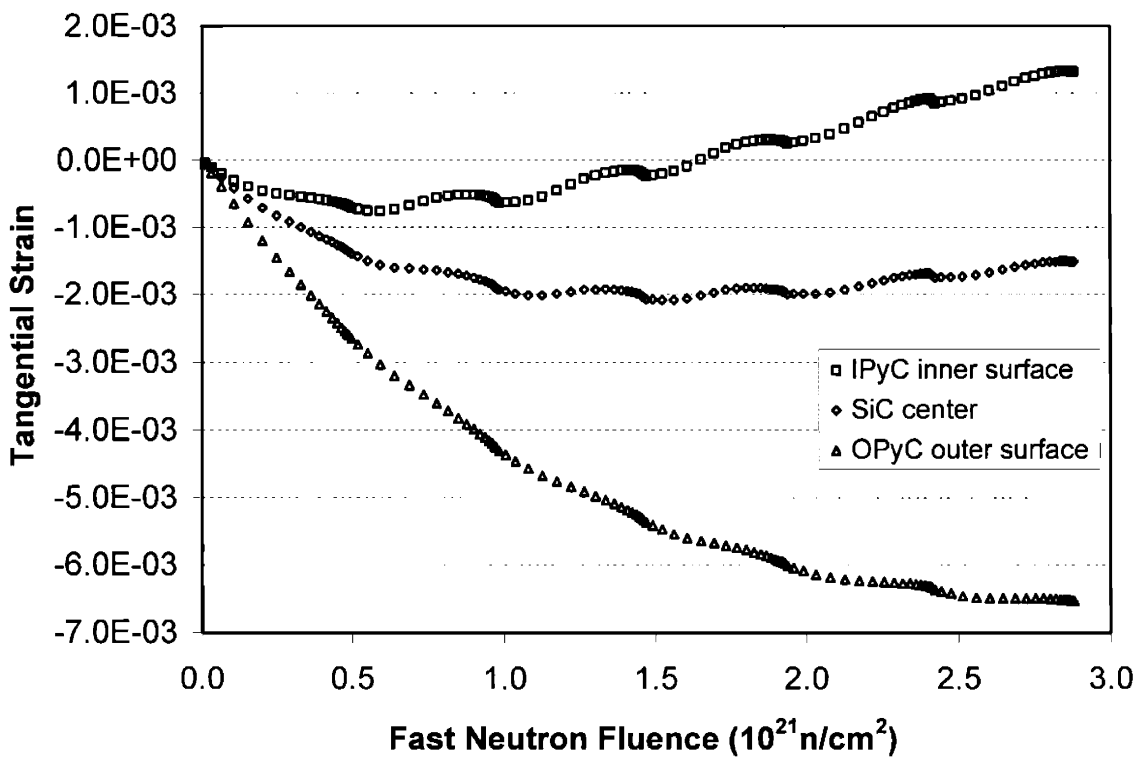
Figure 4-28. Tangential strains of an optimized particle in MPBR2
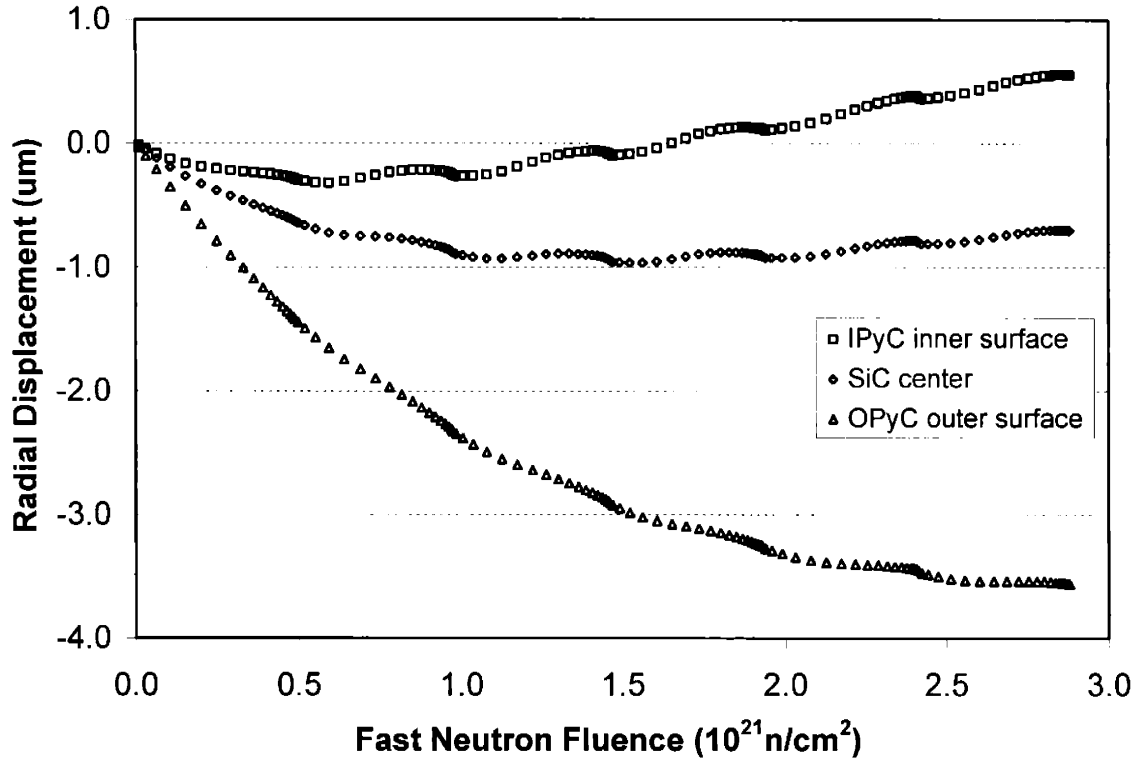
Figure 4-29. Radial displacements of an optimized particle in MPBR2

We take this opportunity to show the strains and displacements in the nominal optimized particle, which we haven't done before. The strain-displacement relationships are

$$\varepsilon_{rr} = \frac{\partial u_r}{\partial r} \text{ and } \varepsilon_{\theta\theta} = \frac{u_r}{r}. \tag{4.2}$$

From Figure 4-29 we see that the OPyC layer has more freedom to move in the radial direction and its outer surface can displace inward by about 3.5μm. The IPyC layer is confined by the SiC layer on one side and the internal pressure on another, so its movement is smaller. Initially the inner surface of IPyC moves toward the fuel kernel, as internal pressure builds up and irradiation induced radial strain turns around, it heads another direction as the figure illustrates. Based on eq. (4.2), tangential strains in Figure 4-28 exhibit similar behaviors as radial displacements. Radial strains are the gradient of radial displacements, and in Figure 4-27 we see the SiC layer is very resistant to radial deformation, so it looks like a rigid wall to pyrocarbon layers. The radial strains in IPyC

196

and OPyC could reach 4% to 5%, but those are the total strains. The elastic strains are much smaller, and the assumption of elastic deformation of structural layers is still valid.

To perform Monte Carlo sampling, we attach two sets of distributions to the parameters of optimized fuel particles: one from design specified LEU-TRISO fuel, and another from as fabricated LEU-TRISO fuel. We call these two cases Optimized 1 and 2, respectively. We also widen the standard deviations IPyC and OPyC BAF_0s from 0.00543 to 0.00816 on Optimized 1 to give a sense of the effect of parameter distributions. This case is called Optimized 3. The predicted failure probabilities are given in Table 4-9.

Table 4-9. Failure Predictions for Optimized Particles in MPBR2

Case	IPyC Failure	OPyC Failure	SiC Failure	Particle Failure
Optimized 1 in MPBR2	3.40% ± 0.191%	0.818% ± 0.0890%	0.0001% ± 0.001%	0.0001% ± 0.001%
Optimized 2 in MPBR2	3.23% ± 0.191%	0.834% ± 0.106%	0.0% ± 0.0%	0.0% ± 0.0%
Optimized 3 in MPBR2	3.52% ± 0.184%	0.867% ± 0.106%	0.0% ± 0.0%	0.0% ± 0.0%

Comparing Table 4-9 with Table 4-7, we see that the IPyC and OPyC failure probabilities are decreased by an order of magnitude. The effect of optimization on SiC failure is even greater. In all three cases the SiC failure probability is not higher than 1×10^{-6}, much lower than the defective SiC level given in Table 4-6. In Optimized 1 simulations, we found one particle failure in a million runs, but statistically it doesn't count because its standard deviation is wider. In the case of Optimized 3, widening the distributions on PyC BAF_0s doesn't increase the particle failure probability.

Now we summarize what we have learned through this chapter. As discussed before, to achieve the optimized fuel performance for coated fuel particles, we can design the environment (basically the irradiation temperature) the particles are in, the material properties the coating layers have, and the dimensions of fuel kernels and various coating layers. We see from Table 4-4 that these three types of input parameters which we can design are almost independent in influencing the stresses in particles, so the three types can be designed separately. The implication of this finding is that basically the optimized

197

particle dimension does not alter with varying coating material properties and irradiaton temperatures, and the optimized coating material properties are not affected by varying particle dimensions. With this said, we give recommendations to the optimized fuel design as follows.

(1) The kernel and layer dimensions show geometric effects on the stresses in the structural layers. Namely, they influence the way that stresses distribute and forces balance in the layers, which has nothing to do with irradiation induced dimensional changes and creep which depend on material properties and irradiation temperature. Of course the kernel diameter and the buffer thickness also affect particle interal pressure which contributes to stresses, but again, this does not depend on material properties. Even if later on the material models change, for example, the function of irradiation creep on irradiation temperature and PyC density (as shown in Figure 2-28) is modified, or new values of the coating material properties arrive, the effects of particle dimensions on stresses should not change. Therefore, we are confident to say that the optimized particle dimensional configuration can be determined by the proposed optimization procedure in Section 4.2, regardless of the material models used in the current fuel performance model and the irradiation temperature. The general guideline for optimal particle dimension is that a particle with large fuel kernel, thin IPyC and SiC layers, and thick OPyC layer is favorable.

(2) The dependence of stresses on irradiation temperature, as shown in Figure 4-11, is primarily due to the increase of the creep coefficient with the increase of temperature in the high temperature range, as shown in Figure 2-28. As long as the effect of irradiation temperature on irradiation creep remains the same, we see from Figure 4-11 that higher temperature environment is better from the fuel mechanical performance point of view.

(3) The BAF_0 and density of the IPyC and OPyC layers influence their irradiation induced dimensional changes and creep, their elastic constants, and their strengths. When different material models are incorporated in the overall fuel performance model, the effects of BAF_0 and density of PyC on stresses in the structural layers may be different. Therefore, we do not have a simple recommendation for the values for them. In Section 4.3.2, the optimized BAF_0 we found based on our material models

was 1.08. This is quite a high value compared with the widely-accepted view that more isotropic pyrocarbon layers are better for coated fuel particles. The reason for this is that the strengths of PyC layers increase as BAF_0 increases, as shown in Figure 2-41, which is physically sound as explained in the last paragraph on Page 100. Furthermore, the strengths of PyC layers increase faster than the stresses in PyC layers as BAF_0 increases, so that the failure probabilities of PyC layers drop accordingly. If indeed the PyC strength does not increase with BAF_0 as fast or even decreases with the increase of BAF_0, we will get a different answer for the optimal value of BAF_0 for pyrocarbon layers. Until experimental data or theoretical study show that the PyC strength model used in this thesis is incorrect, we keep the current optimized result.

The idea of the fuel optimization process presented in this chapter is to show a method in fuel design rather than to give some optimal values for the parameters of coated fuel particles. In the future when better material models are available, the whole fuel optimization concept still applies, but the absolute optimal values may differ.

Chapter 5.

Linking Material Properties to Manufacturing Control Parameters

What we have done so far with fuel performance modeling is to build the connection between a set of input parameters for coated fuel particles, including pyrocarbon and silicon carbide material properties, and the performance of those particles. The missing piece yet is the linkage between controllable deposition conditions and those material properties. In this context silicon carbide is the easy one to deal with because its structure is relatively simple and well characterized. However, the structure of pyrolytic carbon (pyrocarbon) in application is very complicated. It can take any number of quasi-crystalline forms ranging continuously from the near amorphous to the highly crystalline graphitic state. The structure of pyrocarbons is the intermediate layer between deposition conditions and material properties, so knowing the relationships among them is quite important. Bokros [40] did a very comprehensive study on this issue, and for the completeness of this thesis, we give a quick review of the findings of his work. We start with the deposition mechanisms of pyrocarbons in fluidized bed, then talk about the characterization of the microstructure of pyrocarbons, and proceed to the relations between the structure and deposition conditions and between the structure and properties of pyrocarbons.

5.1. Mechanisms of Pyrocarbon Formation in Fluidized Bed

Many qualitative mechanisms, models, and theories have been devised to explain the phenomenology of carbon formation during the pyrolysis of gaseous hydrocarbons. Each attempts to show how carbon in a low molecular weight hydrocarbon can be aggregated during pyrolysis into large planes containing hundreds of carbon atoms arranged in a hexagonal array. Any process that starts with small gaseous hydrocarbons and ends with large carbon particles must obviously involve growth or condensation as well as

dehydrogenation. Grisdale et al. [130][131] suggest that at any moment, there exists in the pyrolyzing atmosphere an entire series of molecular species ranging in size through the aromatics to complex transitional molecules of low hydrogen content and high molecular weight which, in the limit of their existence, become indistinguishable from the deposited carbon itself. The vapor pressure of each species must decrease monotonically as its size increases and its hydrogen content decreases until it becomes possible to nucleate "droplets" whose viscosity increases as pyrolysis proceeds.

This leads to two distinct mechanisms of carbon formation. In one mechanism, nuclei are formed homogeneously in the gas and grow to become soot particles. In the other mechanism, the carbon forms by condensing directly on the walls of the tube and form vitreous surface carbon, thus preventing the formation of gas-borne nuclei. The structures of all kinds of pyrocarbon deposits are determined mainly by the relative rates of (1) formation of gas-borne aggregates which are incorporated into a surface deposit and (2) direct condensation without homogeneous nucleation.

The use of high-temperature fluidized beds to coat fuel particles with pyrolytic carbon has emerged from several processes as the standard manufacturing method. This is because the product has a preferred type of structure and coating sphericity is better than those obtained with other processes. The fluidized bed technique has been briefly mentioned in Chapter 1 and the fluidizing furnace was shown in Figure 1-4. The particles are fluidized normally in a spouted mode throughout the coating operation by injecting gas containing a gaseous hydrocarbon at the base of the graphite coating column. The particles in the vicinity of the axis of the fluidizing vessel are taken into the stream of gas injected through the nozzle and accelerated from an initially negligible speed to one comparable to the gas velocity. When the particles reach the top of the bed, they gain some radial movement so that they fall outside the main zone of upward gas flow. Near the walls of the vessel the particles are closely packed and move downward to be fed again into the spout. The gas mixture is heated by the surrounding wall of the coating vessel either directly or through the circulating particles which receive their heat from the furnace wall in the upper zone of the vessel. Based on the above description, we can identify the independent variables important in controlling the pyrolysis process and thus the structure of the pyrocarbon deposited:

(1) The nature of the parent hydrocarbon and its concentration,

(2) the temperature of pyrolysis,

(3) the contact time - the time allowed for the pyrolysis to occur, and

(4) the geometry of the fluidizing vessel, in particular, the ratio between the surface area to be coated and the volume occupied by the pyrolyzing gas.

5.2. Characterization of the Structure of Pyrocarbons

Pyrocarbon deposits can have any of a variety of complex structures. In these structures, most of the carbon atoms are arranged in planar hexagonal arrays linked together by strong covalent bonds. The layers vary in perfection and are thought to be wrinkled or contain single or multiple vacant lattice sites. Although the layers in most structures are parallel to one another and are bonded by weak van der Waals forces, some structures contain single unassociated layers, a small fraction amorphous carbon, or substantial amounts of hydrogen [38][39]. Because of the anisotropy of the bonding and variations in the crystallinity and preferred orientation of pyrolytic carbon, wide variations in properties are expected, as we mentioned in Section 2.4.1. In order to take advantage of these variations, it is necessary to characterize each deposit.

5.2.1. Characterization by X-ray Diffraction

The characterization of pyrocarbons is expressed by crystallite size, layer spacing, and degree of preferred orientation, i.e. Bacon Anisotropy Factor discussed in Section 2.4.1. Here we talk about crystallite size and layer spacing. In 1941, Warren [132] presented a theoretical analysis of diffraction by random layer lattices and giving equations for both the form and intensity of the (hk) bands. His equation for the mean layer diameter L_a in terms of the breadth $B_{(hk)}$ of a two dimensional lattice reflection

$$L_a = \frac{1.84\lambda}{B_{(hk)}\cos\theta} \tag{5.1}$$

had been used to characterize the structure of many carbon deposits. The quantities λ and θ are the wavelength of the X rays and the diffraction angle, respectively.

202

The usual Scherrer [133] equation for the height of the crystallites is

$$L_c = \frac{0.94\lambda}{B_{(00l)}\cos\theta} . \tag{5.2}$$

Biscoe and Warren found that the L_a and L_c of carbons were proportional to one another. L_a is usually in the range $L_a = L_c$ to $L_a = 2L_c$.

The layer spacing deposited in fluid beds at temperatures in the range of 1200 - 2200°C is near the ideal spacing of $3.44\,\overset{\circ}{A}$. When carbons are deposited above 2200°C, the mean layer spacing will decrease. Bacon [134] gave a relation for mean layer spacing $\overline{d}$ to be

$$\overline{d} = 3.44 - 0.086(1-p) - 0.064p(1-p), \tag{5.3}$$

where p is the fraction of layers that are disordered.

5.2.2. Characterization by the Microstructure of Pyrocarbons

One of the easiest methods used to characterize pyrolytic carbon deposits involves categorizing them according to their appearance when viewed metallographically with polarized light. The deposits formed in fluid beds may or may not show growth features when viewed with polarized light. Deposits without a visible grain structure have been divided into two groups according to the anisotropy revealed by polarized-light examination [135]. When a deposit is optically active, it is called "laminar"; when it is not, it is called "isotropic". Carbon deposits formed in fluid beds that have distinct grains visible in their microstructure are called "granular" when the grains are small and nearly randomly oriented and "columnar" when the grains are larger and more aligned with the growth direction [136]. Examples of the four microstructural types are shown in Figure 5-1. Microstructures made up of distinct grains are formed when deposition conditions favor orderly growth, i.e., there is a low degree of supersaturation of carbon in the gas phase and large gradients in composition and temperature. Microstructures without growth features are formed under large supersaturation when a considerable amount of carbon is available to the surface and gradients in temperature and composition are small. The origin of the microstructures of pyrolytic carbon will be discussed later.
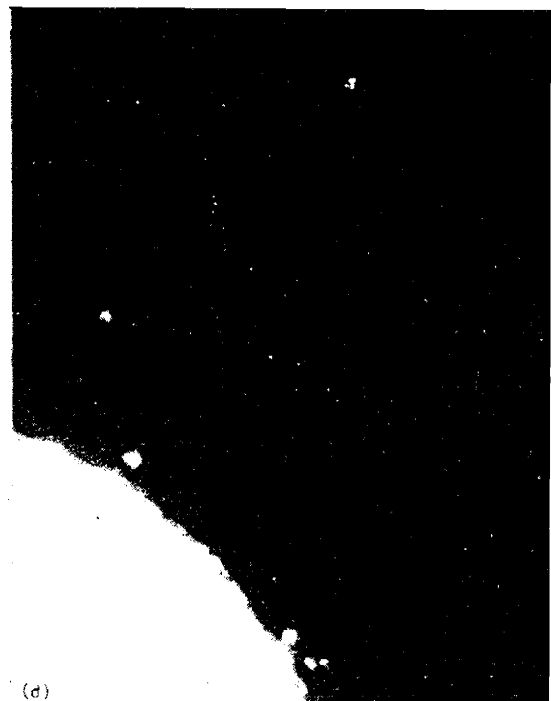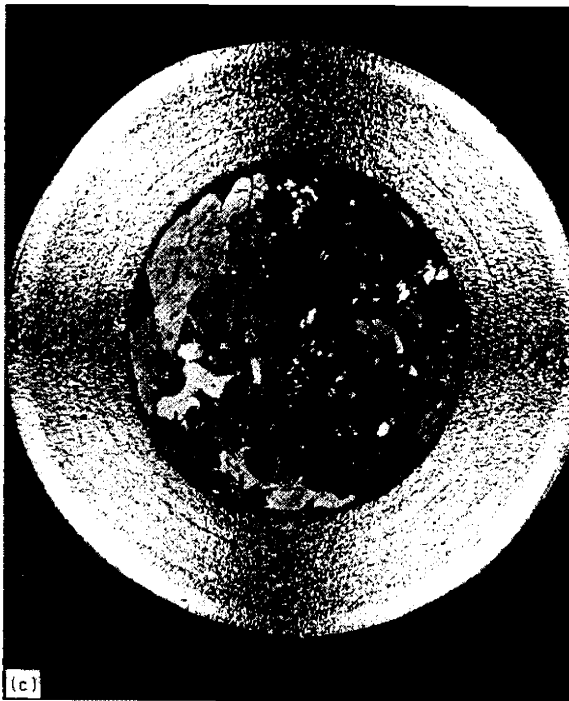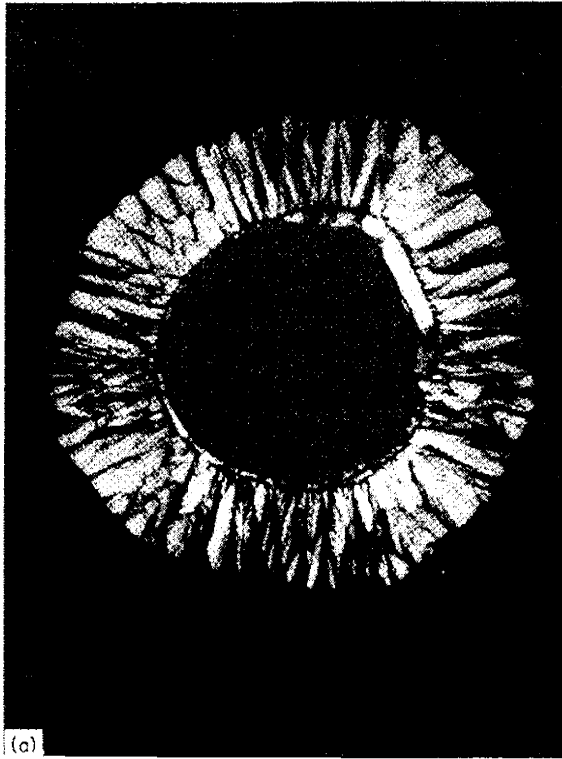
Figure 5-1. Microstructures of pyrolytic carbons deposited in fluid beds: (a) columnar 400× (from Bard et al. [137]), (b) granular 240×, (c) laminar 120×, and (d) isotropic, 240×. Polarized light. (from Bokros [40])

5.3. Relation between Pyrocarbon Structure and Deposition Conditions

Pyrocarbon coatings with the optimum combination of properties were not reproducibly prepared until systematic studies correlating the properties and structures of the carbon deposited with the deposition conditions were performed. For deposition on nuclear fuel particles, experience has shown that all the coating and structural parameters in Figure 5-2 are necessary to uniquely specify the deposition conditions and the structure of pyrocarbon deposited.
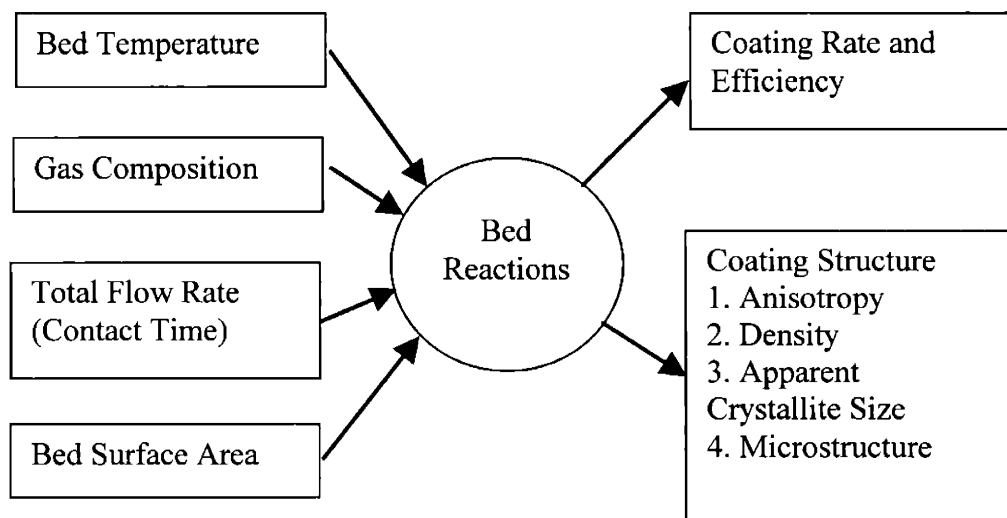
Figure 5-2. Diagram relating four coating parameters, the bed reactions, the coating rate, and the structure of the pyrocarbon deposited (from Bokros [40])

Through systematic variation of the four independent deposition parameters and observation of the structure of the pyrocarbon deposited, numerous useful structures have been identified and insight has been gained into the mechanisms of carbon deposition from gaseous hydrocarbons.

5.3.1. Deposition in Fluidized Beds from Methane

Some experimental results from systematic studies correlating the properties and structures of pyrocarbon deposited with the deposition conditions are shown in Figure 5-3 [135][138]. These data are for deposition in a 2.5cm diameter coater with an initial bed surface area of 400cm^2 and a constant total flow rate (contact time from about 0.1 to 0.2

205

sec). The deposition could be divided into three regimes in Figure 5-3(a) on the basis of the microstructure of the pyrocarbon deposited:

(1) A low temperature region where deposits with laminar micro-structures were formed.

(2) An intermediate region where isotropic deposits were formed.

(3) A high-temperature low-methane-concentration region where granular deposits were formed.
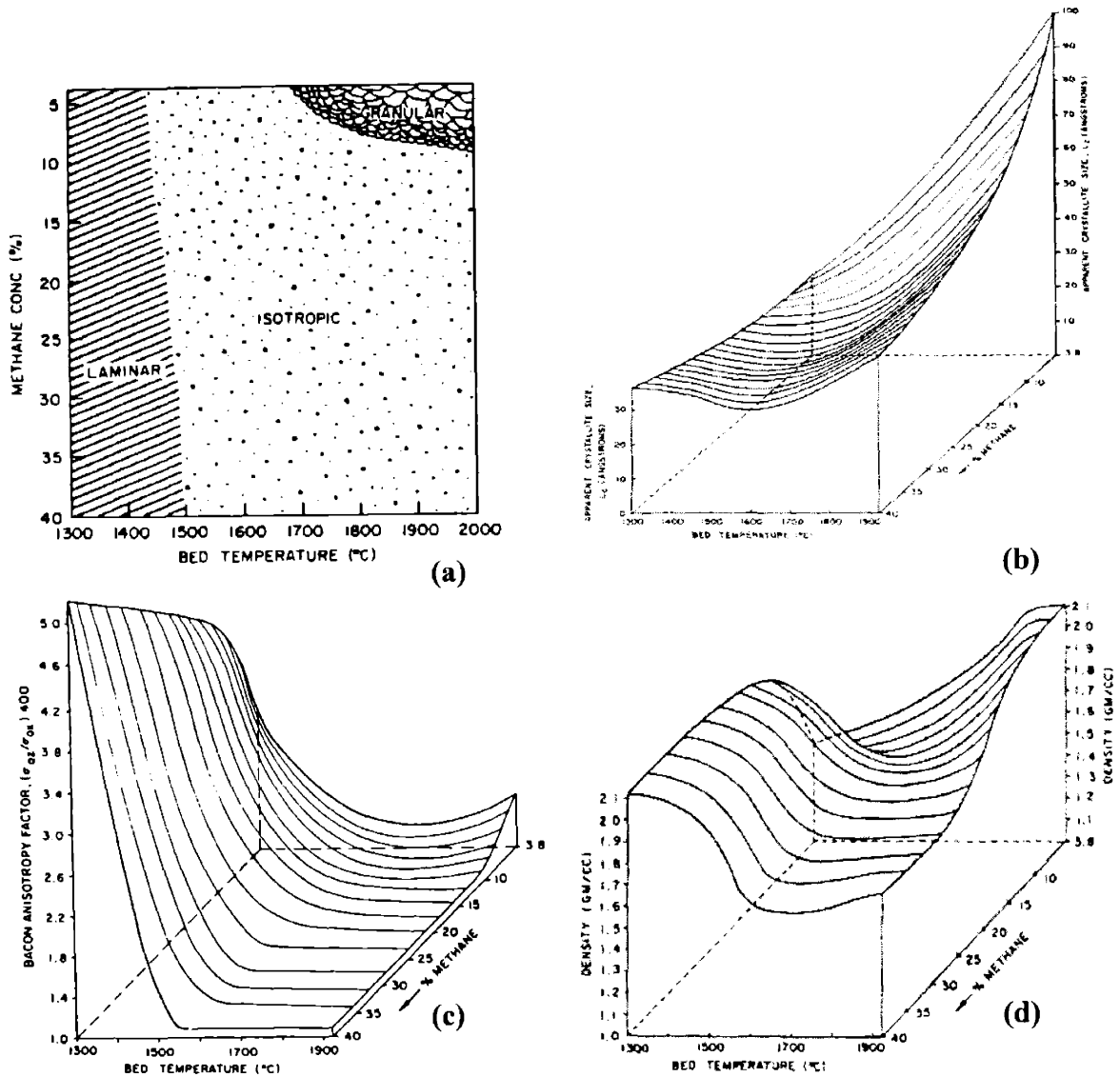
Figure 5-3. Diagrams showing the relationship between the structure of pyrocarbon and its deposition conditions: (a) microstructure, (b) apparent crystallite size, (c) anisotropy factor, (d) density (from Bokros [135])

We should point out that in Figure 5-3(c) the Bacon Anisotropy Factor is not the same measure as we have used throughout this thesis. We should take the values by relative magnitude. The data in Figure 5-3(b), (c) and (d) show that

(1) The deposits with laminar microstructure are anisotropic with small crystallite sizes.

(2) The isotropic carbons have low densities, little preferred orientation and intermediate to small crystallite sizes.

(3) The granular deposits have large crystallite sizes, high densities, and a small amount of preferred orientation.

Figure 5-3(d) shows that there is a low density trough that extends to low temperatures at small methane partial pressures, so that at 1350°C carbons with densities as low as $1.4 g/cm^3$ can be deposited at a methane concentration of about 4%. At the same temperature, but at still lower methane concentrations, Beatty et al. [139] found that carbons with higher densities and microstructures with growth features can be deposited.

Figure 5-3(c) shows that BAF decreases rapidly with the increase of temperature. Above 1550°C, BAF is nearly constant except at high temperature (above 1800°C) with low methane concentration. Grisdale showed further that at a given methane concentration in the laminar region, the anisotropy of deposits is maximum at 1025°C.

Now we look at the effect of fluidized bed surface area. Data reported by Bokros [135] show that an increase in the bed area extends the laminar region to higher temperatures and, at a given temperature and methane concentration, causes the anisotropy and density of the deposits to increase, as shown in Figure 5-4. Since the amount of carbon available for deposition is nearly constant, carbon crystallites deposited at a slow rate per unit area when bed is large have adequate time to do thermal motion and rearrange themselves, therefore the deposits are tend to be denser and more anisotropic than that when the bed area is small. In the laminar region (Figure 5-3(a)), if the bed surface area is reduced, the amount of carbon available for deposition per unit area can be increase to such a high level that polymeric droplets in an advanced state of pyrolysis nucleate in the gas and incorporate into the deposit. When a large bed area is used at 1350°C, the anisotropy increases with methane concentration. For small bed areas, the anisotropy increases, reaches a maximum and then decreases. It has been suggested that the maximum marks the point of supersaturation, where a "rain" of

droplets occurs [135]. The formation of granular structures also depends on the bed surface area. A decrease in bed area expands the granular region shown in Figure 5-3(a) to higher methane concentration and lower temperature. The formation of granular carbons is favored by high temperatures, small bed areas and low concentrations of hydrocarbon.
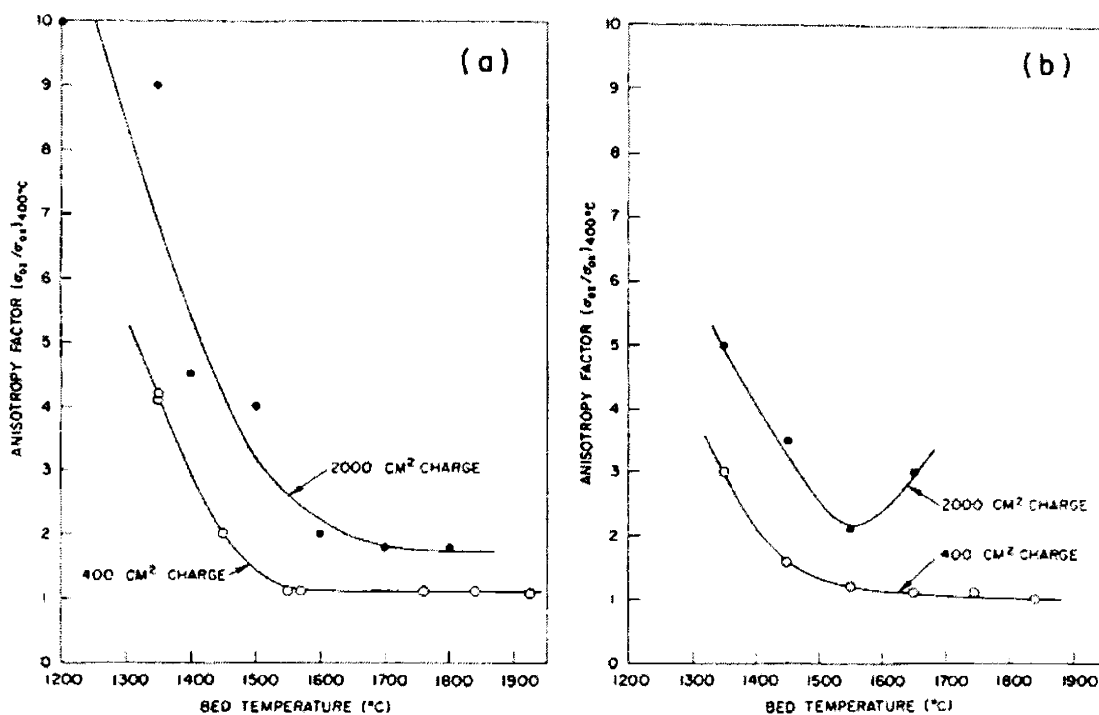
Figure 5-4. Bacon anisotropy factor versus deposition temperature for bed areas of 400 and 2000cm^2; (a) 40% methane in helium; (b) 11% methane in helium. (from Bokros [135])

5.3.2. Deposition in Fluidized Beds from Other Hydrocarbons

The structure of carbon deposited should depend on the nature of the parent hydrocarbons. The statement is given in the sense that all the other deposition conditions are the same. However, if the concentration of the parent hydrocarbons are adjusted to provide the same deposition rate, Bard et al. [137] showed with experiments that the structures of the carbon deposited at a given temperature are nearly identical.

Browning et al. [140] have shown that the variations in the structure of carbons deposited from acetylene with deposition conditions are very similar to the variations

208

observed in carbons deposited from methane. The structure of the carbon deposited under a specific set of conditions when acetylene is used, however, corresponds to structures obtained with methane at somewhat higher temperatures.

A thorough investigation of carbons deposited from propane was reported by Beatty [141]. Comparison of Beatty's data for propane with those for methane and acetylene indicates that carbons with similar structures can be deposited from any of these hydrocarbons but that for a specific set of conditions the depositions have different structures.

The porous pyrocarbon deposited in fluid beds have gained importance in the development of nuclear fuel particles. It is isotropic, with small crystallite size, and has most commonly been deposited from acetylene at temperatures in the range of 900 – 1200°C.

5.4. The Microstructures of Pyrocarbon

The following qualitative description of carbon deposition in fluid bed was generally accepted. At temperatures below about 1500°C, polymerization reactions produce planar arrays of carbon atoms in a variety of states of dehydrogenation. As polymerization and dehydrogenation proceed, the saturation vapor pressure of the planar complexes must eventually be exceeded. When this happens, the complexes can either condense on surfaces in the reaction zone or form stable gas-borne nuclei which, if they remain gas-borne, finally become soot particles. At higher temperatures, only relatively small gas-phase species are stable. The deposits formed are therefore thought to be built up from solid carbon particles that form in the gas during preheat and from carbon deposited directly from relatively small species such as C_2H, C_3H, C_4H, etc. [142].

The morphologies of all pyrocarbon deposits are believed to be determined by the relative importance of deposition by direct condensation of carbon from individual species with sizes depending on temperature and pressure, and deposition of solid particles formed in the gas phase. The gradients in composition and temperature at the surface of a growing deposit strongly influence the formation of distinct growth features in a deposit.

5.4.1. Deposition at Low Temperatures (900 - 1400°C)

At very low hydrocarbon concentrations and low temperatures, gas phase polymerization is restricted and the growth of a deposit must occur by the addition of small aggregates at a rate low enough to allow the evolution of growth features in fairly dense deposits [137]. Increasing the hydrocarbon concentration at constant temperature causes the density of deposits to decrease and the growth features to disappear. At 1400°C and deposition rates near 10μm/hour, the density reaches a minimum and the carbon has a laminar structure. This is the low density trough described before (Figure 5-3(d)). A further increase in hydrocarbon concentration causes the deposition rate, density, crystallite size and anisotropy to increase.

Such phenomenon might be expected if large planar complexes form in the gas phase and condense directly on surfaces in the bed. Since large planar complexes are more likely than smaller ones to align themselves with the deposition surface and with one another, the anisotropy, density, and crystallite size could be expected to increase with hydrocarbon concentration at constant temperature. This leads to the suggestion that the minimum in density as a function of hydrocarbon concentration is a result of the poor alignment of relatively small planar complexes that condense on the bed surface area at a rate too high to allow thermally activated rearrangements in the condensed phase.

At a critical level of super-saturation, the preferred orientation of the carbon deposited reaches a maximum, which marks the degree of super-saturation where stable gas-borne nuclei can form and grow to form droplets. Results of David et al. [143] have revealed direct evidence of droplets incorporated into pyrocarbon deposits. The decrease in anisotropy beyond the maximum is therefore attributed to the incorporation of droplets into deposits. The exact position of the maximum in anisotropy depends on the hydrocarbon concentration, the contact time and the bed area. Large surface area is efficient "collectors" and depresses the degree of saturation of the gas. Increasing the contact time tends to increase the level of saturation of the gas. Thus, the maximum in preferred orientation occurs at lower hydrocarbon concentration when small bed area and long contact time are used. Figure 5-5 summarizes in schematic way the ideas presented

above regarding the origin of carbons deposited at temperature near 1400°C. The deposits depicted in Figure 5-5(a) and (b) are true "surface carbons"; however, deposit in Figure 5-5(c) is made up of carbon particles that were nucleated in the gas phase and subsequently incorporated into the deposit as well as complexes that condensed directly.

(a)

(b)

DROPLET OF CONDENSED,
HIGH MOLECULAR WEIGHT
POLYMER

SINGLE PLANAR
POLYMER MOLECULE

SMALL HYDROCARBON
FRAGMENTS

(c)
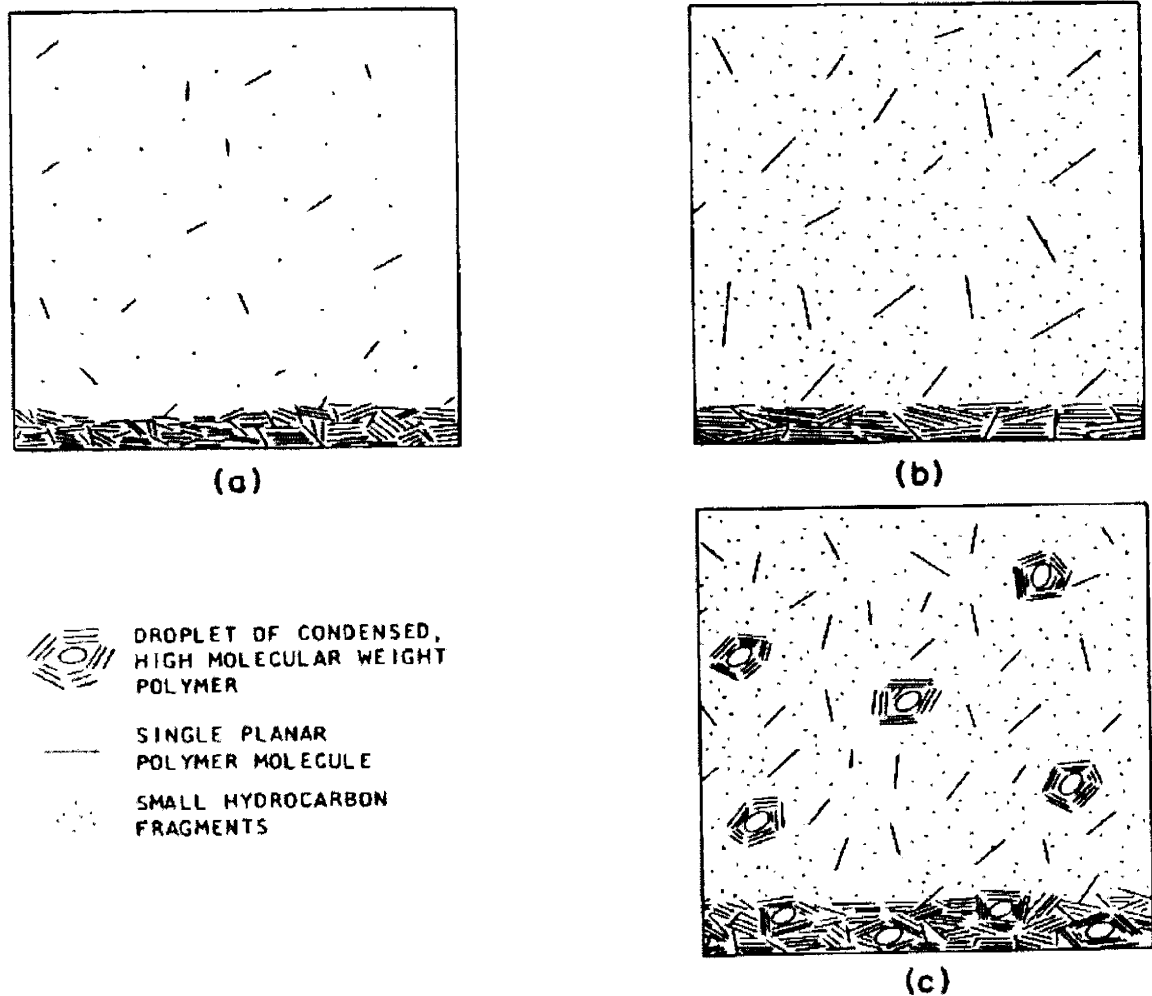
Figure 5-5. Idealized schematic diagram of carbon deposition at 1400°C. (a) low methane concentration and large bed area; (b) high methane concentration and large bed area; (c) high methane concentration and small bed area (from Bokros [135])

5.4.2. Deposition of Isotropic Pyrocarbons at Intermediate Temperatures (1400 - 1900°C)

It has been reported ([130], [131] and [143]) that, in contrast to the droplets formed in the gas phase and deposited at about 1300°C, those formed at about 1600°C are in a more

211

advanced stage of pyrolysis at the instance they are deposited and consequently resemble solid soot particles more than semi-fluid droplets. The restriction imposed by this high viscosity is believed to be the most likely cause of the low density of pyrocarbon deposited at about 1600°C [135][144]. The increase in the density of deposits formed above about 1700°C (Figure 5-3(d)) is taken to be a consequence of thermally activated rearrangement after deposition. Growth features are not visible in microstructures formed in this region (Figure 5-1(d)).

5.4.3. Deposition of Granular and Columnlar Pyrocarbons

The surface area of particles in a fluid bed can influence the deposition in two important ways. Firstly, the agitation in the bed causes mixing of the pyrolyzing gas and prevents pronounced gradients in composition from developing. Secondly, the particles act as heat transfer media which accept radiant thermal energy from the furnace wall and transfer it to the gas. Hence when the surface area is large, gradient in temperature between the particles and the gas is relatively small. In turn, when the bed area is small, gradients in temperature and composition, which favor orderly growth, are attainable in fluid bed. Under such conditions, crystallites develop from the surface of the substrate particles and grow until they are interrupted by the occasional arrival of a solid particle at the surface of the growing deposit. High temperature and low hydrocarbon concentration promote orderly growth because only small species are stable at high temperatures and the rate of gas-borne polymerization decreases with decrease of hydrocarbon concentration [145].

The best evidence of the influence of the bed surface area on the growth of a carbon deposit has been provided by the abrupt transitions from granular to isotropic structures that have been observed in given deposition experiments when the bed area reached a critical value [135][146]. At a given methane partial pressure, the critical surface area increased with increasing deposition temperature, and at a given temperature, the critical area increased with decrease of methane partial pressure. Presumably, at the critical bed area, the heat transfer to the gas is just sufficient to cause an avalanche of stable carbon nuclei to form and be incorporated into the growing deposit. Thus, when small bed areas

212

are used, orderly growth can occur and deposits with microstructures that contain well-developed growth features can be achieved. The conditions favoring the deposition of laminar, granular, and isotropic structures in fluid beds are summarized in Table 5-1.

Table 5-1. Summary of Conditions Favoring Various Structures of Pyrocarbon Deposition in Fluid Beds

Microstructure	Mechanism	Favoring Conditions
Laminar	Planar complexes form in the gas and deposit directly on the particle surfaces	Low temperature, intermediate to high hydrocarbon concentration and large bed surface area
Isotropic	Supersaturation occurs in the gas; gas-borne particles form and are incorporated into carbon deposit	Long contact time, small bed surface area, high hydrocarbon concentration and low to intermediate temperature
Granular and Columnar	Crystallites grow from substrates with little interruption from gas-borne particles	High temperature, low hydrocarbon concentration, and small bed surface area

5.5. Relation between Pyrocarbon Structure and Properties

Actually in Chapter 2 we already presented the models for pyrocarbon properties with respect to its structure represented by degree of preferred orientation and density, but the models are more or less phenomenological. Here we look at some of the pyrocarbon properties from physics point of view, and bring in some connections with deposition conditions. Mechanical properties and irradiation induced dimensional changes will be reviewed next.

5.5.1. Mechanical Properties of Pyrocarbons

The variations in the mechanical properties of carbon deposited in fluid beds provide a good example of the structure sensitive nature of the properties of pyrolytic carbon. For

instance, we know the bonding in a graphite crystallite is highly anisotropic. Young's modulus for such a crystallite in the direction inclined at angle ϕ to the c direction (Figure 2-17) is related to the elastic-compliance constants [147] by

$$\frac{1}{E(\phi)} = S_{11} \sin^4 \phi + S_{33} \cos^4 \phi + (2S_{13} + S_{44}) \cos^2 \phi \sin^2 \phi. \qquad (5.4)$$

It can be shown that the E of a graphite crystallite can vary by two orders of magnitude with direction. It is therefore clear that the properties of an aggregate of crystallites will be a sensitive function of the preferred orientation of the crystallites. If the crystallite elastic-compliance constants were known as a function of crystal perfection, it would be possible to use space-averaging methods, such as those described by Price [42], to estimate the elastic properties of a polycrystalline body.
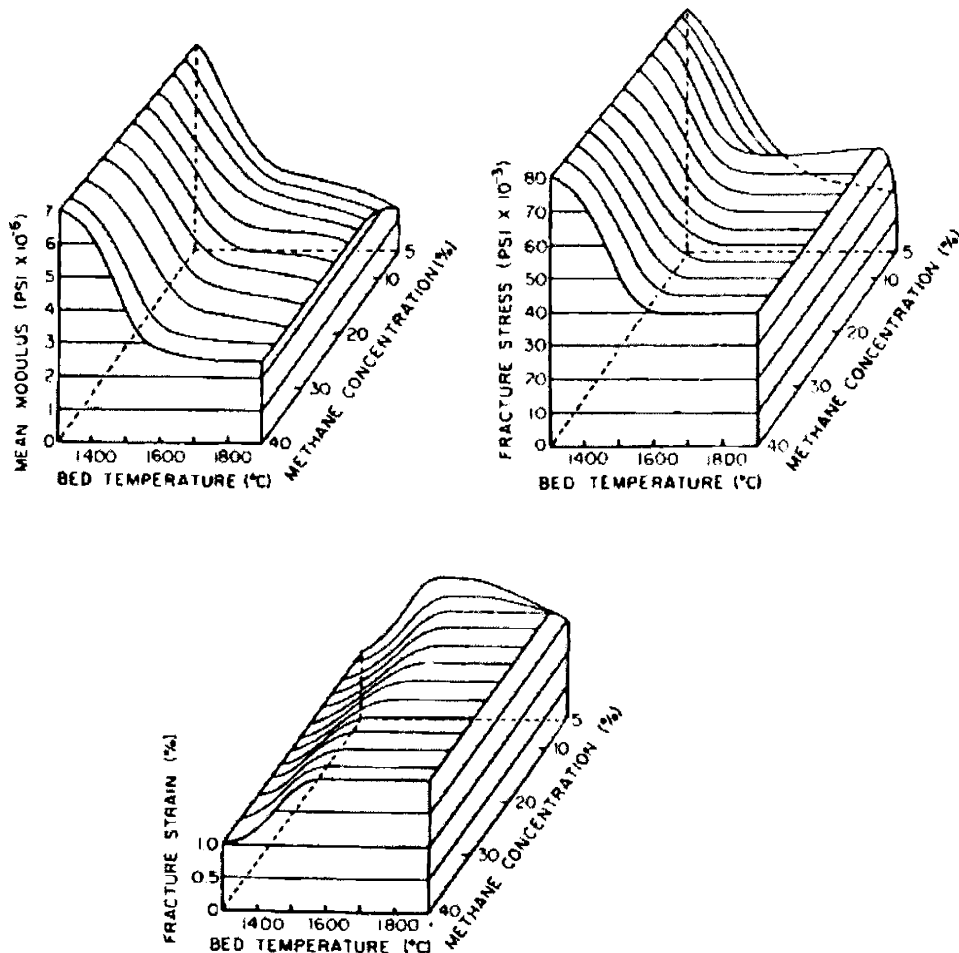
Figure 5-6. Diagrams relating mechanical properties of pyrocarbon to deposition conditions; deposits were prepared in a 2.5cm diameter coater using a 400cm² initial bed area (from Bokros and Price [148])

214

The variations in mechanical properties with deposition conditions for pyrocarbon deposited from methane in fluid bed are shown in Figure 5-6. The corresponding structural data are in Figure 5-3. A striking feature of the data is the high values of the moduli and strength for pyrocarbons deposited at temperature below about 1500°C. These results are consistent with the observations of Blocher et al. [149], which show that the carbon deposited at low temperature are much harder than those deposited at high temperature. Grisdale [131] and Tesner and Timofeeva [150] have reported that the hardness of pyrolytic carbon exhibits a maximum in the range of deposition temperature near 1500°C. The rapid increase in the moduli of all carbons with decreasing deposition temperature cannot be accounted for by the increase in preferred orientation, but rather has been attributed to the presence of cross-links between the layer planes in the deposition at low temperature. Cross links decrease S_{44}, increase moduli and inhibit inter-laminar fracture. Examination of the fracture path for carbon broken in bending shows that cross-linking is prevalent in the as-deposited condition, so the fracture does not favor an interlayer path.

The minimum in strength observed for carbons deposited near 1900°C from low methane concentration (Figure 5-6(b)) is for the deposits with the largest grains visible in their microstructures (see Figure 5-3(a)). The explanation is that cracks which form in grains under stress and ultimately lead to failure are limited by the grain boundaries [148]. Furthermore, abnormally large growth features may act as stress raisers and cause failure under low load [151].

5.5.2. Irradiation Induced Dimensional Changes in Pyrocarbons

This section will show the fundamental studies on how the dimensional behavior of carbon depends on its internal crystalline structure. When carbon is irradiated with fast neutrons, energetic knock-on carbon atoms are generated by collision of neutrons with carbon atoms in the lattice [152]. The displaced carbon atoms and the vacancies produced by the recoiling carbon atoms could recombine, nucleate to form loops, or become annihilated at structural defects such as crystallite boundaries. The competition of them

215

results in structure-sensitive bulk dimensional changes that vary with temperature in a complex way.

Because the bulk dimensional changes induced by neutron irradiation are a direct consequence of the dimensional changes induced in the crystallites, we need to refer again to the crystallite shown schematically in Figure 2-17. During irradiation, such a crystallite expands in the c direction and contracts in the a direction. If there were no accommodation between crystallites, the dimension of a polycrstalline aggregate would change in a neutron flux ϕ at a rate determined by the degree of preferred orientation of the aggregate as

$$\frac{1}{l_i}\frac{dl_i}{d\phi} = \frac{(1-R_i)}{X_c}\frac{dX_c}{d\phi} + \frac{R_i}{X_a}\frac{dX_a}{d\phi}.$$ (5.5)

The quantities $(1/X_a)(dX_a/d\phi)$ and $(1/X_c)(dX_c/d\phi)$ are the fractional rate of crystallite dimensional change in the a and c directions, respectively. The total bulk change after a fixed neutron exposure can be obtained by integrating eq. (5.5),

$$\ln\left(1+\frac{\Delta l_i}{l_i}\right) = (1-R_i)\ln\left(1+\frac{\Delta X_c}{X_c}\right) + R_i\ln\left(1+\frac{\Delta X_a}{X_a}\right).$$ (5.6)

Experimental data from Bokros and Price [153] and Bokros et al. [64] show the dimensional changes agree with the predictions of eq. (5.6), which are plotted in Figure 5-7. From eq. (5.6) we could find that an extrapolation of the data in Figure 5-7 to the ordinate intercepts at the abscissa values R=0 and 1 yields the crystallite changes $\ln[1+(\Delta X_c/X_c)]$ and $\ln[1+(\Delta X_a/X_a)]$, respectively. Eq. (5.6) describes the dimensional change of aggregates due to the dimensional changes of crystallites and anisotropy. In fact, when examined with sufficient precision, all dimensional changes have been found to be accompanied by some change in density. Even though the anisotropic distortion and the densification are not likely to be independent, it is convenient to separate them and superimpose the solutions finally.

When a carbon deposit has a substantial density defect, the deposit is densified during irradiation. For small neutron doses ($<3\times10^{21}$n/cm^2 at ~600°C and $<1\times10^{21}$n/cm^2 at 1200°C), the densification can be described by a simple first-order equation

$$\rho = \rho_{th} - (\rho_{th} - \rho_0)\exp(-k_d\phi),$$ (5.7)

where ρ_0 is the original density, ρ_{th} is the density that is approached at large doses, and K_d is the first-order rate constant for the densification.
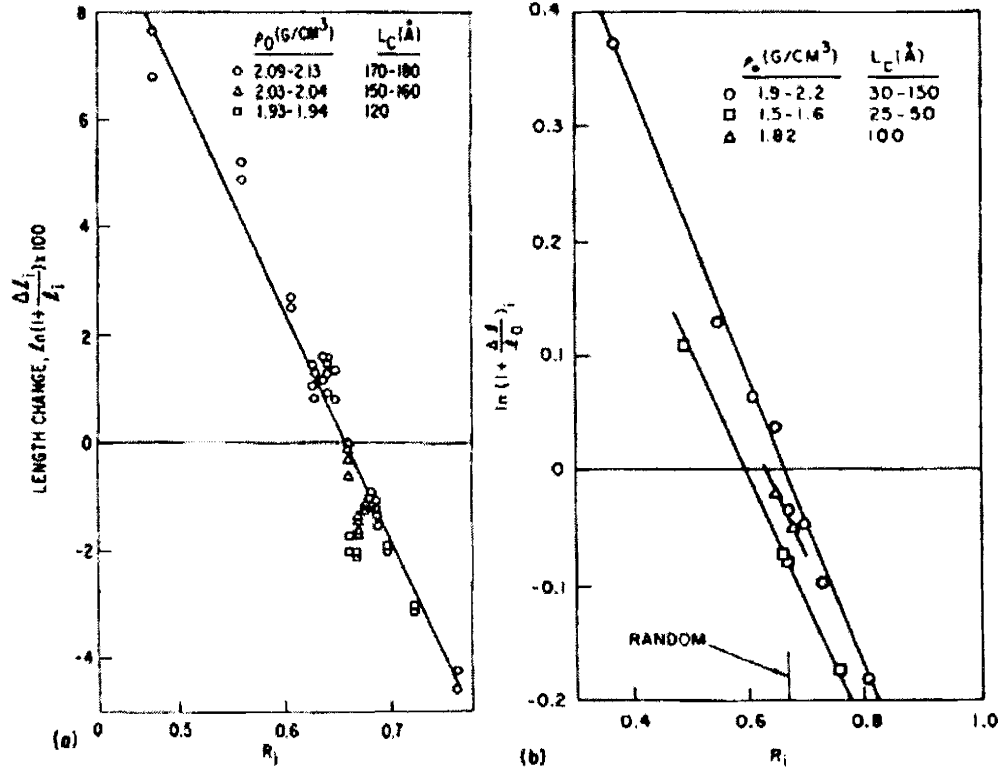
Figure 5-7. Plots of dimensional change versus preferred orientation, (a) carbons irradiated at 510°C to an exposure of 3.8×10^{21}n/cm^2 (E>0.18MeV), (b) carbons irradiated at 1040°C to an exposure of 2.4×10^{21}n/cm^2 (E>0.18MeV) (from Bokros and Price [153])

At low neutron doses, the fractional rate of dimensional change of an isotropic carbon deposit is related to the fractional rate of density change by

$$-\frac{3}{l_i}\frac{dl_i}{d\varphi} = \frac{1}{\rho}\frac{d\rho}{d\varphi} = \frac{k_d(\rho_{th} - \rho_0)\exp(-k_d\varphi)}{\rho_{th} - (\rho_{th} - \rho_0)\exp(-k_d\varphi)}.$$ (5.8)

For an anisotropic pyrocarbon deposit, the rates $(1/l_i)(dl_i/d\varphi)$ for parallel and perpendicular directions are not equal, and the dimensional changes are expressed by

$$\frac{2}{l_{//}}\frac{dl_{//}}{d\varphi} + \frac{1}{l_\perp}\frac{dl_\perp}{d\varphi} = \frac{-k_d(\rho_{th} - \rho_0)\exp(-k_d\varphi)}{\rho_{th} - (\rho_{th} - \rho_0)\exp(-k_d\varphi)}.$$ (5.9)

To predict the rate of dimensional change in a carbon deposit with some preferred orientation, it would be necessary to know the relationship between the anisotropic distortion and the shrinkage resulting from irradiation. Bokros and Schwartz [154] have

217

shown that the dimensional changes induced in oriented carbons with a density defect can be approximated by superimposing the anisotropic distortion of the crystallites and the shrinkage resulting from densification as if they were independent. Then

$$\frac{1}{l_i}\frac{dl_i}{d\varphi} = \frac{1}{X_c}\frac{dX_c}{d\varphi}(1-3R_i/2) - \frac{1}{3}\frac{k_d(\rho_{th}-\rho_0)\exp(-k_d\varphi)}{\rho_{th}-(\rho_{th}-\rho_0)\exp(-k_d\varphi)}, \qquad (5.10)$$

where the first term represents the distortion rate without densification. Under such circumstance, the fact is when R = 2/3 (which means carbon is isotropic), $(1/l_i)(dl_i/d\varphi) = 0$. From eq. (5.5) we get

$$(1/X_c)(dX_c/d\varphi) = -2(1/X_a)(dX_a/d\varphi), \qquad (5.11)$$

therefore the first term in eq. (5.10) had such form. The second term is the contribution of a uniform densification. Integrating eq. (5.10) yields the total dimensional change after a neutron dose φ in the direction of l_i to be

$$\ln\left(1+\frac{\Delta l_i}{l_i}\right) = (1-3R_i/2)\ln\left(1+\frac{\Delta X_c}{X_c}\right) - \frac{1}{3}\ln\left(\frac{\rho_{th}-(\rho_{th}-\rho_0)\exp(-k_d\varphi)}{\rho_0}\right). \qquad (5.12)$$

A comparison between the observed dimensional changes for a series of carbon with a BAF of less than1.3 and those predicted from eq. (5.12) is shown in Figure 5-8.

Although eqs. (5.10) and (5.12) have proved useful in evaluating the operational behavior of coated particles early in their life, they are not useful for predicting the dimensional behavior of pyrocarbon coating after high neutron doses. The reason is that at high neutron exposure and especially at high temperatures, the densification departs from simple first-order behavior and neutron-induced changes in preferred orientation become important [64]. Neutron-induced changes in anisotropy were first reported for carbons irradiated to neutron exposure above 2.6×10^{21}n/cm^2 at temperatures higher than 1100°C. When changes in preferred orientation take place, plots of the dimensional changes versus the original preferred orientation parameter like Figure 5-7 depart from linearity and take on a sigmoidal shape. Because a large amount of internal energy must be released as a result of intercrystallite shear when an isotropic body is irradiated, an increase in the preferred orientation of the crystallite is energetically favored. If a mechanism is available, such changes are to be expected.
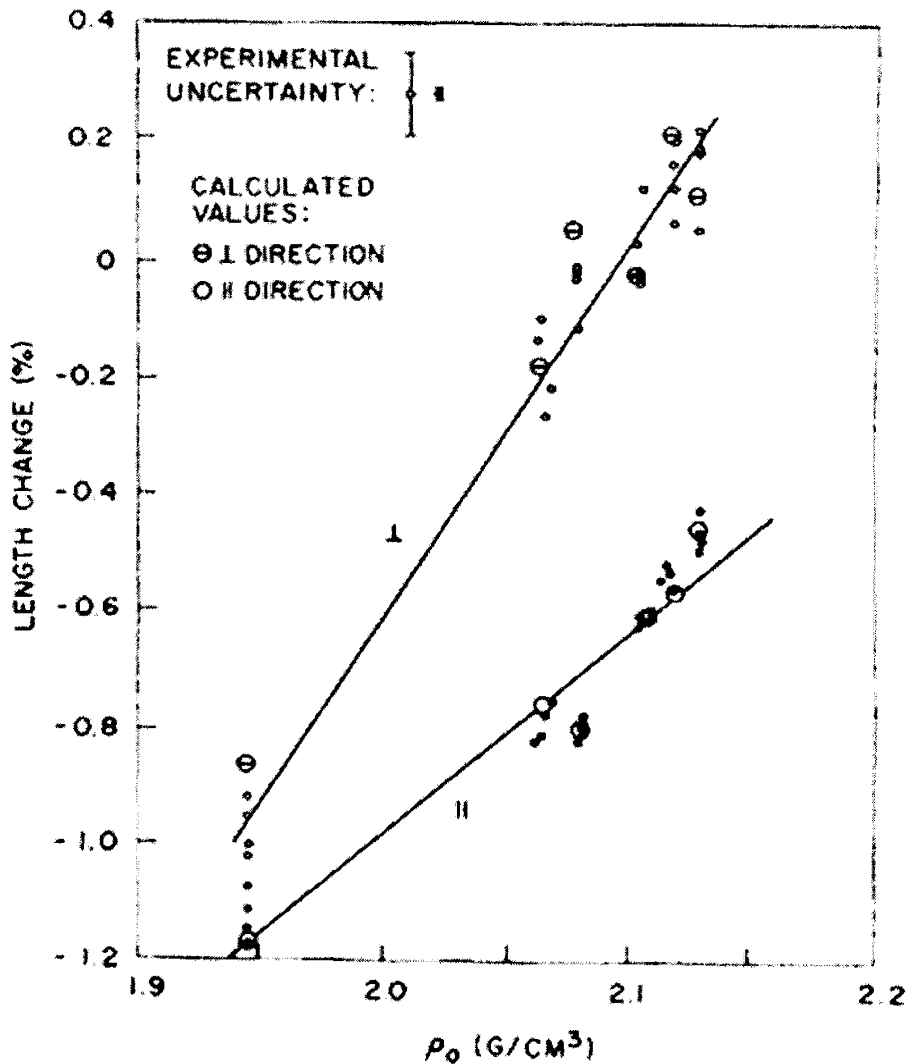
Figure 5-8. Comparison between experimentally observed length changes and those calculated from eq. (5.12). Irradiated at 710°C to 2.2×10^{21} n/cm^2 (E>0.18MeV) (from Castle Jr. [155])

5.6. Recommended Material Properties and Coating Conditions

Although in this work we are not ready to give detailed quantitative recommendations to the manufacturing of the dense pyrocarbon layers and the SiC layer, we can qualititatively discuss what kind of fuel particle coating layers are favorable.

Firstly, we discuss the pyrocarbon layers. From the mechanical behavior point of view, we want the density of pyrocarbon to be high and the BAF_0 of pyrocarbon to be

low. Pyrocarbon layers with higher density are stronger and more resistant to fission product migration, and irradiation induced densification discussed in Section 2.4.3, which induces stresses, will be less. Pyrocarbon layers with lower BAF_0 tend to have lower stresses in the structural layers, as discussed in Section 4.1.1.5. From material strength point of view, higher pyrocarbon density is better, but higher pyrocarbon BAF_0 benefits the pyrocarbon strength, as shown in Section 2.5.1.1 and demonstrated in the fuel optimization exercise in Section 4.3.2. As we said before, the dependence of the pyrocarbon strength on its BAF_0 may indeed to true, but this needs to be verified and discussed further. Right now we assume that nearly isotropic pyrocarbon ($BAF_0 \approx 1$) performs better, which is the common view of the HTGR community. From pyrocarbon microstructure point of view, we want small graphite crysallites and grains, because the strengths of brittle materials increase with decreasing grain size, as mentioned at the bottom of Page 98. In addition, it is harder for fission products to transport through pyrocarbons with smaller grains. We also do not want to see orderly growth features in pyrocarbons, which increase the anisotropy. With these discussons above, we conclude that isotropic pyrocarbons with high density and small grains should be manufactured for the IPyC and OPyC layers. As Figure 5-1 shows, granular and columnar pyrocarbons have larger grains and high anisotropy, and laminar pyrocarbons have small grains but high anisotropy, so they are not of the type that we want. Based on the discussions in this chapter, especially the summary in Table 5-1, the favoring coating conditions for the IPyC and OPyC layers are intermediate coating temperature, low to intermediate hydrocarbon concentration, and small fluidized bed surface area. In Figure 5-3, we see that the coating temperature should be about 1700°C, and the hydrocarbon concentration should be relatively low but not too low to enter the granular pyrocarbon region. The hydrocarbon concentration should not be too high either, otherwise the coating rate is too high and gas-borne droplets will integrate into the deposit, which results in low density of the deposit.

Secondly, we look at the SiC layer. Based on the discussion on the difference of the U.S. and German made SiC layers, as shown in Figure 3-24, we recommend SiC layers with small grains, which are formed in low deposition temperatures. From our discussion on the crack induced fuel failure model in Section 2.5.2.2, small SiC grains provide lower

local stress concentration in the SiC layer and, hence, it is harder for an IPyC or OPyC crack to propagate into the SiC layer. In addition, the SiC layer with smaller grains has higher strength, and the reason is the same as for the PyC layers.

Finally, we discuss the interfaces between the pyrocarbon layers and the SiC layer. Discussions on NPR irradiation results in Section 3.2.4 revealed the difference of PyC/SiC interfaces in the U.S. and German particles. A continuous coating process like the German's is recommended. By doing so, the coating layer interfaces are strong and the debonding problem is minimized.

Chapter 6.

Discussions and Future Work

6.1. Discussions and Recommendations

We have discussed the development of a fuel performance model for HTGR coated particle fuel, the benchmarking and exercise on the model, and the application of it in fuel particle optimization or design. The major task which is accomplished is the establishment of a fuel performance modeling platform on which further improvements and developments could be built. As what was stated at the end of Chapter 1, we have been trying to put an emphasis on the physics of fuel performance, by formulating a mechanical analysis based on continuum mechanics, modeling fuel failure processes with linear elastic fracture mechanics, and simulating irradiation environments according to thermal dynamics and reactor physics. Meanwhile, with practical considerations we use Monte Carlo technique and statistics to account for the variations in particle properties and irradiation paths and incorporate material models with engineering approach (such as interpolation and fitting). This model provides a good representation of the mechanical aspect of every phase of coated fuel particles, from manufacturing, performance, test, to design. With the abovementioned generic considerations and careful structuring of the corresponding computer code, new features and refinements to the model can be integrated with little effort. Now we discuss some directions in which the developed model can be extended.

6.1.1. Chemical Models

The immediate follow-up of this fuel performance model will be the development of chemical models for coated fuel particles. One of the three concentrations is the better calculation of fission product release from various types of fuel kernels, including (Pu, U)O_2 fuel, given arbitrary irradiation temperature, fast neutron fluence level, and burnup.

222

This will update the internal pressure which is fed in the mechanical analysis. The second is the diffusion and vapor transport of fission products through intact structural layers, which is independent from the mechanical model. The third is the interaction of fission products with structural layers. Some chemical models exist in the literature, for example, the strength loss of the SiC layer due to grain boundary corrosion. In the model by Gontard and Nabielek [25], the corrosion of SiC grain boundaries by fission products is considered by modifying the Weibull modulus. The effect as a function of the time t (s) and temperature T (°K) is given by

$$\beta = \beta_0 \left(0.44 + 0.56 e^{-\dot{\eta} t}\right),$$
(6.1)

with the grain boundary corrosion rate

$$\dot{\eta} = 0.565 e^{-187400/(RT)} \ (s^{-1}),$$
(6.2)

where

β_0 is the initial Weibull modulus, and

R is the ideal gas constant (8.31J/mol.K).

Elevated temperature will accelerate corrosion rate and decrease Weibull modulus, hence widen Weibull distribution and produce more particles with weak SiC layers. Such phenomenon obviously influences the prediction of mechanical fuel failures, but in this case the only modification we need to make to the mechanical model is updating Weibull modulus.

Chemical attack also causes local defected region in structural layers, especially the most important SiC layer, as shown in Figure 1-6. Pyrolytic Beta-SiC exposed to cesium vapor (pressure of 2.6KPa) at 1500°C for 8 hours showed cesium penetration of 3.5 to 5μm, with the penetration concentrated along laminations in the microstructure [156]. Pyrolytic SiC exposed to either cesium vapor (pressure of 13KPa) or strontium vapor (pressure of 0.7KPa) at 1700°C underwent a pitting type of attack to a depth of about 20μm in 700ks [157]. Pyrolytic SiC is reduced to a carbon skeleton by molten silver containing oxygen at 1250°C, which is believed to be induced by the corrosive effects of AgO [158].

6.1.2. Extensions to Mechanical Models

IRRADIATION TEMPERATURE (K)

400 600 800 1000 1200 1400

	FROM BULK EXPANSION	FROM LATTICE PARAMETER CHANGE
PYROLYTIC BETA (PRICE)	●	O
ALPHA SINGLE CRYSTALS (PRIMAK ET AL.)	■	□
ALPHA SINGLE CRYSTALS (BALARIN)		△
ALPHA SINGLE CRYSTALS (PRAVDYUK ET AL.)		◉
SELF-BONDED BETA (THORNE ET AL.)	▼	
"DENSE" SELF-BONDED POLYCRYST BETA (MARTIN)	▲	
"CRUSILITE" (DRAGON DATA)	✕	

SATURATION LINEAR EXPANSION (%)

1.5

1.0

0.5

0

0 200 400 600 800 1000 1200

IRRADIATION TEMPERATURE (°C)

Figure 6-1. Irradiation induced expansion of SiC as a function of irradiation temperature (fluences between 0.3×10^{21} n/cm^2 and 5×10^{21} n/cm^2) (from Price [7])

We have treated the SiC layer as an elastic medium with no irradiation effect. In fact, there are also irradiation induced dimensional changes and creep. Price [7] discussed that at irradiation temperatures below 1000°C, and fluences below about 5×10^{21} n/cm^2, SiC undergoes an isotropic expansion. As the neutron fluence increases, the expansion rapidly saturates at a level that decreases with increasing temperature. The changes in lattice parameters are similar to the changes in overall dimensions. Figure 6-1 assembles data from various sources [159]-[165], and remarkably these data fall into the same band. From the figure we see the irradiation induced dimensional changes in SiC at high temperature is much lower than in pyrocarbons, hence this is the secondary effect in the mechanical behavior of coated particles. Similarly, the irradiation induced creep rates for SiC are several orders of magnitude lower than for pyrocarbons, so in practice, creep in

SiC below ~1100°C can be neglected [7]. Nevertheless, the irradiation induced deformation in the SiC layer can be taken into account with ease such like in the pyrocarbon layers, and only minor changes are needed in the formulation of mechanical analysis in Appendix A.
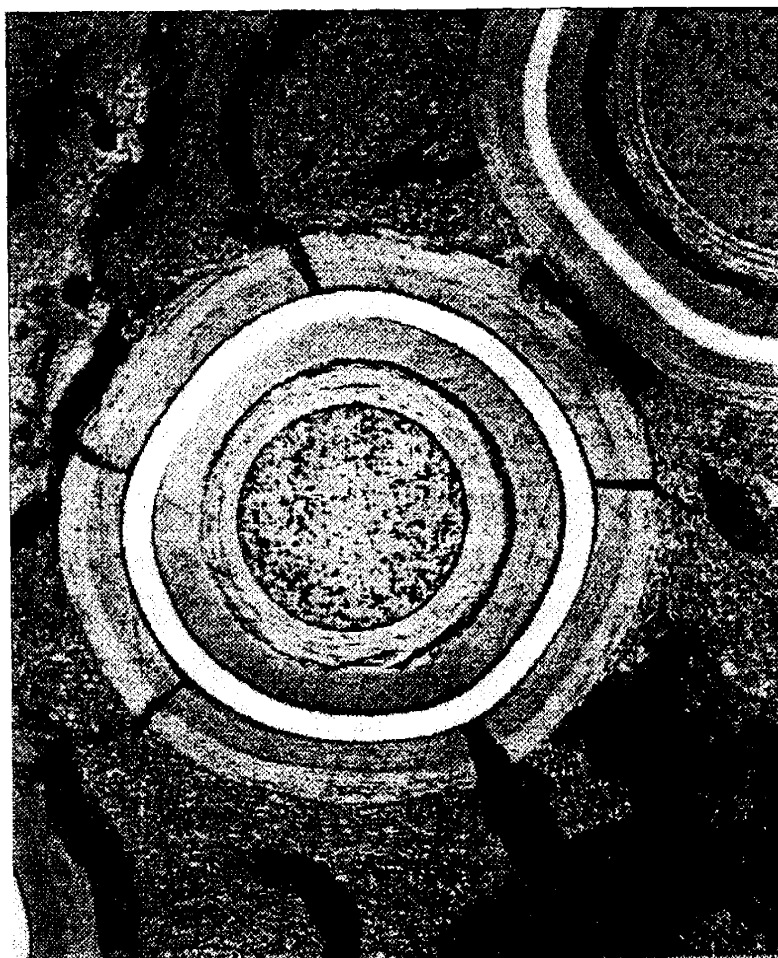
100x   BRIGHT FIELD

Figure 6-2. Irradiation HRB-21 fuel particle with catastrophically failed OPyC and PPyC
(from Leikind et al. [166])

Another important field which needs improvements is the effect of irradiation on the strength and toughness of SiC. There are some publications on SiC strength reduction due to irradiation [116][164], but discrepancy exists in data at various temperatures and irradiation conditions. Little data were reported with regard to the irradiation effect on the fracture toughness of SiC and pyrocarbon. We also discussed briefly in Section 3.2.3 that

fatigue loading could contribute to the crack growth in particles, which needs to be studies further.

In Section 1.3, we also discussed other mechanical fuel failure mechanisms. One is the peel-off and damage of the OPyC layer. We know that the OPyC layer is in direct contact with graphite matrix material or other low density PyC layer (like PPyC layer in NPR fuel mentioned in Section 3.2), which could introduce cracks in OPyC by their own damages. Figure 6-2 shows such an example. We have seen in the simulations of NPR compacts in Section 3.2 that stresses in OPyC are generally lower than in IPyC, but PIE results revealed higher failure probability of the OPyC layers [88]. The reason may lie in the failures of OPyC induced by PPyC and graphite matrix.

One more issue is the role of asphericity of coated fuel particles in fuel performance. Miller and Wadsworth [167] studied two representatives of aspherical particles - faceted particle and ellipsoidal particle by finite element method and concluded that fuel failure probabilities could be increased by a factor of 100 for faceted particles versus spherical particles under typical conditions. They also showed faceted particles are much more prone to failures than elliptical particles. I think the difference lies in the fact that in faceted particles the layer curvature at the connection between spherical part and the facet is much higher than anywhere in ellipsoidal particles with equivalent deviation from spherical geometry[4]. That is to say, the high curvature spots are like shape corners which raise local stresses. In our parametric study in Section 4.1, we have shown the increase in layer radius effectively decreases the layer curvature, and thus acts as a stress releaser. That observation is consistent with the arguments here.

6.1.3. Transient and Accident Conditions

Generally accident means severe temperature rise in a short period of time. When this happens, the internal pressure increases, diffusion and corrosion rates of fission products shoot up, and new problems come into the picture, such as thermal decomposition of the SiC layer. In a neutral or reducing atmosphere, the SiC layer can degrade through the evaporation of silicon to a porous carbon layer. The decomposition becomes important at

---

[4] Measure of the deviations from a spherical geometry was defined in [167].

temperatures greater than 1600°C and severe in a few hours at 2000°C. Measurements of the sublimation of SiC under equilibrium conditions have shown that the most important gaseous species is silicon [168][169]. The decomposition vapor pressure of beta-SiC is [169]

$$p = 7.59 \times 10^{12} \exp(-60926/T),$$ (6.3)

where p is the decomposition pressure in Pa and T is the temperature in K. The decomposition rate of beta-SiC crystals in a static argon atmosphere was measured by Ghoshtagore at 1900 to 2100°C [170], and fitted by the equation

$$k = 2.95 \times 10^{13} \exp(-56252/T),$$ (6.4)

where k is the decomposition rate in $\mu g/m^2.s$.

Goodin and Nabielek [171] expressed thermal decomposition of the SiC layer by the thinning rate relative to the thickness of the SiC layer as

$$k = k_0 e^{-Q/(RT)}, \text{ and}$$ (6.5)

$$\log k_0 = -1.58 + 2.67 \log T + 0.61 \log \phi,$$ (6.6)

where

k_0 is the fractional SiC thermal decomposition rate (s^{-1}),

Q is the experimental activation energy for SiC decomposition (kJ/mole),

T is irradiation temperature (K),

ϕ is fast neutron fluence $(10^{21} n/cm^2, E>0.1 \text{ MeV})$, and

R is the ideal gas constant (8.31J/mol.K).

The activation energy from Gontard and Nabielek [25] is

$$Q = 556 kJ / mole.$$ (6.7)

Some other problems during accidents involve oxidation and other chemical reactions of the particles.

6.1.4. Other Considerations

We have said in Section 2.2 that the current diffusion model for fission gas release assumes constant irradiation temperature, but in many cases the particles experience non-isothermal irradiation histories, so improvements need to be made with this respect. One

possibility is to divide an entire irradiation history into small segments in each of which the irradiation temperature can be regarded as a constant.

In Section 3.2.4 we mentioned various scenarios of cracking in layered materials such as the coatings of fuel particles. Although it seems that PyC/SiC interface debonding is an important phenomenon to be modeled, there are two challenges on the way. One is that there is no data on the strength of PyC/SiC interface, and it is very hard to measure it. Another is that debonding breaks the symmetry in stress analysis and only finite element method seems to be the right choice for such stress calculation, as was used by INEEL [172], but it is time consuming and incompatible with Monte Carlo sampling of millions of particles.

6.2. Conclusions and Future Work

An integrated fuel performance model for the coated fuel particles in High Temperature Gas Cooled Reactors (HTGRs) has been developed to mainly predict the mechanical particle behavior in pebble bed core and prismatic core environments and in arbitrary irradiation test conditions and idealized conditions. The highlights of the contributions of this thesis are as follows.

(1) Linear elastic fracture mechanics is applied for the first time to model the pyrocarbon crack induced particle failure, and exercises have shown encouraging results, which promotes further development efforts in this direction. Meanwhile, mechanisms like creep crack growth and fatigue crack growth (Section 3.2.3) were proposed to be investigated to add refinement to the current fuel failure models.

(2) The mechanical formulation of the structural layers of particles was derived to include varying Poisson's ratio in irradiation creep, which has strong effect on the stresses in layers. The formulation is analytical and couples well with Monte Carlo sampling process. It was verified to be correct in Section 3.1.1. Thermal stress analysis was presented as a stand-alone solution so that it can be applied directly later in accident analysis.

(3) Unlike many fuel performance models which assume certain constant or cyclic irradiation histories for fuel particles, this model can take arbitrary irradiation history

228

based on experimental measurements, furthermore, in the case of pebble bed reactor it can generate irradiation history associated with every simulated particle based on the reactor core environment and the flow path of the particle. The thermal calculation is formed in such a way that the irradiation temperature of a particle can be calculated generically on the spot. This flexibility was not seen in previous fuel performance models.

(4) Parametric studies were conducted to bring insights into the mechanical behavior of fuel particles and how fuel performance varies with parameters. Correlations between parameters were also thoroughly probed to provide useful information for fuel design. Fuel optimization procedure is proposed and optimization fuel configuration is to be compared with other model predictions and tested by experiments.

(5) Monte Carlo sampling technique is adopted to account for the statistical nature of particle dimensions and properties and pebble cycling in pebble bed reactor core. A package of statistics, including mean and uncertainty of fuel failures, maximum and minimum stresses in layers, failure histograms, and the failure paths (refer to Section 2.5.3) of all failed particles, is provided by the corresponding computer code.

(6) Manufacturing and material properties of coated fuel particles, fuel performance, and fuel design is tried to be threaded together organically in this thesis, which serves as a collection of information for future development.

Much more work is needed to fully validate this fuel performance model and expand coverage to the modeling of important fuel particle issues. These two tracks draw out the picture of future work. On one hand, many extensions as described in Section 6.1 should be made to construct a comprehensive fuel performance model to address both mechanical and chemical behavior of fuel particles and the interaction in between. On the other hand, the current model requires constant benchmarking and comparison upon arrival of new models and results. Collaborative efforts are on the way to validate existing models and advance the understanding of coated particle fuel performance in High Temperature Gas Cooled Reactor community.

Appendix A.

Stress Analysis on the TRISO Fuel Particle

As stated before, the TRISO fuel particle consists of a fuel kernel surrounded by a low-density Pyrolytic Carbon layer (Buffer), a inner dense Pyrolytic Carbon layer (IPyC), a dense Silicon Carbide layer (SiC), and a outer dense Pyrolytic Carbon layer (OPyC), which are shown in Figure A-1. Since the buffer is a porous low strength layer, compared to dense IPyC and OPyC, it basically just transports internal pressure imposed by fission gases from the kernel onto the inner surface of IPyC. We then exclude the buffer and just consider IPyC/SiC/OPyC as the system of stress analysis.
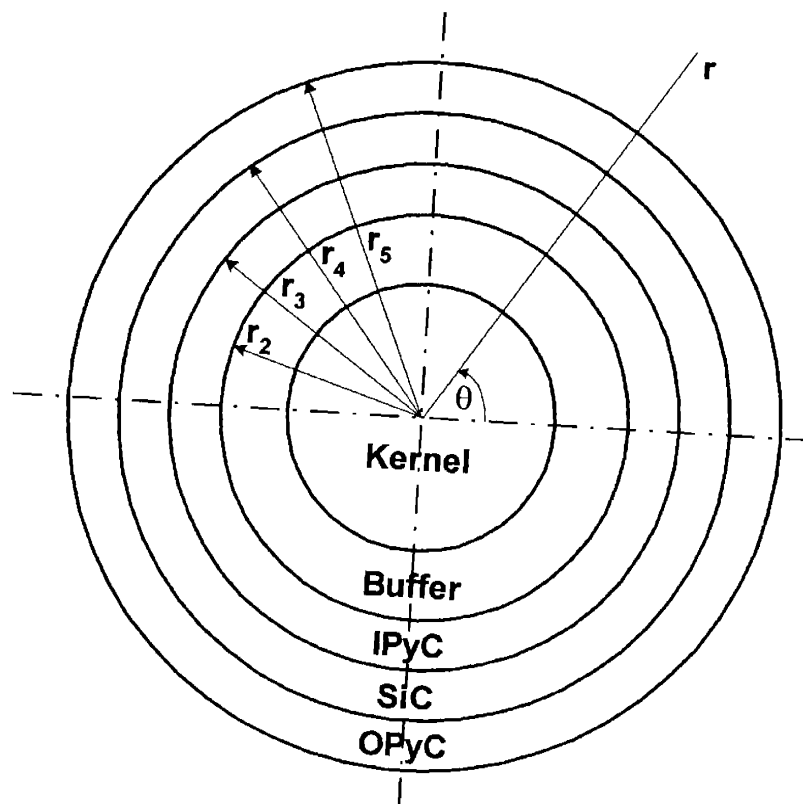
Figure A-1. Sketch of an intact TRISO fuel particle

A.1. The Analytical Solution of Mechanical Stresses, Strains, and Displacements in the TRISO Fuel Particle

To solve for stresses, strains and displacements, we need three sets of equations, which represent equations of equilibrium, strain-displacement relations, and stress-strain relations (constitutive laws). Generally the equations of equilibrium and strain-displacement relations are expressed as

$$\sum_{i=1}^{3} \frac{\partial \sigma_{ij}}{\partial x_i} = 0, \text{ and}$$

(A.1)

$$\varepsilon_{ij} = \frac{1}{2}\left(\frac{\partial u_i}{\partial x_j} + \frac{\partial u_j}{\partial x_i}\right),$$

(A.2)

respectively, where i and j denote any of the three directions of an orthogonal coordinate system, x_i is the i-direction, and σ_{ij}, ε_{ij}, and u_i are the stress, strain and displacement components, respectively [111].

In spherical coordinate system defined by (r, θ, φ), with r and θ directions indicated in Figure A-1 and φ direction being perpendicular to the r-θ plane, the general equations of equilibrium when no body force is present are

$$\frac{\partial \sigma_{rr}}{\partial r} + \frac{1}{r}\frac{\partial \sigma_{r\theta}}{\partial \theta} + \frac{1}{r\sin\theta}\frac{\partial \sigma_{r\phi}}{\partial \phi} + \frac{1}{r}\left(2\sigma_{rr} - \sigma_{\theta\theta} - \sigma_{\phi\phi}\right) = 0,$$

(A.3)

$$\frac{\partial \sigma_{r\theta}}{\partial r} + \frac{1}{r}\frac{\partial \sigma_{\theta\theta}}{\partial \theta} + \frac{1}{r\sin\theta}\frac{\partial \sigma_{\theta\phi}}{\partial \phi} + \frac{3}{r}\sigma_{r\theta} = 0,$$

(A.4)

$$\frac{\partial \sigma_{r\phi}}{\partial r} + \frac{1}{r}\frac{\partial \sigma_{\theta\phi}}{\partial \theta} + \frac{1}{r\sin\theta}\frac{\partial \sigma_{\phi\phi}}{\partial \phi} + \frac{3}{r}\sigma_{r\phi} = 0,$$

(A.5)

and the strain-displacement relations are

$$\varepsilon_{rr} = \frac{\partial u_r}{\partial r},$$

(A.6)

$$\varepsilon_{\theta\theta} = \frac{1}{r}\frac{\partial u_\theta}{\partial \theta} + \frac{u_r}{r},$$

(A.7)

$$\varepsilon_{\phi\phi} = \frac{1}{r\sin\theta}\frac{\partial u_\phi}{\partial \phi} + \frac{u_r}{r},$$

(A.8)

$$\varepsilon_{r\theta} = \frac{1}{2}\left(\frac{1}{r}\frac{\partial u_r}{\partial \theta} + \frac{\partial u_\theta}{\partial r} - \frac{u_\theta}{r}\right),$$ (A.9)

$$\varepsilon_{r\phi} = \frac{1}{2}\left(\frac{1}{r\sin\theta}\frac{\partial u_r}{\partial \phi} + \frac{\partial u_\phi}{\partial r} - \frac{u_\phi}{r}\right),$$ (A.10)

$$\varepsilon_{\theta\phi} = \frac{1}{2}\left(\frac{1}{r\sin\theta}\frac{\partial u_\theta}{\partial \phi} + \frac{1}{r}\frac{\partial u_\phi}{\partial \theta}\right).$$ (A.11)

In our case, we can assume the particle holds its spherical geometry and directions θ and ϕ are equivalent, therefore u_θ and u_ϕ are zero and from eqs. (A.6) through (A.11), it can be shown that

$$\varepsilon_{rr} = \frac{\partial u_r}{\partial r}, \; \varepsilon_{\theta\theta} = \varepsilon_{\phi\phi} = \frac{u_r}{r}, \text{ and } \varepsilon_{r\theta} = \varepsilon_{r\phi} = \varepsilon_{\theta\phi} = 0.$$ (A.12)

Since the shear strains are zero, the shear stresses are zero as well, then from eqs. (A.3) through (A.5), one gets

$$\frac{\partial \sigma_{rr}}{\partial r} + \frac{2}{r}\left(\sigma_{rr} - \sigma_{\theta\theta}\right) = 0, \; \frac{\partial \sigma_{\theta\theta}}{\partial \theta} = 0, \text{ and } \frac{\partial \sigma_{\phi\phi}}{\partial \phi} = 0.$$ (A.13)

We see that from this point forward we only need to worry about r and θ, which are radial and tangential directions of spherical coordinate system. For convenience, we denote

$$u \equiv u_r, \; \sigma_r \equiv \sigma_{rr}, \; \sigma_\theta \equiv \sigma_{\theta\theta}, \; \varepsilon_r \equiv \varepsilon_{rr}, \text{ and } \varepsilon_\theta \equiv \varepsilon_{\theta\theta} \text{ from now on.}$$ (A.14)

The stress-strain relations have different forms in pyrolytic carbon and silicon carbide, which will be discussed below.

A.1.1. Dense Pyrolytic Carbon Layers (IPyC and OPyC)

During irradiation, pyrolytic carbon or pyrocarbon experiences irradiation induced dimensional changes and irradiation induced creep besides elastic response to loadings, and we can apply a visco-elastic model for pyrocarbon to represent its time-dependent behavior, which is written as

$$\frac{\partial \varepsilon}{\partial t} = \frac{1}{E}\frac{\partial \sigma}{\partial t} + c\sigma + \dot{S},$$ (A.15)

where

232

E is the Young's Modulus (MPa),

t represents time, in our case, fast neutron fluence ($10^{21}/cm^2$),

c is the irradiation induced creep coefficient ($10^{-21}cm^2/MPa$),

$\dot{S}$ is the irradiation induced dimensional change rate ($10^{-21}cm^2$).

Express eq. (A.15) in the radial and tangential directions using spherical coordinates, then

$$\frac{\partial \varepsilon_r}{\partial t} = \frac{1}{E}\left(\frac{\partial \sigma_r}{\partial t} - 2v\frac{\partial \sigma_\theta}{\partial t}\right) + c(\sigma_r - 2v_c\sigma_\theta) + \dot{S}_r, \qquad (A.16)$$

$$\frac{\partial \varepsilon_\theta}{\partial t} = \frac{1}{E}\left[(1-v)\frac{\partial \sigma_\theta}{\partial t} - v\frac{\partial \sigma_r}{\partial t}\right] + c[(1-v_c)\sigma_\theta - v_c\sigma_r] + \dot{S}_\theta, \qquad (A.17)$$

where v is the Poisson's ratio, and v_c is the Poisson's ratio in irradiation creep.

With eqs. (A.12), (A.13), (A.16) and (A.17) we can derive solutions for stresses, strains and the radial displacement. Notice from these equations that θ does not appear, which means u, σ_r, σ_θ, ε_r, and ε_θ are independent of θ.

To solve these equations, the following general series solutions are assumed, as proposed by G. Miller, et. al [112],

$$u(r,t) = \sum_{i=0}^{\infty} u_i(r)t^i, \qquad (A.18)$$

$$\sigma_r(r,t) = \sum_{i=0}^{\infty} \sigma_{ri}(r)t^i, \qquad (A.19)$$

$$\sigma_\theta(r,t) = \sum_{i=0}^{\infty} \sigma_{\theta i}(r)t^i, \qquad (A.20)$$

$$\varepsilon_r(r,t) = \sum_{i=0}^{\infty} \varepsilon_{ri}(r)t^i, \qquad (A.21)$$

$$\varepsilon_\theta(r,t) = \sum_{i=0}^{\infty} \varepsilon_{\theta i}(r)t^i, \qquad (A.22)$$

$$\dot{S}_r = \sum_{i=0}^{\infty} \dot{S}_{ri}t^i, \text{ and} \qquad (A.23)$$

$$\dot{S}_\theta = \sum_{i=0}^{\infty} \dot{S}_{\theta i}t^i. \qquad (A.24)$$

Then we have

$$\frac{\partial \varepsilon_r}{\partial t} = \frac{\partial}{\partial t}\left(\frac{\partial u}{\partial r}\right) = \sum_{i=1}^{\infty}\frac{du_i(r)}{dr}it^{i-1},$$

$$(A.25)$$

$$\frac{\partial \varepsilon_\theta}{\partial t} = \frac{\partial}{\partial t}\left(\frac{u}{r}\right) = \sum_{i=1}^{\infty}\frac{u_i(r)}{r}it^{i-1},$$

$$(A.26)$$

$$\frac{\partial \sigma_r}{\partial t} = \sum_{i=1}^{\infty}\sigma_{ri}(r)it^{i-1}, \text{ and}$$

$$(A.27)$$

$$\frac{\partial \sigma_\theta}{\partial t} = \sum_{i=1}^{\infty}\sigma_{\theta i}(r)it^{i-1}.$$

$$(A.28)$$

Substituting eqs. (A.23) through (A.28) into (A.16) and (A.17), we get

$$\sum_{i=1}^{\infty}\frac{du_i(r)}{dr}it^{i-1} = \sum_{i=1}^{\infty}\frac{i}{E}\sigma_{ri}t^{i-1} - \sum_{i=1}^{\infty}\frac{2vi}{E}\sigma_{\theta i}t^{i-1} + \sum_{i=0}^{\infty}c\sigma_{ri}t^i - \sum_{i=0}^{\infty}2cv_c\sigma_{\theta i}t^i + \sum_{i=0}^{\infty}\dot{S}_{ri}t^i, \quad (A.29)$$

$$\sum_{i=1}^{\infty}\frac{u_i(r)}{r}it^{i-1} = \sum_{i=1}^{\infty}\frac{(1-v)i}{E}\sigma_{\theta i}t^{i-1} - \sum_{i=1}^{\infty}\frac{vi}{E}\sigma_{ri}t^{i-1} + \sum_{i=0}^{\infty}c(1-v_c)\sigma_{\theta i}t^i - \sum_{i=0}^{\infty}cv_c\sigma_{ri}t^i + \sum_{i=0}^{\infty}\dot{S}_{\theta i}t^i.$$

$$(A.30)$$

Equate quantities on the two sides of the eqs. (A.29) and (A.30) having like powers of t, for the t^0 term, we obtain

$$\frac{du_1}{dr} = \frac{\sigma_{r1}}{E} - \frac{2v}{E}\sigma_{\theta 1} + c\sigma_{r0} - 2cv_c\sigma_{\theta 0} + \dot{S}_{r0}, \text{ and}$$

$$(A.31)$$

$$\frac{u_1}{r} = \frac{1-v}{E}\sigma_{\theta 1} - \frac{v}{E}\sigma_{r1} + c(1-v_c)\sigma_{\theta 0} - cv_c\sigma_{r0} + \dot{S}_{\theta 0}.$$

$$(A.32)$$

Similarly for the t^i term, we have

$$(i+1)\frac{du_{i+1}}{dr} = \frac{(i+1)}{E}\sigma_{ri+1} - \frac{2v(i+1)}{E}\sigma_{\theta i+1} + c\sigma_{ri} - 2cv_c\sigma_{\theta i} + \dot{S}_{ri}, \text{ and}$$

$$(A.33)$$

$$(i+1)\frac{u_{i+1}}{r} = -\frac{v(i+1)}{E}\sigma_{ri+1} + \frac{(1-v)(i+1)}{E}\sigma_{\theta i+1} - cv_c\sigma_{ri} + c(1-v_c)\sigma_{\theta i} + \dot{S}_{\theta i}.$$

$$(A.34)$$

Firstly we solve the zeroth order equations. (A.31) × (1-v) + (A.32) × 2v gives

$$(1-v)\frac{du_1}{dr} + 2v\frac{u_1}{r} =$$

$$\frac{1-v-2v^2}{E}\sigma_{r1} + [c(1-v) - 2cvv_c]\sigma_{r0} + 2c(v-v_c)\sigma_{\theta 0} + (1-v)\dot{S}_{r0} + 2v\dot{S}_{\theta 0}$$

$$(A.35)$$

Differentiate eq. (A.35) with respect to "r",

234

$$(1-v)\frac{d^2u_1}{dr^2} + 2v\frac{d}{dr}\left(\frac{u_1}{r}\right) =$$
$$\frac{(1+v)(1-2v)}{E}\frac{d\sigma_{r1}}{dr} + [c(1-v)-2cvv_c]\frac{d\sigma_{r0}}{dr} + 2c(v-v_c)\frac{d\sigma_{\theta0}}{dr} \qquad (A.36)$$

Applying eq. (A.13) to eq. (A.36), we get

$$(1-v)\frac{d^2u_1}{dr^2} + 2v\frac{d}{dr}\left(\frac{u_1}{r}\right) =$$
$$-\frac{2}{r}\frac{(1+v)(1-2v)}{E}(\sigma_{r1}-\sigma_{\theta1}) + [c(1-v)-2cvv_c]\frac{d\sigma_{r0}}{dr} + 2c(v-v_c)\frac{d\sigma_{\theta0}}{dr} \qquad (A.37)$$

On the other hand, (A.31) - (A.32) gives

$$\frac{du_1}{dr} - \frac{u_1}{r} = \frac{(1+v)}{E}(\sigma_{r1}-\sigma_{\theta1}) + c(1+v_c)(\sigma_{r0}-\sigma_{\theta0}) + \dot{S}_{r0} - \dot{S}_{\theta0}. \qquad (A.38)$$

Substituting $(\sigma_{r1}-\sigma_{\theta1})$ in eq. (A.38) into eq. (A.37), we get

$$\frac{d^2u_1}{dr^2} + \frac{2}{r}\frac{du_1}{dr} - \frac{2}{r^2}u_1 = \frac{2(v-v_c)c}{1-v}\left(\frac{1}{2}\frac{d\sigma_{r0}}{dr} + \frac{d\sigma_{\theta0}}{dr}\right) + \frac{2(1-2v)}{(1-v)r}\left(\dot{S}_{r0} - \dot{S}_{\theta0}\right). \qquad (A.39)$$

Let

$$l = \frac{1}{E}, \quad h = \frac{2v}{E}, \quad m = \frac{v}{E}, \quad k = \frac{1-v}{E}, \qquad (A.40)$$

then

$$\frac{d^2u_1}{dr^2} + \frac{2}{r}\frac{du_1}{dr} - \frac{2}{r^2}u_1 = \frac{2(m-lv_c)c}{k(0+1)}\left(\frac{1}{2}\frac{d\sigma_{r0}}{dr} + \frac{d\sigma_{\theta0}}{dr}\right) + \frac{2(k-m)}{k(0+1)r}\left(\dot{S}_{r0} - \dot{S}_{\theta0}\right). \qquad (A.41)$$

It can be proved that $\left(\frac{1}{2}\frac{d\sigma_{r0}}{dr} + \frac{d\sigma_{\theta0}}{dr}\right) = 0$. Define

$$f_1 \equiv \frac{1}{k(0+1)}(\dot{S}_{r0} - \dot{S}_{\theta0}), \qquad (A.42)$$

then we get

$$r^2\frac{d^2u_1}{dr^2} + 2r\frac{du_1}{dr} - 2u_1 = 2(k-m)f_1r, \qquad (A.43)$$

which is a Euler's equation. Its standard solution is

$$u_1(r) = A_1r + B_1r^{-2} + \frac{2(k-m)}{3}f_1r\ln r, \qquad (A.44)$$

where A_1 and B_1 are constants to be determined by boundary conditions.

235

Substituting eq. (A.44) into eqs. (A.35) and (A.38), we can obtain

$$\sigma_{r1}(r) = \frac{A_1}{k-m} - \frac{2B_1}{l+m}r^{-3} + 2f_1\frac{\left[(l+m)\ln r + k\right]}{3(l+m)}$$

$$-\frac{c}{l+m}\left\{\left[1 + \frac{m(1-2\nu_c)}{k-m}\right]\sigma_{r0} + \left[\frac{1-2\nu_c}{1-2\nu} - 1\right]\sigma_{\theta0}\right\} - \frac{k\dot{S}_{r0} + h\dot{S}_{\theta0}}{(0+1)(kl-hm)}$$, and   (A.45)

$$\sigma_{\theta1} - \sigma_{r1} = \frac{3B_1}{l+m}r^{-3} - \frac{2f_1(k-m)}{3(l+m)} + \frac{3c}{2(l+m)}\left[\frac{2(1+\nu_c)}{3}(\sigma_{r0} - \sigma_{\theta0})\right] + \frac{\dot{S}_{r0} - \dot{S}_{\theta0}}{(0+1)(l+m)}.$$

(A.46)

Following the same procedure, we can work on eqs. (A.33) and (A.34) and get

$$\frac{d^2u_{i+1}}{dr^2} + \frac{2}{r}\frac{du_{i+1}}{dr} - \frac{2}{r^2}u_{i+1} = \frac{2(m-l\nu_c)c}{k(i+1)}\left(\frac{1}{2}\frac{d\sigma_{ri}}{dr} + \frac{d\sigma_{\theta i}}{dr}\right) + \frac{2(k-m)}{kr(i+1)}\left(\dot{S}_{ri} - \dot{S}_{\theta i}\right).$$ (A.47)

When i = 1, based on eqs. (A.45) and (A.46), it can be shown that

$$\frac{1}{2}\frac{d\sigma_{r1}}{dr} + \frac{d\sigma_{\theta1}}{dr} = \frac{f_1}{r} - \frac{c(1-2\nu_c)}{(k-m)}\left(\frac{1}{2}\frac{d\sigma_{r0}}{dr} + \frac{d\sigma_{\theta0}}{dr}\right).$$

(A.48)

Let $g_0 \equiv \frac{1}{2}\frac{d\sigma_{r0}}{dr} + \frac{d\sigma_{\theta0}}{dr} = 0$, $g_1 \equiv f_1 - \frac{c(1-2\nu_c)}{1\cdot(k-m)}g_0$, and

$$f_2 \equiv -\frac{c}{2k}\frac{2(l\nu_c - m)}{k-m}\frac{f_1}{1+1} + \frac{\dot{S}_{r1} - \dot{S}_{\theta1}}{k(1+1)} = -\frac{c}{2k}\frac{2(l\nu_c - m)}{k-m}\frac{g_1}{1+1} + \frac{\dot{S}_{r1} - \dot{S}_{\theta1}}{k(1+1)}$$, then from eq.

(A.47) we can obtain

$$r^2\frac{d^2u_2}{dr^2} + 2r\frac{du_2}{dr} - 2u_2 = 2(k-m)f_2r.$$ (A.49)

Comparing eq. (A.49) with eq. (A.43), we are able to follow the derivation with i = 0 and obtain

$$u_2(r) = A_2r + B_2r^{-2} + \frac{2(k-m)}{3}f_2r\ln r,$$ (A.50)

$$\sigma_{r2}(r) = \frac{A_2}{k-m} - \frac{2B_2}{l+m}r^{-3} + 2f_2\frac{\left[(l+m)\ln r + k\right]}{3(l+m)}$$

$$-\frac{c}{l+m}\left\{\left[1 + \frac{m(1-2\nu_c)}{k-m}\right]\sigma_{r1} + \left[\frac{1-2\nu_c}{1-2\nu} - 1\right]\sigma_{\theta1}\right\} - \frac{k\dot{S}_{r1} + h\dot{S}_{\theta1}}{(1+1)(kl-hm)}$$, and   (A.51)

$$\sigma_{\theta2}(r) - \sigma_{r2}(r) = \frac{3B_2}{l+m}r^{-3} - \frac{2f_2(k-m)}{3(l+m)} + \frac{3c}{2(l+m)}\left[\frac{2(1+\nu_c)}{3}(\sigma_{r1} - \sigma_{\theta1})\right] + \frac{\dot{S}_{r1} - \dot{S}_{\theta1}}{(1+1)(l+m)}.$$

236

If we proceed by increasing i, and define

$$g_{i+1} \equiv f_{i+1} - \frac{c(1-2v_c)}{(i+1)(k-m)} g_i, \quad (i \geq 0), \text{ and } g_0 = 0, \text{ and}$$

(A.53)

$$f_{i+1} \equiv -\frac{c}{2k} \frac{2(lv_c - m)}{k-m} \frac{g_i}{i+1} + \frac{\dot{S}_{ri} - \dot{S}_{\theta i}}{k(i+1)}, \quad (i \geq 0),$$

(A.54)

we will find the recursive relation

$$\frac{1}{2} \frac{d\sigma_{ri+1}}{dr} + \frac{d\sigma_{\theta i+1}}{dr} = \frac{f_{i+1}}{r} - \frac{c(1-2v_c)}{(i+1)(k-m)} \left(\frac{1}{2} \frac{d\sigma_{ri}}{dr} + \frac{d\sigma_{\theta i}}{dr} \right), \text{ and}$$

(A.55)

$$r^2 \frac{d^2 u_{i+1}}{dr^2} + 2r \frac{du_{i+1}}{dr} - 2u_{i+1} = 2(k-m)f_{i+1}r.$$

(A.56)

From the Euler's equation (A.56), $u_{i+1}(r)$ can be solved, and we plug it into eqs. (A.33) and (A.34), then $\sigma_{ri+1}(r)$ and $\sigma_{\theta i+1}(r)$ can be solved. $\varepsilon_{ri+1}(r)$ and $\varepsilon_{\theta i+1}(r)$ are given by eq. (A.12).

In sum, for any $(i \geq 0)$, we have

$$u_{i+1}(r) = A_{i+1}r + B_{i+1}r^{-2} + \frac{2(k-m)}{3} f_{i+1}r\ln r,$$

(A.57)

$$\sigma_{ri+1}(r) = \frac{A_{i+1}}{k-m} - \frac{2B_{i+1}}{l+m}r^{-3} + 2f_{i+1}\frac{[(l+m)\ln r + k]}{3(l+m)}$$

$$-\frac{c}{l+m}\frac{1}{(i+1)}\left\{ \left[1 + \frac{m(1-2v_c)}{k-m}\right]\sigma_{ri} + \left[\frac{l(1-2v_c)}{k-m} - 1\right]\sigma_{\theta i} \right\} - \frac{k\dot{S}_{ri} + h\dot{S}_{\theta i}}{(i+1)(kl-hm)},$$

(A.58)

$$\sigma_{\theta i+1} - \sigma_{ri+1} =$$

$$\frac{3B_{i+1}}{l+m}r^{-3} - \frac{2f_{i+1}(k-m)}{3(l+m)} + \frac{3c}{2(l+m)}\frac{1}{(i+1)}\left[\frac{2(1+v_c)}{3}(\sigma_{ri} - \sigma_{\theta i})\right] + \frac{\dot{S}_{ri} - \dot{S}_{\theta i}}{(i+1)(l+m)},$$

(A.59)

$$\varepsilon_{ri+1}(r) = A_{i+1} - 2B_{i+1}r^{-3} + \frac{2(k-m)}{3}f_{i+1}(\ln r + 1), \text{ and}$$

(A.60)

$$\varepsilon_{\theta i+1}(r) = A_{i+1} + B_{i+1}r^{-3} + \frac{2(k-m)}{3}f_{i+1}\ln r,$$

(A.61)

where A_{i+1} and B_{i+1} are unknowns to be determined by boundary conditions, and f_{i+1} is given by the recursive relation in eq. (A.54).

Note that $u_0(r)$, $\sigma_{r0}(r)$, $\sigma_{\theta 0}(r)$, $\varepsilon_{r0}(r)$, and $\varepsilon_{\theta 0}(r)$ are not given by the above solutions. In fact, they represent initial mechanical conditions or residual deformations in particle layers that are introduced by thermal expansion and loading during fuel handling process.

A.1.2. Isotropic Silicon Carbide Layer (SiC)

The silicon carbide layer is generally treated as an elastic medium without irradiation induced dimensional changes and creep. SiC is much more resistant to irradiation damage than PyC, hence such as assumption is reasonable. The constitutive laws in SiC are

$$\frac{\partial \varepsilon_r}{\partial t} = \frac{1}{E}\left(\frac{\partial \sigma_r}{\partial t} - 2v\frac{\partial \sigma_\theta}{\partial t}\right), \text{ and} \tag{A.62}$$

$$\frac{\partial \varepsilon_\theta}{\partial t} = \frac{1}{E}\left[(1-v)\frac{\partial \sigma_\theta}{\partial t} - v\frac{\partial \sigma_r}{\partial t}\right]. \tag{A.63}$$

Compared with eqs. (A.16) and (A.17), eqs. (A.62) and (A.63) don't have irradiation related terms, therefore we can easily get the solutions in SiC by dropping out irradiation related terms in eqs. (A.57) through (A.61), and they are

$$u_{i+1}(r) = A_{i+1}r + B_{i+1}r^{-2}, \tag{A.64}$$

$$\sigma_{ri+1}(r) = \frac{A_{i+1}}{k-m} - \frac{2B_{i+1}}{1+m}r^{-3}, \tag{A.65}$$

$$\sigma_{\theta i+1} - \sigma_{ri+1} = \frac{3B_{i+1}}{1+m}r^{-3}, \tag{A.66}$$

$$\varepsilon_{ri+1}(r) = A_{i+1} - 2B_{i+1}r^{-3}, \text{ and} \tag{A.67}$$

$$\varepsilon_{\theta i+1}(r) = A_{i+1} + B_{i+1}r^{-3}. \tag{A.68}$$

A.1.3. Closed Form Solution at v_c of 0.5

When the Poisson's ratio in creep v_c equals to 0.5, the solution in eqs. (A.57), (A.58), and (A.59) reduces to the solution presented by Miller, et al. [112]. In that case, if we set the radial stress components in eq. (A.58) to p_i and q_i at the radii r_2 and r_3, respectively,

for the IPyC layer, then starting with i=0 term and progressing to higher order terms we can get an expression for B_{i+1} as

$$B_{i+1} = \left[p_{i+1} - q_{i+1} - \frac{c}{(l+m)(i+1)} \left[-\frac{3}{2}(p_i - q_i) + f_i \ln \frac{r_2}{r_3} \right] - \frac{2}{3} f_{i+1} \ln \frac{r_2}{r_3} \right] \frac{(l+m)}{2(r_3^{-3} - r_2^{-3})}.$$

(A.69)

Then plugging it into eqs. (A.58), and (A.59) we can get A_{i+1} as

$$A_{i+1} = \frac{k-m}{r_3^{-3} - r_2^{-3}} \left[p_{i+1} r_3^{-3} - q_{i+1} r_2^{-3} + \frac{2}{3} f_{i+1} \left(r_2^{-3} \ln r_3 - r_3^{-3} \ln r_2 \right) \right] + \frac{S_{r,i} + 2S_{t,i}}{3(i+1)}.$$

(A.70)

Substituting eqs. (A.69) and (A.70) back into eqs. (A.58), and (A.59) with v_c of 0.5, we get

$$\sigma_{ri+1}(r) = \frac{r_3^{-3} - r^{-3}}{r_3^{-3} - r_2^{-3}} p_{i+1} + \frac{r^{-3} - r_2^{-3}}{r_3^{-3} - r_2^{-3}} q_{i+1} + \frac{2}{3} \left[\frac{r_2^{-3} - r^{-3}}{r_3^{-3} - r_2^{-3}} \ln r_3 + \frac{r^{-3} - r_3^{-3}}{r_3^{-3} - r_2^{-3}} \ln r_2 + \ln r \right] f_{i+1}, \text{ and}$$

(A.71)

$$\sigma_{ti+1}(r) = \frac{r^{-3} + 2r_3^{-3}}{2(r_3^{-3} - r_2^{-3})} p_{i+1} - \frac{r^{-3} + 2r_2^{-3}}{2(r_3^{-3} - r_2^{-3})} q_{i+1} +$$
$$\left[\frac{r^{-3} + 2r_2^{-3}}{3(r_3^{-3} - r_2^{-3})} \ln r_3 - \frac{r^{-3} + 2r_3^{-3}}{3(r_3^{-3} - r_2^{-3})} \ln r_2 + \frac{2}{3} \ln r + \frac{1}{3} \right] f_{i+1}$$

(A.72)

Since

$$\sum \sigma_{ri} (r)^i = \sigma_r(r,t), \quad \sum \sigma_{ti} (r)^i = \sigma_t(r,t),$$

(A.73)

$$\sum p_i t^i = -P_I(t), \quad \sum q_i t^i = \sigma_{rI}(t) \text{ for IPyC, and}$$

(A.74)

$$\sum f_i t^i = F_I(t) \text{ for IPyC,}$$

(A.75)

are all closed form functions, the following closed form solutions for radial and tangential stresses in IPyC layer can be obtained.

$$\sigma_r(r,t) = \frac{r_3^{-3} - r^{-3}}{r_3^{-3} - r_2^{-3}} (-P_I) + \frac{r^{-3} - r_2^{-3}}{r_3^{-3} - r_2^{-3}} \sigma_{rl} + \frac{2}{3} \left[\frac{r_2^{-3} - r^{-3}}{r_3^{-3} - r_2^{-3}} \ln r_3 + \frac{r^{-3} - r_3^{-3}}{r_3^{-3} - r_2^{-3}} \ln r_2 + \ln r \right] F_I$$

(A.76)

$$\sigma_t(r,t) = \frac{r^{-3} + 2r_3^{-3}}{2(r_3^{-3} - r_2^{-3})} (-P_I) - \frac{r^{-3} + 2r_2^{-3}}{2(r_3^{-3} - r_2^{-3})} \sigma_{rl} +$$
$$\left[\frac{r^{-3} + 2r_2^{-3}}{3(r_3^{-3} - r_2^{-3})} \ln r_3 - \frac{r^{-3} + 2r_3^{-3}}{3(r_3^{-3} - r_2^{-3})} \ln r_2 + \frac{2}{3} \ln r + \frac{1}{3} \right] F_I$$

(A.77)

where σ_{rI} is the radial stress at IPyC/SiC interface, and its closed form solution is given in reference [112]. P_I is the internal gas pressure acting on the inner surface of IPyC layer. The reason of the minus sign in front of P_I in eqs. (A.76) and (A.77) is that the radial stress there equals to negative P_I.

In the same way, for OPyC we get

$$\sigma_r(r,t) = \frac{r_4^{-3} - r^{-3}}{r_4^{-3} - r_5^{-3}}(-P_O) + \frac{r^{-3} - r_5^{-3}}{r_4^{-3} - r_5^{-3}}\sigma_{rO} + \frac{2}{3}\left[\frac{r_5^{-3} - r^{-3}}{r_4^{-3} - r_5^{-3}}\ln r_4 + \frac{r^{-3} - r_4^{-3}}{r_4^{-3} - r_5^{-3}}\ln r_5 + \ln r\right]F_O$$

(A.78)

$$\sigma_t(r,t) = \frac{r^{-3} + 2r_4^{-3}}{2(r_4^{-3} - r_5^{-3})}(-P_O) - \frac{r^{-3} + 2r_5^{-3}}{2(r_4^{-3} - r_5^{-3})}\sigma_{rO} + $$
$$\left[\frac{r^{-3} + 2r_5^{-3}}{3(r_4^{-3} - r_5^{-3})}\ln r_4 - \frac{r^{-3} + 2r_4^{-3}}{3(r_4^{-3} - r_5^{-3})}\ln r_5 + \frac{2}{3}\ln r + \frac{1}{3}\right]F_O$$

(A.79)

where σ_{rO} is the radial stress at SiC/OPyC interface, and its closed form solution is given in reference [112].

For SiC, F is zero due to no irradiation effect, then we have

$$\sigma_r(r,t) = \frac{r_4^{-3} - r^{-3}}{r_4^{-3} - r_3^{-3}}\sigma_{rI} + \frac{r^{-3} - r_3^{-3}}{r_4^{-3} - r_3^{-3}}\sigma_{rO},$$

(A.80)

$$\sigma_t(r,t) = \frac{r^{-3} + 2r_4^{-3}}{2(r_4^{-3} - r_3^{-3})}\sigma_{rI} - \frac{r^{-3} + 2r_3^{-3}}{2(r_4^{-3} - r_3^{-3})}\sigma_{rO}.$$

(A.81)

A.2. The Analytical Solution for Thermal Stresses, Strains, and Displacements in the TRISO Fuel Particle

The reason we separate the formulation of thermal stresses calculation is that we are able to obtain analytical solutions for anisotropic pyrocarbon, which is not true in the general mechanical analysis presented above because recursive relations shown in eqs. (A.53) to (A.56) were not obtained. Moreover, in reactor accident analysis, thermal stresses due to accidental temperature rise need to be calculated, so we present a stand alone thermal stress analysis which can be easily adopted there. The solution of thermal stresses, strains, and displacements can be superimposed on the general mechanical solutions because of the linear behavior of pyrocarbon and silicon carbide. In the case of

pyrocarbon, since creep is time dependent, that superposition needs to be performed at every time step progressively.

A.2.1. Dense Anisotropic Pyrolytic Carbon Layers (IPyC and OPyC)

We can write down the following equations for anisotropic pyrocarbon layers in the spherical coordinate system (independent of ϕ due to symmetry),

$$\varepsilon_r = \frac{1}{E_r}\sigma_r - \frac{2v_{\theta r}}{E_\theta}\sigma_\theta + \alpha_r \Delta T , \tag{A.82}$$

$$\varepsilon_\theta = \frac{1-v_{\theta\theta}}{E_\theta}\sigma_\theta - \frac{v_{r\theta}}{E_r}\sigma_r + \alpha_\theta \Delta T , \tag{A.83}$$

and equations of equilibrium and strain-displacement relations in eqs. (A.12), (A.13), where α_r and α_θ (or α_t) are the thermal expansion coefficients in the radial and tangential directions of spherical system like the coated fuel particle, and ΔT is a temperature change.

By solving the above equations and use $v_{r\theta}E_\theta = v_{\theta r}E_r$, we obtain

$$r^2\frac{d^2 u_r}{dr^2} + 2r\frac{du_r}{dr} - 2\frac{v_{\theta r}(1-v_{r\theta})}{v_{r\theta}(1-v_{\theta\theta})}u_r = 2\left[\left(\frac{1-v_{\theta\theta}-v_{\theta r}}{1-v_{\theta\theta}}\right)\alpha_r - \frac{v_{\theta r}(1-2v_{r\theta})}{v_{r\theta}(1-v_{\theta\theta})}\alpha_\theta\right]\Delta T \cdot r , \tag{A.84}$$

which is a standard Euler's equation. Let $z = \ln r$, eq. (A.84) turns into

$$\frac{d^2 u_r}{dz^2} + \frac{du_r}{dz} - 2\frac{v_{\theta r}(1-v_{r\theta})}{v_{r\theta}(1-v_{\theta\theta})}u_r = 2\left[\left(\frac{1-v_{\theta\theta}-v_{\theta r}}{1-v_{\theta\theta}}\right)\alpha_r - \frac{v_{\theta r}(1-2v_{r\theta})}{v_{r\theta}(1-v_{\theta\theta})}\alpha_\theta\right]\Delta T \cdot e^z , \tag{A.85}$$

which has the following solution,

$$u_r = Le^z + Ce^{z\left(\frac{-1+\sqrt{1+8\lambda}}{2}\right)} + De^{z\left(\frac{-1-\sqrt{1+8\lambda}}{2}\right)} , (\lambda \neq 1), \text{ or} \tag{A.86}$$

$$u_r = Lr + Cr^{\left(\frac{-1+\sqrt{1+8\lambda}}{2}\right)} + Dr^{\left(\frac{-1-\sqrt{1+8\lambda}}{2}\right)} , \tag{A.87}$$

where

$$\lambda = \frac{v_{\theta r}(1-v_{r\theta})}{v_{r\theta}(1-v_{\theta\theta})} , (\lambda \neq 1), \tag{A.88}$$

$$L = \frac{v_{r\theta}(1 - v_{\theta\theta} - v_{\theta r})\alpha_r - v_{\theta r}(1 - 2v_{r\theta})\alpha_\theta}{v_{r\theta}(1 - v_{\theta\theta}) - v_{\theta r}(1 - v_{r\theta})} \Delta T \text{, and}$$ (A.89)

C and D are constants determined by boundary conditions. Substituting eq. (A.87) back into eqs. (A.12), (A.13), (A.82) and (A.83) we get

$$\sigma_r = H + \frac{(1 - v_{\theta\theta})\frac{-1 + \sqrt{1 + 8\lambda}}{2} + 2v_{\theta r}}{1 - v_{\theta\theta} - 2v_{\theta r}v_{r\theta}} E_r C r^{\frac{-3 + \sqrt{1 + 8\lambda}}{2}}$$

$$+ \frac{(1 - v_{\theta\theta})\frac{-1 - \sqrt{1 + 8\lambda}}{2} + 2v_{\theta r}}{1 - v_{\theta\theta} - 2v_{\theta r}v_{r\theta}} E_r D r^{\frac{-3 - \sqrt{1 + 8\lambda}}{2}}$$ (A.90)

$$\sigma_\theta = H + \frac{1 + \sqrt{1 + 8\lambda}}{4} \frac{(1 - v_{\theta\theta})\frac{-1 + \sqrt{1 + 8\lambda}}{2} + 2v_{\theta r}}{1 - v_{\theta\theta} - 2v_{\theta r}v_{r\theta}} E_r C r^{\frac{-3 + \sqrt{1 + 8\lambda}}{2}}$$

$$+ \frac{1 - \sqrt{1 + 8\lambda}}{4} \frac{(1 - v_{\theta\theta})\frac{-1 - \sqrt{1 + 8\lambda}}{2} + 2v_{\theta r}}{1 - v_{\theta\theta} - 2v_{\theta r}v_{r\theta}} E_r D r^{\frac{-3 - \sqrt{1 + 8\lambda}}{2}}$$ (A.91)

$$\varepsilon_r = L + \frac{-1 + \sqrt{1 + 8\lambda}}{2} C r^{\left(\frac{-3 + \sqrt{1 + 8\lambda}}{2}\right)} + \frac{-1 - \sqrt{1 + 8\lambda}}{2} D r^{\left(\frac{-3 - \sqrt{1 + 8\lambda}}{2}\right)} \text{, and}$$ (A.92)

$$\varepsilon_\theta = L + C r^{\left(\frac{-3 + \sqrt{1 + 8\lambda}}{2}\right)} + D r^{\left(\frac{-3 - \sqrt{1 + 8\lambda}}{2}\right)},$$ (A.93)

where

$$H = \frac{v_{\theta r} E_r}{v_{r\theta}(1 - v_{\theta\theta}) - v_{\theta r}(1 - v_{r\theta})}(\alpha_r - \alpha_\theta)\Delta T.$$ (A.94)

A.2.2. Isotropic Silicon Carbide Layer (SiC)

For isotropic SiC layer, because

$$E_r = E_\theta, \ v_{\theta r} = v_{r\theta} = v_{\theta\theta}, \text{ and } \alpha_r = \alpha_\theta,.$$ (A.95)

eq. (A.84) becomes

$$r^2 \frac{d^2 u_r}{dr^2} + 2r \frac{du_r}{dr} - 2u_r = 0 \text{, and then we have}$$ (A.96)

$$u_r = C r + D r^{-2},$$ (A.97)

$$\sigma_r = \frac{E}{1-2v}(C - \alpha\Delta T) - \frac{2E}{1+v}Dr^{-3},$$

(A.98)

$$\sigma_\theta = \frac{E}{1-2v}(C - \alpha\Delta T) + \frac{E}{1+v}Dr^{-3},$$

(A.99)

$$\varepsilon_r = C - 2Dr^{-3},$$

(A.100)

$$\varepsilon_\theta = C + Dr^{-3},$$

(A.101)

A.3. Applying Boundary Conditions to Various Scenarios

A.3.1. Intact Fuel Particle

The fission gases generated from the fuel kernel exerts an internal pressure P_I on the inner surface of IPyC layer, and the graphite matrix in a pebble applies an external pressure P_O on the outer surface of OPyC layer. Also, the radial stress σ_r and displacement u are continuous across interfaces. Based on these boundary conditions, we have

$$\sigma_{rIPyC}(r_2) = P_I, \qquad \sigma_{rOPyC}(r_5) = P_O,$$

$$\sigma_{rIPyC}(r_3) = \sigma_{rSiC}(r_3), \qquad \sigma_{rSiC}(r_4) = \sigma_{rOPyC}(r_4), \qquad (A.102)$$

$$u_{IPyC}(r_3) = u_{SiC}(r_3), \qquad u_{SiC}(r_4) = u_{OPyC}(r_4),$$

where r_2 to r_5 are shown in Figure A-1.

A.3.2. IPyC Failed Particle

If the IPyC layer fails in a particle, it transmits the internal pressure onto the inner surface of SiC layer, i.e. the IPyC/SiC interface. Therefore we can use the following boundary conditions to calculate stresses, strains and displacements in SiC and OPyC layers.

$$\sigma_{rSiC}(r_3) = P_I, \qquad \sigma_{rOPyC}(r_5) = P_O,$$

$$\sigma_{rSiC}(r_4) = \sigma_{rOPyC}(r_4), \qquad u_{SiC}(r_4) = u_{OPyC}(r_4). \qquad (A.103)$$

Although the IPyC layer is cracked, it is still tightly bonded with SiC at the interface, and hence stresses are not fully relaxed. The post-crack stress solutions in failed layers are given in Appendix B.

A.3.3. OPyC Failed Particle

Similar to the IPyC failed particle, the boundary conditions in this case are

$$\sigma_{rIPyC}(r_2) = P_I, \qquad\qquad \sigma_{rSiC}(r_4) = P_O,$$

$$\sigma_{rIPyC}(r_3) = \sigma_{rSiC}(r_3), \qquad\qquad u_{IPyC}(r_3) = u_{SiC}(r_3). \qquad\qquad (A.104)$$

A.3.4. SiC Failed Particle

Due to irradiation induced dimensional change in pyrolytic carbon layers, SiC layer is generally put into compression by IPyC and OPyC layers. Even there is a through-thickness crack formed in SiC layer, it behaves the same as an intact layer under compression. When there is a SiC crack and the SiC layer is in tension, we assume the adjacent PyC layers are also cracked in either of the following two situations. Firstly, SiC is stronger than PyC, so if SiC layer is failed by over-pressurization, the PyC layers also fail that way. Secondly, if the crack in SiC layer is introduced by manufacturing or handling, tensile loading creates a stress concentration that can easily cause the crack to propagate into PyC layers.

A.3.5. IPyC and SiC Failed Particle

Based on the arguments in A.3.4, if the SiC layer is under compression, the case is the same as A.3.2. Otherwise, OPyC layer also fails.

A.3.6. OPyC and SiC Failed Particle

Similar to A.3.5, if the SiC layer is under compression, the case is the same as A.3.3. Otherwise, IPyC layer also fails.

A.3.7. IPyC and OPyC Failure Particle

This case is a simple elastic problem, and the boundary conditions are

$$\sigma_{rSiC}(r_3) = P_I, \qquad \sigma_{rSiC}(r_4) = P_O. \qquad (A.105)$$

Appendix B.

Improved Cracked Induced Fuel Failure Model

This part of the work shows how we calculate the resultant stresses, strains, and displacements when a crack is formed in the IPyC or OPyC layer, as shown in Figure B-1, and evaluate the stress intensity factor in the SiC layer induced by the crack. The assumptions are: (1) the crack is opened in the radial direction due to high tensile stress in the tangential direction, and catastrophically propagate in a circumferential direction to form an axisymmetric crack ring. This assumption is backed by some evidences in micrographs of irradiated fuel particles. (2) In this formulation, the cracked PyC layer is still tightly bonded to the SiC layer at their interface. No debonding is allowed.
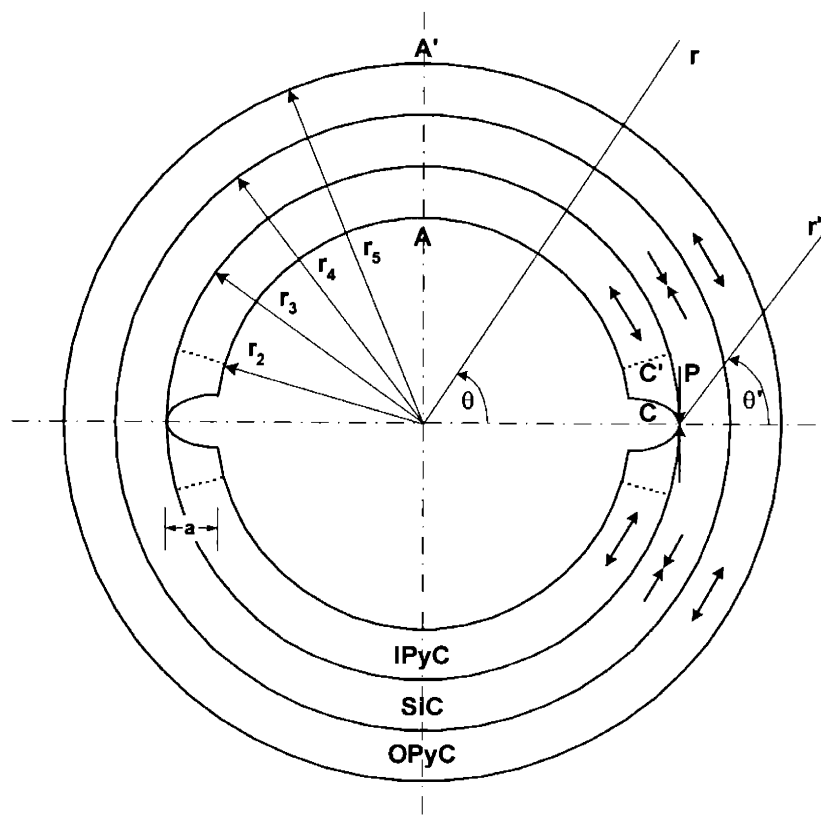
Figure B-1. The schematic of an IPyC cracked TRISO particle

B.1. Crack Opening Displacement

Firstly we deal with a crack in the IPyC layer. Based on fracture mechanics, it is well known that the displacement field around a crack tip is proportional to the square root of the distance to the crack tip. Although in this kind of bi-material system where elastic mismatch exists between PyC and SiC, the displacement field is modified, it doesn't deviate much from the square root dependence. Using polar coordinates (r', θ') snapped onto the crack tip, as shown in Figure B-1, we can write [97]

$$u_{r'}\left(r',\theta'\right) = \frac{K_I}{G}\sqrt{\frac{r'}{2\pi}}\cos\frac{\theta'}{2}\left(\beta - \cos^2\frac{\theta'}{2}\right),$$ (B.1)

$$u_{\theta'}\left(r',\theta'\right) = -\frac{K_I}{G}\sqrt{\frac{r'}{2\pi}}\sin\frac{\theta'}{2}\left(\beta - \cos^2\frac{\theta'}{2}\right),$$ (B.2)

$$G = \frac{E}{2(1+v)},$$ (B.3)

$$\beta = \begin{cases} 2(1-v) & \text{plane strain} \\ 2\dfrac{1}{1+v} & \text{plane stress} \end{cases},$$ (B.4)

where K_I is the Mode 1 stress intensity factor, E is the Young's modulus, v is the Poisson's ratio, and G is the shear modulus.

In this case where an axisymmetric crack exists, we can use the plane strain value of β [113]. Along the crack surface, θ' = π, then according to eqs. (B.1) and (B.2), the displacements describe the crack configuration C are

$$u_{r'}^C\left(r',\pi\right) = 0, \quad (0 \le r' \le a)$$ (B.5)

$$u_{\theta'}^C\left(r',\pi\right) = -\frac{2(1-v)K_I}{G}\sqrt{\frac{r'}{2\pi}}, \quad (0 \le r' \le a)$$ (B.6)

or if we use coordinates (r, θ) as shown in Figure B-1,

$$u_r^C\left(r,0\right) = 0, \quad (r_2 \le r \le r_3)$$ (B.7)

$$u_\theta^C\left(r,0\right) = \frac{2(1-v)K_I}{G}\sqrt{\frac{r_3 - r}{2\pi}}, \quad (r_2 \le r \le r_3).$$ (B.8)

At θ = π/2, $u_\theta^C\left(r,\pi/2\right) = 0$ due to symmetry, so we assume

$$u_\theta^{C}(r,\theta) = u_\theta^{C}(r,0)\frac{\pi/2-\theta}{\pi/2}, \text{ then} \tag{B.9}$$

$$u_\theta^{C}(r,\theta) = \frac{2(1-v)K_I}{G\cdot\pi/2}\sqrt{\frac{r_3-r}{2\pi}}\left(\frac{\pi}{2}-\theta\right). \tag{B.10}$$

B.2. After-Crack Stresses and Strains

Our purpose is to estimate the stresses after PyC cracks, including the interfacial shear stress/shear force P as shown in Figure B-1. To do this, first suppose there is no resistance to free sliding of cracked PyC layer along the SiC layer, and the cracked PyC layer fully relaxes and reaches configuration C' in Figure B-1. Then SiC layer applies shear force P to the cracked PyC layer to close the crack tip, and the configuration should coincide with C.

B.2.1. Configuration C'

The cracked PyC layer, which is still subject to internal pressure p_i, undergoes elastic stress relaxation to C', so

$$\varepsilon_{rr}^{C'}(r) = \frac{-(\sigma_{rr}(r)+p_i)}{E} - \frac{-v\sigma_{\theta\theta}(r)}{E}, \text{ and} \tag{B.11}$$

$$\varepsilon_{\theta\theta}^{C'}(r) = \frac{-\sigma_{\theta\theta}(r)}{E} - \frac{-v(\sigma_{rr}(r)+p_i)}{E}, \tag{B.12}$$

where $\sigma_{rr}(r)$ and $\sigma_{\theta\theta}(r)$ are stresses right before cracking, which are known.

According to strain-displacement relations,

$$\varepsilon_{rr}^{C'}(r) = \frac{\partial u_r^{C'}(r)}{\partial r}, \tag{B.13}$$

$$\varepsilon_{\theta\theta}^{C'}(r) = \frac{1}{r}\frac{\partial u_\theta^{C'}(r,\theta)}{\partial\theta} + \frac{u_r^{C'}(r)}{r}, \tag{B.14}$$

and assuming

$$u_r^{C'}(r_3) = 0, \text{ and} \tag{B.15}$$

$$u_\theta^{C'}\left(r,\frac{\pi}{2}\right) = 0, \text{ (symmetry)} \tag{B.16}$$

248

we have

$$u_r^{C'}(r_3) - u_r^{C'}(r) = \int_r^{r_3} \varepsilon_{rr}^{C'}(r)dr \text{ , so}$$ (B.17)

$$u_r^{C'}(r) = -\int_r^{r_3} \varepsilon_{rr}^{C'}(r)dr \text{ , and}$$ (B.18)

$$\varepsilon_{\theta\theta}^{C'}(r) = \frac{1}{r}\frac{u_\theta^{C'}\left(r,\frac{\pi}{2}\right) - u_\theta^{C'}(r,0)}{\pi/2} + \frac{u_r^{C'}(r)}{r} \text{ , so}$$ (B.19)

$$u_\theta^{C'}(r,0) = \frac{\pi}{2}u_r^{C'}(r) - \frac{\pi}{2}\varepsilon_{\theta\theta}^{C'}(r)\cdot r \text{ .}$$ (B.20)

Assume

$$u_\theta^{C'}(r,\theta) = u_\theta^{C'}(r,0)\frac{\pi/2-\theta}{\pi/2} \text{ , then}$$ (B.21)

$$u_\theta^{C'}(r,\theta) = \left[u_r^{C'}(r) - \varepsilon_{\theta\theta}^{C'}(r)\cdot r\right]\left(\frac{\pi}{2}-\theta\right) .$$ (B.22)

B.2.2. Configuration C' → C due to interfacial stress

Suppose P is the shear force at the crack front per unit length around the circumference, as shown in Figure B-1. P is in the tangential direction of coating layers and induces the displacement $u_\theta^P(r,\theta) = u_\theta^C(r,\theta) - u_\theta^{C'}(r,\theta)$, and according to eqs. (B.10) and (B.22),

$$u_\theta^P(r,\theta) = \left[\frac{2(1-v)K_I}{G\cdot\pi/2}\sqrt{\frac{r_3-r}{2\pi}} + \varepsilon_{\theta\theta}^{C'}(r)\cdot r - u_r^{C'}(r)\right]\left(\frac{\pi}{2}-\theta\right).$$ (B.23)

In spherical coordinates, the strain-displacement relations are

$$\varepsilon_{rr} = \frac{\partial u_r}{\partial r},$$ (B.24)

$$\varepsilon_{\theta\theta} = \frac{1}{r}\frac{\partial u_\theta}{\partial\theta} + \frac{u_r}{r} \text{ , and}$$ (B.25)

$$\varepsilon_{r\theta} = \frac{1}{2}\left(\frac{1}{r}\frac{\partial u_r}{\partial\theta} + \frac{\partial u_\theta}{\partial r} - \frac{u_\theta}{r}\right),$$ (B.26)

and given

$$\sigma_{rr}^P = 0,$$ (B.27)

249

the constitutive laws are

$$\varepsilon_{rr}^{P} = -\frac{\nu}{E}\sigma_{\theta\theta}^{P},$$

(B.28)

$$\varepsilon_{\theta\theta}^{P} = \frac{1}{E}\sigma_{\theta\theta}^{P}, \text{ and}$$

(B.29)

$$\varepsilon_{r\theta}^{P} = \frac{1}{2G}\sigma_{r\theta}^{P}.$$

(B.30)

Now we want to solve for ε_{rr}^{P}, $\varepsilon_{\theta\theta}^{P}$, and $\varepsilon_{r\theta}^{P}$. From eqs. (B.28) and (B.29),

$$\varepsilon_{rr}^{P} = -\nu\varepsilon_{\theta\theta}^{P}.$$

(B.31)

From eqs. (B.23) and (B.25),

$$\varepsilon_{\theta\theta}^{P}(r,\theta) = \frac{1}{r}u_r^{C'}(r) - \varepsilon_{\theta\theta}^{C'}(r) - \frac{2(1-\nu)K_I}{G\cdot\pi/2}\sqrt{\frac{r_3 - r}{2\pi r^2}} + \frac{1}{r}u_r^{P}(r,\theta), \text{ and}$$

(B.32)

from eqs. (B.24) and (B.32),

$$u_r^{P}(r,\theta) = -\int_r^{r_3}\varepsilon_{rr}^{P}(r,\theta)dr = \nu\int_r^{r_3}\varepsilon_{\theta\theta}^{P}(r,\theta)dr, \text{ so}$$

(B.33)

$$\varepsilon_{\theta\theta}^{P}(r,\theta) - \frac{\nu}{r}\int_r^{r_3}\varepsilon_{\theta\theta}^{P}(r,\theta)dr = \frac{1}{r}u_r^{C'}(r) - \varepsilon_{\theta\theta}^{C'}(r) - \frac{2(1-\nu)K_I}{G\cdot\pi/2}\sqrt{\frac{r_3 - r}{2\pi r^2}}.$$

(B.34)

From eq. (B.34) we see that $\varepsilon_{\theta\theta}^{P}$ is independent of θ, which is the result of the assumptions in eqs. (B.9) and (B.21), so

$$\varepsilon_{\theta\theta}^{P}(r,\theta) = \varepsilon_{\theta\theta}^{P}(r).$$

(B.35)

However, we cannot use eq. (B.26) to calculate $\varepsilon_{r\theta}^{P}$ because $\varepsilon_{r\theta}^{P}$ has a point singularity at the crack tip and the assumptions in eqs. (B.9)and (B.21) extend the point singularity to a surface singularity, which makes shear strain energy non-conservative. Therefore, we use the generic shear stress solution at a crack tip [97] to estimate the contribution of shear strain energy due to interfacial shear force P. The shear stress at the crack tip based on (r',θ') coordinates is

$$\sigma_{r'\theta'}^{P}(r',\theta') = \frac{K_I}{\sqrt{2\pi r'}}\sin\frac{\theta'}{2}\cos^2\frac{\theta'}{2}.$$

(B.36)

The shear strain energy density in the cracked IPyC layer is

$$w_{shear}^{P} = \frac{1}{2}\sigma_{r'\theta'}^{P}(r',\theta')\varepsilon_{r'\theta'}^{P}(r',\theta') = \frac{1}{4G}\sigma_{r'\theta'}^{P}(r',\theta')^2.$$

(B.37)

250

If we integrate it in the volume enclosed by $0 \leq r' \leq a$, $\pi/2 \leq \theta' \leq \pi$, and $0 \leq \phi \leq 2\pi$, the total shear strain energy is given by

$$W_{shear}^{P} = \int_{0}^{a} \int_{\pi/2}^{\pi} \int_{0}^{2\pi} w_{shear}^{P} dr' \cdot r' \, d\theta' \cdot (r_3 + r' \cos\theta') d\phi'$$

$$= \frac{K_I^2}{4G} \int_{0}^{a} \int_{\pi/2}^{\pi} (r_3 + r' \cos\theta') \sin^2 \frac{\theta'}{2} \cos^4 \frac{\theta'}{2} dr' \cdot d\theta'$$

$$= \frac{K_I^2}{4G} \left[r_3 a \int_{\pi/2}^{\pi} \sin^2 \frac{\theta'}{2} \cos^4 \frac{\theta'}{2} d\theta' + \frac{a^2}{2} \int_{\pi/2}^{\pi} \sin^2 \frac{\theta'}{2} \cos^4 \frac{\theta'}{2} \cos\theta' d\theta' \right]$$

$$= \frac{K_I^2}{4G} \left[\frac{r_3 a}{4} \int_{\pi/2}^{\pi} \sin^2 \theta' \frac{1+\cos\theta'}{2} d\theta' + \frac{a^2}{8} \int_{\pi/2}^{\pi} \sin^2 \theta' \frac{1+\cos\theta'}{2} \cos\theta' d\theta' \right]$$

$$= \frac{K_I^2}{4G} \left[\frac{r_3 a}{8} \int_{\pi/2}^{\pi} (\sin^2 \theta' + \sin^2 \theta' \cos\theta') d\theta' + \frac{a^2}{16} \int_{\pi/2}^{\pi} (\sin^2 \theta' \cos\theta' + \sin^2 \theta' \cos^2 \theta') d\theta' \right]$$

$$= \frac{K_I^2}{4G} \left[\frac{r_3 a}{8} \left(\frac{\pi}{4} - \frac{1}{3} \right) + \frac{a^2}{16} \left(\frac{\pi}{16} - \frac{1}{3} \right) \right]$$

$$= \frac{a K_I^2}{32G} \left[r_3 \left(\frac{\pi}{4} - \frac{1}{3} \right) + \frac{a}{2} \left(\frac{\pi}{16} - \frac{1}{3} \right) \right] \tag{B.38}$$

Because $\sigma_{rr}^{P} = 0$, as in eq. (B.27), the elastic strain energy due to P is

$$w^{P} = \frac{1}{2} \sigma_{\theta\theta}^{P} \varepsilon_{\theta\theta}^{P} + w_{shear}^{P} = \frac{E}{2} \varepsilon_{\theta\theta}^{P} (r)^2 + w_{shear}^{P}, \tag{B.39}$$

and the total elastic strain energy in the upper half shell of IPyC layer ($r_2 \leq r \leq r_3$) is induced by the work done by P, so we have

$$P \cdot 2\pi r_3 \cdot u_{\theta}^{C'}(r_3, 0) = \int_{r_2}^{r_3} \int_{0}^{\pi/2} \int_{0}^{2\pi} \frac{E}{2} \varepsilon_{\theta\theta}^{P}(r)^2 r^2 \sin\theta \, dr \, d\theta \, d\phi + W_{shear}^{P}. \tag{B.40}$$

Based on eqs. (B.15), (B.20), and (B.40),

$$P \cdot 2\pi r_3 \cdot \left[-\frac{\pi}{2} \varepsilon_{\theta\theta}^{C'}(r_3) r_3 \right] = 2\pi \int_{r_2}^{r_3} \int_{0}^{\pi/2} \frac{E}{2} \varepsilon_{\theta\theta}^{P}(r)^2 r^2 \sin\theta \, dr \, d\theta + W_{shear}^{P}$$

$$-\frac{\pi}{2} r_3^2 \varepsilon_{\theta\theta}^{C'}(r_3) P = \int_{r_2}^{r_3} \frac{E}{2} \varepsilon_{\theta\theta}^{P}(r)^2 r^2 dr + \frac{W_{shear}^{P}}{2\pi}. \tag{B.41}$$

$$P = \frac{1}{-\frac{\pi}{2} r_3^2 \varepsilon_{\theta\theta}^{C'}(r_3)} \left[\int_{r_2}^{r_3} \frac{E}{2} \varepsilon_{\theta\theta}^{P}(r)^2 r^2 dr + \frac{W_{shear}^{P}}{2\pi} \right]$$

For the crack configuration in Figure B-1, the stress intensity factor K_I is [97]

251

$$K_I = 0.413 \frac{1 + r_2/r_3}{\sqrt{1 - a/(r_3 - r_2)}} \overline{\sigma}^P_{\theta\theta}(r)\sqrt{\pi a} \ .$$

(B.42)

We choose

$$a = 0.99(r_3 - r_2),$$

(B.43)

because when the crack length reaches this level, the strain energy release rate plummet towards zero [95], which means the crack doesn't have the energy to grow any more, then

$$K_I = 4.13(1 + r_2/r_3)\overline{\sigma}^P_{\theta\theta}(r)\sqrt{\pi a} \ .$$

(B.44)

From eqs. (B.34) and (B.44) we see that $\varepsilon^P_{\theta\theta}$ and K_I are mutually dependent, so we need to iterate on eq. (B.34) to find the equilibrium between the two.

B.2.3. A Crack in OPyC Layer

If there is a radial crack in OPyC layer, the treatment is the same as for IPyC layer. The different equations are listed below followed by the corresponding equation number for IPyC.

$u^C_r(r,0) = 0$, ($r_4 \le r \le r_5$), eq. (B.5),   (B.45)

$$u^C_\theta(r,\theta) = \frac{2(1-\nu)K_I}{G \cdot \pi/2} \sqrt{\frac{r-r_4}{2\pi}} \left(\frac{\pi}{2} - \theta\right), \text{ eq. (B.10)},$$

(B.46)

$$\varepsilon^{C}_{rr}(r) = \frac{-(\sigma_{rr}(r) + p_O)}{E} - \frac{-\nu\sigma_{\theta\theta}(r)}{E}, \text{ eq. (B.11)},$$

(B.47)

$$\varepsilon^{C}_{\theta\theta}(r) = \frac{-\sigma_{\theta\theta}(r)}{E} - \frac{-\nu(\sigma_{rr}(r) + p_O)}{E}, \text{ eq. (B.12)},$$

(B.48)

$u^{C}_r(r_4) = 0$, eq. (B.15),   (B.49)

$$u^{C}_r(r) = \int_{r_4} \varepsilon^{C}_{rr}(r)dr \text{ , eq. (B.18)},$$

(B.50)

$$u^P_\theta(r,\theta) = \left[\frac{2(1-\nu)K_I}{G \cdot \pi/2} \sqrt{\frac{r-r_4}{2\pi}} + \varepsilon^{C}_{\theta\theta}(r) \cdot r - u^{C}_r(r)\right]\left(\frac{\pi}{2} - \theta\right), \text{ eq. (B.23)},$$

(B.51)

$$\varepsilon^P_{\theta\theta}(r,\theta) + \frac{\nu}{r} \int_{r_4} \varepsilon^P_{\theta\theta}(r,\theta)dr = \frac{1}{r}u^{C}_r(r) - \varepsilon^{C}_{\theta\theta}(r) - \frac{2(1-\nu)K_I}{G \cdot \pi/2} \sqrt{\frac{r-r_4}{2\pi r^2}} \text{ , eq. (B.34)},$$

(B.52)

252

$$W_{shear}^{P} = \frac{aK_I^2}{32G}\left[r_4\left(\frac{\pi}{4}-\frac{1}{3}\right)-\frac{a}{2}\left(\frac{\pi}{16}-\frac{1}{3}\right)\right], \text{ eq. (B.38)}, \qquad (B.53)$$

$$P = \frac{1}{-\frac{\pi}{2}r_4^2\varepsilon_{\theta\theta}^{C}(r_4)}\left[\int_{r_4}^{r_5}\frac{E}{2}\varepsilon_{\theta\theta}^{P}(r)^2 r^2 dr + \frac{W_{shear}^{P}}{2\pi}\right], \text{ eq. (B.41)}, \qquad (B.54)$$

$$K_I = 4.13\left(1 + r_5/r_4\right)\overline{\sigma}_{\theta\theta}^{P}(r)\sqrt{\pi a}, \text{ eq. (B.44)}. \qquad (B.55)$$

B.2.4. Post-Crack Stress Development due to Further Irradiation

After a cracked is formed in IPyC layer, it is still subject to deformation caused by irradiation-induced dimensional change and irradiation-induced creep. We can treat this issue as if the fully relaxed configuration C' is a function of irradiation after cracking. Specifically, suppose $t - \Delta t$ is any time after cracking in the IPyC layer, then

$$\varepsilon_{rr}^{C}(r,t) = \varepsilon_{rr}^{C}(r,t-\Delta t) + \dot{S}_r(t-\Delta t)\Delta t, \qquad (B.56)$$

$$\begin{aligned}\varepsilon_{\theta\theta}^{C}(r,t) &= \varepsilon_{\theta\theta}^{C}(r,t-\Delta t) + c\sigma_{\theta\theta}^{P}(r,t-\Delta t)\Delta t + \dot{S}_t(t-\Delta t)\Delta t \\ &= \varepsilon_{\theta\theta}^{C}(r,t-\Delta t) + cE\varepsilon_{\theta\theta}^{P}(r,t-\Delta t)\Delta t + \dot{S}_t(t-\Delta t)\Delta t\end{aligned}, \text{ and} \qquad (B.57)$$

$$u_r^{C}(r,t) = -\int_{r_4}^{r_3}\varepsilon_{rr}^{C}(r,t)dr. \qquad (B.58)$$

where c is the irradiation-induced creep coefficient ($cm^2/10^{21}$neutron/MPa), and $\dot{S}_r$ and $\dot{S}_t$ are the irradiation-induced dimensional change rate ($cm^2/10^{21}$neutron) in the radial and tangential directions, respectively. The reason there is no creep term in eq. (B.56) is that cracked IPyC layer transmits internal pressure to SiC layer, and only experiences very little radial stress, therefore the radial creep strain contribution in eq. (B.56) is omitted.

With eqs. (B.56) through (B.58) and (B.34), we then have

$$\varepsilon_{\theta\theta}^{P}(r,t) - \frac{v}{r}\int_{r_4}^{r_3}\varepsilon_{\theta\theta}^{P}(r,t)dr = \frac{1}{r}u_r^{C}(r,t) - \varepsilon_{\theta\theta}^{C}(r,t) - \frac{2(1-v)K_I(t)}{G\cdot\pi/2}\sqrt{\frac{r_3-r}{2\pi r^2}}, \qquad (B.59)$$

where K_1 is given by eq. (B.44).

Appendix C.

Fuel Performance Modeling Code – TIMCOAT

C.1. General Description

The computer code TIMCOAT is the FORTRAN implementation of the fuel performance model in this thesis, and it stands for The Integrated Model of COATed Fuel. Besides, TIM is the name of the Beaver - the mascot of MIT. The logical structure of the code can be represented by the flow chart in Figure 2-1. The code assumes typical TRISO fuel particle configuration, i.e. a fuel kernel with a buffer layer and three structural layers (IPyC, SiC, and OPyC), prepares particle material properties and environmental variables, calculates the stresses in the structural layers of the particles, and evaluate fuel failures at every time step during irradiation of fuel particles. The code can sample millions of fuel particles and generate statistics of them in the output files. It can also simulate particles in pebble bed reactor cores, in irradiation tests, and in idealized irradiation conditions.

C.2. Module Description

To facilitate future modification and extension of the code, efforts were made toward the modulation of the code. Major components are placed in separate files for information hiding purpose, and functional blocks are organized into subroutines and functions. In the following, implementation details on modules are provided with the intention to cover most contents of the code. It should be mentioned that by 'module' we mean logical components, not the FORTRAN structure 'MODULE'.

C.2.1. Mechanical Analysis

The formulation of stress analysis has been presented in Appendix A, and the coding of solutions is in the subroutine M_ANALYSIS, with the signature of

M_ANALYSIS(MCODE,PRESS,PAMB,FLU,SIGR,SIGT,EPIR,EPIT,UR), (C.1)

where

MCODE is the analysis type discussed in Section 2.5.3, which can take the values of 'ISO3', 'IS2', 'SO2', and 'S1',

PRESS is the internal pressure exerted on the inner surface of the IPyC layer,

PAMB is the ambient pressure exerted on the outer surface of the OPyC layer,

FLU is the fast neutron fluence,

SIGR, SIGT, EPIR, EPIT, and UR are the radial stresses, tangential stresses, radial strains, tangential strains, and radial displacements, respectively. These are arrays of size NDIV, which is the number of points on the radii of three structural layers at which the variables are calculated. For example, if NDIV = 30, ten points in each layer will divide it into nine equally thick segments.

As stated in Section A.3, the unknowns in eqs. (A.57) through (A.61) are solved by applying appropriate boundary conditions. The solutions to the unknowns are presented below.

(1) MCODE = 'ISO3'

This is the case when all three structural layers are intact, and the corresponding boundary conditions are in Section A.3.1. We denote the unknowns of order 'i' in IPyC as Ai and Bi, in SiC as Di and Fi, and in OPyC as Mi and Ni.

To facilitate programming in Fortran, we define the following variables. Let

$$L1 = l, \quad L2 = h, \quad L3 = m, \quad L4 = k,$$ (C.2)

$$G1 = \frac{1}{k-m} = \frac{1}{L4-L3}, \quad G2 = \frac{1}{l+m} = \frac{1}{L1+L3}, \quad G3 = \frac{k}{l+m} = \frac{L4}{L1+L3}, \text{ and}$$ (C.3)

$$V1 = 1 - 2v_c, \quad V2 = \frac{2(1+v_c)}{3}, \quad V3 = 2(L1v_c - L3)G1, \text{ where}$$ (C.4)

l, h, m, and k are defined in eq. (A.40). These variables can be applied to both IPyC and OPyC layers, so 'I' or 'O' is attached to all the symbols when either IPyC or OPyC is specified

We also define

255

$$G1S = \frac{E_{SiC}}{1 - 2\nu_{SiC}}, \quad G2S = \frac{2E_{SiC}}{1 + \nu_{SiC}}, \text{ for SiC layer.} \tag{C.5}$$

Applying the boundary conditions in Section A.3.1, we get

$$\sigma_{rIPyCi}(r_2) = P_{Ii} = G1I \cdot A_i - 2G2I \cdot B_i r_2^{-3} + \frac{2f_{Ii}}{3}(\ln r_2 + G3I)$$

$$- \frac{cIG2I}{i}\left\{[1 + L3I \cdot G1I \cdot V1I]\sigma_{rIPyCi-1}(r_2) + [L1I \cdot G1I \cdot V1I - 1]\sigma_{\theta IPyCi-1}(r_2)\right\}, \tag{C.6}$$

$$- \frac{L4I \cdot S_{rIi-1} + L2I \cdot S_{\theta Ii-1}}{i(L1I \cdot L4I - L2I \cdot L3I)}$$

with $P_{Ii} = 0$ unless i=0,

$$\sigma_{rOPyCi}(r_5) = P_{Oi} = G1O \cdot M_i - 2G2O \cdot N_i r_5^{-3} + \frac{2f_{Oi}}{3}(\ln r_5 + G3O)$$

$$- \frac{cOG2O}{i}\left\{[1 + L3O \cdot G1O \cdot V1O]\sigma_{rOPyCi-1}(r_5) + [L1O \cdot G1O \cdot V1O - 1]\sigma_{\theta OPyCi-1}(r_5)\right\}, \tag{C.7}$$

$$- \frac{L4O \cdot S_{rOi-1} + L2O \cdot S_{\theta Oi-1}}{i(L1O \cdot L4O - L2O \cdot L3O)}$$

with $P_{Oi} = 0$ unless i=0,

$$G1I \cdot A_i - 2G2I \cdot B_i r_3^{-3} + \frac{2f_{Ii}}{3}(\ln r_3 + G3I)$$

$$- \frac{cIG2I}{i}\left\{[1 + L3I \cdot G1I \cdot V1I]\sigma_{rIPyCi-1}(r_3) + [L1I \cdot G1I \cdot V1I - 1]\sigma_{\theta IPyCi-1}(r_3)\right\}, \tag{C.8}$$

$$- \frac{L4I \cdot S_{rIi-1} + L2I \cdot S_{\theta Ii-1}}{i(L1I \cdot L4I - L2I \cdot L3I)} = G1S \cdot D_i - G2S \cdot F_i r_3^{-3}$$

$$G1O \cdot M_i - 2G2O \cdot N_i r_4^{-3} + \frac{2f_{Oi}}{3}(\ln r_4 + G3O)$$

$$- \frac{cOG2O}{i}\left\{[1 + L3O \cdot G1O \cdot V1O]\sigma_{rOPyCi-1}(r_4) + [L1O \cdot G1O \cdot V1O - 1]\sigma_{\theta OPyCi-1}(r_4)\right\}, \tag{C.9}$$

$$- \frac{L4O \cdot S_{rOi-1} + L2O \cdot S_{\theta Oi-1}}{i(L1O \cdot L4O - L2O \cdot L3O)} = G1S \cdot D_i - G2S \cdot F_i r_4^{-3}$$

$$A_i r_3 + B_i r_3^{-2} + \frac{2}{3G1I} f_{Ii} r_3 \ln r_3 = D_i r_3 + F_i r_3^{-2}, \text{ and} \tag{C.10}$$

$$M_i r_4 + N_i r_4^{-2} + \frac{2}{3G1O} f_{Oi} r_4 \ln r_4 = D_i r_4 + F_i r_4^{-2}. \tag{C.11}$$

Rearranging eqs. (C.6) through (C.11), we have

$$PX_i = Q_i,$$ (C.12)

where

$$X_i^T = \begin{bmatrix} A_i & B_i & D_i & F_i & M_i & N_i \end{bmatrix}, \text{ and}$$ (C.13)

$$P = \begin{bmatrix}
1 & -\dfrac{2G2I}{G1I}r_2^{-3} & 0 & 0 & 0 & 0 \\[2ex]
1 & -\dfrac{2G2I}{G1I}r_3^{-3} & -\dfrac{G1S}{G1I} & \dfrac{G2S}{G1I}r_3^{-3} & 0 & 0 \\[2ex]
1 & r_3^{-3} & -1 & -r_3^{-3} & 0 & 0 \\[2ex]
0 & 0 & -1 & -r_4^{-3} & 1 & r_4^{-3} \\[2ex]
0 & 0 & -\dfrac{G1S}{G1O} & \dfrac{G2S}{G1O}r_4^{-3} & 1 & -\dfrac{2G2O}{G1O}r_4^{-3} \\[2ex]
0 & 0 & 0 & 0 & 1 & -\dfrac{2G2O}{G1O}r_5^{-3}
\end{bmatrix}$$

(C.14)

For i = 0 (initial stresses),

$$Q_0^T = \begin{bmatrix} \dfrac{P_I}{G1I} & 0 & 0 & 0 & 0 & \dfrac{P_O}{G1O} \end{bmatrix}, \text{ and for higher orders,}$$ (C.15)

$$Q_{i+1} = \begin{bmatrix}
-\dfrac{2f_{Ii+1}}{3G1I}(\ln r_2 + G3I) + cI\dfrac{G2I}{G1I}\sigma_{i2} + \dfrac{SIi}{G1I} \\[2ex]
-\dfrac{2f_{Ii+1}}{3G1I}(\ln r_3 + G3I) + cI\dfrac{G2I}{G1I}\sigma_{i3} + \dfrac{SIi}{G1I} \\[2ex]
-\dfrac{2f_{Ii+1}}{3G1I}\ln r_3 \\[2ex]
-\dfrac{2f_{Oi+1}}{3G1O}\ln r_4 \\[2ex]
-\dfrac{2f_{Oi+1}}{3G1O}(\ln r_4 + G3O) + cO\dfrac{G2O}{G1O}\sigma_{i4} + \dfrac{SOi}{G1O} \\[2ex]
-\dfrac{2f_{Oi+1}}{3G1O}(\ln r_5 + G3O) + cO\dfrac{G2O}{G1O}\sigma_{i5} + \dfrac{SOi}{G1O}
\end{bmatrix},$$ (C.16)

where

$$\sigma_{i2} = \dfrac{[1 + L3I \cdot G1I \cdot V1I]\sigma_{rIPyCi}(r_2) + [L1I \cdot G1I \cdot V1I - 1]\sigma_{\theta IPyCi}(r_2)}{i+1},$$ (C.17)

$$\sigma_{i3} = \dfrac{[1 + L3I \cdot G1I \cdot V1I]\sigma_{rIPyCi}(r_3) + [L1I \cdot G1I \cdot V1I - 1]\sigma_{\theta IPyCi}(r_3)}{i+1},$$ (C.18)

$$\sigma_{i4} = \dfrac{[1 + L3O \cdot G1O \cdot V1O]\sigma_{rIPyCi}(r_4) + [L1O \cdot G1O \cdot V1O - 1]\sigma_{\theta IPyCi}(r_4)}{i+1},$$ (C.19)

257

$$\sigma_{i5} = \frac{[1 + L3O \cdot G1O \cdot V1O]\sigma_{rIPyCi}(r_5) + [L1O \cdot G1O \cdot V1O - 1]\sigma_{\theta IPyCi}(r_5)}{i + 1},$$ (C.20)

$$\sigma_{i5} = \frac{[1 + L3O \cdot G1O \cdot V1O]\sigma_{rIPyCi}(r_5) + [L1O \cdot G1O \cdot V1O - 1]\sigma_{\theta IPyCi}(r_5)}{i + 1},$$ (C.21)

$$SIi = \frac{L4I \cdot S_{rIi} + L2I \cdot S_{\theta Ii}}{(i + 1)(L1I \cdot L4I - L2I \cdot L3I)}, \text{ and}$$ (C.22)

$$SOi = \frac{L4O \cdot S_{rOi} + L2O \cdot S_{\theta Oi}}{(i + 1)(L1O \cdot L4O - L2O \cdot L3O)}.$$ (C.23)

Eq. (C.12) can be solved by calling the subroutine DLSARG in IMSL library of FORTRAN. The summations in eqs. (A.18) and (A.22) are evaluated by adding terms of increasing orders until they satisfy a preset convergence criterion. For example, if the criterion is 10^{-4} and order i term contributes to less than 10^{-4} of the summation, then the summation will be truncated there.

(2) MCODE = 'IS2'

This is the IPyC/SiC two layer problem, and following the same procedure as in (1) and using boundary conditions in Section A.3.3, we get

$$PX_i = Q_i,$$ (C.24)

where

$$X_i^T = [A_i \quad B_i \quad D_i \quad F_i], \text{ and}$$ (C.25)

$$P = \begin{bmatrix} 1 & -\dfrac{2G2I}{G1I}r_2^{-3} & 0 & 0 \\ 1 & -\dfrac{2G2I}{G1I}r_3^{-3} & -\dfrac{G1S}{G1I} & \dfrac{G2S}{G1I}r_3^{-3} \\ 1 & r_3^{-3} & -1 & -r_3^{-3} \\ 0 & 0 & 1 & -\dfrac{G2S}{G1S}r_4^{-3} \end{bmatrix}.$$ (C.26)

For i = 0 (initial stresses),

$$Q_0^T = \begin{bmatrix} \dfrac{P_I}{G1I} & 0 & 0 & \dfrac{P_O}{G1S} \end{bmatrix}, \text{ and for higher orders,}$$ (C.27)

$$Q_{i+1} = \begin{bmatrix} -\dfrac{2f_{Ii+1}}{3G1I}(\ln r_2 + G3I) + cI\dfrac{G2I}{G1I}\sigma_{i2} + \dfrac{SIi}{G1I} \\ -\dfrac{2f_{Ii+1}}{3G1I}(\ln r_3 + G3I) + cI\dfrac{G2I}{G1I}\sigma_{i3} + \dfrac{SIi}{G1I} \\ -\dfrac{2f_{Ii+1}}{3G1I}\ln r_3 \\ 0 \end{bmatrix}.$$ (C.28)

The above gives the mechanical solutions in IPyC and SiC layers. In the cracked OPyC layer, we use the derivation in Section B.2 to estimate the stresses, strains, displacements, and stress intensity factors there.

(3) MCODE = 'SO2'

This is the SiC/OPyC two layer problem, and similar to (2) and using boundary conditions in Section A.3.2, we get

$$PX_i = Q_i,$$ (C.29)

where

$$X_i^T = \begin{bmatrix} D_i & F_i & M_i & N_i \end{bmatrix}, \text{ and}$$ (C.30)

$$P = \begin{bmatrix} 1 & -\dfrac{G2S}{G1S}r_3^{-3} & 0 & 0 \\ -\dfrac{G1S}{G1O} & \dfrac{G2S}{G1O}r_4^{-3} & 1 & -\dfrac{2G2O}{G1O}r_4^{-3} \\ -1 & -r_4^{-3} & 1 & r_4^{-3} \\ 0 & 0 & 1 & -\dfrac{2G2O}{G1O}r_5^{-3} \end{bmatrix}.$$ (C.31)

For i = 0 (initial stresses),

$$Q_0^T = \begin{bmatrix} \dfrac{P_I}{G1S} & 0 & 0 & \dfrac{P_O}{G1O} \end{bmatrix}, \text{ and for higher orders,}$$ (C.32)

$$Q_{i+1} = \begin{bmatrix} 0 \\ -\dfrac{2f_{Oi+1}}{3G1O}(\ln r_4 + G3O) + cO\dfrac{G2O}{G1O}\sigma_{i4} + \dfrac{SOi}{G1O} \\ -\dfrac{2f_{Oi+1}}{3G1O}\ln r_4 \\ -\dfrac{2f_{Oi+1}}{3G1O}(\ln r_5 + G3O) + cO\dfrac{G2O}{G1O}\sigma_{i5} + \dfrac{SOi}{G1O} \end{bmatrix}.$$ (C.33)

The above gives the mechanical solutions in SiC and OPyC layers. In the cracked IPyC layer, we use the derivation in Section B.2 to estimate the stresses, strains, displacements, and stress intensity factors there.

(4) MCODE = 'S1'

This is the single elastic SiC layer problem, and using boundary conditions in Section A.3.7 we have

$$\sigma_{r,SiCi}(r_3) = P_{Ii} = G1S \cdot D_i - G2S \cdot F_i r_3^{-3} \quad (P_{Ii} = 0 \text{ unless i=0}), \text{ and} \qquad (C.34)$$

$$\sigma_{r,SiCi}(r_4) = P_{Oi} = G1S \cdot D_i - G2S \cdot F_i r_4^{-3} \quad (P_{Oi} = 0 \text{ unless i=0}). \qquad (C.35)$$

From eqs. (C.34) and (C.35),

$$D_0 = \frac{P_I r_4^{-3} - P_O r_3^{-3}}{G1S\left(r_4^{-3} - r_3^{-3}\right)}, \text{ and} \qquad (C.36)$$

$$F_0 = \frac{P_I - P_O}{G2S\left(r_4^{-3} - r_3^{-3}\right)}, \text{ and} \qquad (C.37)$$

Di and Fi are zeros for all other orders.

In this elastic case of SiC, we have closed form solutions as

$$\sigma_{r,SiC}(r) = \frac{P_I\left(r_4^{-3} - 2r^{-3}\right) + P_O\left(2r^{-3} - r_3^{-3}\right)}{r_4^{-3} - r_3^{-3}}, \qquad (C.38)$$

$$\sigma_{\theta,SiC}(r) = \frac{P_I\left(r_4^{-3} + r^{-3}\right) - P_O\left(r^{-3} + r_3^{-3}\right)}{r_4^{-3} - r_3^{-3}}, \qquad (C.39)$$

$$\varepsilon_{r,SiC}(r) = \frac{P_I r_4^{-3} - P_O r_3^{-3}}{G1S\left(r_4^{-3} - r_3^{-3}\right)} - \frac{2\left(P_I - P_O\right)r^{-3}}{G2S\left(r_4^{-3} - r_3^{-3}\right)}, \qquad (C.40)$$

$$\varepsilon_{\theta,SiC}(r) = \frac{P_I r_4^{-3} - P_O r_3^{-3}}{G1S\left(r_4^{-3} - r_3^{-3}\right)} + \frac{\left(P_I - P_O\right)r^{-3}}{G2S\left(r_4^{-3} - r_3^{-3}\right)}, \text{ and} \qquad (C.41)$$

$$u_{r,SiC}(r) = \frac{P_I r_4^{-3} - P_O r_3^{-3}}{G1S\left(r_4^{-3} - r_3^{-3}\right)}r + \frac{P_I - P_O}{G2S\left(r_4^{-3} - r_3^{-3}\right)}r^{-2}. \qquad (C.42)$$

The above gives the mechanical solutions in SiC layers. In the cracked IPyC and OPyC layers, we use the derivation in Section B.2 to estimate the stresses, strains, displacements, and stress intensity factors there.

(5) MCODE = 'I1' and MCODE = 'O1'

At current stage of the model, we assume that if the SiC layer is failed and it is in tension, then the adjacent PyC layers cannot survive, as discussed in Sections A.3.5 and A.3.6. Therefore, we don't do stress analysis for these two cases.

C.2.2. Thermal Analysis

The thermal calculation in pebble bed system is done in the subroutine

TEMPERATURE(QPPP, T_HE, BURNUP, T_PARTICLE), (C.43)

where

QPPP is the local power density at where the tracked pebble is in W/m^3,

T_HE is the local Helium temperature in °C,

BURNUP is the current burnup of the pebble in FIMA, and

T_PARTICLE(0:5) is an array recording the temperature distribution in a particle.

Thermal conductivities of fuel and coating materials are embedded in this subroutine, and two functions TPEBBLE and TPARTICLE are used to calculate temperatures in a pebble and a particle, respectively.

When irradiation tests are simulated, temperatures are provided as inputs instead of being calculated.

C.2.3. Fission Gas Release

The fission gas release from the fuel kernel and resulting internal pressure are calculated in the subroutine

GASRLS(T_PARTICLE,BURNUP,OPERTIME,DIFFUSION,PRESSURE), (C.44)

where

OPERTIME is the irradiation time in seconds,

DIFFUSION is a logic flag for selecting whether to deploy the diffusion-governed fission gas release model,

PRESSURE is the calculated internal pressure in MPa, and

T_PARTICLE AND BURNUP are given in Section C.2.2.

As stated in Section 2.2, when simulating particle behavior in non-isothermal conditions, we don't use the diffusion-governed gas release model.

C.2.4. Material Properties

Most material property models are assembled in the library file "materprop.lib". The embedded functions and subroutines are described below.

Young's modulus of dense pyrocarbon is calculated by the function

E_PYC(D, BAF0, LC, FLUENCE, T), (C.45)

where

D is the density of dense pyrocarbon in g/cm^3,

BAF0 is the as-fabricated BAF of dense pyrocarbon,

LC is the crystallite size of dense pyrocarbon in A,

FLUENCE is the fast neutron fluence in $10^{21} n/cm^2$, $E > 0.18 MeV$, and

T is the temperature of the material in °C.

The irradiated BAF for pyrocarbon is given by the function

BAFI_PYC(BAF0, FLUENCE). (C.46)

The unrestrained irradiation-induced dimensional change rates in pyrocarbon are given by the subroutine

SWELLU(T,FLUENCE,D,BAF0,CRATE,SR_DOT,ST_DOT), (C.47)

where

CRATE is the coating rate of the pyrocarbon layer in $\mu m/minute$,

SR_DOT is the dimensional change rate in the radial direction in $(10^{21} n/cm^2)^{-1}$, and

ST_DOT is the dimensional change rate in the tangential direction in $(10^{21} n/cm^2)^{-1}$.

The restrained irradiation-induced dimensional change rates in pyrocarbon due to creep strain are given by the subroutine

SWELLR(BAFI, EC, DFLU, SR_DOT, ST_DOT), (C.48)

where

BAFI is the irradiated BAF for pyrocarbon,

EC is an array of size 2 storing the radial and tangential components of apparent creep strain, and

DFLU is the incremental fast neutron fluence gained in one time step in $10^{21} n/cm^2$.

The steady-state irradiation creep in pyrocarbon is given by the subroutine

SSICREEP_PYC(FLUENCE, D, T, EC, CREEP, NU_C), (C.49)

where

CREEP is the creep coefficient in $(MPa.10^{21}n/cm^2)^{-1}$, and

NU_C is the Poisson's ratio in creep.

The strength of pyrocarbon is given by the subroutine

STRENGTH_PYC(LAYER, FLAG, D, BAF0, FLU, T, SIGT, SIGMA0, SIGF, M),

(C.50)

where

LAYER indicates whether IPyC or OPyC is looked at,

FLAG takes the value of 'INI' or 'IRR' to indicate whether the user wants initial strength or irradiated strength, respectively,

SIGT is the array for tangential stresses in the particle (MPa),

SIGMA0 is the initial characteristic strength of pyrocarbon in $MPa.m^{3/\beta}$ (β being the Weibull modulus),

SIGF is the mean fracture strength of pyrocarbon in MPa, and

M is the Weibull modulus of pyrocarbon.

The apparent creep strains in pyrocarbon layers are given by the subroutine

EPI_C(LAYER, SIGR, SIGT, CREEP, NU_C, DFLU, EC), (C.51)

where

LAYER indicates whether IPyC or OPyC is looked at,

SIGR is the array for radial stresses in the particle (MPa), and the rest variables are defined previously.

The Young's modulus of SiC is given simply by the function

E_SIC(T). (C.52)

The strength of SiC is given by the subroutine

STRENGTH_SIC(FLAG, FLU, T, SIGT, SIGMA0, SIGF, M), (C.53)

where

FLAG takes the value of 'INI' or 'IRR' to indicate whether the user wants initial strength or irradiated strength, respectively,

SIGMA0 is the initial characteristic strength of SiC in $MPa.m^{3/\beta}$ (β being the Weibull modulus),

SIGF is the mean fracture strength of SiC, and

M is the Weibull modulus of SiC.

C.2.5. Fuel Failure Evaluation

This module is an implementation of particle state diagram in Figure 2-46. The subroutine is

FAILURE(SIGR, SIGT, FAIL, FAILTYPE), (C.54)

Where

SIGR and SIGT are radial and tangential stresses,

FAIL is a flag indicating whether the particle fails or not, and

FAILTYPE is an INTEGER*4 array of size 3, which counts the number of particle failures in three types: PyC crack induced failure, over-pressurization failure, and chemical failure, in FAILTYPE(0), FAILTYPE(1), and FAILTYPE(2), respectively.

The module also updates two COMMON blocks /NFAIL/ and /CRACKED_PYC/ which interface with the main program and the mechanical analysis module to provide information about fuel failure. The block /NFAIL/ is defined as

COMMON /NFAIL/ IPYCFAIL, SICFAIL, OPYCFAIL, PARFAIL, (C.55)

& IPYCFAILED, SICFAILED, OPYCFAILED, PARFAILED,

& NCHAR, FMODE, PSTATE, MCODE, FAILUREPATH

The INTEGER*4 variables IPYCFAIL, SICFAIL, OPYCFAIL, and PARFAIL count the number of failures of IPyC, SiC, OPyC, and the whole particle when a batch of particles are simulated. An INTEGER*4 variable has 31 bits to store a number and 1 bit for the sign, so the largest positive number it can hold is 2^{31}-1 = 2,147,483,647, which means it can support simulations of over 2 billion particles.

The INTEGER variables IPYCFAILED, SICFAILED, OPYCFAILED, PARFAILED are for the currently examined particle. They take values of 0, 1, and 2, which have the following meanings. Take IPYCFAILED for example, if it is '0', then the IPyC layer is fine; if it is '1', then IPyC has just failed; if it is '2', then IPyC failed at certain previous time step. The reason we distinguish cases '1' and '2' is because when a layer cracks and stresses in it haven't relaxed, the layer may have bigger impact to other layers than when

stresses re-distribute after cracking. These variables are the transition flags in Figure 2-46.

The variables PSTATE and MCODE correspond to particle state and analysis type in Figure 2-46. We already see how MCODE controls the type of mechanical analysis in Section C.2.1. FMODE takes the values '0', '1', and '2' to indicate PyC crack induced failure, over-pressurization failure, and chemical failure. CHARACTER*42 variable FAILUREPATH records what path a particle goes through in the particle state diagram and NCHAR records the current number of characters which are stored in FAILUREPATH.

The COMMON block / CRACKED_PYC / is defined as

COMMON /CRACKED_PYC/ EPIRCP, EPITCP, URCP, KIIPYC, (C.56)

& **KIOPYC, KI1, KI2, SHEARIPYC, SHEAROPYC, DF**

EPIRCP, EPITCP, and URCP are radial strain, tangential strain, and radial displacement distributions in cracked PyC layers with C' configuration as discussed in Section B.2.2. KIIPYC, and KIOPYC are the stress intensity factors in IPyC and OPyC layers, respectively. KI1 and KI2 are the stress intensity contributions to the SiC layer from KIIPYC and KIOPYC, respectively. SHEARIPYC and SHEAROPYC are the shear forces per unit length on the SiC surface induced by IPyC crack and OPyC crack, respectively.

C.2.6. Monte Carlo Sampling

In TIMCOAT, many coated particle properties are sampled based on Weibull distribution, triangular distribution, or normal distribution, as discussed in Section 2.7. In such processes, the generation of random numbers is very important. We take the random number generator RAN from the FUEL code [114], which is based on the lagged Fibonacci method [173]. RAN passed a number of stringent tests, including Parking Lot, Lattice, Overlapping M-Tuple, Overlapping-Pairs-Sparse-Occupancy (OPSO), OPERM, RUNS, RANK, and Birthday Spacing Test [174].

Users can supply a random number seed by turning on the flag USERSEED in the input file, which will be described in Section C.3.1, or let the code initialize a random

number seed according to the time of the day when the program starts to run. To use the function RAN, one should execute RAN(SEED) to initialize the random number generator, then use RAN(0) for subsequent calls to get random numbers.

C.2.7. Error Handling

The error handling functionality still leaves great space for further improvement. Right now the error handling in TIMCOAT mainly does two things. One is to check whether inputs are correctly formatted or input files could be located. The other is to check whether material properties for the particles are within appropriate ranges specified by the material database and material models. If errors arise, error messages are sent to the subroutine XERROR [114] to determine if the program should be terminated or recovered and to write error information to an output file called 'xerror.msg'.

C.3. Code Execution

The logical block diagram of the code TIMCOAT is shown in Figure C-2. The code asks users to provide an input file, as shown in Figure C-1 which contains the particle specification, simulation environment parameters, and program control parameters.
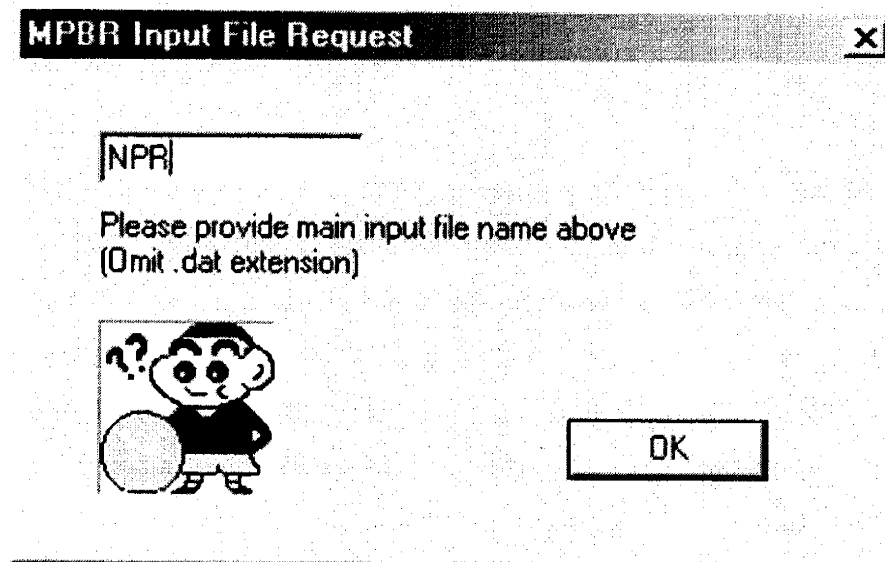
Figure C-1. TIMCOAT input file dialog
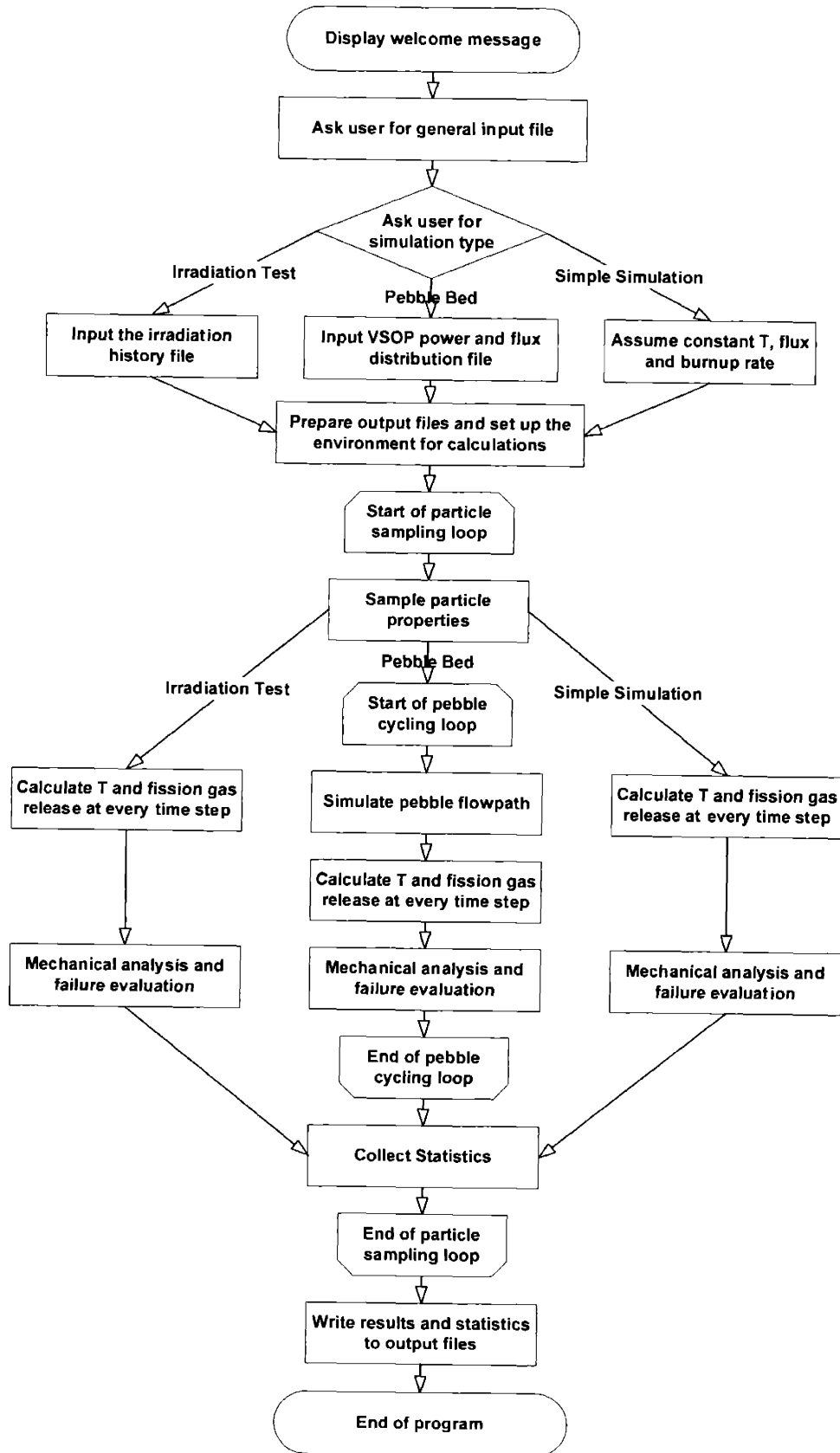
Figure C-2. Block diagram of TIMCOAT code

C.3.1. The General Input File

The description of the parameters in this input file is given below. The parameters are read in by the program via a NAMELIST called 'INPUT'. The example input file here is for design specified LEU-TRISO coated fuel particles simulated in new Modular Pebble Bed Reactor (MPBR2) discussed in Section 4.3.1.

$INPUT

    CORE_HEIGHT = 11.0D0, core height (m)

    CORE_RADIUS = 1.75D0, core radius(m)

    P_CORE = 400.0D0, core power (MWth)

    QPPP_AVG = 4.77689D6, averaged power density (W/m^3)

    T_IRR = 1000.0D0, irradiation temperature (°C)

    IRRTIME = 936.0D0, irradiation time(Day)

    T_GASIN = 500.0D0, coolant inlet temperature (°C)

    T_GASOUT = 900.0D0, coolant outlet temperature (°C)

    MF_HE = 154.6D0, helium mass flow rate (kg/s)

    PEBRADIUS = 3.0D-2, pebble radius (m)

    PFZRADIUS = 2.5D-2, pebble fuel zone radius (m)

    NPEBBLE = 451600, number of pebbles in core

    NPARTICLE = 15000, number of particles per pebble

    DT = 7.2576D5, time step size (s)

    OUTTIME = 7.2576D5, time pebble is taken out of the core in each cycle (s)

    EOLBUP = 0.9775D0, EOL burnup (FIMA)

    EOLFLU = 2.66D0, EOL fluence (10^{21}n/cm^2)

    SHUFFLE = 6, number of fueling cycles

    FUELTYPE = 'UO2', fuel kernel type

    CURAT = 0.0D0, Carbon to Uranium ratio

    OURAT = 2.0D0, Oxygen to Uranium ratio

    U235ENR = 9.600D0, U235 enrichment (%)

    U235VAR = 0.1D0, standard deviation on U235 enrichment (%)

    KERND = 10.4D0, kernel density (g/cm^3)

KERNDVAR = 0.01D0, standard deviation on kernel density (g/cm^3)

KERNT = 10.95D0, kernel theoretical density (g/cm^3)

KERNDIA = 500.0D0, kernel diameter (μm)

KERNVAR = 20.0D0, standard deviation on kernel diameter (μm)

BUFFD = 1.05D0, buffer density (g/cm^3)

BUFFDVAR = 0.05D0, standard deviation on buffer density (g/cm^3)

BUFFT = 2.25D0, buffer theoretical density (g/cm^3)

BUFFTHK = 90.0D0, buffer thickness (μm)

BUFFVAR = 18.0D0, standard deviation on buffer thickness (μm)

IPYCBAF0I = 1.05788D0, IPyC as-fabricated BAF

IPYCBAFVAR = 0.00543D0, standard deviation on IPyC as-fabricated BAF

IPYCCRATE = 1.5D0, IPyC coating rate (μm/min)

IPYCLC = 29.98D0, IPyC crystallite length (μm)

IPYCD = 1.90D0, IPyC density (g/cm^3)

IPYCF = 24.0D0, IPyC characteristic strength (MPa.m^3/modulus)

IPYCM = 9.5D0, IPyC Weibull modulus

IPYCTHK = 40.0D0, IPyC thickness (μm)

IPYCVAR = 10.0D0, standard deviation on IPyC thickness (μm)

OPYCBAF0I = 1.05788D0, OPyC as-fabricated BAF

OPYCBAFVAR = 0.00543D0, standard deviation on OPyC as-fabricated BAF

OPYCCRATE = 1.5D0, OPyC coating rate (μm/min)

OPYCLC = 29.98D0, OPyC crystallite length (μm)

OPYCD = 1.90D0, OPyC density (g/cm^3)

OPYCF = 24.0D0, OPyC characteristic strength (MPa.m^3/modulus)

OPYCM = 9.5D0, OPyC Weibull modulus

OPYCTHK = 40.0D0, OPyC thickness (μm)

OPYCVAR = 10.0D0, standard deviation on OPyC thickness (μm)

SICTHK = 35.0D0, SiC thickness (μm)

SICVAR = 4.0D0, standard deviation on SiC thickness (μm)

SICF = 9.0D0, SiC characteristic strength (MPa.m^3/modulus)

SICKIC0 = 3500.0D0, SiC fracture toughness (MPa.μm$^{1/2}$)

SICKVAR = 530.72D0, standard deviation on SiC fracture toughness

SICM = 6.0D0, SiC Weibull modulus

PAMB = 0.10D0, ambient pressure (MPa)

TITLE = 'Reference LEU TRISO fuel_Design Specification', particle description

OSPEC = 'nPBMR_DS', output file name

DEBUG = .TRUE., flag for debugging

ISEED = 30285171, initial seed for random number generator

NBURP = 1, send intermediate outputs for every NBURP sampled particles

NCASES = 1, number of particles to be sampled

NOMINAL = .TRUE., flag turning on/off Monte Carlo sampling

DIFFUSION = .FALSE., flag turning on/off diffusion model for gas release

HISTOGRAM = .FALSE., flag turning on/off histogram outputs

RUNIRR = 'STRESS', flag turning on/off fuel failure evaluation

USERSEED = .TRUE., flag determining whether ISEED from users is used

$END

Depending on the type of simulations users want to run, different subsets of the above parameters are taken and different control parameters are set, which will be detailed below in Section C.3.2. The parameters from 'FUELTYPE' to 'OSPEC' form a shared subset.

C.3.2. Simulation Type

The program allows users to run three types of simulations: simulation in pebble bed reactor environments, simulation of fuel irradiation tests, and simulation under constant irradiation conditions. The user selection dialog is shown in Figure C-3.
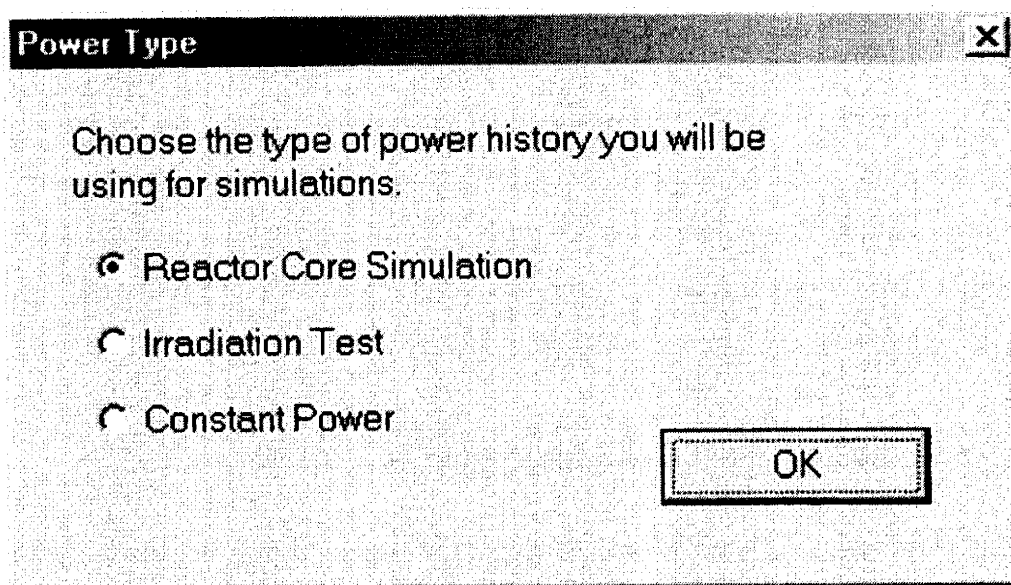
Figure C-3. Simulation type selection dialog

C.3.2.1.Simulation in Pebble Bed Reactor Environments

To run simulations in pebble bed systems, the steady state power and fast neutron flux distributions for the systems need to be provided. In out case, the program interfaces with VSOP outputs to obtain the information. One major VSOP output file is organized in the following way and is fed into TIMCOAT via the input file 'pdistr.dat', as shown in Section C.4.3. From left to right, the listed data are Batch Number, Batch Volume, Conversion Ratio, Batch Power Peaking Factor, Burnup, and Fast Neutron Fluence. VSOP model setup and channels, blocks, and batches are discussed in Section 2.6. Beside this file, two more input files need to be provided. 'blocks.dat' supplies axial position and fast neutron flux of each block. 'channels.dat' depicts the radial and axial positions of channels, as plotted in Figure 2-48. As said in Section 2.6, pebbles flow in channels and simulations pick up irradiation conditions on the way and various analyses are performed at each time step. The batches in each block represent pebbles which come to this block via different number of cycles. In the general input file in Section C.3.1, CORE_HEIGHT, CORE_RADIUS, P_CORE, QPPP_AVG, T_GASIN, T_GASOUT, MF_HE, PEBRADIUS, PFZRADIUS, NPEBBLE, NPARTICLE, DT, OUTTIME, SHUFFLE will be used in this type of simulations. They are not meaningful in another two types of simulations.

271

C.3.2.2. Simulation of Irradiation Tests

In this case, the irradiation histories of irradiated particles are provided as inputs and all the simulated particles run into the same history, which is different from the pebble bed reactor case. The irradiation history for NPR1-A5 compact (see Section 3.2) is given in Section C.4.4. From left to right, the data are Irradiation Time, Effective Full Power Days, Irradiation Temperature, Fast Neutron Fluence, and Burnup.

C.3.2.3. Simulation under Constant Irradiation Conditions

This is the simplest simulation case where the general input file can fully specify the irradiation conditions. T_IRR gives the irradiation temperature, IRRTIME gives the irradiation duration, fast neutron flux is determined by dividing EOLFLU by IRRTIME, and burnup rate is determined by dividing EOLBUP by IRRTIME.

C.3.3. Output Control

With a set of control parameters in the general input file, users can choose the output files they want. The common output file is named by OSPEC+'.out', where OSPEC is the output file name specified in the input file. A sample output file for NPR1-A8 compact (See Section 3.2) is given in Section C.4.5. The file first provides an echo of the input parameters, then lists the failure histories of particles and their individual layers, and finally prints the statistics of stresses and failures in particles. In the example below, because one million particles were sampled, NOMINAL was set to .FALSE. to enable Monte Carlo sampling. When NOMINAL is .FALSE., an output file 'failures.dat' will be created to record the very detailed information of every failed particle. When NOMINAL is .TRUE., the code looks at the behavior of a nominal fuel particle and output lots of useful information. It creates 'out_sigr.dat', 'out_sigt.dat', 'out_epir.dat', 'out_epit.dat', 'out_ur.dat', and 'out_swel.dat' for radial stresses, tangential stresses, radial strains, tangential strains, radial displacements, and irradiation induced dimensional change rates, respectively. Besides, if pebble bed simulation is chosen, 'out_core.dat' is produced to record the actual irradiation history for the particle, 'out_temp.dat' records the

272

temperature distribution in the particle, and 'test.dat' shows which channels the pebble/particle has gone through in subsequent cycles. If irradiation test is simulated, 'irr_history.out' contains the irradiation history. If constant irradiation simulation is used, 'cap_test.out' contains the irradiation history. Different output file names are used to help users recognize what type of simulations they have run.

If we set DEBUG to .TRUE., an output file called OSPEC+'.dbg' will be created. The file provides values for many other intermediate variables which are not contained in the general output file. It helps users to look closely at what is going on during the calculations and to locate potential problems in the code.

If we set HISTOGRAM to .TRUE., particle failure histograms with respect to irradiation time, stresses, fast neutron fluence, and burnup will be written to the output file OSPEC+'.his'. The number of bins for the histograms is specified by the parameter NHIS in the main program. The ranges for time, stress, fluence, and burnup are set by 0 to TIMELIMIT, SIG_LOWER to SIG_UPPER, 0 to EOLFLU, and 0 to EOLBUP, respectively. It is obvious that only when NOMINAL is .FALSE. and Monte Carlo sampling is run on many particles is the flag HISTOGRAM meaningful.

Finally, if we set RUNIRR to 'STRESS', the program will only calculate stresses without performing fuel failure evaluation. If RUNIRR is 'FAILURE', then fuel failure models will be applied to look at various types of fuel particle failures.

C.4. Samples

C.4.1. Input File for Nominal Type 1 Particle in Section 2.4.6

'Type1.dat'

```
$INPUT
        CORE_HEIGHT = 10.0D0,
        CORE_RADIUS = 1.75D0,
        P_CORE = 250.0D0,
        QPPP_AVG = 3.65186D6,
        T_IRR = 1000.0D0,
        IRRTIME = 1000.0D0,
        T_GASIN = 450.0D0,
        T_GASOUT = 850.0D0,
        MF_HE = 118.0D0,
```

```
PEBRADIUS = 3.0D-2,
PFZRADIUS = 2.5D-2,
NPEBBLE = 360000,
NPARTICLE = 11000,
DT = 2.88D6,
OUTTIME = 2.88D6,
EOLBUP = 0.10D0,
EOLFLU = 3.0D0,
SHUFFLE = 10,
FUELTYPE = 'UCO',
CURAT = 0.36D0,
OURAT = 1.51D0,
U235ENR = 93.15D0,
U235VAR = 0.01D0,
KERND = 10.52D0,
KERNDVAR = 0.01D0,
KERNT = 11.03D0,
KERNDIA = 195.0D0,
KERNVAR = 5.2D0,
BUFFD = 0.95D0,
BUFFDVAR = 0.05D0,
BUFFT = 2.25D0,
BUFFTHK = 100.0D0,
BUFFVAR = 10.2D0,
IPYCBAF0I = 1.03D0,
IPYCBAFVAR = 0.00543D0,
IPYCCRATE = 1.0D0,
IPYCLC = 29.98D0,
IPYCD = 1.90D0,
IPYCF = 24.0D0,
IPYCM = 9.5D0,
IPYCTHK = 53.0D0,
IPYCVAR = 3.68D0,
OPYCBAF0I = 1.03D0,
OPYCBAFVAR = 0.00543D0,
OPYCCRATE = 1.0D0,
OPYCLC = 29.98D0,
OPYCD = 1.90D0,
OPYCF = 24.0D0,
OPYCM = 9.5D0,
OPYCTHK = 43.0D0,
OPYCVAR = 4.01D0,
SICTHK = 35.0D0,
SICVAR = 3.12D0,
SICF = 9.0D0,
SICKIC0 = 3500.0D0,
```

```
        SICKVAR = 530.7227776,
        SICM = 6.0D0,
        PAMB = 6.38D0,
        TITLE = 'Type 1 fuel specifications_nominal',
        OSPEC = 'Type1',
        DEBUG = .TRUE.,
        ISEED = 30285171,
        NBURP = 1,
        NCASES = 1,
        NOMINAL = .TRUE.,
        DIFFUSION = .TRUE.,
        HISTOGRAM = .FALSE.,
        RUNIRR = 'STRESS',
        USERSEED = .TRUE.,
$END
```

C.4.2. Input File for NPR2-A4 Particles – 1,000,000 Cases

'NPR2_A4s.dat'

```
$INPUT
        CORE_HEIGHT = 10.0D0,
        CORE_RADIUS = 1.75D0,
        P_CORE = 250.0D0,
        QPPP_AVG = 3.65186D6,
        T_IRR = 746.0D0,
        IRRTIME = 172.0D0,
        T_GASIN = 450.0D0,
        T_GASOUT = 850.0D0,
        MF_HE = 118.0D0,
        PEBRADIUS = 3.0D-2,
        PFZRADIUS = 2.5D-2,
        NPEBBLE = 360000,
        NPARTICLE = 11000,
        DT = 1.728D5,
        OUTTIME = 1.728D5,
        EOLBUP = 0.79D0,
        EOLFLU = 3.8D0,
        SHUFFLE = 10,
        FUELTYPE = 'UCO',
        CURAT = 0.36D0,
        OURAT = 1.51D0,
        U235ENR = 93.15D0,
        U235VAR = 0.01D0,
        KERND = 10.52D0,
        KERNDVAR = 0.01D0,
```

```
KERNT = 11.03D0,
KERNDIA = 200.0D0,
KERNVAR = 5.2D0,
BUFFD = 0.9577D0,
BUFFDVAR = 0.05D0,
BUFFT = 2.25D0,
BUFFTHK = 102.0D0,
BUFFVAR = 10.2D0,
IPYCBAF0I = 1.05788D0,
IPYCBAFVAR = 0.00543D0,
IPYCCRATE = 1.5D0,
IPYCLC = 29.98D0,
IPYCD = 1.923D0,
IPYCF = 24.0D0,
IPYCM = 9.5D0,
IPYCTHK = 53.0D0,
IPYCVAR = 3.68D0,
OPYCBAF0I = 1.05154D0,
OPYCBAFVAR = 0.00622D0,
OPYCCRATE = 3.0D0,
OPYCLC = 29.98D0,
OPYCD = 1.855D0,
OPYCF = 20.0D0,
OPYCM = 9.5D0,
OPYCTHK = 39.0D0,
OPYCVAR = 4.01D0,
SICTHK = 35.0D0,
SICVAR = 3.12D0,
SICF = 9.0D0,
SICKIC0 = 3500.0D0,
SICKVAR = 530.7227776,
SICM = 6.0D0,
PAMB = 0.10D0,
TITLE = 'Capsule NPR2-A4 specifications_MC sampling',
OSPEC = 'NPR2_A4s',
DEBUG = .TRUE.,
ISEED = 30285171,
NBURP = 10000,
NCASES = 1000000,
NOMINAL = .FALSE.,
DIFFUSION = .FALSE.,
HISTOGRAM = .TRUE.,
RUNIRR = 'FAILURE',
USERSEED = .FALSE.,
$END
```

C.4.3. Input File for Pebble Bed Power Distribution

'pdistr.dat'

BATCH	VOLUME (cm^3)	CONV RATIO	POWER (Batch/Avg.)	BURNUP (MWD/T)	FASTDOSE (1n/cm^2)
1	150038.	0.151162	0.672659	239.580	0.434750E+19
2	150038.	0.221972	0.619413	17546.3	0.385081E+21
3	150038.	0.285530	0.541503	33263.5	0.766169E+21
4	150038.	0.346953	0.471931	47140.6	0.114755E+22
5	150038.	0.403075	0.413497	59406.7	0.152946E+22
6	150020.	0.455331	0.365060	70330.5	0.191236E+22
7	1.00000	1.94230	0.452071E-04	20.5760	0.434750E+19
8	150038.	0.198445	1.31505	948.250	0.176820E+20
9	150038.	0.237766	1.20622	18199.2	0.398442E+21
10	150038.	0.303120	1.05352	33836.1	0.779569E+21
11	150038.	0.366442	0.917780	47641.2	0.116099E+22
12	150038.	0.424746	0.803866	59847.1	0.154293E+22
13	150020.	0.479397	0.709493	70720.4	0.192584E+22
14	1.00000	2.34851	0.939720E-04	83.8685	0.176820E+20
15	150038.	0.227188	1.90059	2094.74	0.400510E+20
16	150038.	0.266280	1.75503	19257.3	0.420838E+21
17	150038.	0.332928	1.54173	34765.3	0.801998E+21
18	150038.	0.397275	1.34993	48454.7	0.118344E+22
19	150038.	0.456473	1.18800	60563.2	0.156541E+22
20	150020.	0.511827	1.05340	71355.1	0.194832E+22
21	1.00000	2.29009	0.153465E-03	196.451	0.400510E+20
22	150038.	0.239633	2.42080	3635.84	0.704222E+20
23	150038.	0.284463	2.21651	20675.5	0.451234E+21
24	150038.	0.353030	1.94449	36011.7	0.832418E+21
25	150038.	0.418931	1.70229	49547.2	0.121389E+22
26	150038.	0.479918	1.49817	61526.0	0.159588E+22
27	150020.	0.537255	1.32868	72209.7	0.197877E+22
28	1.00000	2.02092	0.225467E-03	369.688	0.704222E+20
29	150038.	0.259572	2.64021	5440.19	0.106362E+21
30	150038.	0.308606	2.41909	22329.7	0.487196E+21
31	150038.	0.377998	2.13087	37467.2	0.868396E+21
32	150038.	0.444034	1.87341	50825.4	0.124988E+22
33	150038.	0.504990	1.65567	62654.6	0.163189E+22
34	150020.	0.562100	1.47454	73213.6	0.201476E+22
35	1.00000	1.78591	0.291619E-03	606.861	0.106362E+21
36	150038.	0.268631	2.74052	7358.92	0.144857E+21
37	150038.	0.323689	2.48810	24080.3	0.525709E+21
38	150038.	0.394242	2.18874	39008.7	0.906916E+21
39	150038.	0.460908	1.92439	52181.7	0.128841E+22
40	150038.	0.522682	1.70140	63854.7	0.167043E+22

......

C.4.4. Input File for NPR1-A5 Irradiation History

'irrhis_NPR1A5.dat'

Time (Days)	EFPD (Days)	Irradiation T (°C)	Fluence (10^{21} n/cm^2)	Burnup (%FIMA)
0	0.00000	1128.389709	0.00000	0.00000
1.550406693	1.55041	1152.995557	0.00541	1.80477
4.312607496	4.31261	1142.862262	0.01504	5.02014
7.077159775	7.07716	1126.590942	0.02468	8.23826
9.535236312	9.53524	1110.308872	0.03325	11.09961
11.68605328	11.68605	1096.062061	0.04075	13.60330
14.14804895	14.14805	1069.54995	0.04933	16.46921
15.68199531	15.68200	1065.511681	0.05468	18.25482
17.52398506	17.52399	1057.392146	0.06111	20.39901
18.75615863	18.75616	1041.067078	0.06540	21.83334
20.48	20.44800	1026.798767	0.07141	23.84000
33.56800	20.44800	982.2488175	0.07141	23.84000
34.37936703	21.25937	1060.029382	0.07424	24.51492
35.90782661	22.78783	1070.313172	0.07958	25.78633
37.140784	24.02078	1051.942095	0.08388	26.81194
39.29081715	26.17082	1039.741293	0.09138	28.60039
39.8967142	26.77671	1058.176867	0.09349	29.10439
41.43066056	28.31066	1054.138598	0.09884	30.38037
42.6495091	29.52951	1072.595671	0.10309	31.39424
45.10445034	31.98445	1064.497635	0.11166	33.43633
46.02074226	32.90074	1072.713917	0.11485	34.19853
47.86194819	34.74195	1066.64039	0.12128	35.73009
49.70315411	36.58315	1060.566863	0.12770	37.26166
52.1565277	39.03653	1056.560843	0.13626	39.30244
53.81500	40.69500	1060.706607	0.14204	40.68200
63.96400	40.69500	1056.980077	0.14204	40.68200
66.86971478	43.60071	1050.938799	0.15128	42.21793
69.02131557	45.75232	1034.64598	0.15811	43.35524
69.93603985	46.66704	1046.954278	0.16102	43.83875
72.70137595	49.43238	1028.63695	0.16981	45.30047
74.22983553	50.96084	1038.92074	0.17467	46.10840
75.45730615	52.18831	1034.871721	0.17857	46.75722
77.2930253	54.02403	1043.120252	0.18440	47.72756
80.05444227	56.78544	1035.032965	0.19318	49.18721
82.81821073	59.54921	1020.807654	0.20196	50.64811
85.80900	62.54000	1004.547083	0.21147	52.22900
96.61800	62.54000	1021.291386	0.21147	52.22900
98.13651104	64.05851	1035.667192	0.26081	53.25657
98.73613749	64.65814	1070.470833	0.28030	53.66234
101.1949979	67.11700	1052.142755	0.36020	55.32625

......

278

C.4.5. Output File for NPR1-A8 Particles – 1,000,000 Cases

'NPR1_A8s.out'

05/05/03   13:22:19

```
##### ### #   #  ###  ##      ##    #####
  #   #  ## ## #   #  #  # #       #
  #   #  ## ## #   #  # # #  #      #
  #   #  #  ##     #  # ##### #     #
  #   #  #  ##     #  # #  #  #      #
  #   #  #  # #    #  # #   #  #     #
  #  ### #  #  ### ## #     #   #
```

Monte Carlo calculation of failures in a statistical sample of TRISO-coated fuel particles for the High Temperature Gas-cooled Reactors (HTGRs).

THE MIT FUEL PERFORMANCE MODEL FOR HTGR -- v 1.0

```
&INPUT
BUFFD  = 0.957700000000000    ,
BUFFDVAR     = 5.000000000000000E-002,
BUFFT  = 2.25000000000000    ,
BUFFTHK =  102.000000000000    ,
BUFFVAR =  10.2000000000000    ,
CORE_HEIGHT    =  10.0000000000000    ,
CORE_RADIUS    =  1.75000000000000    ,
CURAT  = 0.360000000000000    ,
DEBUG  = T,
DT    =  172800.000000000    ,
EOLBUP = 0.740000000000000    ,
EOLFLU =  2.40000000000000    ,
IPYCBAFOI    =  1.05788000000000    ,
IPYCBAFVAR    = 5.430000000000000E-003,
IPYCCRATE    =  1.50000000000000    ,
IPYCD  =  1.92300000000000    ,
IPYCF  =  24.0000000000000    ,
IPYCLC =  29.9800000000000    ,
IPYCM  =  9.50000000000000    ,
IPYCTHK =  53.0000000000000    ,
IPYCVAR =  3.68000000000000    ,
IRRTIME =  170.000000000000    ,
ISEED  =    1981137,
KERND  =  10.5200000000000    ,
KERNDIA =  200.000000000000    ,
KERNDVAR     = 1.000000000000000E-002,
KERNT  =  11.0300000000000    ,
```

279

```
KERNVAR =  5.20000000000000   ,
MF_HE   =  118.000000000000   ,
NBURP   =      10000,
NCASES  =    1000000,
NOMINAL = F,
NPEBBLE =     360000,
NPARTICLE    =      11000,
QPPP_AVG     =  3651860.00000000   ,
OPYCBAF0I    =  1.05154000000000   ,
OPYCBAFVAR   =  6.220000000000000E-003,
OPYCCRATE    =  3.00000000000000   ,
OPYCD   =  1.85500000000000   ,
OPYCF   =  20.0000000000000   ,
OPYCLC  =  29.9800000000000   ,
OPYCM   =  9.50000000000000   ,
OPYCTHK =  39.0000000000000   ,
OPYCVAR =  4.01000000000000   ,
OSPEC   = NPR1_A8s,
OURAT   =  1.51000000000000   ,
OUTTIME =  172800.000000000   ,
P_CORE  =  250.000000000000   ,
PAMB    =  0.100000000000000   ,
PEBRADIUS    =  3.000000000000000E-002,
PFZRADIUS    =  2.500000000000000E-002,
RUNIRR  = FAILURE ,
SHUFFLE =         10,
SICF    =  9.00000000000000   ,
SICKIC0 =  3500.00000000000   ,
SICKVAR =  530.722777600000   ,
SICM    =  6.00000000000000   ,
SICTHK  =  35.0000000000000   ,
SICVAR  =  3.12000000000000   ,
T_GASIN =  450.000000000000   ,
T_GASOUT     =  850.000000000000   ,
T_IRR   =  845.000000000000   ,
TITLE   = Compact NPR1_A8 specifications_MC sampling          ,
U235ENR =  93.1500000000000   ,
U235VAR =  1.000000000000000E-002,
USERSEED     = F,
FUELTYPE     = UCO,
DIFFUSION    = F,
HISTOGRAM    = T,
PSWITCH =          2,

Initial Random Number SEED =     1981137
The number of divisions for stress distributions:      15
```

The calculation starts at: 05/05/03   13:22:19

Start of Sampling: 1000000 Cases

Cases Completed	Elapsed Time (sec)	Particle Failures (Irrad)	SiC Failures (Irrad)	IPyC Failures (Irrad)	OPyC Failures (Irrad)
10000	908.	325	325	6057	569
20000	1816.	646	646	12129	1146
30000	2725.	937	937	18116	1694
40000	3637.	1204	1204	24034	2186
50000	4546.	1507	1507	30039	2725
60000	5454.	1804	1804	36076	3285
70000	6361.	2107	2107	42124	3837
80000	7269.	2430	2430	48085	4438
90000	8178.	2745	2745	54044	5004
100000	9085.	3071	3071	60088	5582
......					
900000	81749.	27134	27134	542388	50163
910000	82656.	27466	27466	548406	50758
920000	83565.	27748	27748	554445	51284
930000	84474.	28045	28045	560451	51853
940000	85381.	28360	28360	566500	52422
950000	86292.	28662	28662	572398	52953
960000	87200.	28980	28980	578410	53540
970000	88108.	29263	29263	584465	54097
980000	89016.	29558	29558	590522	54650
990000	89925.	29843	29843	596587	55170
1000000	90832.	30127	30127	602726	55705

Elapsed calculation time: 25 hours 13 minutes and 52 seconds

========================= Statistical Report =========================

Average number of particles per second =   11.0093359168575

Sample maximum tangential stress in IPyC   0.3146E+03 +/- 0.3137E+02
Sample maximum tangential stress in SiC   0.2894E+01 +/- 0.1472E+02
Sample maximum tangential stress in OPyC   0.2231E+03 +/- 0.1167E+02
Sample minimum tangential stress in IPyC -0.8647E-01 +/- 0.3011E+00
Sample minimum tangential stress in SiC   -0.6336E+03 +/- 0.8990E+02
Sample minimum tangential stress in OPyC -0.8820E-01 +/- 0.1927E-02
Sample EOL tangential stress in IPyC   0.1688E+03 +/- 0.5664E+02
Sample EOL tangential stress in SiC   -0.2758E+03 +/- 0.1996E+03

Sample EOL tangential stress in OPyC   0.1397E+03 +/- 0.6727E+01

Number of failed particles: 30127
Number of particle with SiC crack: 30127
Number of particle with IPyC crack: 602726
Number of particle with OPyC crack: 55705
Particle failure probability: 0.3013E-01 +/- 0.1703E-02
SiC layer failure probability: 0.3013E-01 +/- 0.1703E-02
IPyC layer failure probability: 0.6027E+00 +/- 0.4773E-02
OPyC layer failure probability: 0.5570E-01 +/- 0.2239E-02
Fracture induced by IPyC cracking: 30127
Overpressure rupture: 0
Chemical failure - Ag diffusion: 0
Dumped particles exceeding EOL burnup   0

================== End of Statistical Report ====================

The calculation ends at: 05/06/03   14:36:11

C.4.6. Output Debug File for NPR1-A8 Particles – 1,000,000 Cases

'NPR1_A8s.dbg'

REACTOR PARAMETERS:
&REACTOR
CORE_HEIGHT   = 10.0000000000000   ,
CORE_RADIUS   = 1.75000000000000   ,
P_CORE = 250.000000000000   ,
T_IRR   = 845.000000000000   ,
T_GASIN = 450.000000000000   ,
T_GASOUT   = 850.000000000000   ,
MF_HE   = 118.000000000000   ,
PACKING = 0.000000000000000E+000,
NPEBBLE =   360000,
EOLBUP = 0.740000000000000   ,
EOLFLU = 2.40000000000000   ,
QPPP_AVG   = 3651860.00000000   ,
DT   = 172800.000000000   ,
OUTTIME = 172800.000000000   ,
OPERTIME   = 26634873.6000000   ,
IRRTIME = 170.287000000000   ,
/

FUEL PEBBLE PARAMETERS:
&PEBBLES
PEBRADIUS   = 3.000000000000000E-002,

282

```
PFZRADIUS    = 2.500000000000000E-002,
K_PM  = 0.000000000000000E+000,
K_PFM  = 0.000000000000000E+000,
K_PFZ  = 0.000000000000000E+000,
NPARTICLE     =     11000,
/

FUEL PARTICLE PROPERTIES AND STATISTICS:
&PARTI
R1     =  99.9682539245634    ,
R2     =  215.401535440268    ,
R3     =  273.101208068349    ,
R4     =  304.953006394871    ,
R5     =  344.616897578707    ,
PRESS  =  16.5058784668681    ,
BURNUP  =  0.729754500000000    ,
FLUENCE =  2.324170000000000E+021,
IPYCALPHA     =  5.980141000000000E-006,
IPYCBAFI     =  1.06467834079086    ,
IPYCD  =  1.92300000000000    ,
IPYCE  =  45707.7275996672    ,
IPYCNU  =  0.330000000000000    ,
IPYCCNU  =  0.400000000000000    ,
IPYCREEP     =  1.001300623439216E-004,
OPYCALPHA     =  5.696785000000001E-006,
OPYCBAFI     =  1.06446847302092    ,
OPYCD  =  1.85500000000000    ,
OPYCE  =  44703.0676176537    ,
OPYCNU  =  0.330000000000000    ,
OPYCCNU  =  0.400000000000000    ,
OPYCREEP     =  1.172735459248838E-004,
SICALPHA     =  4.900000000000000E-006,
SICE   =  377609.221090229    ,
SICNU  =  0.130000000000000    ,
SIGFIPYC     =  349.806308076458    ,
SIGFOPYC     =  319.345110724864    ,
SIGFSIC =  482.650744136976    ,
KICSIC =  3356.51582233004    ,
KIIPYC =  11734.3281469804    ,
KIOPYC =  0.000000000000000E+000,
CL     =  15.0000000000000    ,
SIGTIPYC     =  118.576548433318    ,
SIGTSIC =  -165.779013337648    ,
SIGTOPYC     =  140.292280898784    ,
SIGXIPYC     =  333.046750576709    ,
SIGXSIC =  -0.406581980866324    ,
```

```
SIGXOPYC      =  226.994315584270   ,
SIGMIPYC     = -6.825852423310885E-002,
SIGMSIC = -780.954913930043   ,
SIGMOPYC     = -9.099448267402202E-002,
SIGLIPYC     =  118.576548433318   ,
SIGLSIC = -165.779013337648   ,
SIGLOPYC     =  140.292280898784   ,
SIGFCIPYC    =  309.989640693704   ,
SIGFCSIC     =  482.650744136976   ,
SIGFCOPYC    =  280.838343861978   ,
IPYCFAIL     =     602726,
OPYCFAIL     =      55705,
SICFAIL =     30127,
PARFAIL =     30127,
/


CONTROL VARIABLES FOR HISTOGRAMS:
TIMELIMIT =   86400000.0000000
EOL FLUENCE =   2.40000000000000
EOL BURNUP =  0.740000000000000
STRESS UPPER LIMIT =   1000.00000000000
STRESS LOWER LIMIT =  -1000.00000000000
HISTOGRAM INTEVALS =      200

End of debug file.
```

C.4.7. Output Irradiation History in MPBR2 for LEU-TRISO Particles

'out_core.dat'

Time (day)	Fluence (10E21nvt)	QPPP (W/m^3)	Burnup (FIMA)	Coolant T (°C)
8.400	0.010	0.26266E+07	0.0002	509.048
16.800	0.031	0.51885E+07	0.0009	526.868
25.200	0.064	0.77615E+07	0.0019	553.853
33.600	0.106	0.10039E+08	0.0034	588.582
42.000	0.153	0.11056E+08	0.0052	627.144
50.400	0.201	0.11517E+08	0.0070	667.100
58.800	0.248	0.10956E+08	0.0089	705.274
67.200	0.291	0.10166E+08	0.0106	740.569
75.600	0.329	0.89163E+07	0.0122	771.624
84.000	0.362	0.77690E+07	0.0136	798.632
92.400	0.390	0.65815E+07	0.0148	821.540
100.800	0.414	0.55592E+07	0.0158	840.871
109.200	0.434	0.46208E+07	0.0166	856.953
117.600	0.450	0.38159E+07	0.0173	870.227

126.000	0.463	0.30858E+07	0.0179	880.967
134.400	0.474	0.24134E+07	0.0183	889.363
142.800	0.482	0.18011E+07	0.0187	895.630
151.200	0.487	0.12540E+07	0.0190	900.000
168.000	0.497	0.24121E+07	0.0194	509.048
176.400	0.518	0.47494E+07	0.0200	526.868
184.800	0.551	0.71526E+07	0.0210	553.853
193.200	0.592	0.91906E+07	0.0223	588.582
201.600	0.639	0.10143E+08	0.0239	627.144
210.000	0.688	0.10487E+08	0.0256	667.100
218.400	0.735	0.99707E+07	0.0273	705.274
226.800	0.778	0.92007E+07	0.0289	740.569
235.200	0.816	0.80655E+07	0.0304	771.624
243.600	0.849	0.70040E+07	0.0316	798.632
252.000	0.877	0.59280E+07	0.0327	821.540
260.400	0.901	0.49974E+07	0.0336	840.871
268.800	0.920	0.41517E+07	0.0343	856.953
277.200	0.937	0.34246E+07	0.0350	870.227
285.600	0.950	0.27684E+07	0.0355	880.967
294.000	0.961	0.21634E+07	0.0359	889.363
302.400	0.969	0.16140E+07	0.0362	895.630
310.800	0.973	0.11246E+07	0.0364	900.000
327.600	0.983	0.21057E+07	0.0368	509.048
336.000	1.005	0.41434E+07	0.0373	526.868
344.400	1.037	0.62749E+07	0.0382	553.853
352.800	1.079	0.80586E+07	0.0394	588.582
361.200	1.126	0.89362E+07	0.0408	627.144
369.600	1.174	0.92352E+07	0.0423	667.100
378.000	1.221	0.88080E+07	0.0438	705.274
386.400	1.264	0.81268E+07	0.0452	740.569
394.800	1.302	0.71408E+07	0.0465	771.624
403.200	1.335	0.62014E+07	0.0476	798.632
411.600	1.364	0.52549E+07	0.0485	821.540
420.000	1.387	0.44305E+07	0.0493	840.871
428.400	1.407	0.36837E+07	0.0500	856.953
436.800	1.423	0.30388E+07	0.0506	870.227
445.200	1.437	0.24577E+07	0.0510	880.967
453.600	1.447	0.19206E+07	0.0514	889.363
462.000	1.455	0.14331E+07	0.0517	895.630
470.400	1.460	0.99938E+06	0.0519	900.000
487.200	1.470	0.22544E+07	0.0519	509.552
495.600	1.491	0.43841E+07	0.0524	528.155
504.000	1.522	0.64485E+07	0.0533	555.376
512.400	1.561	0.81317E+07	0.0545	589.790
520.800	1.605	0.89491E+07	0.0560	627.558
529.200	1.651	0.91926E+07	0.0575	666.459

537.600	1.694	0.87601E+07	0.0590	703.490
546.000	1.734	0.80546E+07	0.0603	737.603
554.400	1.770	0.70631E+07	0.0616	767.494
562.800	1.801	0.61147E+07	0.0627	793.399
571.200	1.827	0.51754E+07	0.0636	815.321
579.600	1.849	0.43559E+07	0.0644	833.781
588.000	1.868	0.36160E+07	0.0651	849.104
596.400	1.883	0.29794E+07	0.0656	861.734
604.800	1.896	0.24218E+07	0.0661	871.999
613.200	1.906	0.19569E+07	0.0664	880.295
621.600	1.914	0.15837E+07	0.0667	887.010
630.000	1.920	0.12292E+07	0.0670	892.223
638.400	1.925	0.10536E+07	0.0672	896.691
646.800	1.928	0.78038E+06	0.0673	900.000
663.600	1.938	0.14551E+07	0.0682	508.583
672.000	1.958	0.28826E+07	0.0686	525.604
680.400	1.990	0.45215E+07	0.0692	552.038
688.800	2.031	0.58822E+07	0.0700	586.450
697.200	2.078	0.66278E+07	0.0711	624.898
705.600	2.126	0.68848E+07	0.0722	664.853
714.000	2.173	0.66276E+07	0.0733	703.092
722.400	2.216	0.61393E+07	0.0744	738.510
730.800	2.254	0.54375E+07	0.0753	769.744
739.200	2.287	0.47396E+07	0.0762	796.959
747.600	2.315	0.40369E+07	0.0769	820.087
756.000	2.339	0.34128E+07	0.0775	839.631
764.400	2.359	0.28451E+07	0.0781	855.901
772.800	2.375	0.23546E+07	0.0785	869.362
781.200	2.389	0.19163E+07	0.0789	880.307
789.600	2.399	0.15241E+07	0.0792	889.010
798.000	2.407	0.11527E+07	0.0794	895.589
806.400	2.412	0.77396E+06	0.0796	900.000
823.200	2.422	0.17439E+07	0.0796	509.552
831.600	2.442	0.33892E+07	0.0800	528.155
840.000	2.474	0.50320E+07	0.0807	555.376
848.400	2.513	0.63470E+07	0.0817	589.790
856.800	2.557	0.70437E+07	0.0828	627.558
865.200	2.602	0.72428E+07	0.0839	666.459
873.600	2.646	0.69448E+07	0.0851	703.490
882.000	2.686	0.63946E+07	0.0862	737.603
890.400	2.722	0.56339E+07	0.0872	767.494
898.800	2.753	0.48839E+07	0.0881	793.399
907.200	2.779	0.41446E+07	0.0889	815.321
915.600	2.801	0.34919E+07	0.0895	833.781
924.000	2.820	0.29038E+07	0.0900	849.104
932.400	2.835	0.23942E+07	0.0905	861.734

940.800	2.847	0.19482E+07	0.0909	871.999		
949.200	2.857	0.15750E+07	0.0912	880.295		
957.600	2.865	0.12750E+07	0.0914	887.010		
966.000	2.872	0.98984E+06	0.0916	892.223		
974.400	2.876	0.84856E+06	0.0918	896.691		
982.800	2.879	0.62884E+06	0.0919	900.000		

C.4.8. Output Tangential Stresses in a LEU-TRISO Particle in MPBR2

'out_sigt.dat'

Fluence (10E21nvt)	R2 (µm)		R3 (µm)		R4 (µm)		R5 (µm)
	342.500	363.000	383.500	401.500	419.500	439.500	459.500
0.010	8.337	8.041	7.819	-16.584	6.514	6.291	6.116
0.031	25.870	24.901	24.170	-49.703	20.183	19.466	18.896
0.064	52.196	50.113	48.524	-98.734	40.374	38.851	37.629
0.106	83.989	80.421	77.670	-156.801	64.167	61.591	59.508
0.153	115.370	110.215	106.208	-212.881	86.992	83.317	80.324
0.201	141.408	134.871	129.765	-258.417	105.455	100.844	97.073
0.248	161.308	153.732	147.800	-293.070	119.629	114.316	109.962
0.291	175.412	167.154	160.688	-317.779	129.938	124.161	119.425
0.329	188.646	179.829	172.933	-341.027	139.440	133.300	128.273
0.362	199.692	190.468	183.266	-360.440	147.293	140.901	135.677
0.390	209.587	200.031	192.586	-378.114	154.455	147.858	142.477
0.414	217.739	207.937	200.315	-392.774	160.396	153.649	148.157
0.434	224.905	214.895	207.125	-405.783	165.671	158.797	153.210
0.450	230.943	220.763	212.874	-416.799	170.139	163.160	157.497
0.463	236.372	226.036	218.035	-426.781	174.188	167.110	161.374
0.474	241.425	230.934	222.823	-436.151	177.989	170.810	164.998
0.482	246.086	235.443	227.221	-444.861	181.524	174.242	168.350
0.487	249.965	239.182	230.856	-452.173	184.512	177.130	171.159
0.497	253.367	242.549	234.205	-461.910	186.921	179.499	173.503
0.518	260.801	249.804	241.342	-476.045	192.619	185.085	179.013
0.551	270.430	259.249	250.678	-494.486	199.913	192.278	186.147
0.592	277.299	266.137	257.627	-507.780	204.847	197.281	191.237
0.639	278.584	267.739	259.527	-510.489	205.344	198.078	192.315
0.688	274.133	263.875	256.171	-502.112	201.529	194.760	189.440
0.735	269.749	260.087	252.898	-493.830	198.111	191.831	186.945
0.778	265.791	256.689	249.983	-486.315	195.267	189.437	184.951
0.816	265.621	256.903	250.543	-486.125	195.467	189.948	185.748
0.849	266.171	257.763	251.684	-487.302	196.233	190.965	186.998
0.877	268.460	260.250	254.363	-491.834	198.299	193.198	189.393
0.901	270.710	262.653	256.915	-496.262	200.286	195.314	191.636
0.920	273.418	265.456	259.818	-501.559	202.571	197.685	194.095

0.937	276.032	268.132	262.565	-506.655	204.739	199.912	196.385
0.950	278.990	271.111	265.579	-512.414	207.130	202.330	198.839
0.961	282.466	274.568	269.037	-519.188	209.884	205.081	201.599
0.969	286.303	278.353	272.796	-526.674	212.889	208.058	204.563
0.973	290.311	282.276	276.664	-534.490	215.999	211.112	207.579
0.983	291.547	283.528	277.932	-543.551	216.470	211.557	208.004
1.005	295.006	286.836	281.130	-550.667	219.008	213.999	210.374
1.037	298.985	290.717	284.955	-559.556	221.964	216.907	213.257
1.079	299.363	291.243	285.627	-562.451	222.145	217.229	213.717
1.126	294.050	286.400	281.190	-554.804	218.050	213.515	210.342
1.174	283.694	276.765	272.156	-536.860	210.346	206.369	203.681
1.221	273.738	267.564	263.584	-518.838	203.332	199.929	197.736
1.264	265.051	259.574	256.172	-502.505	197.495	194.612	192.871
1.302	260.411	255.474	252.533	-493.750	194.809	192.331	190.948
1.335	257.258	252.752	250.180	-487.648	193.172	191.016	189.920
1.364	256.224	252.034	249.738	-485.653	193.035	191.118	190.239
1.387	255.730	251.781	249.698	-484.637	193.182	191.449	190.738
1.407	256.056	252.282	250.357	-485.236	193.845	192.248	191.663
1.423	256.700	253.053	251.246	-486.454	194.658	193.161	192.672
1.437	257.956	254.394	252.670	-488.927	195.865	194.439	194.018
1.447	259.966	256.453	254.783	-492.968	197.592	196.210	195.837
1.455	262.554	259.060	257.421	-498.223	199.714	198.354	198.010
1.460	265.600	262.093	260.458	-504.447	202.131	200.769	200.435
1.470	265.797	262.312	260.689	-514.322	201.532	200.124	199.749
1.491	267.540	263.837	262.038	-517.797	202.597	201.044	200.544
1.522	268.944	265.086	263.167	-521.537	203.440	201.791	201.215
1.561	266.735	262.941	261.083	-519.272	201.568	199.988	199.476
1.605	259.755	256.299	254.720	-507.976	196.223	194.910	194.629
1.651	249.083	246.157	245.005	-488.470	188.367	187.454	187.510
1.694	239.265	236.914	236.228	-469.499	181.569	181.080	181.497
1.734	231.203	229.378	229.121	-453.096	176.299	176.195	176.939
1.770	226.884	225.488	225.589	-443.979	173.933	174.143	175.161
1.801	224.076	223.017	223.403	-437.729	172.603	173.061	174.297
1.827	223.058	222.255	222.863	-435.182	172.510	173.159	174.567
1.849	222.580	221.971	222.748	-433.737	172.688	173.483	175.024
1.868	222.822	222.358	223.266	-433.864	173.304	174.211	175.855
1.883	223.338	222.983	223.990	-434.617	174.036	175.027	176.751
1.896	224.203	223.928	225.012	-436.177	174.960	176.016	177.802
1.906	225.070	224.857	225.998	-437.793	175.828	176.933	178.767
1.914	225.744	225.577	226.763	-439.026	176.501	177.644	179.515
1.920	226.951	226.819	228.044	-441.482	177.557	178.731	180.635
1.925	226.683	226.574	227.817	-440.718	177.424	178.615	180.534
1.928	228.042	227.949	229.214	-443.600	178.540	179.747	181.686
1.938	227.534	227.490	228.785	-454.933	177.161	178.321	180.212
1.958	228.428	228.102	229.157	-456.676	177.373	178.335	180.052
1.990	229.567	228.939	229.742	-459.319	177.758	178.511	180.046

2.031	228.903	228.097	228.749	-459.000	176.842	177.480	178.915
2.078	224.801	224.030	224.705	-451.966	173.485	174.163	175.628
2.126	217.377	216.837	217.687	-437.404	167.897	168.753	170.361
2.173	209.181	208.991	210.113	-420.201	162.126	163.240	165.058
2.216	201.336	201.529	202.949	-402.810	156.885	158.274	160.317
2.254	195.473	196.028	197.737	-389.271	153.284	154.930	157.189
2.287	190.788	191.652	193.608	-378.082	150.534	152.400	154.843
2.315	187.577	188.696	190.860	-370.149	148.816	150.863	153.461
2.339	185.102	186.423	188.752	-363.887	147.533	149.724	152.444
2.359	183.443	184.924	187.383	-359.543	146.760	149.065	151.883
2.375	182.258	183.862	186.424	-356.348	146.248	148.641	151.536
2.389	181.650	183.352	185.996	-354.558	146.095	148.560	151.517
2.399	181.573	183.352	186.064	-354.073	146.282	148.804	151.813
2.407	182.212	184.055	186.827	-355.336	146.964	149.536	152.594
2.412	183.892	185.787	188.614	-359.130	148.387	151.003	154.108
2.422	183.071	185.066	187.964	-372.400	146.644	149.231	152.304
2.442	183.875	185.611	188.290	-373.559	146.868	149.276	152.191
2.474	184.664	186.170	188.659	-375.233	147.145	149.398	152.182
2.513	183.729	185.145	187.563	-374.056	146.240	148.444	151.187
2.557	180.025	181.536	184.032	-367.288	143.425	145.713	148.527
2.602	173.960	175.709	178.393	-354.712	139.090	141.560	144.525
2.646	167.613	169.683	172.620	-340.499	134.876	137.582	140.742
2.686	161.940	164.343	167.546	-326.945	131.370	134.316	137.677
2.722	158.051	160.774	164.238	-317.132	129.301	132.478	136.035
2.753	155.146	158.141	161.830	-309.443	127.906	131.279	135.005
2.779	153.331	156.559	160.442	-304.352	127.241	130.781	134.654
2.801	152.023	155.437	159.476	-300.514	126.835	130.510	134.500
2.820	151.266	154.831	159.000	-298.095	126.743	130.529	134.618
2.835	150.833	154.521	158.795	-296.548	126.805	130.680	134.849
2.847	150.721	154.510	158.873	-295.875	127.037	130.987	135.225
2.857	150.735	154.604	159.038	-295.579	127.299	131.309	135.602
2.865	150.732	154.665	159.154	-295.298	127.495	131.552	135.888
2.872	151.117	155.109	159.654	-296.041	127.961	132.065	136.445
2.876	150.714	154.728	159.288	-294.854	127.742	131.861	136.252
2.879	151.291	155.344	159.943	-296.179	128.282	132.432	136.854

References

[1]. IAEA Technical Document, "Current Status and Future Development of Modular High Temperature Gas Cooled Reactor Technology", IAEA-TECDOC-1198, February 2001

[2]. R.A. Moore, et al., "HTGR Experience, Programs, and Future Applications", Nuclear Engineering and Design, 72, 153-174 (1982)

[3]. F.A. Silady, L.L. Parme, "The Safety Approach of the Modular High Temperature Gas Cooled Reactor (MHTGR)", 11th International Conference on the HTGR, Dimitrovgrad, June 13-16, 1989

[4]. K. Sawa, K. Minato, "An Investigation of Irradiation Performance of High Burnup HTGR Fuel", Journal of Nuclear Science & Technology, 36, No. 9, 781-791 (1999)

[5]. R.A.U. Huddle, J.R.C. Gough, H. Beutler, Dragon Project Report 116, October 1962

[6]. Proceedings Symposium Ceramic Matrix Fuels Containing Coated Particles, Battelle Memorial Institute, USAEC Report TID-7654, November 1962

[7]. R.J. Price, "Properties of SiC for Nuclear Fuel Particle Coatings", Nuclear Technology, 35, 320-336, (1977)

[8]. J.K. Kaae, Carbon, 13, 51 (1975)

[9]. R.E. Bullock, "Fission Product Release during Post-irradiation Annealing of Several Types of Coated Fuel Particles", Journal of Nuclear Materials, 125, 304 (1984)

[10]. J.W. Ketterer, R.E. Bullock, "Capsule HRB-15B Post-irradiation Examination Report", GA-A15940, June 1981

[11]. T. Ogawa, et al., Journal of the American Ceramic Society, 22, 2982 (1992)

[12]. K. Fukuda, K. Ikawa, K. Iwamoto, "Fission Product Diffusion in ZrC Coated Fuel Particles", Journal of Nuclear Materials, 87, 367-374 (1979)

[13]. R.L.R. Lefevre, M.S.T. Price, "Coated Nuclear Fuel Particles – The Coating Process and Its Model", Nuclear Technology, 35(2), 263 (1977)

[14]. M.T. Morgan, "Review of HTGR Coated Fuel Particle Stability", ORNL/TM-4882, August 1975

[15]. C.L. Smith, "Fuel Particle Behavior under Normal and Transient Conditions", General Atomic Report GA-A12971 (GA-LTR-15), October 1974

[16]. L.W. Graham, H. Hick, "Performance Limits of Coated Particle Fuel", Proceedings International Conference on Nuclear Fuel Performance, London, October 15-19, 1973

[17]. M. Wagner-Loffler, "Amoeba Behavior of UO_2 Coated Particle Fuel", Nuclear Technology, **35**, 392-402 (1977)

[18]. T.B. Lindemer, H.J. deNordwall, "An Analysis of Chemical Failure of Coated UO_2 Particles in HTGRs", Union Carbide Corp. Nuclear Div., ORNL-4926, 1974

[19]. J.W. Ketterer, B.F. Myers, "Capsule HRB-16 Post-irradiation Examination Report", HTGR-85-053, September 1985

[20]. F.J. Homan, et al., "Stoichiometric Effects on Performance of HTGR Fuels from the U-C-O System", Nuclear Technology, **35(2)**, 428 (1977)

[21]. H. Grubmeier, et al., "SiC Corrosion in HTGR Fuel Particles", Nuclear Technology, **35**, 413-427 (1977)

[22]. W.J. Scheffel, I.M. Tang, "Technical Support Document for the MHTGR Fuel Production Specification", GA Doc 903728, Issue D, 1989

[23]. T.D. Gulden, et al., "The Mechanical Design of TRISO Coated Particle Fuels for the Large HTGR", GA-A12051, July 1972

[24]. P.R. Kasten, et al., "Fuel Performance in Modular High-Temperature Gas-Cooled Reactors", Internal Report KFA-ISR-IB-12/94, October 1994

[25]. R. Gontard, H. Nabielek, "Performance Evaluation of Modern HTR TRISO Fuel", KFA Report HTA-IB-05/90, Julich, Germany, Appendix C, 1990

[26]. H.S. Carslaw, J.C. Jaeger, Conduction of Heat in Solids, Second Edition, 243-244, (Oxford University Press, 1959)

[27]. P.R. Kasten, et al., "Development of Correlations Between Fuel Performance and Test Parameters in Modular High-Temperature Gas-Cooled Reactors", Internal Report KFA-ISR-IB-9/94, June 1994

[28]. D. Dobranich, "Heat Transfer and Thermal Stress Analysis of the Multilayerd Spherical Particles of a Particle Bed Space Reactor", SAND90-1032, 1991

[29]. A.F. Mills, Heat and Mass Transfer, Sec. 4.5.2, (Irwin, 1995)

[30]. R.B. Bird, W.E. Stewart, E.N. Lightfoot, Transport Phenomena, (John Wiley & Sons, 1960)

[31]. M.M. El-Wakil, Nuclear Heat Transport, 104, (The American Nuclear Society, 1993)

[32]. R.J. Price, "Thermal Conductivity of Neutron-Irradiated Pyrolytic β-Silicon Carbide", Journal of Nuclear Materials, **46**, 268 (1973)

[33]. J. Li, et al., "Atomistic Modeling of Finite-Temperature Properties of Crystalline β-SiC (Part II)", Journal of Nuclear Materials, **255**, 139-152 (1998)

[34]. R.E. Taylor, et al., "Thermophysical Properties of CVD SiC", TRPL 1336, Thermalphysical Properties Research Laboratory Report, School of Mechanical Engineering, Purdue University, November 1993

[35]. D.J. Senor, et al., Fusion Technology, **30**, 943 (1996)

[36]. M.J. Kania, H. Nickel, "Performance Assessment of the $(Th,U)O_2$ HTI-BISO Coated Particle Under PNP/HHT Irradiation Conditions", JUL-1685, 1980

[37]. F. Ho, "Material Models of Pyrocarbon and Pyrolytic Silicon Carbide", CEGA-002820, Rev. 1, July 1993

[38]. A. Thomas, Combustion and Flame, **6**, 46 (1962)

[39]. B.E. Warren, Journal of Chemical Physics, **2**, 551 (1934)

[40]. J.C. Bokros, "Deposition, Structure, and Properties of Pyrolytic Carbon", Chemistry and Physics of Carbon, **5**, 8-115 (1969)

[41]. G.E. Bacon, Journal of Applied Chemistry, **6**, 477 (1956)

[42]. R.J. Price, "Young's Modulus of Pyrolytic Carbon in Relation to Preferred Orientation", Philosophical Magazine, **12**, 561 (1965)

[43]. P.P. Gillis, "Calculation of Elastic Constants of Graphite", Carbon, **22**, 387 (1984)

[44]. R.J. Price, J.C. Bokros, "Mechanical Properties of Neutron-Irradiated Pyrolytic Carbon", Journal of Nuclear Materials, **21**, 158 (1967)

[45]. J.L. Kaae, "Effect of Irradiation on the Mechanical Properties of Isotropic Pyrolytic Carbons", Journal of Nuclear Materials, **46**, 121 (1973)

[46]. J.L. Kaae, "The Mechanical Behavior of Biso-Coated Fuel Particles During Irradiation, Part I: Analysis of Stresses and Strains Generated in the Coatings of a Biso Fuel Particle During Irradiation", Nuclear Technology, **35**, 359 (1977)

[47]. J.L. Kaae, "The Mechanical Behavior of Biso-Coated Fuel Particles During Irradiation, Part II: Prediction of Biso Particle Behavior During Irradiation With a Stress Analysis Model", Nuclear Technology, **35**, 368 (1977)

[48]. J.L. Kaae, "Relation Between the Structure and the Mechanical Properties of Fluidized-Bed Pyrolytic Carbons", Carbon, **9**, 291 (1971)

[49]. F. Ho, "Graphite Design Handbook", DOE-HTGR-88111/0, September 1988

[50]. R.J. Price, J.L. Kaae, "Poisson's Ratio of Pyrolytic Carbon", Carbon, **7**, 707 (1969)

[51]. R.J. Price, "Structure and Properties of Pyrolytic Silicon Carbide", Bulletin of American Ceramic Society, **48**, 859 (1969)

[52]. T.D. Gulden, "Mechanical Properties of Polycrystalline β-SiC", Journal of American Ceramic Society, **52**, 585-590 (1969)

[53]. K. Bongartz, et al., "Measurement of Young's Modulus and Fracture Stress on HTR Particle Coatings by the Brittle Ring Test", Journal of Nuclear Materials, **45**, 261 (1972)

[54]. K. Bongartz, et al., "The Brittle Ring Test: A Method for Measuring Strength and Young's Modulus on Coatings of HTR Fuel Particles", Journal of Nuclear Materials, **62**, 123 (1976)

[55]. E. Wallura, et al., "Characteristic Study of the Silicon Carbide Coating Layer of a Fuel Particle", Nuclear Research Center Julich, Gmbh, Institute for Reactor Materials, Jul-1871, September 1983

[56]. B.O. Yavuz, R.E. Tressler, "High Temperature Mechanical Behavior of a Chemically Vapor Deposited Beta Silicon Carbide", Ceramics International, **8**, 19 (1992)

[57]. J. Gibson, "Calculations of TRISO Particle Behavior with the TRISO Stress Analysis", GA 906291/1, September 1981

[58]. J.L. Kaae, "Irradiation-Induced Microstructural Changes in Isotropic Pyrolytic Carbons, Journal of Nuclear Materials, **57**, 82-92 (1975)

[59]. J.C. Bokros, et al., "Radiation-Induced Dimensional Changes and Creep in Carbonaceous Materials", Journal of Nuclear Materials, **31**, 25 (1969)

[60]. J.L. Kaae, J.C. Bokros, "Irradiation-Induced Dimensional Changes and Creep of Isotropic Carbon, Carbon, **9**, 111 (1969)

[61]. J.L. Kaae, et al., "Dimensional Changes and Creep of Poorly Crystalline Isotropic Carbons and Carbon-Silicon Alloys During Irradiation", Carbon, **10**, 571 (1972)

[62]. J.L. Kaae, "Behavior of Pyrolytic Carbons Irradiated Under Mechanical Restraint", Carbon, **12**, 577 (1974)

[63]. J.L. Kaae, et al., "Dimensional Changes Induced in Poorly Crystalline Isotropic Carbons by Irradiation", Carbon, **10**, 561 (1972)

[64]. J.C. Bokros, et al., "Effect of High Neutron Exposure on the Dimensions of Pyrolytic Carbons", Carbon, **7**, 143 (1969)

[65]. D. Pelessone, "PISA: A Coupled Thermal-Stress Code for the Mechanical Analysis of Irradiated Fuel Particles", CEGA-002550, Rev. 0, July 1993

[66]. J.L. Kaae, "On Irradiation-Induced Creep of Pyrolytic Carbon in a General State of Stress", Journal of Nuclear Materials, **34**, 208 (1970)

[67]. H.O. Pierson, Handbook of Carbon, Graphite, Diamond and Fullerenes, 58-60, (Park Ridge, N.J., U.S.A.: Noyes Publications 1993)

[68]. F. Ho, "H-451 Graphite Irradiation Creep Design Model", DOE-HTGR-88097/1, July 1988

[69]. J.J. Gebhardt, J.M. Berry, "Mechanical Properties of Pyrolytic Graphite", AIAA Journal, **3**, 302 (1964)

[70]. Z. Li, C. Bradt, Journal of Material Science, **21**, 4366 (1986)

[71]. A. Taylor, R.M. Jones, in: Silicon Carbide, a High-Temperature Semiconductor, ed. J.R. O'Connor and J. Smiltens, 147, (Pergamon, Oxford, 1960)

[72]. L.J. Porter, J. Li, S. Yip, "Atomistic Modeling of Finite-Temperature Properties of β-SiC (Part I)", Journal of Nuclear Materials, **246**, 57 (1997)

[73]. J.W. Prados, J.L. Scott, "Analysis of Stress and Strain in Spherical Shells of Pyrolytic Carbon", ORNL-3533, 1964

[74]. W. Weibull, "A Statistical Distribution Function of Wide Applicability", Journal of Applied Mechanics, **18** (1951)

[75]. E.Y. Robinson, "The Statistical Nature of Fracture", Lawrence Radiation Laboratory Report No. UCRL-50622, 1969

[76]. A.S. Jayatilaka, "Fracture of Engineering Brittle Materials", Appliced Science, 1979

[77]. A.M. Freudenthal, "Statistical Approach to Brittle Fracture", Fracture, An Advanced Treatise, **2**, 591, (H. Liebowitz, ed., Academic Press 1968)

[78]. E. Ryshkewith, "Compression Strength of Porous Sintered Alumina and Zirconia", Journal of American Ceramic Society, **36**, 65 (1953)

[79]. W. Duckworth, "Discussion of Ryshkewith Paper", Journal of American Ceramic Society, **36**, 68 (1953)

294

[80]. E. Orowan, "Fracture and Strength of Solids", Reports on Progress in Physics, **12**, 186 (1948)

[81]. N.J. Petch, "Cleavage Strength of Polycrystals", Journal of the Iron and Steel Institute, London, **174**, 25 (1953)

[82]. F.P. Knudsen, "Dependence of Mechanical Strength of Brittle Polycrystalline Specimens on Porosity and Grain Size", Journal of American Ceramic Society, **42**, 376 (1959)

[83]. A.G. Evans, et al., "Strength of Pyrolytic SiC Coating of Fuel Particles for High Temperature Gas-cooled Reactors", Journal of American Ceramic Society, **56**, 36-41 (1973)

[84]. A. Briggs, et al., "Crushing Behavior of High Temperature Reactor Coated Fuel Particles", Journal of Nuclear Materials, **61**, 233 (1976)

[85]. R.E. Bullock, "Design of Coated Fuel Particles for a Hybrid Fusion-Fission System", Nuclear Engineering and Design, **61**, 331 (1980)

[86]. J.W. Ketterer, "Coated Particle Mechanical Properties Test Evaluation Report", General Atomics Document 910105 N/C, March 1990

[87]. N.N. Nemeth, et al., "Design of Ceramic Components with the NASA/CARES Computer Program", Ceramic Bulletin, **68**, 2064 (1989)

[88]. R.R. Hobbins, et al., "NP-MHTGR Fuel Development Program Results", Idaho National Engineering Laboratory, Lockheed Idaho Technologies Company, 1993

[89]. D. Petti, et al. "Key Differences in the Fabrication, Irradiation and Safety Testing of U.S. and German TRISO-coated Particle Fuel and Their Implications on Fuel Performance", Idaho National Engineering Laboratory, INEEL/EXT-02-00300, , 148 – 151, April 2002

[90]. G.K. Miller, et al., "Consideration of the Effects on Fuel Particle Behavior from Shrinkage Cracks in the Inner Pyrocarbon Layer", Journal of Nuclear Materials, **295**, 205-212 (2001)

[91]. G. Tsamasphyros, A.E. Giannakopoulos, "The Use of Conformal Mapping for Creating Singular Elements", Engineering Fracture Mechanics, **28**, No. 1, 55-65 (1987)

[92]. S.K. Chan, et al., "On the Finite Element Method in Linear Fracture Mechanics", Engineering Fracture Mechanics, **2**, 1-17 (1970)

[93]. J.E. Akin, "The Generation of Elements with Singularities", International Journal for Numerical Methods in Engineering, **10**, 1249-1260 (1976)

[94]. T.L. Anderson, Fracture Mechanics: Fundamentals and Applications, 2nd Ed., 111, (CRC Press LLC 1995)

[95]. J. Hutchinson, Z. Suo, "Mixed Mode Cracking in Layered Materials", Advances in Applied Mechanics, **29**, 129-138 (1992)

[96]. J. Dundurs, "Edge-Bonded Dissimilar Orthogonal Elastic Wedges", Journal of Applied Mechanics, **36**, 650-652 (1969)

[97]. H. Tada, P.C. Paris, G.R. Irwin, The Stress Analysis of Cracks Handbook, 3rd ed., (ASME Press 2000)

[98]. M.J. Slavin, G.D. Quinn, "Mechanical Property Evaluation at Elevated Temperature of Sintered ß-Silicon Carbide," International Journal of High Technology Ceramics, **2**, 47-63 (1986)

[99]. S. W. Freiman, et al., "Fracture of Si3N4 and SiC", Ceramic Microstructures, 824-834 (1976)

[100]. Material Specification No. SC-001, Morton Advanced Materials, 185 New Boston Street, Woburn, MA 01801

[101]. L.A. Simpson, "Microstructural Considerations for the Application of Fracture Mechanics Techniques", Fracture Mechanics of Ceramics, **2**, 567-577 (1974)

[102]. J.R. McLaren, et al., "The Relationship Between Temperature and Environment, Texture and Strength of Self-Bonded Silicon Carbide", Proceedings of the British Ceramic Society, **20**, 259-274 (1972)

[103]. R.B. Matthews, et al., "A Relation Between Fracture and Flaws in Reaction-Bonded Silicon Carbide", Journal of the Canadian Ceramic Society, **42**, 1-9 (1973)

[104]. R.W. Rice, et al., "Grain-Size Dependence of Fracture Energy in Ceramics: I, Experiment", Journal of the American Ceramic Society, **64**, No. 6, 345-350 (1981)

[105]. A.G. Evans, E.A. Charles, "Fracture Toughness Determinations by Indentation", Journal of the American Ceramic Society, **59**, No. 7-8, 371-372 (1976)

[106]. J.L. Henshall, et al., "Fracture Toughness of Single-Crystal Silicon Carbide", Journal of the American Ceramic Society, **60**, No. 7-8, 373-375 (1977)

[107]. E. Techert, et al., "V.S.O.P (94) Computer Code System for Reactor Physics and Fuel Cycle Simulation", Research Center, Julich GmbH Jul-2897, April 1994

[108]. E. Kreyszig, Advanced Engineering Mathematics, 5th ed., 927, (John Wiley & Songs, Inc. 1983)

[109]. W. Press, Numerical Recipes, (Cambridge, Cambridge University Press, 1986)

[110]. M.F. Bryan, "Evaluation of NP-MHTGR Performance Test Fuel Quality Control Data", EGG-NPR-10130, 38-46, February 1992

[111]. A.S. Argon, S. Backer, F.A. McClintock, G.S. Reichenbach, E. Orowan, M.C. Shaw, E. Rabinowicz, Mechanical Behavior of Materials (Addison-Wesley, Reading, Massachusetts, 1966).

[112]. G. Miller, R. Bennett, "Analytical solution for stresses in TRISO-coated particles", Journal of Nuclear Materials, 206, 35-49 (1993).

[113]. L.A.De Lacerda, L.C. Wrobel, "Dual Boundary Element Method for Axisymmetric Crack Analysis", International Journal of Fracture, 113, 267-284 (2002)

[114]. R.G. Bennett, et al., "User's Manual for the NP-MHTGR Fuel Code", EG&G Idaho, Inc., Idaho National Engineering and Environmental Laboratory, 1993

[115]. K. Sawa, et al. "Fabrication of the First-Loading Fuel of the High Temperature Engineering Test Reactor", Journal of Nuclear Science and Technology, 36, No. 8, 683-690 (1999)

[116]. K. Sawa, et al. "Development of a Coated Fuel Particle Failure Model under High Burnup Irradiation", Journal of Nuclear Science and Technology, 33, No. 9, 712-720 (1996)

[117]. D.R. Olander, "Fundamental Aspects of Nuclear Reactor Fuel Elements", TID-26711-P1, 1976

[118]. C.A. Baldwin, et al., "The New Production Reactor Fuel Post Irradiation Examination Data Report for Capsules NPR1, NPR2, and NPR1A", ORNL/M-2849, September 1993

[119]. J.D. Landes, J.A. Begley, "A Fracture Mechanics Approach to Creep Crack Growth", ASTM STP 590, American Society for Testing and Materials, Philadelphia, 128-148 (1976)

[120]. K. Ohji, et al., Transactions, Japanese Society of Mechanical Engineers, 42, 350-358 (1976)

[121]. K.M. Nikbin, et al., ASTM STP 601, American Society for Testing and Materials, Philadelphia, 47-62 (1976)

[122]. N.J. Hoff, "Approximate Analysis of Structures in the Presence of Moderately Large Creep Deformations", Quarterly of Applied Mathematics, 12, 49-55 (1954)

[123]. H. Riedel, "Creep Crack Growth", ASTM STP 1020, American Society for Testing and Materials, Philadelphia, 101-126 (1989)

[124]. J. Saurwein, L. Shilling, "Final Report – Testing of As-Manufactured NPR-PTF, German and U.S. Historical Fuel", General Atomics, Doc. No. 910647 N/C, September 1993

[125]. PBMR Safety Analysis Report, Chapter 4, Document No. 001929-207/4, Rev. B, 6-17 (PBMR 2000)

[126]. H. Nabielek, et al., "Development of Advanced HTR Fuel Elements", Nuclear Engineering Design, **121**, 199-210 (1990)

[127]. K. Verfondm, "Fuel Performance and Fission Product Behavior in Gas-Cooled Reactors", FZJ-ISR-IB-3/97, April 1997

[128]. H. Ragoss, "Experimental Safety of the Fuel Elements for Normal and Accident Conditions of the HTR-Modul", INTERATOM 76.00526.9, September 1987

[129]. H. Nabielek, "Quantitative Evaluation of the Performance of German HTR Fuel under Normal Operating and under Accident Conditions", KFA ISR-IB-19/93, December 1993 (Reprinted August 1999)

[130]. R.O. Grisdale, Journal of Applied Physics, **24**, 1082 (1953)

[131]. R.O. Grisdale, et al., Bell System Technical Journal, **30**, 271 (1951)

[132]. B.E. Warren, Physics Review, **59**, 693 (1941)

[133]. P. Scherrer, Nachr. Akad. Ges. Wiss. Goettingen, **2**, 98 (1918)

[134]. G. E. Bacon, Acta Crystallographica, **4**, 558 (1951)

[135]. J.C. Bokros, Carbon, **3**, 17-201 (1965)

[136]. R.W. Dayton, et al., Ceramic Matrix Fuels Containing Coated Particles Process Symposium, Battelle Memorial Institute, USAEC Rept. TID-7654, 10-68, November 1962

[137]. R.J. Bard, et al., Carbon, **6**, 603 (1968)

[138]. J.C. Bokros, et al., Nature, **204**, 371 (1964)

[139]. R.L. Beatty, et al., Nuclear Applications, **1**, 560 (1965)

[140]. M.F. Browning, et al., Battelle Memorial Institute, USAEC Rept. BMI-1735, July 1965

[141]. R.L. Beatty, Oak Ridge National Laboratory, USAEC Rept. ORNL-TM-1649, January 1967

[142]. R.E. Duff, S.H. Bauer, Los Alamos Scientific Laboratory, USAEC Rept. LA-2556, 1961

[143]. C. David, et al., Carbon, **1**, 139 (1964)

[144]. R.J. Diefendorf, Journal de Chimie Physique (Paris), **57**, 815 (1960)

[145]. F. Fischer, Proceedings of Second International Conference on Bit. Coal, **2**, 789 (1928)

[146]. R.J. Price, et al., Carbon, **4**, 263 (1966)

[147]. G.B. Spence, Proceedings of the Fifth Conference on Carbon, **2**, 531, (Pergamon Press, New York, 1962)

[148]. J.C. Bokros, R.J. Price, Carbon, **3**, 503 (1966)

[149]. J.M. Blocher Jr., et al., Nuclear Science and Engineering, **20**, 153 (1964)

[150]. P.A. Tesner, I. M. Timofeeva, Khim. Prom., **3**, 52 (1962)

[151]. D.J. Cole, G.J. Minkoff, Proceedings of Royal Society (London), **A239**, 280 (1957)

[152]. J.H.W. Simmons, "Radiation Damage in Graphite", (Macmillan (Pergamon), New York, 1965)

[153]. J.C. Bokros, R.J. Price, Carbon, **4**, 441 (1966)

[154]. J.C. Bokros, A.S. Schwartz, Carbon, **5**, 481 (1967)

[155]. J.G. Castle, Jr., Proceedings of the First and Second Conferences on Carbon, 13, (Pergamon Press, New York, 1956)

[156]. V. Coen, et al., "Cesium Migration in Silicon Carbide", Journal of Nuclear Materials, **45**, 96 (1972/73)

[157]. V. Coen, et al., "Interaction between Silicon Carbide, Cesium, and Strontium", Proceedings of BNES International Conference of Nuclear Fuel Performance, British Nuclear Energy Society, London, 19.1 (1973)

[158]. E.H. Voice, et al., "The Behavior of Silicon Carbide Coatings in the HTR", Proceedings of BNES International Conference of Nuclear Fuel Performance, British Nuclear Energy Society, London, 20.1 (1973)

[159]. E.H. Voice, "Silicon Carbide as a Fission Product Barrier in Nuclear Fuels", Silicon Carbide-1968, S331, (H.K. Henisch and R. Roy, Eds., Pergamon Press, New York, 1969)

[160]. R.J. Price, "Effects of Fast Neutron Irradiation on Pyrolytic Silicon Carbide", Journal of Nuclear Materials, **33**, 17 (1969)

[161]. W. Primak, et al., "Radiaton Damage in Diamond and Silicon Carbide", Physical Review, **103**, 1184 (1956)

[162]. M. Balarin, "The Temperature Dependence of Irradiation Saturation in SiC", Physica Status Solidi., **11**, K67 (1965)

[163]. R.P. Thorne, et al., "Radiation Induced Changes in Porous Cubic Silicon Carbide", Proceedings of British Ceramic Society, **7**, 449 (1967)

[164]. R.B. Matthews, "Irradiation Damage in Reaction Bonded Silicon Carbide", Journal of Nuclear Materials, **51**, 203 (1974)

[165]. R. Stevens, "Neutron Irradiation Damage in SiC Whiskers", Philosophical Magazine, **25**, 523 (1972)

[166]. B.J. Leikind, et al., "MHTGR TRISO-P Fuel Failure Evaluation Report", General Atomics, DOE-HTGR-90390, Revision 0, 3-36, October 1993

[167]. G.K. Miller, D.C. Wadsworth, "Treating Asphericity in Fuel Particle Pressure Vessel Modeling", Journal of Nuclear Materials, **221**, 57-69 (1994)

[168]. J. Drowart, et al., "Thermodynamic Study of SiC Using a Mass Spectrometer", Journal of Chemical Physics, **29**, 1015 (1958)

[169]. P. Grieveson, C.B. Alcock, "The Thermodynamics of Metal Silicides and Silicon Carbide", Special Ceramics, 183, (P. Popper, Ed., Academic Press, Inc., New York, 1960)

[170]. R.N. Ghoshtagore, "Decomposition of Single Crystal Silicon Carbide", Solid State Electronics, **9**, 178 (1966)

[171]. D.T. Goodin, H. Nabielek, "The Performance of HTR Fuel in Accidents", KFA Report HBK-TN-19/85, December 1985

[172]. "Development of Improved Models and Designs for Coated-Particle Gas Reactor Fuels", I-NERI Annual Report, INEEL/EXT-02-01493, 53, November 2002

[173]. D.E. Knuth, The Art of Computer Programming, 2nd Ed., **2**, 28, (Addison-Wesley, 1981)

[174]. G. Marsaglia, "A Current View of Random Number Generators", Computer Science and Statistics: The Interface, L. Billard (ed.), (Elsevier Science Publishers B. V. (North-Holland), 1985)